Offshore Loading and Discharge in Heavy Marine Transport

Peters, Onno

DOI
10.4233/uuid:ea734d91-bd46-4180-9ccb-1ee86c54e775

Publication date
2019

Document Version
Final published version

Citation (APA)
Peters, O. (2019). *Offshore Loading and Discharge in Heavy Marine Transport*. [Dissertation (TU Delft), Delft University of Technology]. https://doi.org/10.4233/uuid:ea734d91-bd46-4180-9ccb-1ee86c54e775

Offshore Loading and Discharge in Heavy Marine Transport

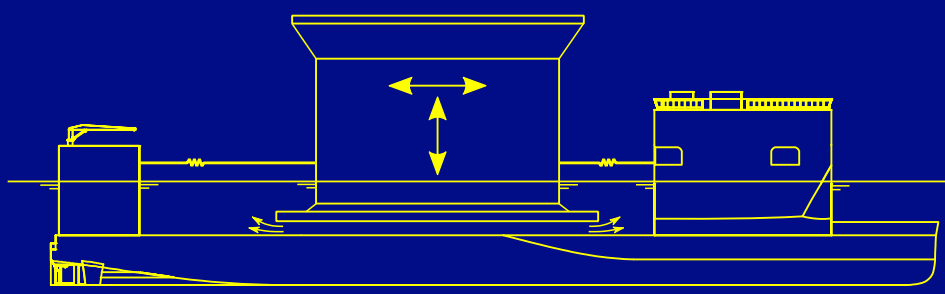

O.A.J. Peters

Offshore Loading and Discharge

in Heavy Marine Transport

Offshore Loading and Discharge

in Heavy Marine Transport

Proefschrift

ter verkrijging van de graad van doctor
aan de Technische Universiteit Delft,
op gezag van de Rector Magnificus Prof.dr.ir. T.H.J.J. van der Hagen,
voorzitter van het College voor Promoties,
in het openbaar te verdedigen op dinsdag 3 december 2019 om 12:30 uur

door

Onno Anton Johan PETERS

Maritiem ingenieur
Technische Universiteit Delft, Nederland
geboren te 's-Hertogenbosch, Nederland

Dit proefschrift is goedgekeurd door de promotoren:

Prof. dr. ir. R.H.M. Huijsmans
dr. ir. S.A. Miedema

Samenstelling promotiecommissie:

Rector Magnificus,	voorzitter
Prof. dr. ir. R.H.M. Huijsmans,	Technische Universiteit Delft, promotor
dr. ir. S.A. Miedema	Technische Universiteit Delft, promotor

onafhankelijke leden:

Prof. dr. B. Molin	Ecole Généraliste d'Ingenieurs
Prof. dr. P. Ferrant	Ecole Centrale de Nantes
Prof. dr. ir. C.H. Venner	Universiteit Twente
Prof. dr. A. Metrikine	Technische Universiteit Delft
dr. ir. J.L.F. van Kessel	Shell
Prof. dr. ir. M.L. Kaminski	Technische Universiteit Delft, reservelid

The research reported in this document has been supported and completely funded by Dockwise (subsidiary of Royal Boskalis Westminster N.V.)

Keywords: Heavy Marine Transport, multi-body dynamics, potential theory, multi-domain diffraction, squeeze flow, offshore discharge, offshore loading, mooring, relative motions, motion control, handling equipment, hydraulic cylinder, fenders

Front & Back: Submerging before discharge of the FPSO P67 from the Boka Vanguard

An electronic version of this dissertation is available at `http://repository.tudelft.nl/`.

To inspire Puck, Kick and Luiz.

Be who you want to be.

Summary

Dry transporting large heavy floating structures has been an important development in the innovative history of Heavy Marine Transport. This is done by carrying these type of cargoes on the deck of Heavy Transport Vessels. Loading and discharge is preformed by submerging the transport vessel, and positioning the cargo above the deck using tugger winches. Traditionally, these operations take place in sheltered locations, like harbours, where virtually no waves occur.

From the beginning Heavy Marine Transport has served the oil and gas industry in the exploration, development and production phase of offshore oil and gas fields. In search of optimizing profitability of remote offshore fields, optimizing fabrication and installation of facilities is essential. Delivering the facilities directly at the remote fields is recognized as a potential cost saving. Also, Inspection, Maintenance and Repair by offshore dry-docking is a potential cost optimisation. Both imply that loading and discharge operations need to be carried out in exposed areas, where wave conditions do occur. It is evident that, to ensure acceptable workability and safe operation, it is important to accurately prediction the dynamic motions and to assess and design the mooring and handling equipment.

Experience and model testing has shown that prediction of vertical relative motions using industry standard software was inaccurate; generally, the relative vertical motions were significantly over-predicted. Also, it has been shown that horizontal relative motions are too large to safely place the cargo on cribbing support, while using the standard handling equipment. These issues have resulted in the development of an accurate method to predict relative vertical motions and the development of cargo handling equipment for accurate positioning of the cargo.

The first part of the research has focused on the relative vertical motions. Based on fundamental model test, CFD calculations and literature, the highly non-linear effects of squeeze flow between the cargo bottom and

the deck of the transport vessel are proven. The largest contribution to this non-linear effect is the changing of added mass depending on the gap between the cargo bottom and the vessel deck. To a lesser extend, also viscous effects in terms of eddy making are present. To determine the added mass depending on the gap height, potential flow programs are used. However, numerical issues exist for industry standard software when very small gaps are analysed. Different methods have been explored to improve the accuracy of predicting the added mass.

Validation with forced oscillation tests showed a good resemblance between measurement and simulation. Also, a large reduction of the vertical motion for a free-floating object is shown when accounting for the non-linear effects.

The second part of the research entails the development of systems to significantly reduce the horizontal relative motions with respect to the motions resulting from the use of standard equipment. When designing the systems, the three main considerations are creating a stiff connection and/or damping the motions and/or applying active control. This has lead to two concepts.

First concept is the Clamping System, which relies on creating a stiff connection with stiffness equivalent to a structural support. To realize this safely without damaging the cargo, the system needs to transition from a soft to a stiff connection. This is achieved by applying a hydraulic cylinder in a fender. The cylinder contains a control valve through which the fluid flows when the fender is compressed, and it contains a one-way valve when the flow is returning when the fender is de-compressed. By gradually closing the control valve of the cylinder, the reaction load will be higher than the fender compression load during compression stroke, while the one-way valve ensures that the reaction load is lower than the fender compression load at the return stroke. As such, enough damping is created to avoid resonant behaviour when the changing system natural period is passing the wave excitation periods. Finally, when the control valve is fully closed, a stiff connection is achieved.

Second concept is the Line Tension Actuating System (LTAS). This system originates from the idea to compensate the stretch in the mooring lines. A system which would react on line tension would be unstable, therefore an active system with close-loop control is developed. Such a system is similar to Dynamic Positioning Systems, however the LTAS also compensates the

wave frequent motions. Based on measured relative motion, the required compensation load is determined, which is allocated to a set of line tension actuators. The actuator is based on a hydraulic cylinder, which actuation load is controlled using stored pneumatic energy. Stored energy is needed to be able to exert high loads, possible up to 600 [t], within 2 to 3 seconds.

Analyses has shown that both concepts are able to reduce the relative horizontal motions in a controlled and safe manner. Whether both systems or only the LTAS will be used for a specific operation mainly depends on the type and/or size cargo. The size and strength of the systems will depend on allowable positioning offset, operational sea-state limit and structural strength of both HTV and cargo. Also, operational aspects like line handling by crew must be considered during design of the equipment.

Concluding, with this research it is possible to accurately predict the relative motions between HTV and cargo during an Offshore Loading or Discharge Operations and to define operational limits and thus determine the workability.

List of Symbols

Constants

e		2.7182818...	
g	gravity	9.80665	$\mathrm{m/s^2}$
i	imaginary number	$i = \sqrt{-1}$	
π		3.1415927...	

Latin Letters

a_m	amplitude of motion, motion	mm, m
$\tilde{a}$	oscillating motion	mm, m
$\mathbb{A}$, $\mathbb{B}$, $\mathbb{C}$	domain area identifier	
A	added mass	
$\mathbf{A}$	added mass matrix	
A_f	accumulator face plate area	$\mathrm{m^2}$
A_i	piston area at cylinder chamber side i	$\mathrm{m^2}$
A_v	valve area	$\mathrm{m^2}$
b	damping factor	
$\mathbf{B}$	damping matrix	
$\mathbf{C}$	stiffness matrix	
C_D	drag coefficient	
$\tilde{C}_D$	linear damping term	m/s
d	draft	m

D	domain boundary surface		
$D_{id,jd}$	boundary surface part between domain id and jd		
$D_{id \leftarrow jd}$	boundary surface part between domain id and jd with normal direction towards id		
f	frequency	Hz	
$\tilde{\mathbf{F}}_{\mathbf{w}}$	wave force and moment vector	N, Nm	
F	force	N	
F_D	drag force	N	
$G(..)$	Green's function		
$\mathbf{G}$	Green's function matrix		
$\mathcal{G}$	normal derivative of Green's function matrix		$\frac{\partial}{\partial n}\mathbf{G}$
h	gap height	mm, m	
$\bar{h}$	mean or initial gap height	mm, m	
$\vec{h}$	gap height and inclination vector		$[z_r, \varphi_r, \psi_r]$
H, H_{id}	global waterdepth or waterdepth for domain id	m	
H_s	significant wave height id	m	
k	stiffness	N/m	
k_0	wave number		
k_d	discharge coefficient of valve		
K_a	accumulator spring stiffness	N/m	
$\bar{m}$	location integration point in planar coordinates $\bar{x}$		
M	moment	Nm	
n	direction normal to the body surface as in $\partial/\partial n$		
$\vec{n}$	normal direction	m	$[n_1, n_2, n_3]$
n_b	number of bodies		
n_d	number of domains		
$\vec{N}$	direction cosinus vector		
N_j	normal velocity boundary condition for mode j		

$p(\vec{x})$	fluid pressure at location $\vec{x}$	N/m^2	
$\mathbf{p}(\vec{x}, t)$	fluid pressure at location $\vec{x}$ as a function of time	N/m^2	
p_i	pressure at cylinder chamber side i	N/m^2	
P_{sf}	squeeze flow fluid pressure	N/m^2	
r	radial distance	m	
R	cylinder or disk radius	mm, m	
s	piston stroke	m	
S	body surface	mm^2, m^2	
S_b	bounded surface to represent the gap domain		
$S_{ib,id}$	surface part of body ib at boundary to domain id		
t	time	s	
T_n	natural period	s	
U	vertical velocity	m/s	
$\vec{v}$	fluid velocity vector	m/s	$[\dot{x}, \dot{y}, \dot{z}]$
v_j^D	velocity boundary condition on interface surface D		
$V_{ac,ini}$	initial volume in accumulator	m^3	
V_i	volume at cylinder chamber side i	m^3	
$\bar{x}$	planar coordinates	m	$[\check{x}, \check{y}]$
$\vec{x}$	spacial coordinates	m	$[x, y, z]$
$\tilde{x}$	motion vector		
$\dot{\tilde{x}}$	velocity vector		
$\ddot{\tilde{x}}$	acceleration vector		

Greek Letters

α	wave direction	deg
β	bulk modulus	Pa

ζ_a	wave amplitude	m	
θ	rotation about y-axis	deg	
κ	wave number	1/m	$\kappa = 2\pi/\lambda$
λ	wave length	m	
ν	dispersion relation	1/m	
$\bar{\xi}$	planar coordinate vector for a point on a bounded surface	m	$[\check{\xi}, \check{\eta}]$
$\vec{\xi}$	coordinate vector for a point on a wetted surface	m	$[\xi, \eta, \zeta]$
ρ	water density	kg/m^3	
σ_j	source strength due to velocity potential mode j	m/s	
τ	integrator constant	s	
$\phi(\vec{x})$	spacial velocity potential at location $\vec{x}$	m^2/s	
ϕ_j	velocity potential j	m^2/s	
ϕ_j^D	pressure boundary condition on interface surface D	m^2/s	
ϕ_b	velocity potential at the boundary of a gap domain	m^2/s	
ϕ_d, ϕ_7	diffracted wave velocity potential	m^2/s	
ϕ_w, ϕ_0	undisturbed incident wave velocity potential	m^2/s	
φ	rotation about x-axis	deg	
$\Phi(\vec{x}, t)$	total velocity potential	m^2/s	
Φ_d, Φ_7	total velocity potential due to the diffracted wave	m^2/s	
Φ_R	total velocity potential due to the radiated wave	m^2/s	
Φ_w, Φ_0	total velocity potential due to the undisturbed incident wave	m^2/s	
ψ	rotation about z-axis	deg	
ω	wave frequency	rad/s	
ω_n	natural frequency	rad/s	

Subscripts & Indices

1, 2, ...	body numbering
a, b, ...	domain numbering
ib, jb	body number index
id, jd	domain number index
j	potential component index
m, n	mode of motion
r	relative

Nomenclature

CFD	Computational Fluid Dynamics
CIF	Convolution Integral Function
CS	Clamping System
DLL	Dynamic Link Library
FPSO	Floating Production, Storage and Offloading tanker
HMDDM	Hybrid Multi Domain Diffraction Method
HMPE	High Modulus PolyEthylene
HMT	Heavy Marine Transport
HTV	Heavy Transport Vessel
IMR	Inspection, Maintenance and Repair
LMU	Leg Mating Unit
LTAS	Line Tension Actuating System
MBL	Minimum Breaking Load
MDDM	Multi Domain Diffraction Method
MWS	Marine Warranty Surveyor
RAO	Response Amplitude Operator
SWL	Safe Working Load
T&I	Transport & Installation
TLP	Tension Leg Platform
VoF	Volume of Fluid method

Contents

Background

CHAPTER 1

Introduction

1.1 History of Heavy Marine Transport

The Dutch were the first to realize the savings that could be made when transporting large, heavy pieces of cargo in one go (Hoogenhuyze and Vandersmissen [13]). Shipowner Van der Laan was the first to build a 'Big-lift' ship, followed by the companies like Mammoet Transport and Jumbo Shipping. Since mid 1950's, Heavy Marine Transport (HMT) was recognized by ships with cranes being able to lift-on and lift-off heavy cargo (Krabbendam and Beerendonk [19]). As the weight and size of cargo gradually increased, innovative solutions for loading and discharge were found, like roll-on/-off and skid-on/-off. Also, crane capacities increased, and — to accommodate heavier cargo — stability pontoons were developed to increase the vessel stability.

Simultaneous with the evolving heavy lift ships, the heavy transport vessels were developed. The first self propelled semi-submersible dock-type heavy transport vessel (HTV), named *Docklift 1* and built in 1972 (van Hoorn [14]), was ordered by Van der Laan, co-founder of BigLift. This same man started the company Dock Express Shipping in 1978 and ordered three dock-type ships with a capacity of about 13,000 ton. The dock-type vessel was capable of floating on and floating off cargo into its cargo hold via the stern. As such the cargo size was limited by the dimensions of the dock. Therefore, initially, floating cargo like jack-up and semi-submersible rigs were only wet towed all over the world.

In 1973 the first rig was dry transported on a towed barge. A couple of years later, the first custom-built semi-submersible barges and the first

heavy transport vessel, from converted tankers, were introduced. Then, in 1979, the first self-propelled HTV with an open deck — capable of transporting cargo with larger width than the HTV itself — came in to service, being the *Super Servant I*; soon followed by the *Might Servants*, all owned by Wijsmuller. An alternative design was introduced in 1981, being the so-called closed stern type; vessel with a lower cargo deck section amidships.

With the *Transshelf* coming into service in 1986, the development and growth of heave transport vessels came to a stop for 13 years. From 1999, new HTVs came in the market and existing HTVs were increased in size by lengthening and widening. Since between 2008 and 2010, many new-built HTVs were ordered; most of them have a deadweight capacity of about 50,000 metric tons. The most recent innovation in HMT is the so-called type-0 concept with about 110,000 metric tons deadweight capacity; the first of this type with an open stern and bow came in to service as the *Dockwise Vanguard* (Figure 1.1) at the end of 2012.

Figure 1.1: SSHTV *Dockwise Vanguard*

When looking at the innovative history of the Heavy Marine Transport, one should not forget the tragic and unfortunate accidents. The *Mighty Servant 2* capsized on 2 November 1999 near the Indonesian island of Singkep. The ship was en route from Singapore to Cabinda, Angola, carrying the North Nemba Topsides 8,790-ton offshore production module. The vessel tipped over onto its side in 35 meters of water in reportedly calm seas. A hydro-graphic survey of the area later discovered an unmarked single isolated pinnacle of granite directly on the ship's course. Five crew members perished. On 6 December 2006 Mighty Servant 3 sank in 62 m (203 ft) near the port of Luanda, Angola, while offloading the drilling platform Aleutian Key. During submerging to unload cargo, the ship developed a trim and continued to submerge beyond design limits. There were no casualties, nor damage to the transported platform. On the night of 26-27 October 2008, a jack-up lift boat used to install wind turbines was lost at sea in the Atlantic. *KS Titan-1* was loaded aboard the semi-submersible heavy-lift vessel *Ancora*, which was en route from Pascagoula to Liverpool, when the heavy transport vessel encountered main engine problems in mid-Atlantic. The rolling and tilting motion resulted in *KS Titan-1* shifting to the port side and capsizing.

1.2 Heavy Marine Transport Operations

The HMT operations involve much more than sailing from one to another location, as illustrated in Figure 1.2. Basically, the HMT scope consist of transport engineering, preparation of the HTV (and possibly the cargo), loading operation, voyage and discharge operation. The technical scope starts with engineering a transport, consisting of designing cargo support, sea-fastenings and all that is needed to safely transport a cargo on a HTV. An important part of transport engineering is establishing the design

Figure 1.2: Heavy Marine Transport Scope

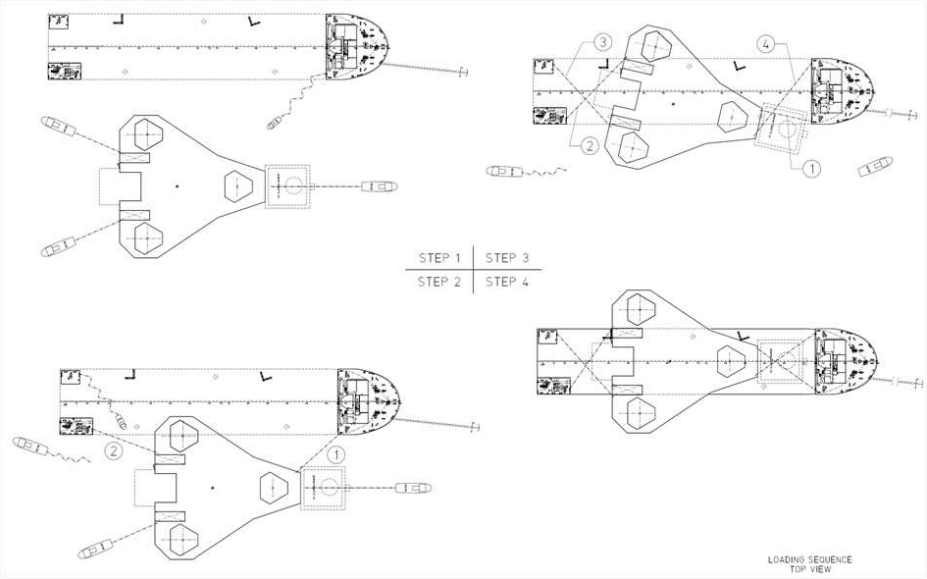

Figure 1.3: Loading sequence

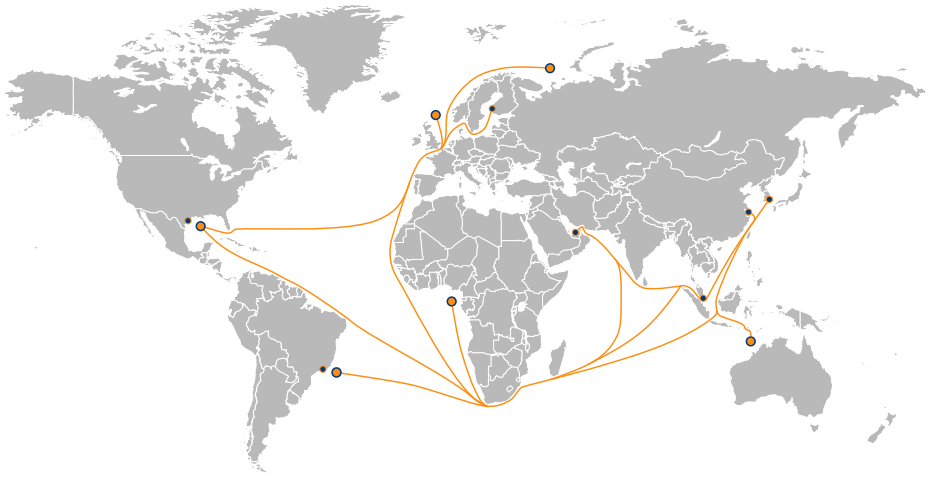

Figure 1.4: Major routes and operational areas

environmental conditions and design motions and accelerations. For each transport, the specific loading condition is used to predict motions most commonly using fast methods like 2D-strip theory programs. Investigating motions and/or mooring loads during loading or discharge operation is in general never done. If a mooring assessment is done, it is mostly limited to verifying the global positioning by anchor mooring, possibly assisted by tugs, based on wind and current loads only. Assessing the cargo handling mooring is never done.

The execution of a transport starts with preparing the deck with a support system for the cargo; mostly cribbing wood is used, but sometimes a steel grillage support is fabricated. Also a combination has been used. A new development is use of plastic cribbing beams.

At the right in Figure 1.2 a skidded load-out is shown, where a cargo is skidded from the quay side on to the HTV deck. After transport, the cargo is floated off, as shown at the left. However, most of the buoyant cargoes are loaded by float-on method. By submerging the HTV the cargo is shifted over the submerged deck, as shown in Figure 1.3. When correctly positioned above the HTV, the cargo is set on the deck by slowly de-ballasting the HTV. Then, sea-fastenings are installed, after which the Marine Warranty Surveyor (MWS) gives his final approval before the voyage is commencing. Basically, discharge is a reversed sequence of loading. During loading and discharge the cargo is handled by tugs and cargo mooring winches, see Figure 1.3. Normally, the mooring winches are operated manually by the crew of the HTV. Winch crew and tug masters are commanded by the superintendent and/or HTV master.

Despite of a few accidents or damages in the past, loading and discharge operations is considered very safe; accidents or damages were never related to excessive motions in waves. This is mainly because these operations take place in sheltered locations during extremely benign conditions, i.e. low wind speeds and virtually no waves. In the rare occasion that operations had to be carried out in areas open to the elements — near shore operations — exposure to weather gave a higher risk of downtime. Then, "Go-No-Go" of the operations is decided by the Master, the Superintendent and the MWS, normally based on general guidelines set at beforehand, weather forecasts and visual estimate of HTV and cargo behaviour. The general guidelines are based on long term experience; not on extended analyses and/or model testing.

With further focus on loading and discharge, the most important equipment items used during these operations are:

1. cribbing wood for the support of cargo on the HTV deck,
2. guideposts as reference for positioning the cargo,
3. a work-boat to handle mooring ropes,
4. mooring ropes and winches (together with tugs) to position cargo.

In Figure 1.3 the steps are shown for the loading of a jack-up rig. In step 1, the cargo is towed to the HTV. In step 2, a small work-boat handles over mooring ropes from the winches on the HTV to the cargo. With the winches, the cargo is pulled over the HTV deck, as shown in step 3. Finally, in step 4 the cargo is positioned against the guideposts — indicated by the symbol ⌟ — accurately above the cribbing wood. The HTV starts de-ballasting, while the mooring ropes need to keep the cargo in position until the cargo is supported by the cribbing wood.

The size and strength characteristics of the above equipment items are all related to operation in calm environmental conditions. Only in calm weather forces can be kept at a low level for which cribbing, guideposts and handling ropes are suitable. Impact is to be kept low first to avoid crushing of cribbing wood and thus losing support area, and second to avoid damage to the cargo. Main purpose of the guideposts is to guide the cargo to the correct location above the pre-laid cribbing arrangement; secondary purpose is to stop movement of the cargo. However this is limited, as the design of the standard guideposts, present on most of the HTVs, is such that the allowed force to avoid deformation is low. Horizontal forces during loading and discharge, due to wind, waves and inertia, are mainly handled by the mooring ropes and winches. The winches on most HTVs have a pulling capacity below 50 [t], and holding capacity below 140 [t].

1.3 Offshore Loading & Discharge Operations

With a growing demand for fossil fuels combined with the decline of economically recoverable oil and gas reservoirs in the established regions of the world, the offshore oil and gas industry has been actively exploring the undiscovered parts of the globe. These efforts have led to many successful

discoveries, which include some of the largest finds in the history of offshore drilling, and major developments are taking place in regions such as Gulf of Mexico, Northwest Australia, West Africa, Barents Sea and Brazil. However, there are many challenges associated with developing oil and gas fields in these remote regions, and one of the main challenges is the transportation of the facilities required for the developments of those fields. Often, the production platforms for the mega fields in these regions are built in East Asia and have to be transported to very distant production sites (Figure 1.4).

To optimize profitability of the remote oil and gas fields, optimizing fabrication and installation of facilities is essential. Generally, the investment costs are less when facilities are fully integrated at the fabrication yard, instead of integrating them in blocks at the offshore location. As such, simplifying the offshore installation method and reducing installation time would be beneficial as the offshore installation work is much more expensive than performing the work in the yard. Furthermore, delivering a fully integrated facility to the final destination means a reduction in the deployment of large installation vessels and large number of labourers.

Next, dry transport instead of wet tow over a long distance contributes to time saving. Average speed during dry transport can be as much as two times faster than wet tow. Finally, another optimization is found, when considering discharge operation at the remote location, instead of at a sheltered location. Especially when the sheltered location is not at close distance, offshore operation would avoid the necessity to tow the facilities to the field using tugs. Thus, taking fully integrated facilities to remote areas directly by dry transport and discharge them in the field is an optimization that can reduce field development time; and thus earlier production and earlier revenues can be accomplished.

As mentioned, normal operational areas for loading and discharge of cargo are sheltered location. Downtime (or waiting-on-weather) at these locations is generally related to wind conditions only, and not so much on exceeding of wave limits; in fact hardly any waves are generated and thus encountered in these sheltered location. This means that downtime is normally limited to a few days, and has no or minor impact on costs. Still, there have been occasions where operations took place at unsheltered location with wave conditions pushed slightly above the standard limits, for example the drilling rig *Ocean Endeavor* was discharged from the HTV *Blue Marlin*

outside Port Fourchon in sea conditions close to $H_s = 1.0$ [m], where normally an acceptable limit is a sea-state less than $H_s = 0.5$ [m].

Apart from improving and extending the transport capabilities, the HMT providers are also seeking for new opportunities to employ HTVs. A potential market is offshore dry-docking [33] of FPSOs. It is beneficial to perform inspection, maintenance and repair (IMR) of an FPSO without disconnecting from the anchor mooring and riser system, thus possibly allowing for production even during IMR work. When the offshore dry-docking is not permissible due to severe sea-states, an alternative method called quay-side dry-docking may undertake IMR work at a sheltered location close to the production field, thus using local content, instead of using dry-docks far away.

During offshore operations it is evident that the HTV and cargo are likely to be exposed to waves. Not only wind generated wave may be encountered, but also swell may exist. As such, it is clear that the dynamics between HTV and cargo during offshore operation will be very different compared to operation in sheltered areas. Also, risk of downtime is different and much more related to wave characteristics. This means that a motion and mooring assessment becomes important and workability analysis may be required.

A concise definition for Offshore Loading and Discharge is:

> *Loading and Discharge operations in non-sheltered location, while exposed to wave conditions, with acceptable workability*

Problem

CHAPTER 2

Problem Statement

2.1 Hydrodynamic Characteristics

The diffraction theory (Appendix A) is extensively used especially in the offshore engineering. Many different problems are accurately solved, like behaviour of moored FPSO's , SPAR buoys, semi-submersible structures (e.g. TLP's). Often, also behaviour of floating structures in close proximity of each other is investigated; examples are the side-by-side (see Figure 2.1) and tandem moored operations of FPSO and shuttle tankers. Here, the first issues with industry standard diffraction methods is becoming evident, which is the difficulty to predict water behaviour in the narrow region between the FPSO and shuttle tanker (Hong et al. [12], Naciri et al. [24]). As mentioned by Huijsmans et al. [15], the linear potential theory may lead to unrealistic high water velocities, which are in practice limited

Figure 2.1: Side-by-side Offshore Offloading Operations.

by either viscous or other non-linear effects. To limit the water velocities a numerical solution is found in applying a lid covering or damping the free-surface between the vessels.

Also in HMT and Transport & Installation (T&I) , the linear potential theory is often used. For transport analyses, the theories with forward speed are used to predict expected acceleration in a seaway; an example in T&I is float-over analysis for which hydrodynamic simulations are performed. In the past, also several research studies were carried out to investigate the motion behaviour of submerged HTV and cargo during loading or discharge in a seaway using industry standard multi-body diffraction methods. From these studies in combination with model testing and practical experience it became evident that the prediction tools were not accurate. Similar and other numerical issues are encountered as seen at the above mentioned side-by-side configuration.

(a) Dock domain (b) Shallow water wave

Figure 2.2: Submerged HTVs

In conventional (multi-body) diffraction analysis, explaind in Appendix A.4 and A.5, only one domain with one linear potential theory solution and one water depth is applied. This theory basically assumes that bodies are transparent, and that flow is diverted by distributed dipole sources on the surfaces of each body to fulfil the no-leak boundary condition. Also, each source is influenced by each other. Sometimes however, this may physically not be right. For example, when looking at a submerged dock-type HTV (Figure 2.2(a)), the inside of the dock needs to be modelled, where the distance between the inside and outside of the dock wall is relative small compared to the wave length range of interest. In the

conventional diffraction method, the influence function between inside and outside panels depends on the dock wall width, while "flow" distance is actually going round along the outside through the dock opening. Also, the undisturbed incoming waves are directly influencing the panels inside the dock, which is physically impossible especially for head waves. Instead, the behaviour of the water inside the dock should only be effected by the flow through the dock opening and the walls inside the dock. Also, the water level above deck is relative small compared to the wave length range of interest. This implies that waves inside the dock should be modelled as "shallow" water waves. This is also clearly seen in Figure 2.2(b), where waves easily start breaking above the submerged deck of an HTV. Lastly, there is the issue similar to the side-by-side configuration, which is the gap between the deck of the submerged HTV and the bottom of a cargo. The relative motion between HTV and cargo causes water being squeeze out or pulled in this narrow gap domain. This squeeze flow is extensively investigated in this thesis.

Generally, for cases where surfaces are close to each other, independent of the fact if their normal direction is towards or away from each other, the numerical solution of the linear potential problem may become inaccurate.

2.2 Motion and Mooring Assessment

Loading and discharge operations in sheltered location never required a lot of engineering attention, as loads are virtually static, dynamic motions are very small and experience ensures that available equipment and solutions can be applied safely. Of course, this will not be the case for offshore operations.

In the past many desk studies were conducted to predict the relative horizontal motions between a submerged HTV and a cargo. Due to the complexity of the problem (i.e. two-body system with a complex mooring system), mostly time-domain simulations have been performed using standard cargo handling systems. The studies showed the difficulty to keep control of cargo in the horizontal plane, i.e. the relative horizontal motions and the cargo handling loads can be substantial using standard equipment. And, large vertical relative motions were predicted. Generally, it was judged that the predictions are being overestimated by the available

engineering tools; this judgement was mainly based on the experience of superintendents. However, as a limited number of operations were done in higher conditions exceeding the standard limits — however not higher than wind seas of $H_s = 1.0$ [m] — and with no exact measurements available, it was neither possible to conclude to which extend the simulations were over-estimated, nor was it possible to tune the calculations.

Therefore, to get more insight in the relative behaviour during offshore loading and discharge operations and to be able to tune calculations, several model test campaigns were carried out. Main purpose of the tests was to investigate relative motions between the cargo and HTV deck, and to assess the cargo mooring loads. In 2011, a model test campaign with the Type-0 HTV and a 110,000-t ring-shape semi-submersible were executed. Details and relevant results are shown in Appendix D. General conclusion from these tests is that within the targeted operational conditions (i.e. wind sea of $H_s = 2.0$ [m]):

- the mooring loads are not unrealisticly high, however the horizontal motions are too large to accurately position the cargo on the standard cribbing support.
- shifting the cargo over the HTV deck can be done with a 2.0 [m] vertical deck clearance.
- relative vertical motions are indeed much less extreme than would be found based on analysis using linear theory.
- an absolute value for impact loads cannot be established, however an indicative correlation with impact velocity is shown.

So, in case of Offshore Loading and Discharge project, the requirement to assess the operation in more detail is evident. To ensure a feasible and safe offshore operation and to establish the operational limits, engineering assessment and cargo handling design is essential. The best applicable method is the quasi-dynamic multi-body time-domain analysis (Brun et al. [6]); quasi-dynamic means that it is not likely that dynamic behaviour of mooring lines (or equivalent equipment) is required. Applicable known theories are described in Appendix B. Whether or not the frequency-domain approach is possible to use depends on which non-linear effects need to be accounted for and/or if these effects can be linearised. Certainly, the time-domain approach can be used with the disadvantage that this would be more time-consuming.

2.3 Research Goals

The main goal of this research project is:

> *Making Offshore Loading and Discharge operation possible by finding a suitable engineering approach.*

In this goal several aspects are recognized, which results in the following sub-goals.

Making the operation possible - An operation can be considered possible, when all parties involved agree that the operation can be executed safely within an appropriate time-window, which may include down-time due to adverse weather conditions. Clearly, the aim is to be able to operate in the highest possible environmental condition, while ensuring the safety of crew, HTV and cargo. At the same time, this limiting environmental conditions should result in an acceptable level of workability. Further, it means firstly that the crew must be able to work safely with and around the equipment needed to perform an offshore loading or discharge operation and secondly that damage to HTV and/or cargo must be avoided at all times. Naturally, workability and equipment, which depend on each other, are a trade-off with project or investment costs. Summarizing, the first sub-goal is:

> *Develop cargo handling equipment, which maximizes the operational conditions, while keeping a high level of safety for crew, HTV and cargo.*

Suitable engineering approach - All necessary design and engineering needs to be performed to proof feasibility and to establish the limiting environmental conditions. The scope of it may depend on the project phase; as shown Table 2.1 the scope of work during tender phase of a project may be limited as available time is limited. Generally, during a tender phase at least a good indication of workability should be given and the technical concept should be made clear. Thus, depending on the project phase, a suitable engineering approach needs to be selected. To summarize, the second sub-goal is:

> *Develop an analysis method suitable for different stages of an offshore loading and discharge project, each with an appropriate level of accuracy.*

Table 2.1: Project phase dependent criteria

	Project Phase	
	Tender	Execution
Available time	1-6 week	6-12 months
Accuracy	Low	Medium/High
Scope	Workability Concept Design Assess critical items	Operations Manual Detailed Design Specifications
Model tests	no	optional

2.4 Outline of the Thesis

To reach the above goals, the research is split in two parts. The investigated topics are illustrated in Figure 2.3. First, the vertical relative motions (1) between cargo bottom and HTV deck is investigated. As such, an accurate estimation method needs to be developed to account for the effects of the narrow gap (h). Therefore, the phenomenon involved in squeeze flow (2) is looked at. Second, the horizontal relative motions (3) are investigated. Methodology and equipment to control and reduce these motions need to be developed. The characteristics of the equipment (4) are properly modelled and incorporated in estimation tools.

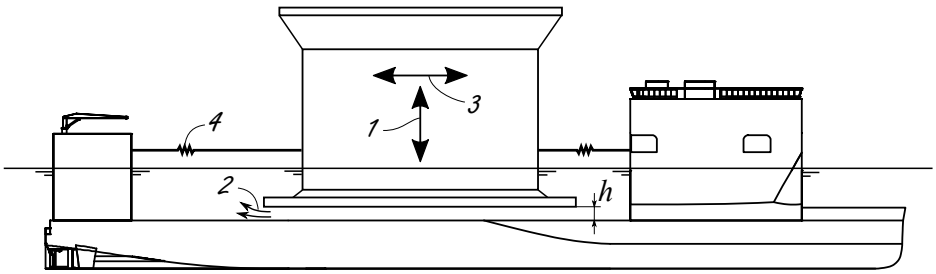

Figure 2.3: Illustration of investigated topics

Vertical Relative Motions

CHAPTER 3

Squeeze Flow Problem

For the development of a more accurate method to predict the relative vertical motions between cargo and HTV with a small gap, more understanding of the squeeze flow problem is needed. First, the linear potential flow problem is discussed to motivate the interest in squeeze flow. Then, analytical approaches found in literature are studied. Following, fundamental model test experiments were carried out to show the relation between motions and hydrodynamic loads. And finally, CFD calculations have been performed, mainly to verify the model tests and to give more insight in the flow phenomenon in and around the gap.

3.1 Linearisation Issue

As mentioned in the problem statement, conventional (multi-body) diffraction method is widely used in the offshore and shipping industry. This method is based on linear potential flow theory with its well-know assumptions as given in Appendix A.4. One important assumption is repeated here:

> *The amplitudes of waves and motions are assumed to be small compared to the wave length*

This linearisation should in fact be extended or generalized to the assumption that the wave and motion amplitudes are small with respect to any relevant parameter. This would lead to the simplification that the hydrodynamic characteristics of a system do not change due to a large relative motion of a body in close proximity of a fixed or other moving body.

This means that in the case of a cargo floating above the HTV deck, the relative motion amplitude between them must be small compared to the initial gap. As this is not the case when it is desired to operate in as high as possible sea-state and actually impact between cargo bottom and HTV deck will occur, it is evident that the hydrodynamic characteristics will change. To find out which chrateristics change and how this change needs to be accounted for in the prediction method, analytical approaches are investigated first.

3.2 Analytical Approach

3.2.1 Molin

Molin et al. [23] has formulated the analytical solution for the non-linear hydrodynamic load on an oscillating submerged disk at close distance h to the fixed sea bottom, as illustrated in Figure 3.1. This investigation was related to the hydrodynamic loads on the jack-up leg footing (i.e. spudcans) when approaching the sea-floor. The presented problem is similar to the free-floating vertical cylinder with a narrow space; but with the difference that in Molin's case the disk is fully submerged, instead of protruding the free water surface. In Molin's solution, it is assumed that the free surface has no effect on the hydrodynamic characteristics of the submerged disk, because the water depth H is very large with respect to the gap h. The theoretical predictions by Molin were compared to experiments, from which a good match was found and from which it was concluded that viscous effects play a secondary role. As such, Molin's work gives a valuable insight in the different contributions to the non-linear loads.

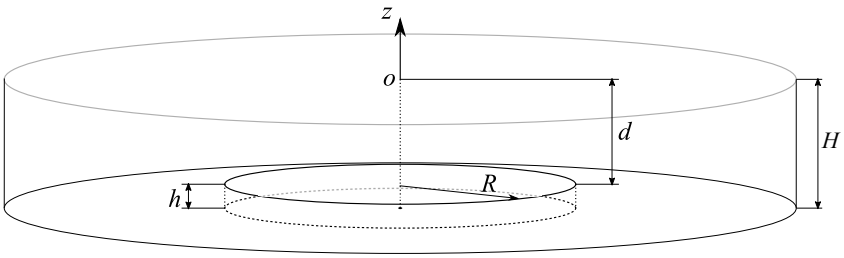

Figure 3.1: Submerged disk

Starting from the expression of the kinetic energy in the fluid domain, Molin deduced that the hydrodynamic effort F applied to an object at close distance to the fixed sea bottom is given by:

$$F = -\frac{1}{2U}\frac{d}{dt}(M_a U^2) = -M_a\frac{dU}{dt} - \frac{1}{2}U\frac{dM_a}{dt} = -M_a\frac{dU}{dt} - \frac{1}{2}\frac{dM_a}{dh}U^2 \quad (3.1)$$

Where the added mass M_a is a function of gap height h and $U = {}^{dh}/_{dt}$ is the vertical velocity. In the equation, the first term is recognized as the well known inertial load working on the surrounding fluid to be accelerated, i.e. the added mass term. The latter term represents the effort needed to change the amount of added mass; this is related to the energy dissipated to change the accelerated surrounding fluid, that is the amount of added mass is increasing or decreasing. Nielsen [26] refers to this second term as "slamming" as change of added mass is often used as a measure for slamming force, however in squeeze flow it can better be expressed as a lifting force, this is further explained in Section 3.6. An important assumption leading to (3.1) was that the fluid domain is bound only by the fixed sea bottom and not by the free water surface. Thus, Molin assumes infinite water depth, therefore no free surface boundary condition needed to be applied. As a result, Molin deduced a frequency independent relation for the added mass. This is a valid assumption as long as the characteristic size (i.e. diameter and thickness) of the disk is small and the submerged draft is large with respect to the water depth.

Molin gives an analytical solution of the added mass for a disk with very small thickness, where he solved the problem via the potential flow theory and the method of matched asymptotic expansions by splitting the fluid in three domains; i.e domain under the disk, domain at the outlet of the gap and the outer domain. Also Brennen [5] and Vinje [35] investigated the thin plate problem, a summary of the added mass definition is given in Table 3.1.

Using the definition of added mass from Molin, (3.1) is then written as follows:

$$F = -\rho \cdot R^3\left(\frac{\pi}{8}\frac{R}{h} + \frac{1}{2}\ln\frac{8\pi R}{h} - \frac{4}{3} + \frac{\pi}{2}\frac{h}{R}\right)\frac{dU}{dt} + \ldots \\ \frac{1}{2}\rho \cdot R^2\left(\frac{\pi}{8}\frac{R^2}{h^2} + \frac{1}{2}\frac{R}{h} - \frac{\pi}{2}\right)U^2 \quad (3.2)$$

Table 3.1: Comparison of analytical heave added mass

	Analytical formulation	Note
Brennen	$\frac{2}{3}\rho a^3 \frac{1}{h} L$	plate $2a \times L$
Vinje	$\rho \cdot R^3 \left(\frac{\pi}{8} \frac{R}{h} + \frac{1}{2} \ln \frac{8\pi R}{h} - \frac{5}{6} \right)$	circular disk
Molin	$\rho \cdot R^3 \left(\frac{\pi}{8} \frac{R}{h} + \frac{1}{2} \ln \frac{8\pi R}{h} - \frac{4}{3} + \frac{\pi}{2} \frac{h}{R} \right)$	circular disk

Molin's Equation (3.2) is only valid for a submerged infinitely thin disk. Based on a numeric method, Molin showed that the added mass increases with the thickness of the disk; apparently this is caused by the vertical sides of the disk. As "free-floating" bodies with small aperture — and sides up to the free water surface — are investigated in this thesis, one would expect that the added mass could be corrected for the fluid domain above the disk. Again, assuming that the water level above the disk is large and the sea-bottom and gap-outflow influence can be neglected, one would expect that the added mass could be reduced by the mass equivalent to the volume of half a sphere. Although, this reasoning seems logic, this correction cannot be applied as the free-surface plays a roll. In other words, the frequency dependent terms (i.e. added mass and radiation damping) need to be accounted for. This is further discussed in Chapter 4.

Based on comparison between experiment (Guérin [11]) and (3.2), Molin proposed a correction for viscous effects — related to flow separation at the sharp edge of the disk — based on the flow velocity at the edge and the in-/outflow area (gap height h multiplied by circumference of the interstitial space), thus:

$$F_D(U,h) = -\frac{1}{2}\rho C_D (2\pi R h) \frac{UR}{2h} \left| \frac{UR}{2h} \right| = -\frac{\pi}{4} \rho C_D \frac{R^3}{h} U|U| \tag{3.3}$$

Again with de gap height h varying in time. Molin recommended to use a drag coefficient in the order of $C_D = 1$.

Equation (3.1) including the Morison alike correction (3.3) — representing the squeeze flow effort, thus the effort excluding the hydrostatic varying part — becomes:

$$F(U,h) = -A(h) \cdot \dot{U} - \frac{1}{2} \frac{A(h)}{dh} \cdot U^2 + F_D(U,h) \tag{3.4}$$

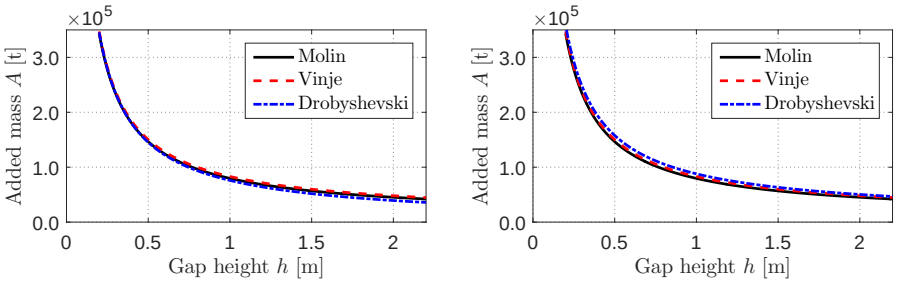

(a) draft $T = 5$ [m] (b) draft $T = 25$ [m]

Figure 3.2: Comparison added mass based on analytical approach

3.2.2 Yeung and Drobyshevski

Yeung [38] and Drobyshevski [8] both provided an analytical solution for the frequency dependent hydrodynamic characteristics of a truncated cylinder in finite water; a more relevant case compared to the gap problem investigated here. They too followed the potential flow theory and the method of matched asymptotic expansions. Their solutions showed to be very similar. Also, the results from numeric analyses based on theory presented in Appendix A are matching with the analytical solutions. As such, their solutions verify the numerical methods based on linearised potential flow theory. Yeung and Drobyshevski focussed on added mass at given gap height and did not discuss the non-linear effort and/or damping force depending on U^2 and/or $U|U|$.

Drobyshevski [8] is showing that the heave added mass is determined by a frequency independent and frequency dependent term; the first is dependent of gap height, whereas the latter is not. It is important to note that the radiation damping is not dependent on the gap height, but only on the wave frequency. The importance becomes clear when the gap dependent added mass is accounted for in time-domain, see Section 4.2. Also, the wave excitation force is independent of gap height.

A simplified notation, showing the height dependent part, is:

$$A_{33} = \rho\pi R^3 \left\{ \frac{R}{8h} + \frac{1}{\pi} \left[1 - \ln\left(\frac{4h}{H} \right) \right] + \mathrm{f}(\omega) \right\} \tag{3.5}$$

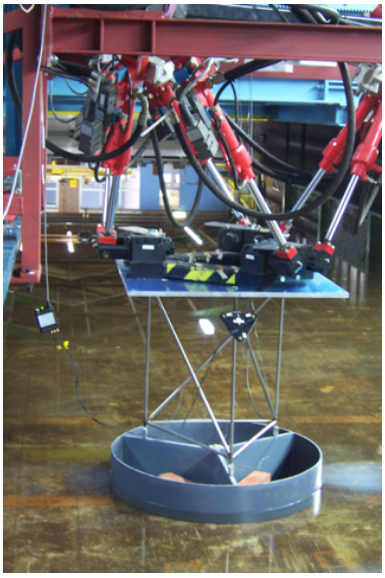

(a) 2008

(b) 2010

Figure 3.3: Fundamental squeeze flow tests

In Figure 3.2, the frequency independent part from (3.5) is compared with the added mass given by Molin and Vinje; assuming $R = 20$ [m] and $H = d + h$. Noticeably, for Drobyshevski the added mass increases with increasing water depth H, whereas Molin and Vinje are independent of water depth. This is evident as Molin and Vinje assumed that disk is deeply submerged, such that in their analytical solution the influence of the free surface could be neglected.

3.3 Fundamental Model Tests

To acquire more insight in the loads involved with the squeeze flow phenomenon present in a narrow gap between two parallel surfaces, fundamental model tests have been performed. The model set-up is shown in Figure 3.3. First in 2008, forced oscillation tests were carried out with a circular shape just above a wave basin floor in shallow water. Then in 2010, additional test including other shapes were carried out. The shapes are shown in Figure 3.4. The area of the triangle and square were the same as for the cylinder; the area of the ring shape was smaller. Tests were carried for different gap heights, oscillation frequencies and amplitudes.

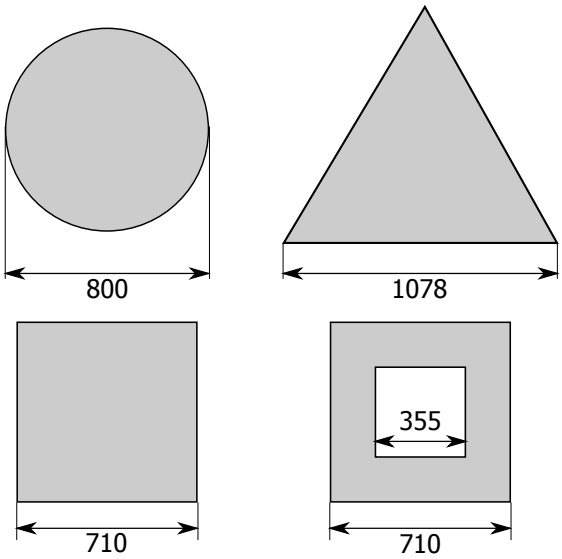

Figure 3.4: Basic shapes

Table 3.2: Test Matrix - heave oscillations

Frequency	Gap	year		Amplitude [mm]						
[Hz]	[mm]	2008	2010	2.5	5	7.5	10	15	20	30
0.225	10	x		x	x	x				
	20	x	x		x		x	x		
	40		x				x		x	x
0.281	10									
	20		x		x		x	x		
	40		x				x		x	x
0.338	10	x		x	x	x				
	20	x	x		x		x	x		
	40		x				x		x	x
0.394	10									
	20		x		x		x	x		
	40		x				x		x	x
0.450	10	x		x	x	x				
	20	x	x		x		x	x		
	40		x				x		x	x

Table 3.3: Test Matrix - roll/pitch oscillations

Frequency	Gap	Amplitude [deg]		
[Hz]	[mm]	0.5	1.0	2.0
0.225	20	x	x	
	40		x	x
0.338	20	x	x	
	40		x	x
0.450	20	x	x	
	40		x	x

3.3.1 Heave oscillation

The test matrix for the heave oscillation tests is shown in Table 3.2; for each combination the tested oscillating amplitudes were 25%, 50% and 75% of the gap height.

Results are shown in Appendix C.1. The hydrostatic varying part is subtracted from the measurement, so the plotted force presents only the dynamic squeeze flow effort. It must be noted that the measurements showed a high noise level in the force signals, for which filtering of the signals were required. After noise filtering, investigating the different measurements showed that resonant behaviour in the test set-up (i.e. frame, force transducers, etc.) seemed to occur, resulting in a higher order load component. As a result, some measurements may show higher order oscillations, which may not be explained by physical phenomena.

In the following paragraphs, the test results are discussed based on aspects like test set-up, non-linearity and model shape; where dependencies of frequency, amplitude and gap height have been considered.

Test Set-up: As can be seen in Table 3.2, three tests from 2008 have been repeated in 2010. Reasons were repeatability and the fact that the basin size may influence test results. The tests from 2008 were done in the shallow water basin of MARIN (Wageningen), where the influence of basin walls can be neglected, while the tests in 2010 were carried out in the short towing tank at TU Delft, which has a width of about 2.5 [m], where the diameter of the cylindrical model was 0.40 [m]. Figure C.1 to C.3 show that the force measured in both years have similar trends and that difference is seen in phase lag and in the measured force during upward motion. Very similar force measurement is seen for the lowest oscillating frequency, as can been seen in Figure C.1. The phase lag is most clearly noticeable in Figure C.2(c) and C.3(c). The difference during upward motion is clearly observed in Figure C.2(a) and C.2(b).

Shape: In Figure C.4 to C.6, the measurements for different shapes are shown. Since the flat bottom area of the ring shape is smaller than for the other shapes, the results are presented as average pressure. Clearly, the cylinder, triangle and square — with the same bottom area — show very similar trend, from which it may be concluded that the measured effort is independent of the shape. It must be noted that this may not be

the case for a slender rectangle, however no data is available to verify this. Further it is seen that the ring shape shows a completely different trend, which is explained by the so-called moon-pool effects; a heavily oscillating water level was observed during the tests.

Non-linearity: Figure C.7 to C.10 are shown to illustrate the influence of the initial gap height and oscillating amplitude. Measurement with the same amplitude at different gap heights are given in Figure C.7 and C.8. Measurement with the same frequency at different amplitudes are given in Figure C.9 and C.10. Evidently, for a large initial gap height with low frequency and small amplitude oscillation, the measured effort follows the regular oscillation of the motion; meaning that the response is linear dependent to the motion. Noticeable, with increasing amplitude and reducing gap height, this is not the case; especially just after the lower position of the motion — gap at smallest value — the effort is sharply peaking to a large suction load.

3.3.2 Pitch oscillations

During the model tests in 2010, a limited number of pitch oscillation tests were carried out for the cylindrical shape. The test matrix for these oscillation tests is shown in Table 3.3. The measurements are shown in Figure C.11. The plots show that there is no dependency on amplitude of motion, as for a given gap height the unit load response is equal for the two selected motion amplitudes. As expected, the load is dependent on gap height; with reducing mean gap height the load amplitude increases. Further it seems that there are no distinct velocity dependent loads, because the load seems sinusoidal and in phase with the motion. However, looking at the shape of the peaks (note that also the negative value is considered a peak due to the symmetric oscillation) in Figure C.11(b) and C.11(c), it is seen that the peaks are flattened. This means that the effort increases more than proportional with the acceleration. This additional effort — pitch moment — is similar to the lifting force as seen for the heave motion; i.e. the second term in (3.1). Geometrically, this can be explained by separating the parts at both sides of the rotation axis, where one side is moving up and the other side is moving down. As for the moving down part the lifting force is larger than for the moving up part, an additional pitching moment contribution will exist.

3.4 CFD Calculations

As the fairly simple fundamental model tests give limited insight in actual flow phenomenon inside and outside the gap, CFD calculations have been performed [18]. An attempt was made to reproduce the tests and investigate streamlines and vortices. Also, scale effect was investigated to establish if the model tests are scalable. Further, different turbulence models and solution methods were used. Results are shown in Appendix C.2. All simulation were done for a gap height of 20 [mm], an oscillating amplitude of 10 [mm] and a oscillating frequency of 0.45 [Hz]. The following test cases were done:

1. **Reference case**: the flow model unsteady 3D Navier-Stokes is used, including the kω-SST turbulence model (this was used after comparing different turbulence models). To directly reproduce the oscillation test, simulation was done for the model test dimensions.

2. **Full scale case**: the same flow model is used as for the reference case, only the geometry is scaled by a factor 1:50, representing a realistically sized object. This is done to investigate scale effect on turbulence and viscosity.

3. **Euler case**: As the reference calculations showed that the viscous part of the vertical effort is insignificant compared to the pressure part,it is expected that the Euler approach could give good results and may be interesting to decrease the computational cost. Thus, the flow is 3D Euler, unsteady. There is no turbulence model in the Euler calculation. Therefore, "laminar" option is chosen in the FINE™/Marine GUI.

4. **Wall effect case**: To try to explain the difference between the model tests in 2008 and 2010 due to the test set-up, a simulation including the basin side walls (as in the 2010 tests) was performed. Here, the Euler approach was used.

In Figure C.12, the streamline plots for the reference case are shown. Clearly shown by the CFD results is the similarity between pipe-flow with sudden contraction/expansion and the in- and out-flow at the gap entrance of the oscillating squeeze flow problem. The characteristic flow lines are

illustrated in Figure 3.5. The left side column of Figure C.12 shows the downward motion, where the sudden "expansion" from the gap to the outer domain results in flow separation similar as shown in Figure 3.5(a). The right side column of Figure C.12 shows the upward motion, where the sudden "contraction" from the outer domain to the gap results in flow separation and so-called vena contracta similar as shown in Figure 3.5(b). Notice that due to vena contracta the inflow opening seems smaller than the actual size of the opening. This impacts the inflow speed and thus the local pressure distribution.

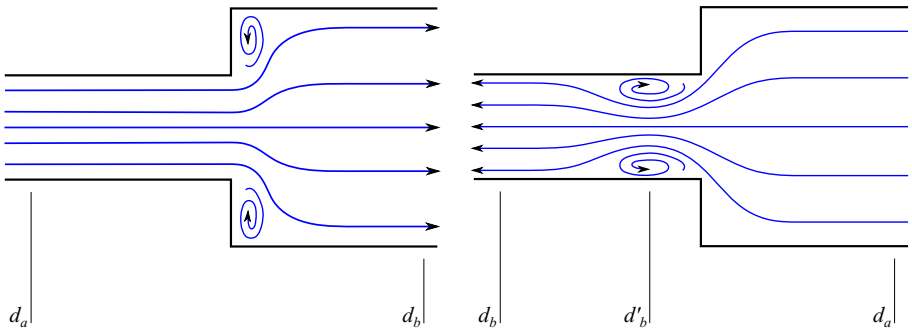

(a) Expansion (b) Contraction

Figure 3.5: Characteristic flow in pipes

The reference case is compared with the measurement of the oscillation test carried out in 2008, see Figure 3.6(a). The CFD simulation follows the trend of the measurement, where the positive peak tends to be higher. As mentioned in Section 3.3.1, the measurement shows a higher order oscillation, not recognized in the CFD simulation, which is much smoother and shows a 25% lower negative peak.

To investigate if Froude scaling of the measurements is acceptable, the reference case is compared with the full scale case. First, the streamlines of both cases in Figure C.12 and C.13 are compared. The full scale result shows a smaller eddy or vortex in front of the cylinder, which seems logic from viscous point of view. The contraction at upward motion seems very similar, in fact when investigating the velocities this seems more or less scalable according to Froude's Law. The smaller vortex is further explained by comparing the effort of the reference case with the effort of the full

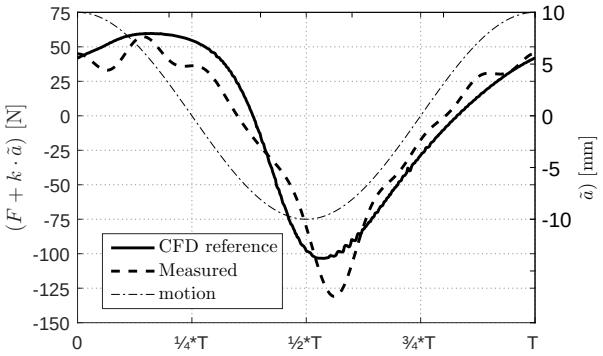

(a) Comparison reference case vs. measured

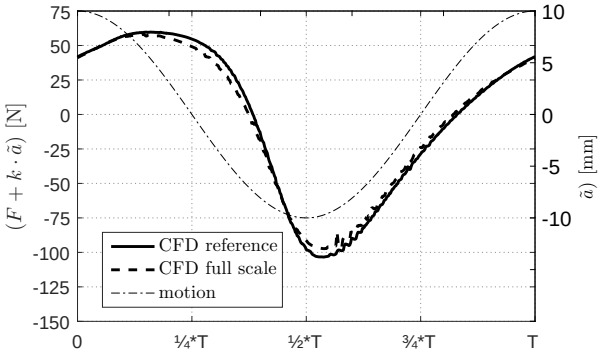

(b) Comparison reference case vs. full scale case

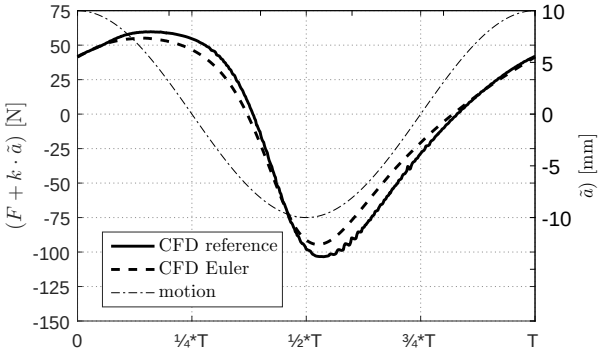

(c) Comparison reference case vs. Euler case

Figure 3.6: Effort based on CFD simulation

scale case; based on Froude's law, the latter is scaled to model scale values. The effort is shown in Figure 3.6(b). For the full scale case slightly less effort is required, which implies that less energy is exerted to the flow and thus a smaller vortex is observed. The difference in negative amplitude is 5.8% and the difference in positive amplitude is 3.3%. Furthermore, the reference case shows a steeper slope during upward and downward motion. The positive and negative peak of the reference case are both slightly lagging behind with respect to the full scale case. As the difference between model and full scale is small, Froude scaling is applicable.

Next, the Euler case is compared with the reference case. The streamline plots are shown Figure C.14. The Euler calculation gives a solution which is not as smooth as the base case. The streamlines present angles and a singular point due to the lack of viscosity. Despite this, some big structures of the flow (alike vortices) can be recognized near the entrance of the gap. As shown in Figure 3.6(c), clearly a lower effort is predicted. The difference in negative amplitude is 8.5% and the difference in positive amplitude is 7.6%. It can be concluded that the Euler solution gives a reasonable estimate of the squeeze flow effort.

The wall effect case is compared to the Euler case in Figure C.15; the dynamic effort excluding hydrostatic varying part is shown. Not a large difference is observed. A more distinct difference is seen when comparing the dynamic effort including the hydrostatic varying part are shown for the CFD calculation (Figure C.16(a)) and the measurements (Figure C.16(b)). The difference around $0.75 \cdot T$ explains the difference observed when comparing the 2008 and 2010 measurements.

3.5 Measurements versus Analytical Approach

To get insight in the contribution of Molin's non-linear effort given by (3.1) and the importance of the Morison alike correction (3.3), measurements are compared with the forced ocsillation applied to (3.4). It must be noted that Molin's work is applicable to a submerged disk, whereas the measurement is done on a truncated floating cylinder. Therefore the Morison alike correction will contain this difference.

Initial comparison between the oscillation tests and (3.4) was done by varying the C_D value as to match the measurements as good as possible. From

this comparison it was concluded that the C_D value is strongly dependent on oscillating frequency and weakly dependent on oscillating amplitude. Investigating the trend of C_D values with respect to oscillating frequency and amplitude showed a dependency on the inverse of the instantaneous oscillation velocity. So, an acceptable match between measurement and analytical solution was found by using:

$$C_D = \frac{\tilde{C}_D}{|U|} \tag{3.6}$$

Thus (3.3) is changed from Morison alike drag to linear damping:

$$F_D = -\frac{1}{2}\rho C_D(2\pi Rh)\frac{UR}{2h}\left|\frac{UR}{2h}\right| = -\frac{\pi}{2}\rho\tilde{C}_D\frac{R^3}{2h}U \tag{3.7}$$

With $\tilde{C}_D = 3.0$ [m/s], a good match between the measurements and analytical solution is found. Note that in fact $\tilde{C}_D$ is not dimensionless. The chosen $\tilde{C}_D$ value also corrects for radiation damping present in the measurement, whereas Molin's method assumes there is no radiation damping, because the disk is deeply submerged. When the radiation damping can be determined, the $\tilde{C}_D$ value may need to be corrected. This is further discussed and investigated in Chapter 5.

Using (3.7) in (3.4), a comparison between measurement and analytical result for each oscillation test is shown in Appendix C.3. In Figure 3.7, a comparison between Molin with and without linear damping, and measurement from the 2008 tests is shown. Molin's solution combined with (3.7) is showing an acceptable match, except for a small phase shift observed when looking at the negative peak. This shift may be explained by the so-called Basset force Basset [3]; this term is considered to be a viscous effect and describes the force due to the lagging boundary layer development with changing relative velocity (acceleration) of bodies moving through a fluid. In other words, some time is needed to reverse the flow and to build up the contraction at the inflow area. The Basset term is difficult to implement and is commonly neglected for practical reasons Johnson [16]. In Figure 3.8, the three terms from (3.4) are plotted. Figure 3.7 and 3.8 show that the Basset term is partly covered by the drag term.

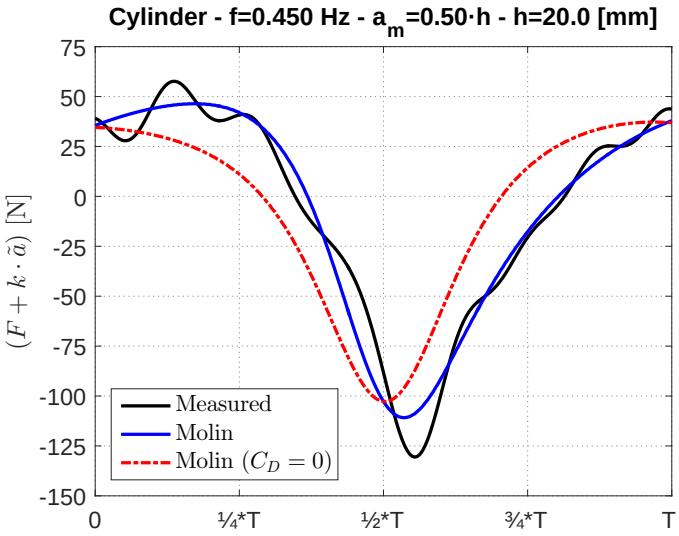

Figure 3.7: Analytical versus measurement

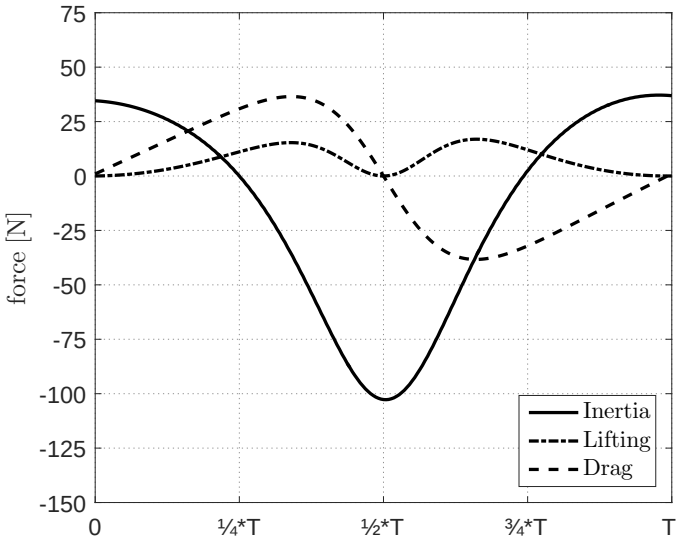

Figure 3.8: Force components

3.6 Summary of Squeeze Flow Phenomenon

From the model test measurements, the analytical estimates and CFD calculations, two distinct phenomenon are observed, which are related to the oscillating squeeze flow. This is schematically illustrated in Figure 3.9. First, the cushioning effect seen during downward motion. When the gap is closing — water is squeezed out — a higher upward effort with respect to a linear trend can be observed, which seems to maximize in the second quarter of the oscillation period. This cushioning effect is noticed by the HTV crew during operations; which is the basis of the fact that in reality relative vertical motions are less severe than theoretical predictions. Second, the sticking effect is seen during upward motion. When the motion is reversed to an upward motion, the outflow needs to be turned around and fluid needs to be sucked in to the gap. As can be observed, a large effort is required in this stage. This is a known effect when objects are lifted from a surface; even in case the fluid is air.

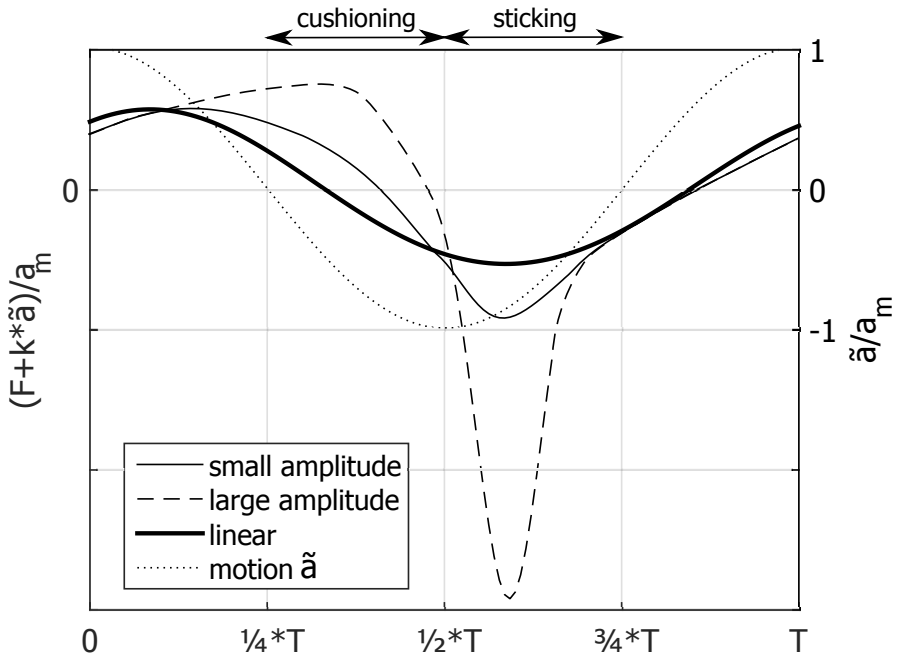

Figure 3.9: Squeeze flow phenomenon

Other observations are the contraction phenomenon during inflow and vortex shedding during outflow. During inflow a small vortex area is generated close to the edge of the gap, resulting in a virtual narrowing of the inflow area and thus a local increase of inflow velocity. This vortex area stays at the same location. CFD analysis shows a local change in pressure in this contraction area. During outflow a large eddy is generated, which travels away from the body. Both phenomena are strongly present due to the sharp edge of the tested bodies; and thus will be less pronounced when the edge is rounded or streamlined.

From analytical results and comparison with measurement and CFD calculations, three components contributing to the oscillating squeeze load are recognized:

1. The first component is the well known inertia load of surrounding fluid to be accelerated, i.e. added mass. This needs no further explanation.

2. The second component is the load representing effort needed to change the amount of added mass. This load always works as a separation load regardless of the motion direction, it therefore can be defined as a lifting force. The physic interpretation of the lifting force is that the body will experience a force associated with the change of added mass due to change of gap height. When the gap is closing, the added mass increases, which can be compared to the snowball effect; more and more effort in the direction of motion is needed to move a snowball at constant speed as it is growing in size. When the gap is opening, the added mass reduces, which can be compared to melting of the snowball; energy is needed to melt the snowball.

3. The third component is due to viscous effect of which eddy making can be recognised as the main contributor.

CHAPTER 4

Prediction Method

The previous chapter focused on the squeeze flow phenomenon and the gap height dependent effort. To a lesser extend, also the wave frequent dependency and/or free surface influence was investigated. Molin's Equation 3.1 is only valid for a submerged infinitely thin disk, where the disk is submerged deep enough such that the influence of the free surface can be ignored.

Since free-floating bodies with a small under keel clearance — and sides up to the free water surface — are investigated, more relevant analytical solutions as mentioned in Chapter 3.2.2 should be used. The analytical and numerical work of Drobyshevski [9] is most relevant, where the three dimensional flow problem was reduced to an integral equation in two dimensions formulated at the waterline of the arbitrary shaped vertical sided structure. As such, it was possible to use matched asymptotic expansions to solve the gap height and wave frequency dependent problem. However, Drobyshevski's method is only available for single bodies and for the structure's bottom parallel to the sea floor.

As explained in Chapter 2, for cases where surfaces are close to each other, the standard numerical solution of the linear potential problem may become inaccurate. To be able to analyse the multi-body hydrodynamics of a cargo above an HTV — including gap height and frequency dependency — an accurate method to predict added mass for small gap heights needs to be found. Therefore, alternative diffraction methods are investigated below. Also, a motion prediction method is developed to account for the non-linear effects as mentioned in Chapter 3.

4.1 Exploring Diffraction Methods

4.1.1 Multi-Domain Diffraction Method

The principle of the multi domain diffraction method (MDDM) is to divide the fluid domain in two or more parts (Zhu and Saito [39]). This approach was used for example to investigate hydrodynamic behaviour of ships in harbour basins, which was studied extensively by Pinkster [30]. In MDDM, the domain as used in the single domain methods (see Appendix A.4) is called the outer domain; in this domain the waves are initiated. Other domains inside the outer domain are called inner domains. The potential Φ in the outer domain is defined by summation of the undisturbed wave potential and the disturbance potential. The disturbance potential represents the disturbance of the flow by the diffraction of the wave on any free-floating or fixed body and by the motions of any free-floating body. This is described by the following equation:

$$\Phi^{out} = \Phi_w + \Phi^a \tag{4.1}$$

And inside each inner domain, the potential is defined only by the disturbance potential, as the wave potential is transferred via the domain boundaries. This is described by the following equation:

$$\Phi^{in} = \Phi^{id} \; \forall \; id = b..N_{domain} \tag{4.2}$$

In addition, at the boundary between two domains, a boundary condition must be defined. This is required to ensure that the flow across the domain boundary is continuous with respect to momentum flux. This is achieved by the following definition (Pinkster [29]):

> *At the domain boundary the normal velocity and pressure on both sides must be equal.*

The normal velocity condition at an interface boundary D is defined by (4.3), in which the minus sign appears because of the opposite normal direction of the surface side adjacent to domain id and the surface side adjacent to domain jd.

$$\left\{\frac{\partial \phi}{\partial n}\right\}_{id} = \left\{-\frac{\partial \phi}{\partial n}\right\}_{jd} \; \forall \; D \in \{id, jd\} \tag{4.3}$$

The pressure condition follows from Bernoulli's Equation (A.19), in which constant terms and velocity-squared terms are neglected in accordance with the linear theory:

$$\{\phi\}_{id} = \{\phi\}_{jd} \; \forall \; D \in \{id, jd\} \tag{4.4}$$

In Appendix A.6 examples are shown of multi-domain problems with the derivation of the set of linear equations. Also, generalized equations are given. Verification of this method is shown in Appendix A.6.5. A more extensive verification was done by Pinkster [30].

4.1.2 Gap solution used in MDDM

Drobyshevski [9, 8] worked on an analytic solution for the frequency dependent added mass of a truncated (i.e. vertical side) cylinder with a small under-keel clearance in shallow water. The solution is based on two-dimensional flow in the gap domain. With this knowledge, Drobyshevski developed a numerical solution to analyse arbitrary truncated shapes. To analyse more arbitrary shapes (i.e. non-vertical walls) and multi-body problems with a gap domain, incorporating Drobishevski' 2D gap solution in MDDM is investigated.

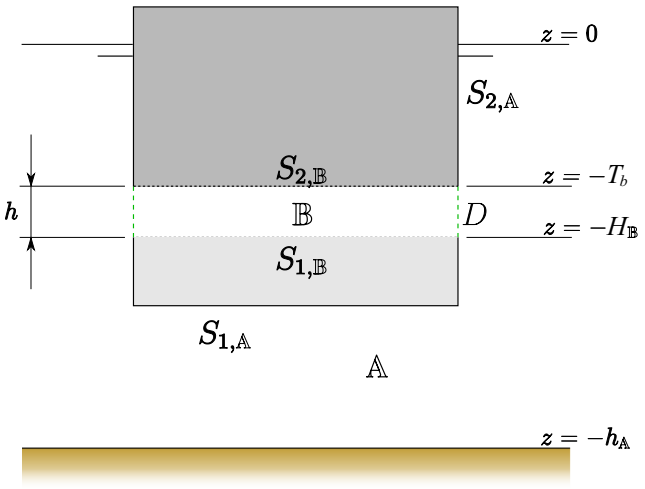

Figure 4.1: Defintion gap geometry

The fluid flow inside the gap domain is assumed to be a two-dimensional flow parallel to the bounding surface S_b (i.e. the fused surface of $S_{1,\mathbb{B}}$ and $S_{2,\mathbb{B}}$). This assumption implies that the gap height — i.e. distance between surface $S_{1,\mathbb{B}}$ and $S_{2,\mathbb{B}}$, see Figure 4.1 — is small compared to the characteristic size of these surfaces, thus:

$$T_b/H_{\mathbb{B}} = O(1);\ h/H_{\mathbb{B}} = \varepsilon;\ \varepsilon << 1 \tag{4.5}$$

The flow through the contour boundary D resembles an oscillating source distributed along this contour line. Both the flow inside the gap and the source strength along the contour are unknown. Based on this essential assumption, the potential problem in domain $\mathbb{B}$ reduces to a two dimensional flow satisfying the Poisson equation:

$$\left(\frac{\partial^2}{\partial \breve{x}^2} + \frac{\partial^2}{\partial \breve{y}^2}\right)\phi(\bar{x}) = \frac{f(\bar{x})}{h} \tag{4.6}$$

The boundary conditions on the overlapping surface are:

$$\frac{\partial \phi}{\partial n} = \left\{ \begin{array}{l} f_1(P)\ \forall\ P \in S_{1,\mathbb{B}} \\ f_2(P)\ \forall\ P \in S_{2,\mathbb{B}} \end{array} \right\} \wedge f(P) = f_1(P) + f_2(P) \tag{4.7}$$

By applying the Green theorem to the two-dimensional Poisson's equation in $\mathbb{B}$, one can show that the potential satisfies the following relation:

$$\phi(\bar{x}) = \frac{1}{2\pi}\iint_{S_b} \frac{f(\bar{x},\bar{\xi})}{h} \ln r(\bar{x},\bar{\xi}) dS - \ldots \\ \frac{1}{2\pi}\oint_D \left(\frac{\partial \phi(\bar{x})}{\partial \bar{n}} \ln r(\bar{x},\bar{\xi}) - \phi_0(\bar{\xi})\frac{\ln r(\bar{x},\bar{\xi})}{n}\right) dl \tag{4.8}$$

Here r is the distance between the field point $\bar{x}$ anywhere in domain $\mathbb{B}$ and the integration point $\bar{\xi}$ on bounding surface S_b and contour D respectively, and $\phi_0(\bar{\xi})$ denotes the potential values on contour D. With $h \to 0$, the first term will become very large and provides the dominating contribution to the potential, whereas the second term stays finite. With the gap height tending to zero, the second term may be neglected such that, by combining with (A.12), the influence function $G(\bar{x},\bar{\xi})$ becomes:

$$G(\bar{x},\bar{\xi}) = \frac{2\ln r(\bar{x},\bar{\xi})}{h} \tag{4.9}$$

Then, the normal and directional derivatives of (4.9) are simply:

$$\frac{\partial G(\bar{x},\bar{\xi})}{\partial \bar{n}} = \frac{2}{h}\frac{1}{r(\bar{x},\bar{\xi})}; \quad \frac{\partial G(\bar{x},\bar{\xi})}{\partial \bar{x}} = \frac{2}{h}\frac{(\check{\xi}-\check{x})}{r(\bar{x},\bar{\xi})^2}; \quad \frac{\partial G(\bar{x},\bar{\xi})}{\partial \bar{y}} = \frac{2}{h}\frac{(\check{\eta}-\check{y})}{r(\bar{x},\bar{\xi})^2} \tag{4.10}$$

As these derivatives limit to infinity for $\bar{\xi} = \bar{x}$, this domain solution cannot be solved when used in the Multi-Domain diffraction Method.

4.1.3 Hybrid Multi-Domain Diffraction Method

As shown above, applying the 2D solution directly in MDDM is not possible. Therefore, following the work of de Jonge [17], an approximate solution is found by combining Drobyshevski's 2D solution with the standard 3D potential flow solution in a step-by-step approach. Again, the fluid domain is split in multiple parts as shown in Figure 4.2. In domain $\mathbb{A}$, the standard diffraction solution is used, where the domain is bound by body surface $S_{1,\mathbb{A}}$, gap boundary D, the free surface, the sea-bottom and a cylindrical surface at great distance of the body.

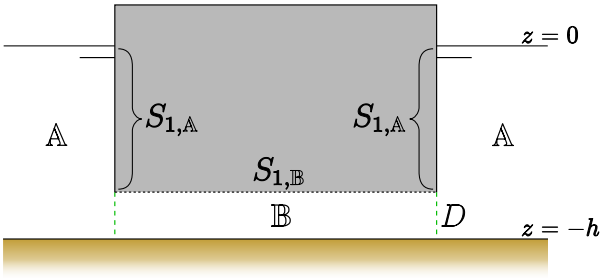

Figure 4.2: Domain boundary definition - single body with two domains

In this Hybrid Multi-Domain Diffraction Method (HMDDM), instead of directly solving the normal velocity and pressure at the domain boundary, the pressure is solved indirectly following the steps:

1. First, the in-/outflow velocity at domain boundary D from the gap domain $\mathbb{B}$ is determined using a 2D potential method. This normal velocity is defined as the boundary condition at domain boundary D at domain $\mathbb{A}$ side.

2. Then the 3D diffraction solution is found for domain $\mathbb{A}$ to find the source strength on each body surface and the boundary domain surface D. Then, the velocity potential at domain boundary D is determined.
3. Next, with the normal velocity and velocity potential known at the domain boundary, the velocity potential in domain $\mathbb{B}$ using the 2D solution is determined.
4. Finally, all hydrodynamic properties like wave load, added mass and radiation damping are calculated.

This approach relies on the assumption that the gap height is small, i.e. $h \to 0$, so again with the first term of (4.8) becoming large and the second term remaining finite. Physically, it can be related to the fact that when the gap is nearly zero, only motions with non-zero velocities on the bottom (heave, roll, pitch) will result in the significant flux of fluid through the gap. For other motions and diffraction, the flux will be small and the outside potential will not "feel" the presence of the gap; in this case the gap potential in the outside domain $\mathbb{A}$ will tend to zero. However, the effect of the outside potential on the potential in domain $\mathbb{B}$ remains finite, as does the ratio f/h.

The solution in step 2 is based on the set of equations similar to the multi-body problem (A.27), where boundary D is treated as a separate body. For a single body problem as presented in Figure 4.2, this results in multi-domain equation:

$$\begin{bmatrix} \mathcal{G}_{S_{1,\mathbb{A}},S_{1,\mathbb{A}}} & \mathcal{G}_{S_{1,\mathbb{A}},D} \\ \mathcal{G}_{D,S_{1,\mathbb{A}}} & \mathcal{G}_{D,D} \end{bmatrix} \begin{bmatrix} \sigma_{S_{1,\mathbb{A}},j} \\ \sigma_{D,j} \end{bmatrix}_{ib} = \dots$$
$$\begin{bmatrix} N_{S_{1,\mathbb{A}},j} & 0 \\ 0 & N_{D,j} \end{bmatrix} \forall\ ib \in \{S_{1,\mathbb{A}}, D\}\ \wedge\ j = 0..7 \quad (4.11)$$

Where the boundary condition $N_{S_{1,\mathbb{A}},j}$ are the standard direction cosines (A.16) due to motion mode $j = 1..6$ of the body and the boundary condition $N_{D,j}$ represents the gap in-/outflow velocity due to motion mode $j = 1..6$ of the body. The wave ($j = 0$) and diffraction ($j = 7$) potentials are solved based on the normal boundary conditions (A.17) and (A.18)) as defined on surface $S_{1,\mathbb{A}}$ and surface D.

When considering the multi-body problem as presented in Figure 4.1, the in-/outflow velocity at domain boundary D needs to be determined for each body interacting with the gap domain, because the velocity perpendicular to the fused surface S_b depends on the distance between the centre of contour D and the centre of gravity of the body. In (4.12), this is indicated by the indices D^1 and D^2. For the solution of the wave and diffraction potentials, one does not have to distinguish between the bodies.

$$\begin{bmatrix} \mathcal{G}_{S_{1,\mathbb{A}},S_{1,\mathbb{A}}} & \mathcal{G}_{S_{1,\mathbb{A}},S_{2,\mathbb{A}}} & \mathcal{G}_{S_{1,\mathbb{A}},D} \\ \mathcal{G}_{S_{2,\mathbb{A}},S_{1,\mathbb{A}}} & \mathcal{G}_{S_{2,\mathbb{A}},S_{2,\mathbb{A}}} & \mathcal{G}_{S_{2,\mathbb{A}},D} \\ \mathcal{G}_{D,S_{1,\mathbb{A}}} & \mathcal{G}_{D,S_{2,\mathbb{A}}} & \mathcal{G}_{D,D} \end{bmatrix} \begin{bmatrix} \sigma_{S_{1,\mathbb{A}},j} \\ \sigma_{S_{2,\mathbb{A}},j} \\ \sigma_{D,j} \end{bmatrix} = N_j \; \forall \; j = 0..7 \quad (4.12)$$

With:

$$N_j = \begin{bmatrix} N_{S_{1,\mathbb{A}},j} & 0 & 0 & 0 \\ 0 & N_{S_{2,\mathbb{A}},j} & 0 & 0 \\ 0 & 0 & N_{D^1,j} & N_{D^2,j} \end{bmatrix} \forall \; j = 1..6 \quad (4.13)$$

And,

$$N_j = \begin{bmatrix} N_{S_{1,\mathbb{A}},j} \\ N_{S_{2,\mathbb{A}},j} \\ N_{D,j} \end{bmatrix} \forall \; j = 0, 7 \quad (4.14)$$

4.1.4 Verification of HMDDM

Figure 4.3 shows the comparison of the dimensionless added mass based on the standard 3D diffraction method, the combined Drobyshevski-3D diffraction method and Drobyshevski's analytical solution (3.5) for a cylinder with different under-keel clearances. For the different cases the draft is the same, while the water depth is varied. The presented added mass is made dimensionless by the buoyancy of the cylinder. Clearly, for large gap height both numerical methods give similar results. In fact one may consider that the standard 3D diffraction method is more accurate as the combined method is based on the assumption that the gap is very small. As the gap height reduces, the 3D diffraction deviates more from the combined method, even with panel size smaller than the gap height. As such, one can postulate that the 3D-diffraction solution is inaccurate

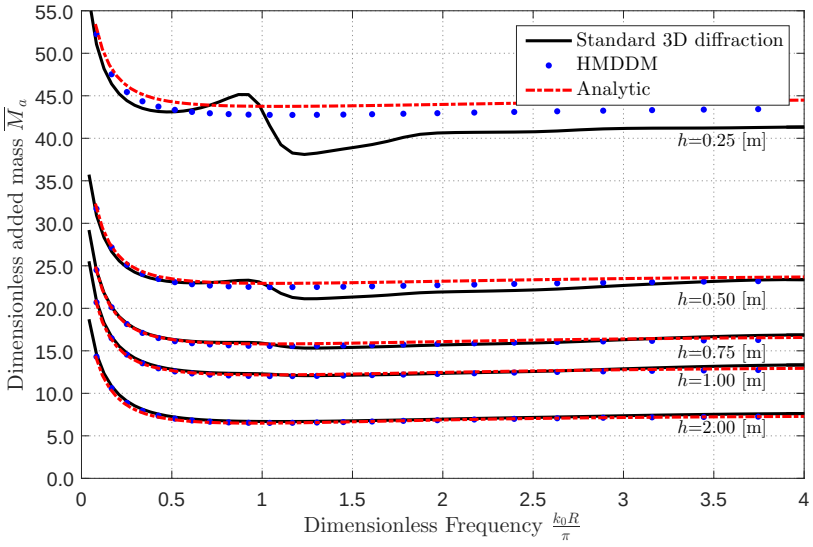

Figure 4.3: Heave added mass, cylinder at 5.0 [m] draft

for a small gap height, which was identified as one of the hydrodynamic issues. An acceptable difference between HMDDM and Drobyshevski's analytical solution is seen. This verification also confirmed that the radiation damping is independent of gap height, as was found analytically by Drobyshevski.

4.2 Coupled Time-domain Approach

To predict motions of a floating body in waves, the time-domain approach using the convolution theorem is the most appropriate method when the non-linear loads have a significant influence. With the convolution theorem, the frequency dependent hydrodynamic characteristics are accounted for appropriately. For the one degrees of freedom case, the general motion equation in time domain with convolution (B.16) becomes:

$$\{M + A_\infty\}\,\ddot{z}\,(t) + C\dot{z}\,(t) + Kz\,(t) + \int_0^t H\,(t-\tau)\,\dot{z}\,(\tau)\,d\tau = F\,(t) \quad (4.15)$$

The radiation force is expressed as the convolution form, in which $H(t-\tau)$ is the Convolution Integral Function (CIF):

$$H(t) = \frac{2}{\pi}\int_0^\infty B(\omega)\cos(\omega t)d\omega = \frac{2}{\pi}\int_0^\infty \{A(\omega) - A(\infty)\}\frac{\sin(\omega t)}{\omega}d\omega \quad (4.16)$$

Equation (4.16) implies that the added mass and radiation damping are directly related. Because of the fact that the added mass due to the gap domain is dependent of wave frequency and gap height, while the radiation damping is only frequency dependent, this hypothesis does not hold any more. Therefore, in line with Drobyshevski's findings, the added mass characteristics are investigated to split it in a frequency dependent part and a gap height dependent part $A(h)$, thus:

$$A(\omega, h) = A(\omega) + A(h) \quad (4.17)$$

Then, if for a given mean gap height $\bar{h}$ the added mass is known, a fitting function $f(h)$ may be used, such that (4.17) becomes:

$$A(\omega, h) = A_{\bar{h}}(\omega) + (f(h) - 1)\cdot A_{\bar{h}}(\infty) \quad (4.18)$$

Numerical calculation have been performed for a cylinder with different drafts at a specific water depth (thus with a range of gap heights), using HMDDM. As per (4.17), the added mass at infinity — being the constant part — is subtracted from the total added mass to arrive at the frequency part. The resulting components for the different gap height values are shown in Figure 4.4(a). Clearly, the frequency part for the different gap height values are virtually on each other, Figure 4.4(b) shows the difference in frequency dependent added mass with respect to the frequency dependent added mass for h=1.0 [m].

After adding the non-linear squeeze flow effort given by (3.4) to the right hand side of (4.15) and and combining with (4.18), the following time-domain equation for single body 1-DOF problem is found:

$$\{M + f(h)\cdot A_{\bar{h}}(\infty)\}\ddot{z}(t) + \frac{1}{2}f'(h)\dot{z}^2(t) + B\dot{z}(t)\cdots + Cz(t) + \int_0^t H_{\bar{h}}(t-\tau)\ddot{z}(\tau)\,d\tau = F(t) + F_D \quad (4.19)$$

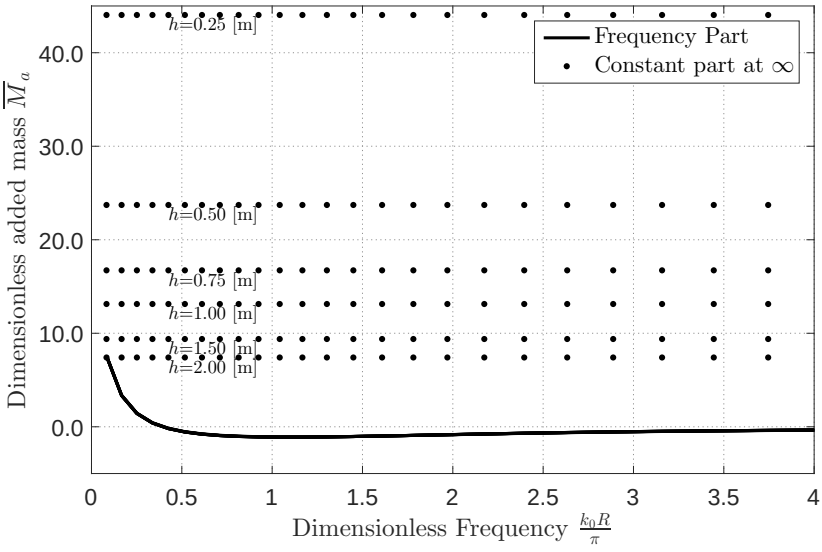

(a) Comparison of added mass components for different gap heights

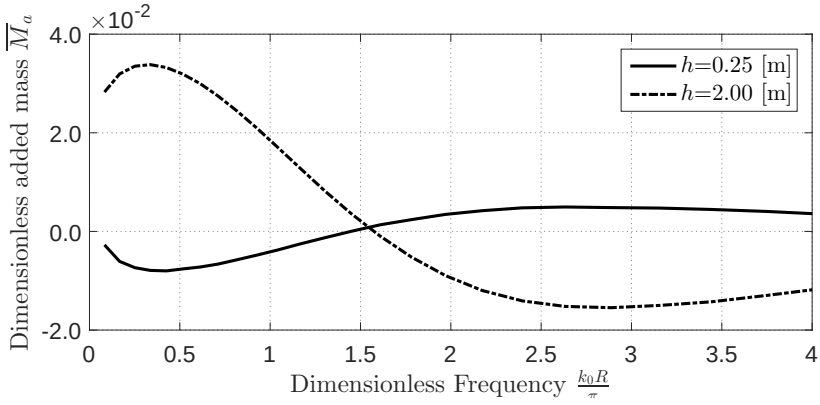

(b) Frequency Part, difference w.r.t. h=1.00 [m]

Figure 4.4: Gap and frequency dependent part

Equation (4.19) is used in Section 5.2 to show the influence of the non-linear gap force for the 1-degree of freedom. The general case with n_b bodies each with 6-DOF is given by:

$$\left\{\mathbf{M} + \mathbf{A}(\infty, \vec{h}(t))\right\} \ddot{\mathbf{X}}(t) + \left\{\mathbf{b} + \frac{d}{dt}\mathbf{A}(\infty, \vec{h}(t))\right\} \dot{\mathbf{X}}(t) \cdots + \mathbf{C}\mathbf{X}(t) + \int_0^t \mathbf{H}_{\bar{\mathbf{h}}}(t-\tau)\dot{\mathbf{X}}(\tau)d\tau = \mathbf{F}(t) \quad (4.20)$$

The Convolution Integral Function (CIF) $\mathbf{H}_{\bar{\mathbf{h}}}$ in (4.20) only uses the added mass characteristics for the mean gap height, thus:

$$\mathbf{H}_{\bar{\mathbf{h}}}(t) = \frac{2}{\pi} \int_0^\infty \left\{\mathbf{A}(\omega, \bar{h}) - \mathbf{A}(\infty, \bar{h})\right\} \frac{\sin(\omega t)}{\omega} d\omega \quad (4.21)$$

Practically, this means that the non-linear gap force can be implemented as an external function in existing time-domain hydrodynamic software.

CHAPTER 5

Verification and Validation Studies

To further examine the non-linear effect of squeeze flow, a simple single degree of freedom problem was evaluated for the floating cylinder above a fixed surface, as presented in Figure 4.2. Both forced oscillation response and free-floating response due to regular and irregular wave excitation are investigated. To validate the proposed method of separating the added mass components, first the forced harmonic oscillation tests (as presented in Section 3.3.1) are simulated. Second, simulations for a free-floating cylinder in shallow water are performed. Both simulation sets are carried out for a 40 [m] diameter truncated cylinder with a draft of $d = 4.5$ [m] and an under keel clearance of $\bar{h} = 1.0$ [m], see Figure 5.1.

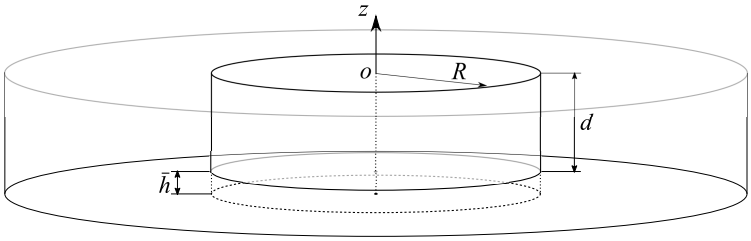

Figure 5.1: Reference system

First the function $f(h)$ in (4.18) must be defined. This function must be equal to one for $h = \bar{h}$ and should be of asymptotic form (i.e. $A(h) \propto \frac{1}{h}$). Investigating the added mass of a truncated floating cylinder, a good fit is found, when using:

$$f(h) = \left(\frac{h}{\bar{h}}\right)^b \tag{5.1}$$

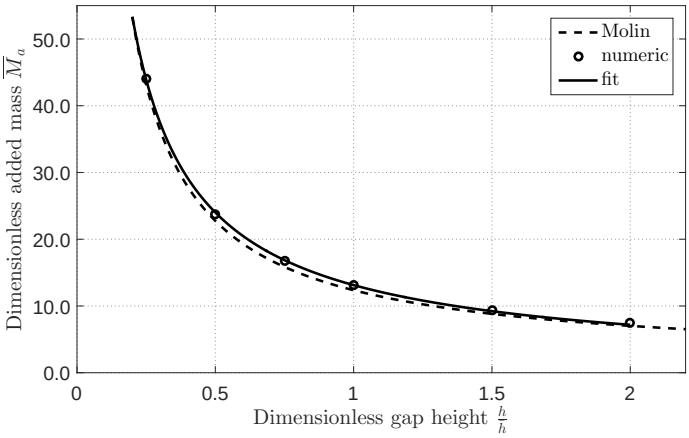

Figure 5.2: Gap dependent part

The gap dependent part (i.e. constant part at ∞), taken from Figure 4.4(a), is shown in Figure 5.2 and is compared to the added mass according to Molin and Vinje as per Table 3.1. Figure 5.2 also shows the fit on the numerical result using (5.1) with parameter b=-0.8710. It must be noted that this parameter will be different for other contour shapes.

As parameter b is always negative due to the asymptotic behaviour of the gap dependent part, (5.1) will become infinite for h is zero. This invokes numerical issues for a time-domain solver. A practical solution to avoid this problem is to extrapolate or limit the function below a specified gap height.

5.1 Forced Oscillation

As regular response is investigated, the convolution part of the time-domain (4.19) does not apply. So, after including the added mass and radiation damping as a function of the wave frequency in (3.4), the force acting on the oscillated body becomes:

$$F(t) = -(A_{\bar{h}}(\omega) + (f(h(t)) - 1) \cdot A_{\bar{h}}(\infty)) \cdot \ddot{h}(t) - B(\omega) \cdot \dot{h}(t) - ... \\ \frac{1}{2} f'(h(t)) \cdot A_{\bar{h}}(\infty) \cdot \dot{h}^2(t) + F_D(\dot{h}(t), h(t)) \quad (5.2)$$

The oscillation tests and simulations have been performed for different oscillation frequencies ω and different motion amplitudes a_m. Using the fit function shown in Figure 5.2 and using a $\tilde{C}_D = 1.5$ [m/s] for the linear damping component F_D (3.7), a good match with the measurements. The results are shown in Figure 5.3. The same trend is observed as presented in Figure 3.9. The simulated loads show a much smoother trend than the measurements, as also was shown in CFD calculations (see Figure 3.6).

Clearly, the non-linear effect is seen in all results, as the load does not follow a sinusoidal trend and an increase in motion amplitude shows a drastic increase in the load around $t = 1/2 \cdot T$, due to the asymptotically increasing added mass for smaller values of $\bar{h} - a_m$.

Sensitivity due to selected added mass prediction method on the forced oscillation effort is investigated. A fit on the added mass based on the standard 3D diffraction result as presented in Figure 4.3 is made, resulting in parameter b=-0.8144; as standard 3D diffraction under-predicts the added mass at very small gaps, the fitted curve is more flat at lower gap heights. With using a $\tilde{C}_D = 1.5$ [m/s] for the linear damping component F_D, the resulting load is shown in Figure 5.4. Clearly, the negative peak reduces due to lower added mass. The sensitivity due to the velocity squared term in (5.2) is insignificant, as the difference around $t = 1/4 \cdot T$ and $t = 3/4 \cdot T$ is small.

5.2 Free-floating Behaviour

To give more insight in the effect of the non-linear gap loads, simulations for the free-floating cylinder are carried out. Use is made of the ANSYS-AQWA® capabilities; the modules AQWA-NAUT (for regular wave simulation) and AQWA-DRIFT (for irregular wave simulation) are both using (B.16) and accept forces calculated at each time-step by a user-defined routine. This routine is accessed through a compiled dynamic link library (DLL).

A comparison is made between simulations using the standard linear theory — i.e. constant added mass value — and simulations with the gap dependent added mass $A(h)$ and the linear damping F_D (with $\tilde{C}_D = 1.5$ [m/s]) incorporated in the user-defined routine. Simulations have been

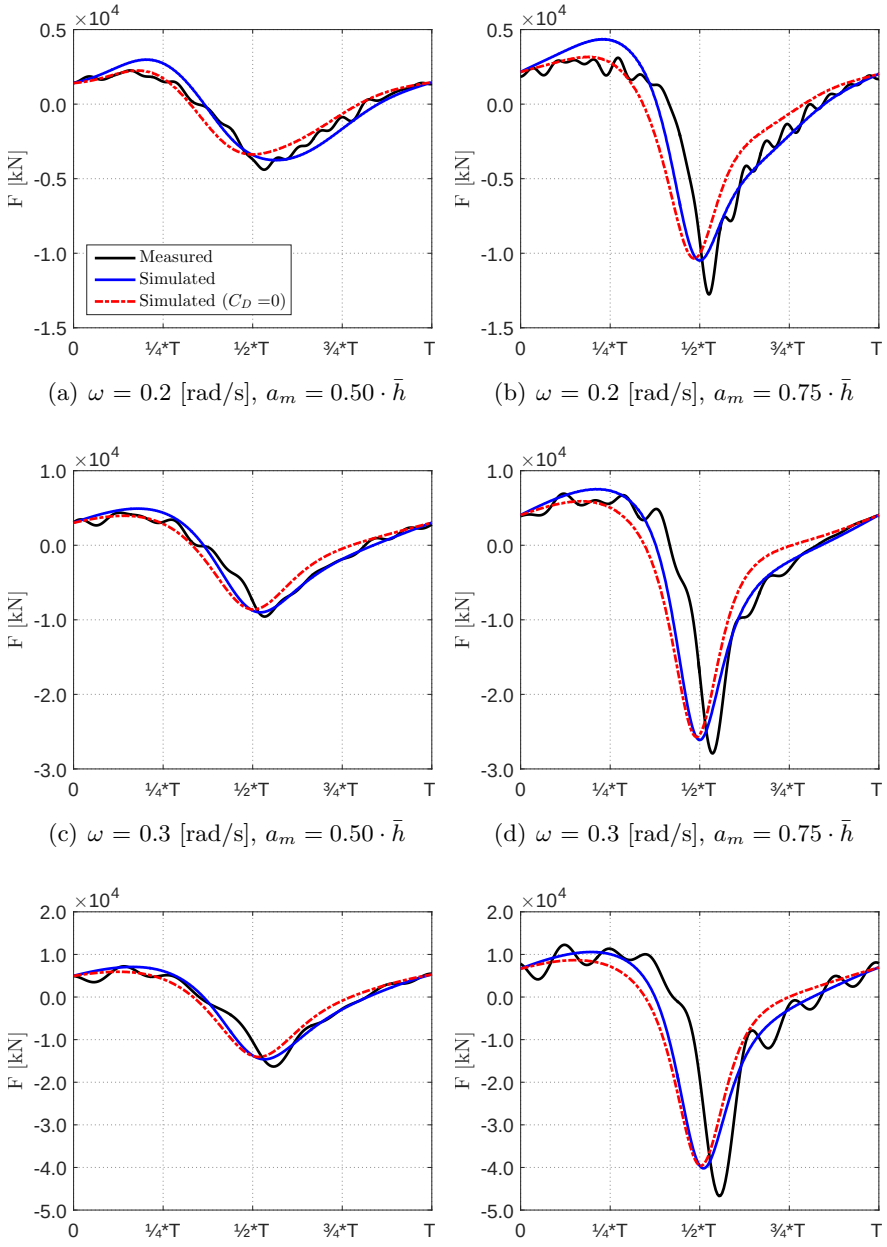

(a) $\omega = 0.2$ [rad/s], $a_m = 0.50 \cdot \bar{h}$

(b) $\omega = 0.2$ [rad/s], $a_m = 0.75 \cdot \bar{h}$

(c) $\omega = 0.3$ [rad/s], $a_m = 0.50 \cdot \bar{h}$

(d) $\omega = 0.3$ [rad/s], $a_m = 0.75 \cdot \bar{h}$

(e) $\omega = 0.4$ [rad/s], $a_m = 0.50 \cdot \bar{h}$

(f) $\omega = 0.4$ [rad/s], $a_m = 0.75 \cdot \bar{h}$

Figure 5.3: Comparison forced oscillation test and simulation ($\bar{h}$=1.0 [m])

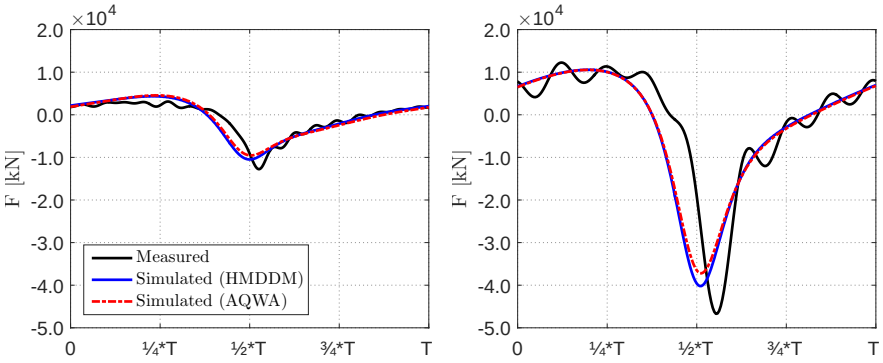

(a) $\omega = 0.2$ [rad/s], $a_m = 0.75 \cdot \bar{h}$ (b) $\omega = 0.4$ [rad/s], $a_m = 0.75 \cdot \bar{h}$

Figure 5.4: Sensitivity to selected added mass prediction method

performed for a heaving free-floating cylinder with a radius $R = 20$ [m], a draft of $d = 5.0$ [m] and an initial gap of $\bar{h} = 1.0$ [m].

First, simulations in regular waves have been performed. Figure 5.6 is showing the time traces of the heave motion for some of the regular wave frequencies, again comparing non-linear and linear responses. Also the regular wave elevation is plotted. It is observed in Figure 5.6(c) that the response does not repeat after each period for a wave frequency close to the natural frequency, therefore at $\omega = 0.3$ [rad/s] both peak values are plotted in Figure 5.5. Figure 5.5 is showing the maximum peak and trough values for the non-linear model compared to the linear model. The response is given for regular waves with an amplitude of 1.0 [m] at different wave frequencies. The linear results are found from the frequency-domain solution. From the time-traces, the cushioning and sticking effect as explained above is recognized during the shape of the troughs; the motion clearly decelerates when the body approaches the sea-floor and has a low acceleration when moving away. It is obvious that a frequency-domain solution cannot be used for the non-linear behaviour, because the peak and trough values are not of equal amplitude.

Second, one simulation is performed for a irregular wave condition. A Pierson-Moskowitz wave spectrum is used with a significant wave height H_s=1.2 [m] and peak period T_p=18 [s], which is close to the linear natural heave period. Figure 5.7 is showing time-traces of heave elevation and

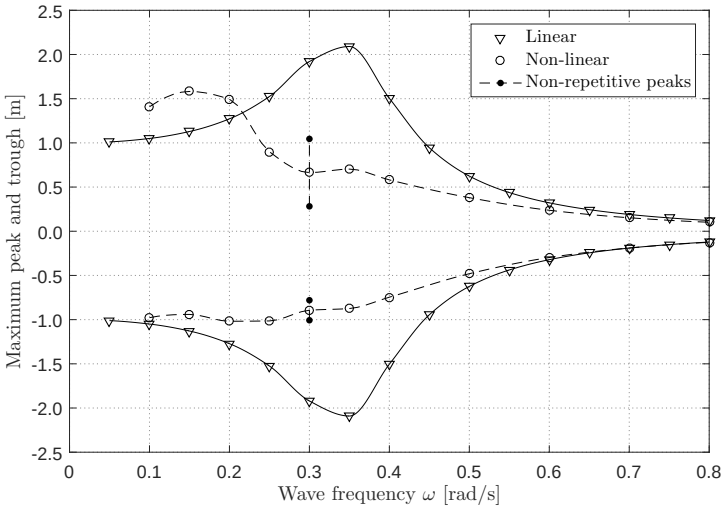

Figure 5.5: Vertical motion response to regular waves

velocity. Again, the non-linear model is compared to the linear model; for both models the same wave registration is used. Markers indicate impact events and corresponding velocity at impact. The number of impacts in a 3-hour simulation and maximum impact velocity are given in Table 5.1. Again, the cushioning effect is evident, resulting in a large reduction in the impact velocity. The importance of applying the non-linear model

Table 5.1: Impact results

	Counts	Max. Velocity [m/s]
Linear	36	0.37
Non-Linear	10	0.05

becomes clear when considering workability. The significant wave height would need to be reduced from H_s=1.2 [m] to approximately H_s=0.8 [m] for the linear model to establish the same level of impact velocity as found with the non-linear model. Such a difference is important when judging if an operation can be performed within an acceptable time-frame.

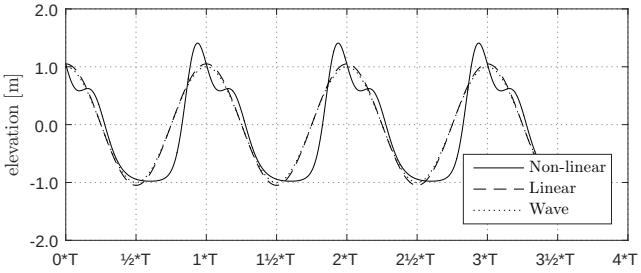

(a) $\omega = 0.1$ [rad/s]

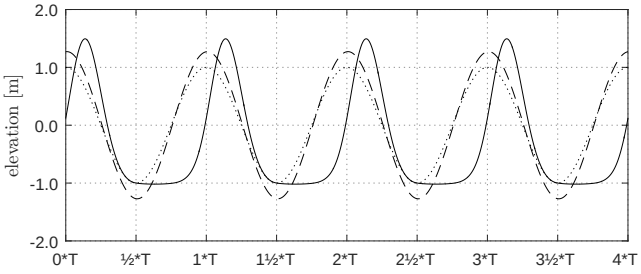

(b) $\omega = 0.2$ [rad/s]

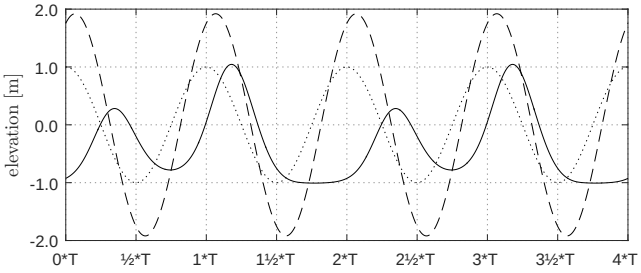

(c) $\omega = 0.3$ [rad/s]

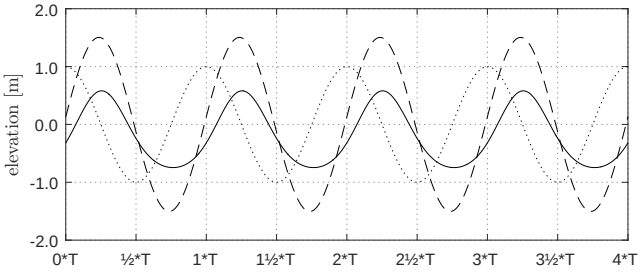

(d) $\omega = 0.4$ [rad/s]

Figure 5.6: Regular wave response ($\bar{h} = 1.0$ [m])

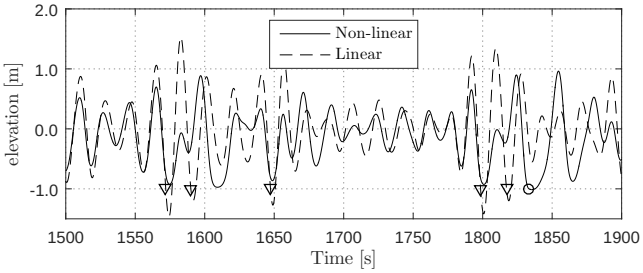

(a) Motion

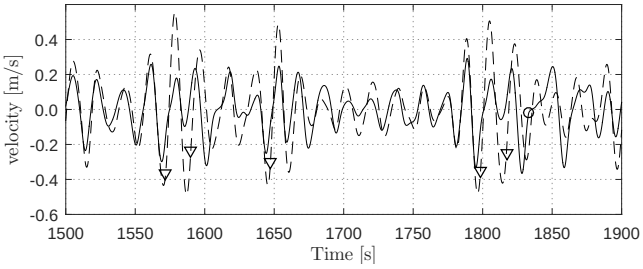

(b) Velocity

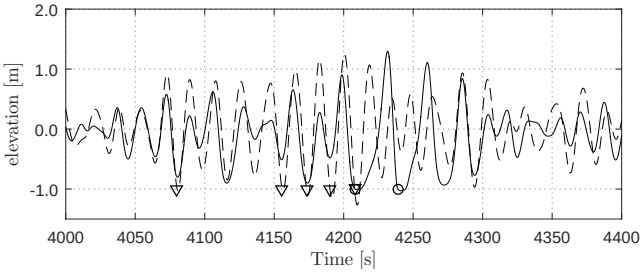

(c) Motion

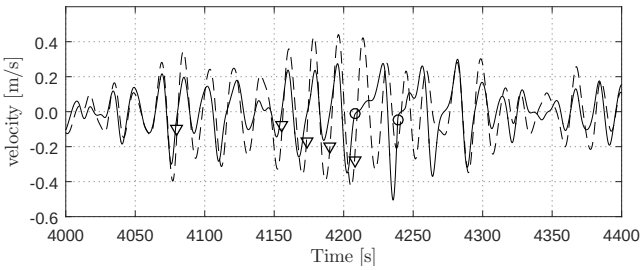

(d) Velocity

Figure 5.7: Irregular wave response ($\bar{h} = 1.0$ [m])

Horizontal Relative Motions

CHAPTER 6

Cargo Handling Equipment

The following chapters are dealing with positioning the cargo on the deck of an HTV. In this chapter, more insight is given in the support system and positioning requirement, and the standard equipment used for sheltered operation is described. Then, the concept equipment needed to reduce and control the relative horizontal motions between cargo and HTV in offshore conditions is outlined. In the next chapter, the performance of the new cargo handling concepts is compared with the standard system.

6.1 Cargo Support and Positioning Tolerance

To support the cargo on the HTV deck, cribbing is laid out on the HTV deck, see Figure 6.1. Normally, cribbing is made of wood, a natural product with a wide range of load capacity and stiffness. In recent years, also plastic cribbing has become available; this type can generally have a higher load capacity and the characteristics (i.e. capacity and stiffness) are controlled during fabrication. During loading and discharge operation in sheltered location, the impact loads on cribbing are extremely low and well within capacity range of cribbing and cargo structural strength.

Still, it is important to realize that cribbing is only used underneath strong point of the cargo, which requires accurate positioning by the mooring equipment. As generally, cribbing beams of 300 [mm] width is used, the positioning tolerance is about $\pm$ 100 [mm] from the centre line of the cribbing beams, see Figure 6.2. Generally, this tolerance is easily met during operations in sheltered location with standard environmental limitations.

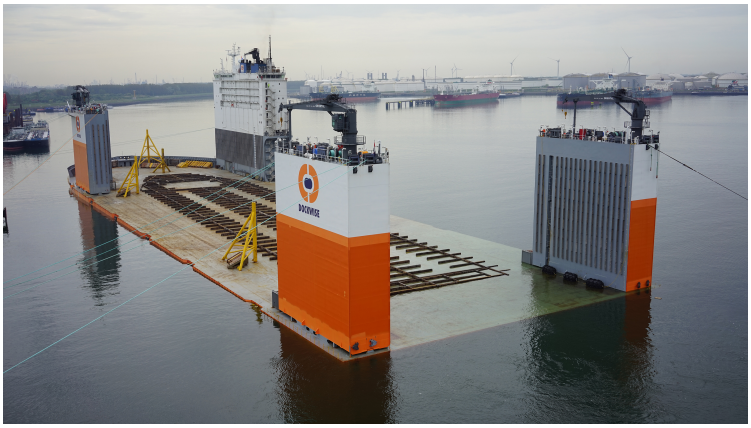

Figure 6.1: Guidepost (yellow tripods) and cribbing beams on HTV deck

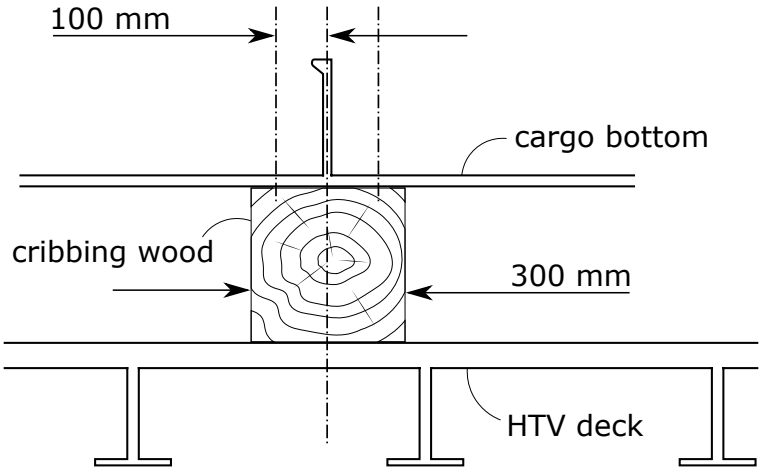

Figure 6.2: Positioning tolerance

6.2 Standard Equipment for Sheltered Operation

As mentioned in Section 1.2, equipment needed to position the cargo — within the tolerance — consists of one or more guideposts and a number of mooring ropes.

The main purpose of the guidepost is to give an accurate (visual) reference; in general it does not have the function to stop the motion of the cargo; occasionally these guideposts have been sheared off from the HTV deck. An example of a guidepost is shown in Figure 6.1. A more robust guiding system is shown in Figure 6.3. This system has an upper and lower part. The upper part consists of a fender-board, thus ensuring a soft impact when the cargo hits the guiding system and as such it allows for some horizontal relative motion. As this is undesired when positioning on the cribbing, the lower part of the guiding system is much stiffer by using wood fendering. When the HTV is de-ballasting the cargo touching area will shift from the upper to the lower part.

(a) (b)

Figure 6.3: Guiding system

Mooring ropes are connected to the cargo from either so-called tugger winches or supporting towing tugs. Size and strength of this type of equipment are such that it is suitable for operation in sheltered area with virtually no wave condition and limited wind and current speed. Furthermore, the size of mooring equipment is such that it can be handled by the HTV crew with the aid of a small handling boat. Typically, soft poly-prop rope or stiff lines (either steel wire of dyneema) with short stretchers are used.

The tugger winches are located on the HTV forecastle or accommodation tower and on the stability casing. The winch pulling capacity generally range between 25 and 50 [t] at slow speed on the winch motor. Brake capacity is generally more than twice this pulling capacity. Handling of the winches is done by crew members next to the winch; the crew members communicate with the superintendent.

The number of lines and layout to be used during the float-on and/or float-off operation is determined on beforehand. Drawings are made for different steps of the operation to show which line needs to be connected or changed sequentially; see for example Figure 1.3.

6.3 Concept Equipment for Offshore Operation

During years of research, it has been identified that just scaling the standard handling equipment to be able to cope with higher sea-states is not possible. Analyses showed that relative motions between cargo and HTV become large when using standard type of equipment or that loads become unrealistically high - and thus equipment unrealistically large - when trying to limit the relative motions. With the analogy to the assessment of harbour mooring, several investigations have been conducted, which were covering fender systems and tension control.

First, attempts were made to include fender systems, however as these generally work as springs like the tugger lines and the stiffness of a fender system is higher, the loads tend to increase even with reducing motion. It is even possible that, due to introducing more stiffness, resonance issues will occur, and as such the motions may increase also. To avoid resonance, damping needs to be added to the system.

Second, also other innovative systems have been looked at. Vreeburg [36] studied the effect of the ShoreTension® system attached to the handling equipment. Although very successful in harbours, it is shown that during offshore loading or discharge the system is only able to effectively reduce the low frequent motions and is not effective in reducing wave frequent motions. This confirms the basic issue to constrain motion due to high wave frequency load.

The above systems are all passive solutions to hold the cargo in position. These systems react to a motion to exert load between HTV and cargo. In other words, the systems react on the motions as a result of wave excitation, whereas one desires to react on these wave load itself to avoid that the motion is induced. As such the mooring system always reacts to late. Besides, as the load in the mooring system is built up, it will exert this load back to this system when it becomes larger then the excitation load. In other words, elastic potential energy is stored in the mooring system, which will be released to the system as kinetic energy. In the offshore and maritime industry also many active and passive motion control systems exist, well-known examples are dynamic positioning, heave compensation and motion compensated gangways. Active control for offshore loading and discharge was investigated by Lee [20]. This study clearly showed that with the right control settings, the motions can be reduced significantly.

Based on above mentioned investigations, the following aspects are considered, when inventing a system to limit the relative horizontal motion between the HTV and cargo:

1. Stiff connection; the relative motions would ultimately be minimal, when an almost infinite stiff connection can be made. Only structural deformation in the stiff connection would still exist. Practically it is impossible to create a stiff connection as the operation starts with two independently moving bodies, and as such a stiff connection cannot be made instantaneously without exerting high impact loads to the cargo.

2. Damped system; damping in a dynamic system is related to velocity, but in essence is about dissipating energy from the system. Damping cannot reduce motions to zero, because otherwise damping would not exist. However, damping may be essential to avoid resonance in the system.

3. Active control; both stiffness and damping are applied in traditional active control systems. Control systems can be effective in reducing motions, however are bound by the performance of actuators which need to apply the required control loads.

Based on these aspects, two concepts have been developed (Beelen [4]). The first concept is based on the principle of establishing a stiff connection between the HTV and cargo; the stiffness must be equivalent to a structural support. This concept is further referred to as Clamping System (CS). The second concept is based on the principle of actively compensating the stretch in the tugger lines; stretch is compensated by actuating the line tension. As such, the force in the tugger line becomes an active load instead of a reaction load. This concept is further called Line Tension Actuating System (LTAS).

6.3.1 Clamping System

The basic idea of the Clamping System is to create a rigid connection bewteen HTV and cargo, such that the natural frequencies of the horizontal relative motions are much higher than the wave excitation frequencies. However, establishing such a connection is not instantaneously possible due to the relative motion between HTV and cargo. The impact loads — occurring when the connection is made — would be too high for the cargo and the system, which would results in damage to the cargo structure and/or equipment. Therefore, the connection needs a transition from a soft to a rigid state. As such, with the stiffness changing, the natural frequencies will shift from a low value (i.e. ω_n in the order of 0.2-0.3 [rad/s]) to a high value (i.e. $\omega_n \gg 3.0$ [rad/s]). During the transition, the natural frequencies will coincide with the excitation frequencies. If this process is too slow, resonant behaviour may built up (Metrikine [22]), which may amplify the loads in the system. Therefore, the connection system should also exert enough damping during the transition.

The solution is found in combining a soft fender with a hydraulic cylinder. The hydraulic cylinder incorporates a control valve, which is gradually closed during the transition. With the control valve initially opened, the soft fender allows for relative motions resulting in low level loads in the Clamping System. While closing the control valve, the stiffness

and damping characteristics of this damping device change such that the relative motions are steadily reducing. Once the control valve is completely closed a virtually rigid connection is established.

The Clamping System exists of a number of supporting structures on two opposite sides of the cargo, as illustrated in Figure 6.4. Both or one of the sides of the structures will be movable, as to be able to initially manoeuvre the cargo between them. The fender-hydraulic-cylinder systems will be located at the top of the supporting structures; the height depends on the clearance between HTV deck and cargo bottom and the strong point and geometry of the cargo sides. Once the cargo is between the Clamping System, the system is engaged such that a small pretension in the soft fenders is established. Following, the control valves of the hydraulic cylinders are gradually closed.

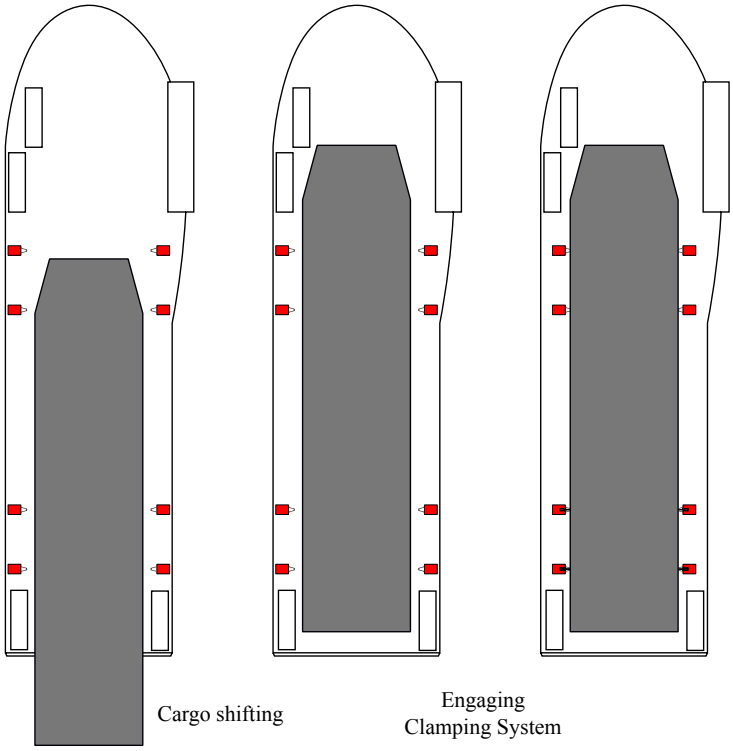

Figure 6.4: Clamping System

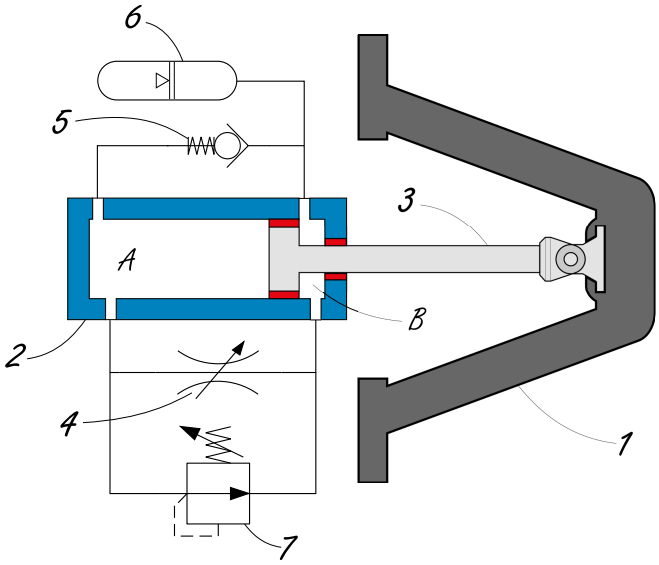

Figure 6.5: Damping device

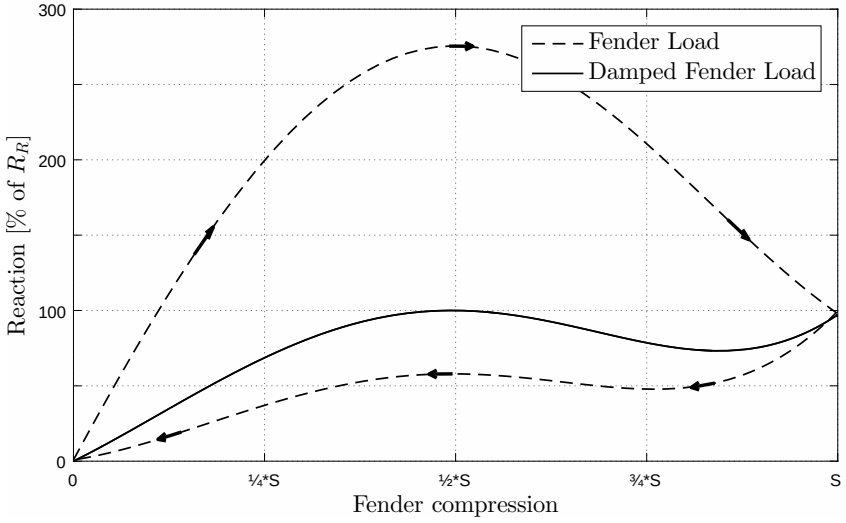

Figure 6.6: Load curve

Figure 6.5 is showing a schematic design of the damping device. The fender (1) and the cylinder housing (2) are connected to the supporting structure. The piston (3) is connected directly or indirectly to the fender (1). The hydraulic cylinder incorporates the control valve (4) and one-way valve (5), where the latter ensures free return flow. At the piston side a gas-charged or spring-loaded accumulator (6) is required to store the excess fluid. Finally, a pressure relief valve (7) is incorporated, which avoids overloading of the device.

The force generated by the damping device is the result of the pressure difference over and the velocity of the piston head. The control valve (4) and the one-way valve (5) are used to control this pressure differential. The generated force should be different for pushing in and heaving out. When the cargo pushes against the damping device, a large pressure difference is desired. This is achieved by throttling the flow through the control valve. When the cargo moves away from the device, heaving out of the piston rod depends on the restoring spring load of the fender and the hydraulic flow through the control valve and one-way valve. During this stage, it is beneficial if the fender is not pushing the cargo, as this would accelerate the cargo motion. As mentioned, the elastic potential energy should not be exerted to the cargo. Still, it is desired that the fender stays in touch with the cargo. This depends on the characteristics of the one-way valve and fender stiffness.

Figure 6.6 shows the load-extension curve of the damped fender subjected to a forced regular oscillation. The fender is compressed with piston stroke s, with a maximum velocity occurring at $\frac{1}{2}s$. In this example, a typical cone fender with non-linear stiffness is used. The direction of the load trace is indicated by the arrows. When the piston is moving from position zero to s, the hydraulic fluid is pushed through the control valve, which results in large pressure difference depending on the velocity. When the piston is moving from s to zero position, the fluid is pushed through both control valve and one-way valve. As the total flow area is larger, the pressure difference will be less. At this stage the reaction load will be below the fender load. Naturally, the maximum load depends on the control valve setting.

The principles of fluid mechanics is used to develop a simplified model describing the dynamic behaviour of the damping device (Symans et al.

[32]). The following mass flow rate continuity equation is used:

$$\frac{dV_i}{dt} + \frac{V_i}{\beta}\frac{dp_i}{dt} = Q_i \tag{6.1}$$

The flow rate is found from Bernoulli's equation:

$$Q = -k_d A_v \sqrt{\frac{2|\Delta p|}{\rho}}\,\mathrm{sgn}(\Delta p) \tag{6.2}$$

The fluid volume as a function of piston displacement x at chamber A side ($i = 1$) and at chamber B side ($i = 2$) including the accumulator (i.e. the accumulator is part of the volume domain at chamber side B) are respectively:

$$\begin{aligned} V_1 &= (s - x) \cdot A_1 \\ V_2 &= x \cdot A_2 + V_{ac,ini} + \tfrac{p_2 A_f}{K_a} A_f \end{aligned} \tag{6.3}$$

Further, the flow rate is $Q = Q_1 = -Q_2$ and the pressure difference is $\Delta p = p_2 - p_1$. Combining the equations results in the following set of first order non-linear differential equations:

$$\begin{aligned} \tfrac{dp_1}{dt} &= \frac{\left(\dot{x}A_1 - k_d A_v \sqrt{\frac{2|p_2 - p_1|}{\rho}}\,\mathrm{sgn}(p_2 - p_1)\right)\beta}{(s - x)A_1} \\ \tfrac{dp_2}{dt} &= \frac{-\dot{x}A_2 + k_d A_v \sqrt{\frac{2|p_2 - p_1|}{\rho}}\,\mathrm{sgn}(p_2 - p_1)}{\frac{A_f^2}{K_a} + \left(xA_2 + V_{ac,ini} + \frac{p_2 A_f^2}{K_a}\right)\frac{1}{\beta}} \end{aligned} \tag{6.4}$$

In (6.4) the term $k_d A_v$ depends on the travel direction of the piston; when the piston is pushed in the control valve and pressure relieve valve contribute to this term, whereas when the piston is heaved out the control valve and one-way valve contribute to this term.

6.3.2 Line Tension Actuating System

The concept of the LTAS originates from the idea to compensate the stretch in a mooring line by winching in or out. In other words, a line

actuator is applied, which should react on the line tension. However, as the line tension increases — and thus the stretch will increase — winching in will in itself increase the line tension. As such, a basically unstable system is found. Therefore, an actively controlled actuator instead of a reactive actuator is designed, such that the line actuator needs to deliver a specified tension. This is achieved by applying a closed-loop control system to the relative motion, which is similar to the principles of Dynamic Positioning Systems.

The closed-loop control system consists of a motion reference unit (MRU) and a PID-controller; the measured relative motion is translated to a required force to compensate the relative motion. Following, the required force is allocated to a combination of line tension actuators. The main difference with the well-known DP-systems is that also wave frequency motions will be compensated, whereas DP-systems use controllers to only compensate the drift frequency motions, because normally DP-actuators — i.e. thrusters — cannot react fast enough. A simple representation of the closed-loop system is shown in Figure 6.7.

Since the wave frequency relative motions are controlled, it is evident that the line tension actuators need to act in the same frequency range. Furthermore, the required line tensions are expected to be in the same order of magnitude as the line tensions for a standard passive system. In perspective, one should realize that a peak tension of 1000-4000 [kN] needs to be exerted within a quarter of the oscillating frequency, thus on average within 2-3 [s]. Using industry available mooring lines, the involved stretch in the lines is expected to be in the same order as the relative motions of the passive system. This implies that there will be a demanding power requirement for the LTAS.

Figure 6.8 is showing a schematic of the LTAS. The system employs a hydraulic cylinder (1) to tension the mooring line (2). The mooring line runs from a winch or connection (3) on the HTV (4) over several sheaves (5) through fairlead (6) to the connection (7) on the cargo (8). The line may run over the sheaves a second time, see Figure 6.9, to reduce the required stroke but increasing the cylinder load by a factor 2.

The tension in the line is controlled through regulating the fluid flow from and to the hydraulic cylinder, based on a feedback controller (9), which measures the line tension in sheave (5c). The flow direction depends on

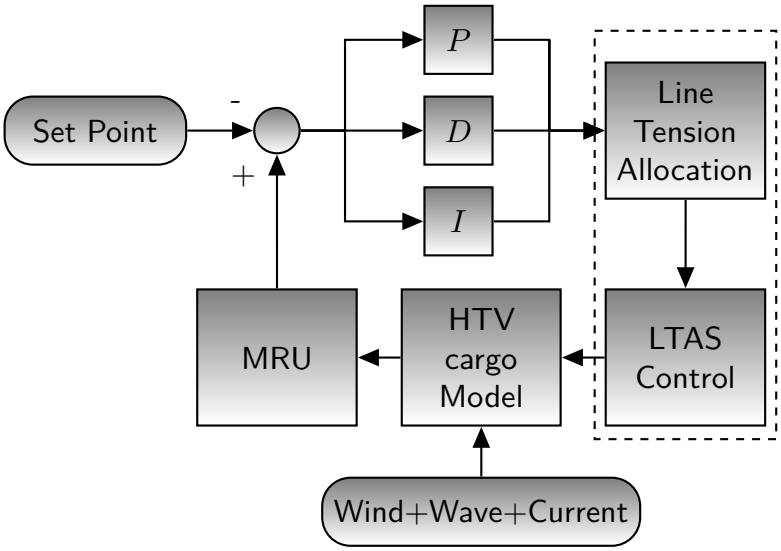

Figure 6.7: Closed-loop system

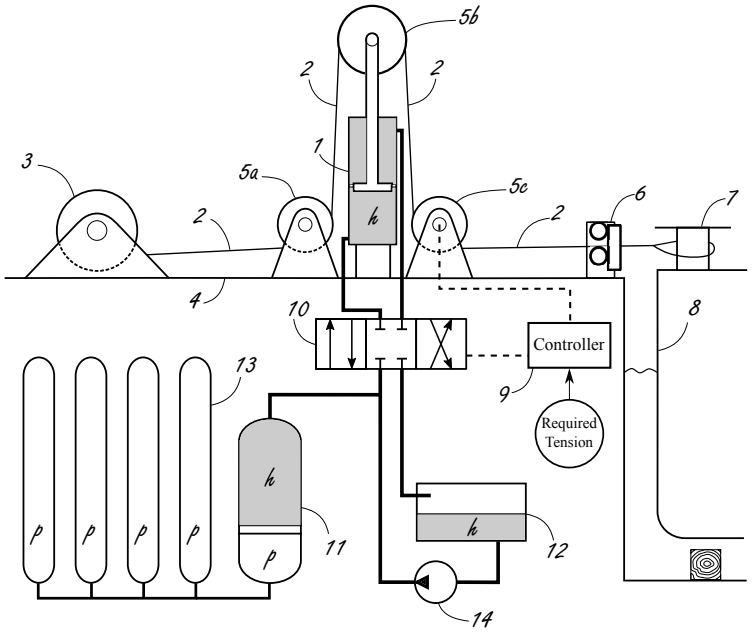

Figure 6.8: Line Tension Actuator System

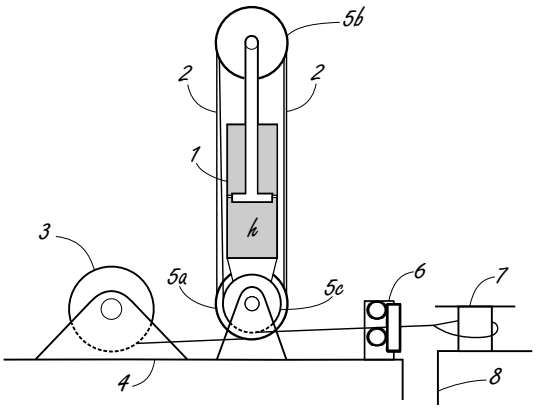

Figure 6.9: Line Tension Actuator System - double fall sheave alternative

the sign of the difference between required and measured force. When the tension difference is positive, the 4-way valve (10) is moved to the right to allow the hydraulic fluid (h) to flow from the accumulator (11) to the lower chamber of the cylinder; at the same time hydraulic fluid will flow from the upper chamber to the hydraulic tank (12). Vice versa, when tension difference is negative, the valve is moved to the left to allow flow from the lower chamber of the cylinder to the hydraulic tank; at the same time hydraulic fluid will flow from the accumulator to the upper chamber of the cylinder.

The power demand is achieved by using stored pneumatic energy, the pneumatic air is stored in the pressure vessels (13); the pressure in the vessels should be such that pressure difference over valve (10) will be enough to achieve the desired fluid flow. As gradually hydraulic fluid is used from the accumulator and is flowing to the storage tank, a hydraulic pump (14) is incorporated to keep enough pressurized hydraulic fluid available in the accumulator.

For the LTAS, the same principles of fluid mechanics as presented by (6.1) and (6.2) are applied to the hydraulic cylinder and 4-way control valve. For the pneumatic pressure vessels the adiabatic gas law is assumed. And a PD-controller is used for the 4-way valve.

6.3.3 Applicability of Concepts

The applicability and use of either or both of the systems depends on operational aspects, structural design and dimensions and type of cargo and performance. To judge the applicability, first the advantages and disadvantages need to be recognised, second the performance is shown through analysing theoretical models.

By comparing the Clamping System and Line Tension Actuator System based on versatility, energy use, size and complexity, the advantages and disadvantages are recognised:

1. The arrangement of the LTAS can be made in such a way that reduction of both longitudinal and transverse motions is possible. The Clamping System can only reduce the motion in one direction, because during the operation it must be possible to manoeuvre the cargo in between the system. When the Clamping System is engaged, frictional loads will influence the perpendicular movements. This friction load must be low enough to allow for vertical movement due to HTV draft change and must not restrict the perpendicular horizontal movement for positioning on the cribbing support.

2. In principle, the Clamping System is a passive system except that an adjustment system is needed to position the support structure, and that the control valve needs to be actuated. However, this is done at low energy cost. On the other hand, the LTAS is an active system, which requires pneumatic energy to keep enough hydraulic fluid available to actively control the tension during the critical phase of the operation.

3. The feasibility to use the Clamping System may depend on available deck space around the cargo and available cargo side-shell space. Here, the structural and mechanical design of the Clamping System and the structural integrity of the cargo play a roll. The type of adjustment system, e.g. skidding or pivoting, influences the foot-print of the Clamping System. It is expected that the LTAS will require less space, and is more flexible in the design by possibly decentralizing parts of the system. Also, the LTAS can possibly be incorporated in the standard handling equipment.

4. The LTAS is a complex system, where the actuators (and their auxiliary) are coupled to a computer system. Still, the system is built up from known components. However, the complexity increases when redundancy is required and to make the system fail-safe. The Clamping system is less complex — the different damping devices do not need to be synchronized — and it is easier to make it fail-safe (i.e. bring the system to a safe-state).

CHAPTER 7

Performance of Concept Cargo Handling Equipment

7.1 Clamping System

To give insight in the performance of the damping device, simulations have been carried out, where the 12-DOF problem — i.e. the relative motions between two bodies — is simplified to a one degree of freedom system. This elimination of motion coupling is done to limit the number of parameters, which influence the performance of the Clamping System. First, ANSYS-AQWA® simulations have been performed for an FPSO connected by a standard mooring system floating above a HTV. Second, a number of 1-DOF simulations in the MATLAB-Simulink® environment are performed using a regular excitation force and applying the damping device with different settings.

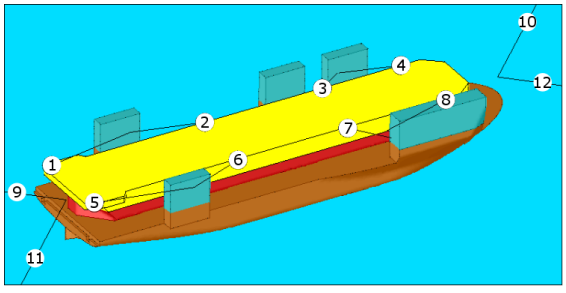

Figure 7.1: 12-DOF AQWA simulation model

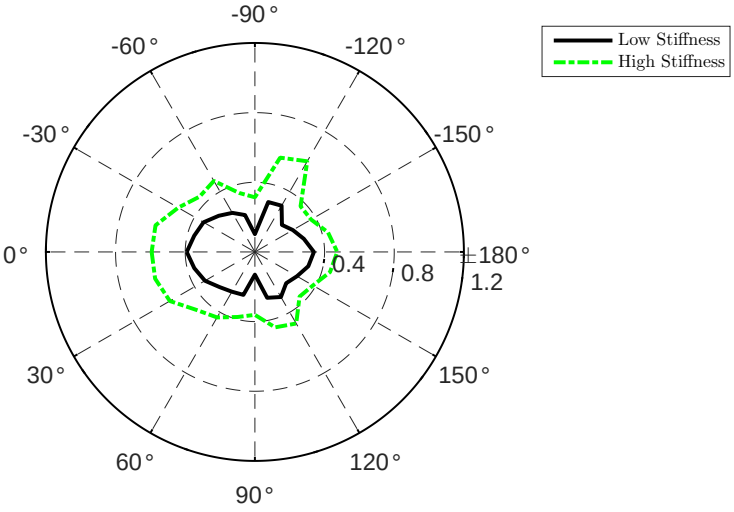

(a) Maximum relative surge amplitude [m]

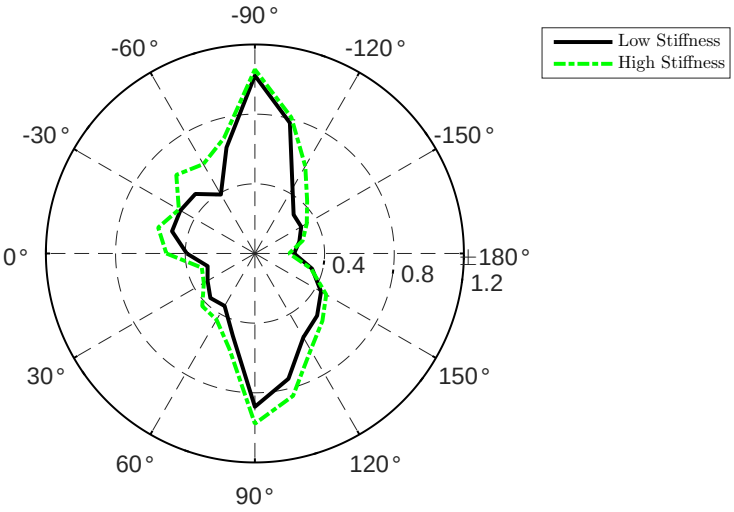

(b) Maximum relative sway amplitude [m]

Figure 7.2: Time-domain simulation results - motions

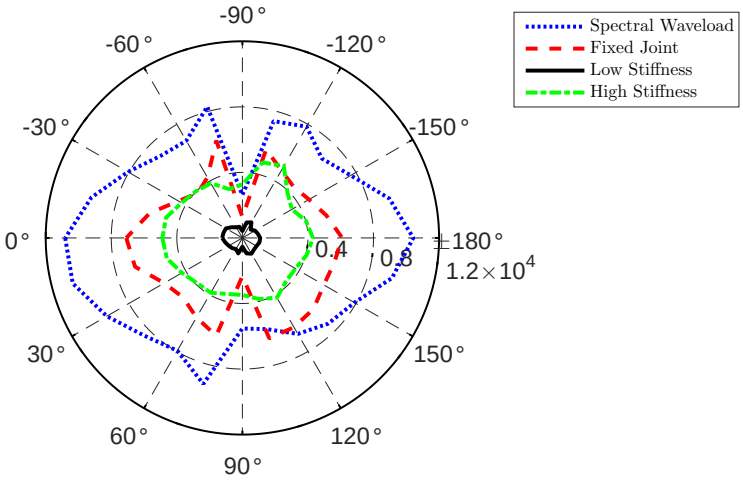

(a) Maximum F_{Surge} amplitude [kN]

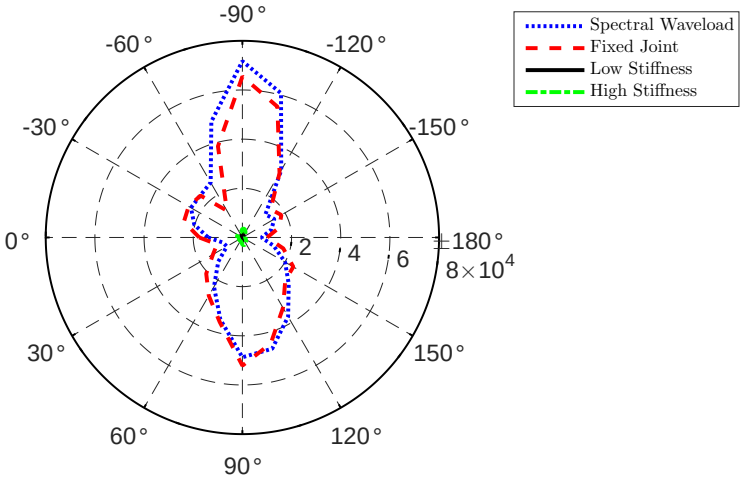

(b) Maximum F_{Sway} amplitude [kN]

Figure 7.3: Time-domain simulation results - loads

7.1.1 Reference simulation

A number of AQWA simulations are performed to give more insight in the relative motions and the excitation and mooring loads. The 12-DOF simulation model is shown in Figure 7.1. Lines 1 to 8 represent the standard cargo handling mooring. Lines 9 to 12 are soft springs for global positioning of the double-body system. The stiffness of the soft springs is chosen low enough, such that the springs do not influence the loads between HTV and FPSO.

Three variations are made on the mooring system to give more understanding of the motions and loads between FPSO and HTV; a low and a high line stiffness value is applied to show the influence on motion and mooring load response, and a fixed joint connection between HTV and FPSO is used to show the maximum excitation load to be handled by the Clamping System. Simulations were done with a Pierson-Moskowitz wave spectrum (H_s =2.0 [m], T_p =10 [s]) at different wave headings. The relative surge and sway motion results, versus incoming wave direction with respect to stern, are shown in Figure 7.2. The total mooring load is shown in Figure 7.3, for comparison this figure also includes the spectral result based on the wave load transfer function of the FPSO. All results are presented as most probable maximum amplitude for a 3-hour storm duration.

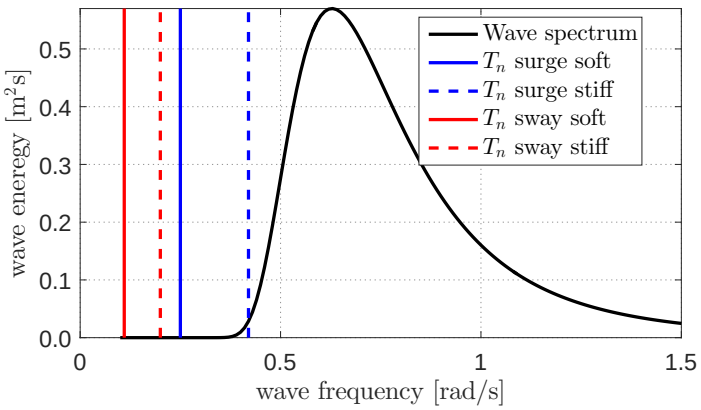

Figure 7.4: Natural frequencies

As concluded from Figure 7.2, the simulations show that the line stiffness does not strongly influence the sway motion. While, due to increase in stiffness, the surge motion increases. This is caused by the natural frequency shifting towards the wave spectrum. For sway, less difference is found, which is explained by the fact that the natural frequency is further away the wave spectrum than the natural frequency for surge. Dynamic mode analysis in AQWA shows the natural frequency for relative surge increased from about 0.25 [rad/s] to about 0.42 [rad/s] by increasing the mooring line stiffness. For sway the increase is from about 0.11 [rad/s] to about 0.20 [rad/s]. The natural frequencies are compared to the wave spectrum in Figure 7.4. This was further confirmed by investigating the spectral energy plots of the relative motions.

Further, the result show that the mooring system hardly compensates the excitation load. This is concluded from Figure 7.3, where the spectral wave load for the sway direction has the same magnitude as the fixed joint load, whereas for surge direction a large difference is found. This is explained by interaction between the FPSO and HTV, which is more pronounced for the surge direction than for the sway direction. And it is explained by the mooring configuration, which shows that the lines are mainly oriented in surge direction.

7.1.2 Clamping System performance

Next, a 1-DOF simulation is performed. Therefore, the mass, mooring stiffness, wave damping and excitation load and period are chosen such that the motion response for the 1-DOF system with the standard (soft) mooring system is reproduced with the same order of magnitude. The 1-DOF simulation paramters are given in Table 7.1, where the total mass is the sum of the FPSO weight and the added mass. The wave load and damping are estimated from the 12-DOF simulation results, whereas the added mass is tuned to establish the desired response. As example, the 150 [deg] wave direction sway motion result from Figure 7.2(b) is chosen. A motion of about 0.4 [m] as indicated by the dashed line in Figure 7.5(a) is matched. This figure shows the envelope of the oscillating motion.

Following, the Clamping System — equivalent to 4 pairs of damped fenders of realistic size — are added to the simulation, where the fenders are pre-compressed to 0.1 [m]. Each fender has a linear stiffness of 1200 [kN/m] and

Table 7.1: 1-DOF simulation parameters

	parameter	units
Total mass	98,500	t
Mooring stiffness	1,150	kN/m
Linear wave damping	50,000	kNs/m
Natural frequency	0.11	rad/s
Critical damping	21,300	kNs/m
Excitation force amplitude	20,000	kN
Oscillation period	10	s

has a hydraulic cylinder with a piston diameter of 0.75 [m]. By adding the fenders the response would increase as the stiffness of the system increases, however as the fenders are damped no increase is observed. Starting at 100 [s], the control valve is gradually closing. Next at 400 [s], the control valve is kept at 10 [%] of maximum opening, at this stage the oscillations stay constant. Starting at 600 [s], the control valve is closing further. Finally, the control valve is completely closed at 700 [s], then the motion response is almost zero, shown in Figure 7.5(a).

As the control valve closes, the damping device peak load slowly increases until the pressure reaches the relief valve settings, as seen Figure 7.5(b). Since the motions are larger than the pre-compression of the fender, fender impacts will occur. At the impacts, the fluid will virtually have an instantaneous velocity, resulting in a instant pressure difference in the control valve. Depending on the impact velocity and the control valve closure, this may result in high peak loading, as seen in Figure 7.5(c) for $t < 400$ [s]. With the pressure relief valve set at $P_r = 150$ [bar], this peak loading is avoided, see Figure 7.5(d). Once the motions reduce to less than the pre-compression at $t = 400$ [s], the load will behave as illustrated in Figure 6.6 for $t > 400$ [s]. The influence of pre-compression is also investigated. A comparison between 0.1 and 0.2 [m] pre-compression is shown in Figure 7.6. With larger pre-compression, the impact velocity and thus the peak loading will reduce, and starting at larger motion amplitude (i.e. 0.2 [m]) no impact will occur any more. It is concluded

that the maximum damping device load can be reduced by increasing the pre-compression, even such that the maximum load will not exceed the loads during stiff connection (i.e. control valve fully closed). Since the allowable load depends on the structural capacity of the cargo, the operational workability can be optimized by making a trade-off between the damping device design, the pre-compression, the pressure relief valve setting and the structural design of the supporting system.

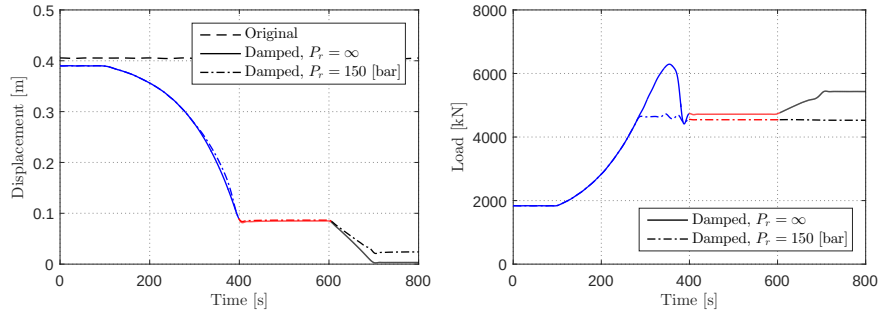

(a) Response amplitude envelope

(b) Device load envelope

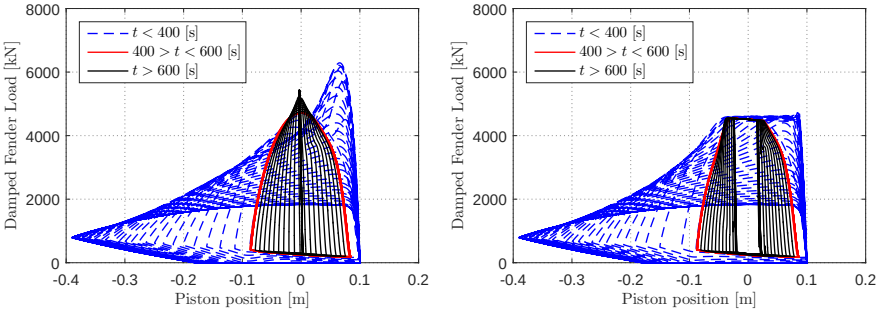

(c) Device reaction $P_r = \infty$

(d) Device reaction $P_r = 150$ [bar]

Figure 7.5: Damping device performance

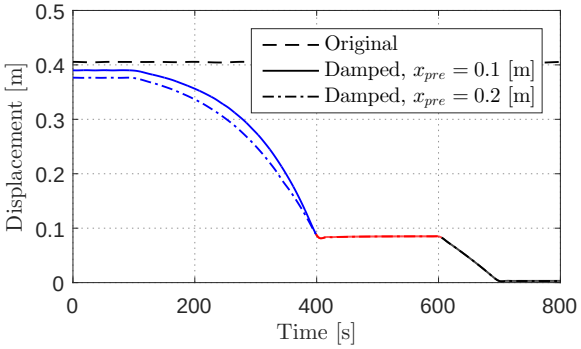

(a) Response amplitude envelope

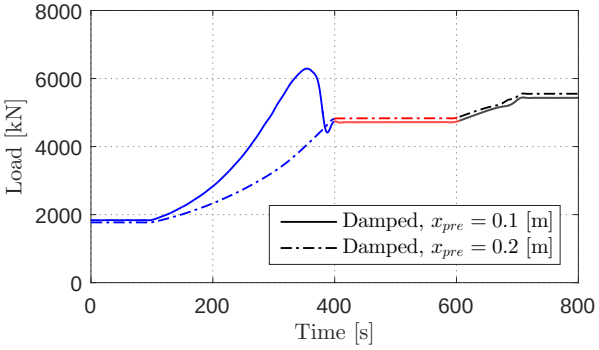

(b) Device load envelope

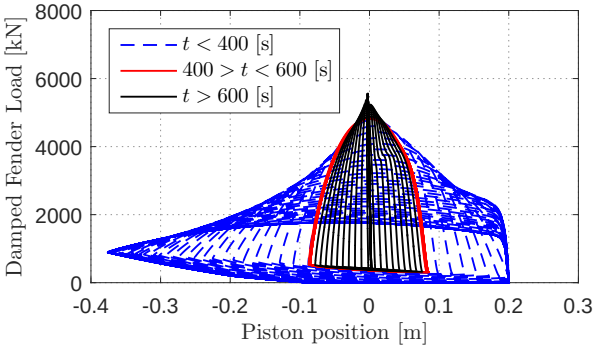

(c) Damping device reaction ($x_{pre} = 0.2$[m])

Figure 7.6: Influence pretension

7.2 Line Tension Actuating System

The performance and effectiveness of the Line Tension Actuating System is investigated in a number of steps. Starting point of this investigation is the model tests carried out in 2011. The first step is to reproduce the model test in a simulation environment. Thereto, AQWA time-domain calculations with the model shown in Figure 7.7 are performed using the wave registrations from the model tests. Tuning is done by adding damping terms, such that the significant values of relevant responses are matched to an acceptable accuracy. Comparison between model tests and simulations are provided in Appendix D.

7.2.1 PID tuning

Second step is performing a time-domain simulation using the same AQWA model combined with the PID-controller block presented in Figure 6.7. In this step the line tension allocation and LTAS Control block is excluded to ensure that the required load is always obtained and thus avoiding disturbance by the LTAS performance. For the PID settings the following equations are used:

$$\begin{aligned} P_m &= M_m \cdot K_p \quad \text{with} \quad K_p = \frac{\omega_n^2}{1 - 2 \cdot b/(\tau \cdot \omega_n)} \\ D_m &= M_m \cdot K_d \quad \text{with} \quad K_d = \frac{K_p}{\tau \cdot \omega_n^2} + 2 \cdot b \cdot \omega_n \\ I_m &= M_m \cdot K_i \quad \text{with} \quad K_i = \frac{K_p}{\tau} \end{aligned} \tag{7.1}$$

where

M_m	:	mass incl. low frequent added mass	[t]
m	:	motion mode $m = [1, 2, 6]$	[-]
ω_n	:	natural frequency $= \frac{2\pi}{T_n}$	[rad/s]
b	:	damping factor	[-]
τ	:	integrator constant	[s]

The natural period T_n and damping factor b are varied to get better insight in the influence and tuning possibilities of the PID-controller. Initially, the LTAS capacity (i.e. allowable line tension) is unlimited and the PID setting are varied to get insight in achievable positioning accuracy and

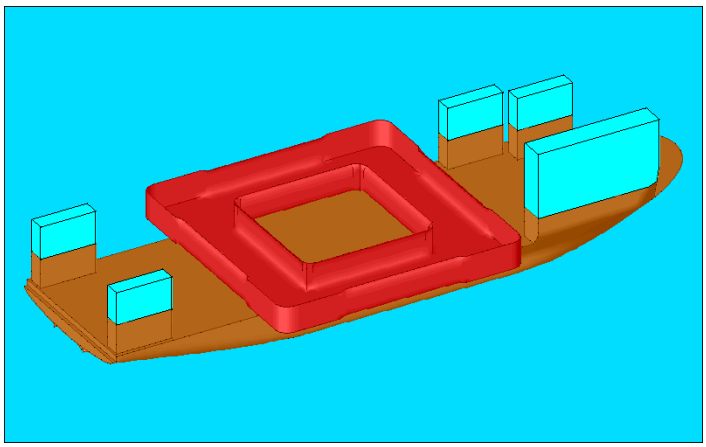

Figure 7.7: Simulation model

Table 7.2: Mass properties

	parameter	units
Cargo mass	107,250	t
Yaw radius of gyration	49.93	m
Added mass surge	96929	t
Added mass sway	64462	t
Added mass yaw	4.61E+07	tm^2

required control force. An integrator constant τ =120 [s] was used. the same PID parameters T_n, b and τ were used for relative surge, sway and yaw motion. The mass properties are shown in Table 7.2.

Figure 7.8 shows the influence of the PID settings on the required longitudinal load and resulting relative surge motion for a head sea condition. In this figure it is observed that the optimal b is found where the motion and force contour lines are more or less parallel; this is found at $b \approx 0.5 \cdot \frac{1}{2}\tau\omega_n$. For larger b the required force increases and with $b \to \frac{1}{2}\tau\omega_n$, the denominator of K_p limits to zero and $K_p \to \infty$, unstable control is found.

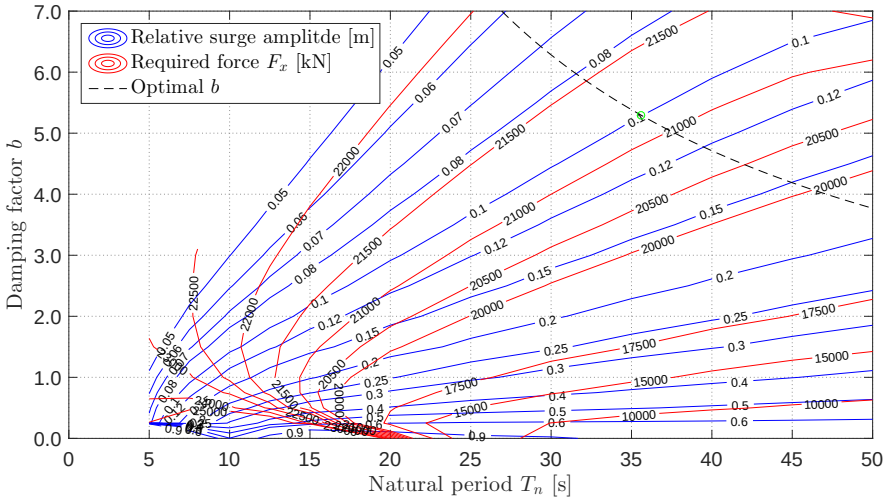

Figure 7.8: PID influence

PID tuning is also investigated by using the frequency-domain approach. The method to account for the specific feature of the LTAS in the frequency-domain solution is explained in Appendix B.2. The control force is based on the reference locations on the HTV and cargo, while the actuators are located at another level. This means that the stiffness and damping matrices related to the PID-controller need transformations, such that the motions at the body centres of gravity are solved. In Figure 7.9, a comparison between time-domain and frequency-domain is made for the optimal damping factor b and $T_n = 32$ to 50 [s], dotted lines connect the time- and frequency-domain results for each period. A significant difference, where the frequency-domain approach is over-estimating the response. Therefore, the frequency-domain approach is considered not accurate enough for engineering purpose.

7.2.2 Line tension allocation

As third step, a time-domain simulation is carried out using the PID-settings $T_n = 35.7$ [s], $b = 5.28$ and $\tau = 120$ [s]. After 400 [s], the LTAS is switched on with a ramp up time of 120 [s]. Now, the line tension allocation block is included; the LTAS Control block is still excluded.

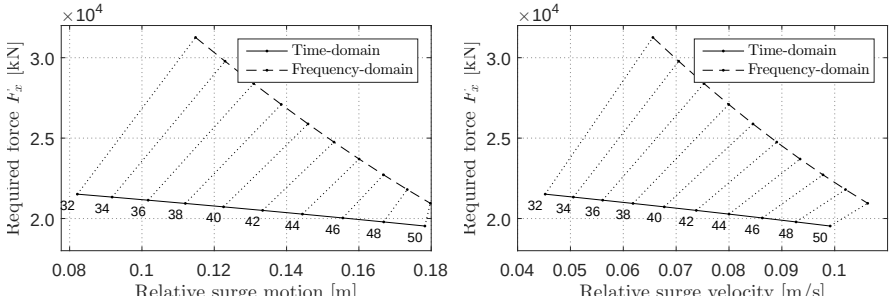

(a) Position (b) Velocity

Figure 7.9: Comparison frequency-domain versus time-domain

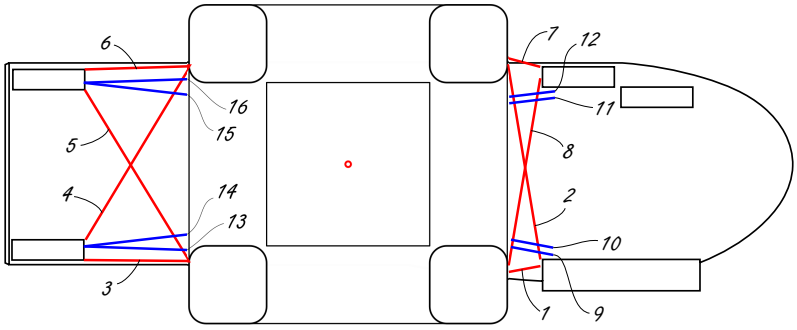

Figure 7.10: Mooring line configuration

The line tension allocation is based on a constrained least square method. The mooring line configuration is shown in Figure 7.10. Lines 1 to 8 are the standard handling lines each equipped with a LTAS. These lines are initially used to shift the cargo above the HTV deck. These lines have a safe working load (SWL) of 140 [t], which is equivalent to the brake capacity of the installed winches. In this example, lines 8 to 16 — also each with a LTAS — are additional lines connected to the cargo after finalized shifting; for these lines a SWL of 600 [t] was chosen to be able to obtain the required control load. The most important design parameters are shown in Table 7.3. For the mooring lines typical strength and stretch values for HMPE mooring rope are used.

Table 7.3: Mooring line and LTAS design parameters

Line numbers	1 - 8	9 - 16	
Line diameter	56	115	[mm]
Minimum breaking load (MBL)	241	1002	[t]
Safe Working Load (SWL)	140	600	[t]
Line stretch	3%		
Cylinder diameter	730		[mm]
Rod diameter	630		[mm]
Cylinder stroke	1500		[mm]
Initial position	750		[mm]
Sheave fall	double	single	

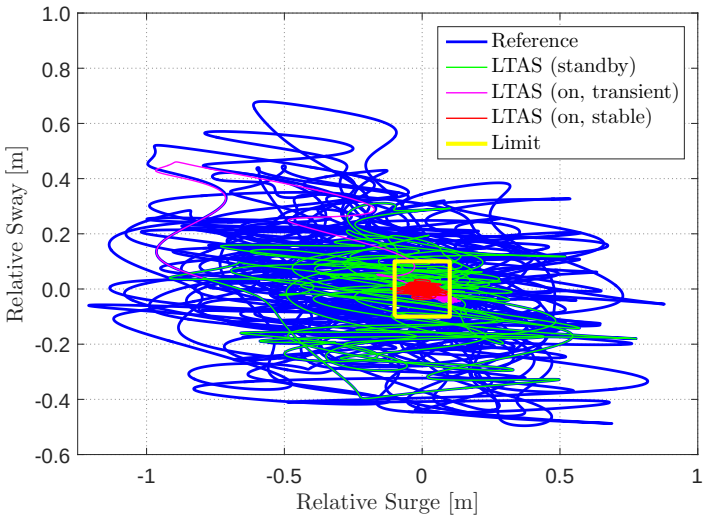

Figure 7.11: Relative motion

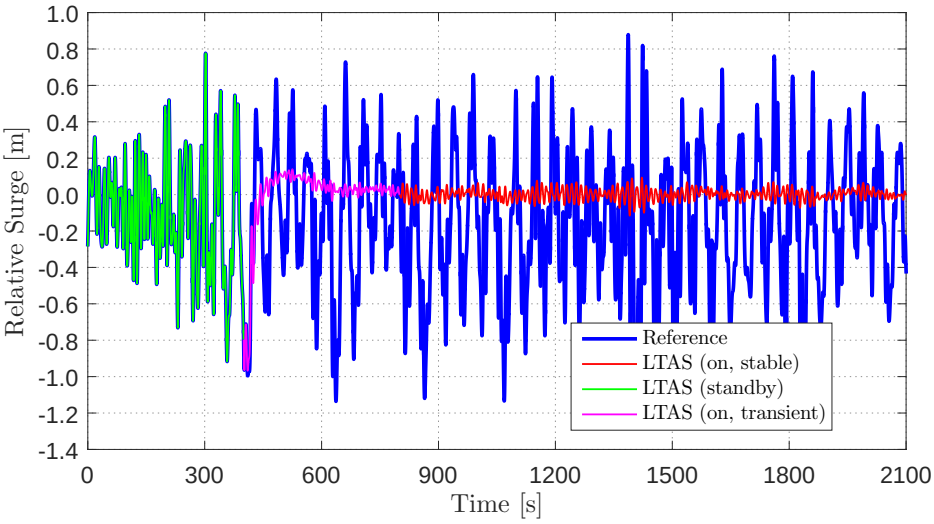

(a) Surge

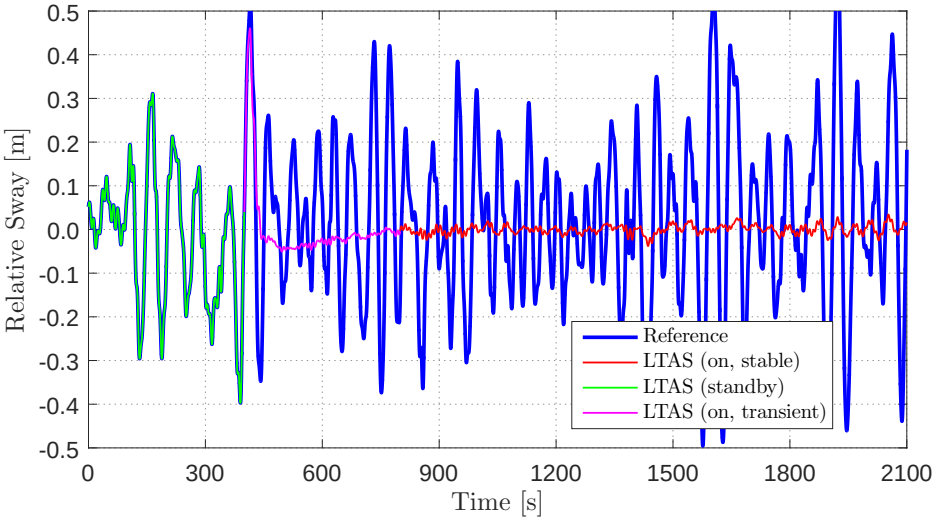

(b) Sway

Figure 7.12: Relative surge and sway motion

A comparison of the relative surge behaviour for the reference simulation and simulation with LTAS is shown in Figure 7.11 and 7.12. The time at which the LTAS is switched on was chosen arbitrarily; in Section 7.2.3 it is shown how this impacts the LTAS design; the large initial offset needs to be compensated by the cylinders, thus the cylinder piston will move from the initial position to an average position. It takes 300 to 400 [s] for the system to stabilize. Clearly, the LTAS Control is very effective in reducing the relative surge motion. Both relative surge and sway motion are reduced to about 10% of the uncontrolled motion.

7.2.3 LTAS Control performance

Fourth step is using the allocated line tension and fairlead distance in a pneumatic-hydraulic simulation model to see how accurate the LTAS can obtain the required tension. In Appendix E, the Simulink model is shown in Figure E.1. The subsystems for the cylinder is shown in Figure E.2, which is based on calculating the piston acceleration due to the external, hydraulic and friction forces. The subsystems for the 4-way valve is shown E.3, which calculates the flow velocity through the orifices depending on the valve position. Figure E.4 shows subsystem for the accumulator using the adiabatic process and the hydraulic pump. The line tension subsystem is a straight forward calculation of line stiffness times difference in line start and line end position.

Zooming in to the time range with highest loading, a comparison of the required and obtained forces and moment is given in Figure 7.13. Generally, the obtain forces and moment follow the required load with a very small delay of about 37 [ms]. Furthermore, this figure is showing that the peak values are closely matched with a very small overshoot. Of course, the difference between required and obtained force will result in slightly different relative motion, however the difference is considered too small to give a significant change in behaviour.

The line tension and line end positions for all lines are shown in Figure E.5 to E.10. For lines 3 and 9, the LTAS performance is shown in Figure 7.14. Figure 7.14(a) and 7.14(b) show that the obtained tension is accurately following the required tension, however during rising and falling the obtained tension is lagging behind with 35-100 [ms]. This is inherent to the feed-back control.

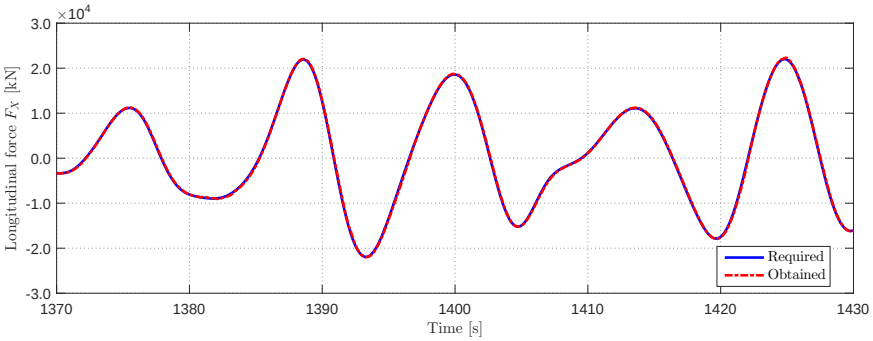

(a) Longitudinal force

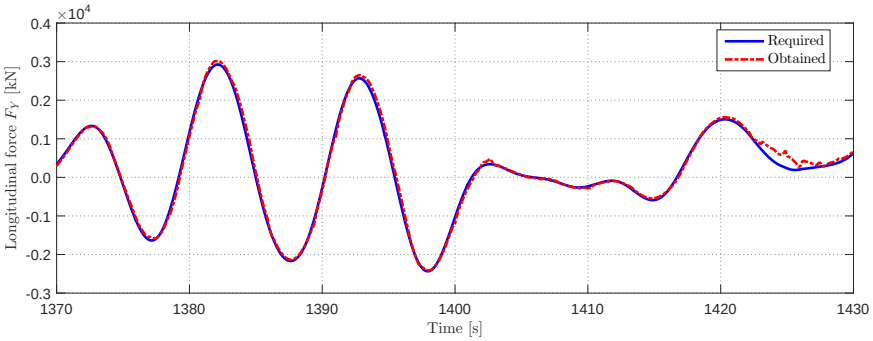

(b) Transverse force

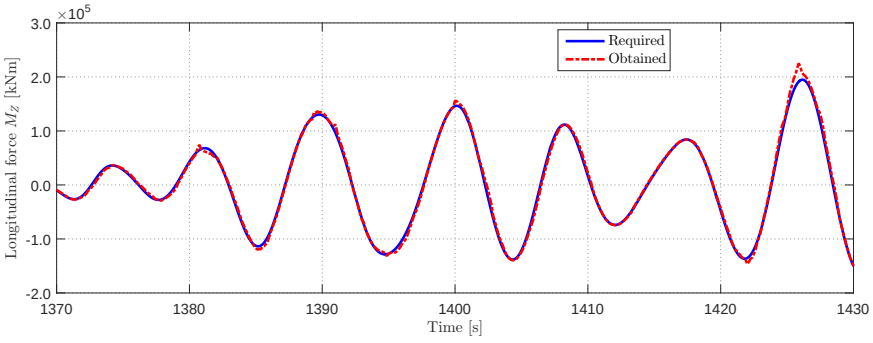

(c) Horizontal moment

Figure 7.13: LTAS control force

In Figure 7.14(d), it is observed that the lower chamber pressure is exceeding the supply pressure. This may occur when the required fluid flow is low, the tension is high and piston motion just reversed. To limit the pressure at 350 [bar] in the cylinder, pressure safety valves are incorporated as indicated in Figure E.2. At this stage the 4-way valve ensures that the obtained tension is achieved by controlling the in-flow and pressure of the upper cylinder chamber.

The piston position and line ends motion (w.r.t initial values) are shown in Figure 7.14(e) to (h). These figures clearly show that the LTAS is compensating the stretch in the lines. For line 9, a tension of 600 [t] is equivalent to approximately 0.55 [m] line stretch, being the difference between line end position and line start position as seen in Figure 7.14(h). As this line is on a single fall configuration, the cylinder stroke is half of the stretch (i.e. 0.3 [m]). At the moment of switching on the LTAS the cargo had a large offset, while the cylinder positions were 0.75 [m]. As a result the average cylinder position for line 9 is close to 1.2 [m] to compensate for the initial offset. Together with the line stretch compensation a total stroke of 1.5 [m] was chosen as indicated in Table 7.1. Note that the period before activating the LTAS is not investigated. During this period a constant tension is desirable, which would require line adjustment, in other words the hydraulic piston should follow the relative motions. This should not be done by the LTAS directly to avoid large hydraulic fluid consumption from the accumulator. Instead, line adjustment should be done by the winch or through solutions similar to the heave compensation. With such a system, the design cylinder stroke can be reduced.

The accumulator and hydraulic pump power for all lines are shown in Figure E.11 tot E.18. For line 14, the accumulator filling and hydraulic pump power compared to the line tension are shown in Figure 7.15. This figure shows that after 5 large line pulls (between 1375 and 1435 [s]) the accumulator is almost completely emptied. The length of line 14 is much larger than line 9, which results in lower stiffness and thus larger stretch at 600 [t] tension. Therefore, the cylinder is consuming a large amount of hydraulic fluid at each stroke. To keep hydraulic fluid available, each system has a hydraulic pump with a maximum power of 540 [kW]. The pump power for line 14 is shown in Figure 7.15(c). The total pump power is shown in Figure 7.16.

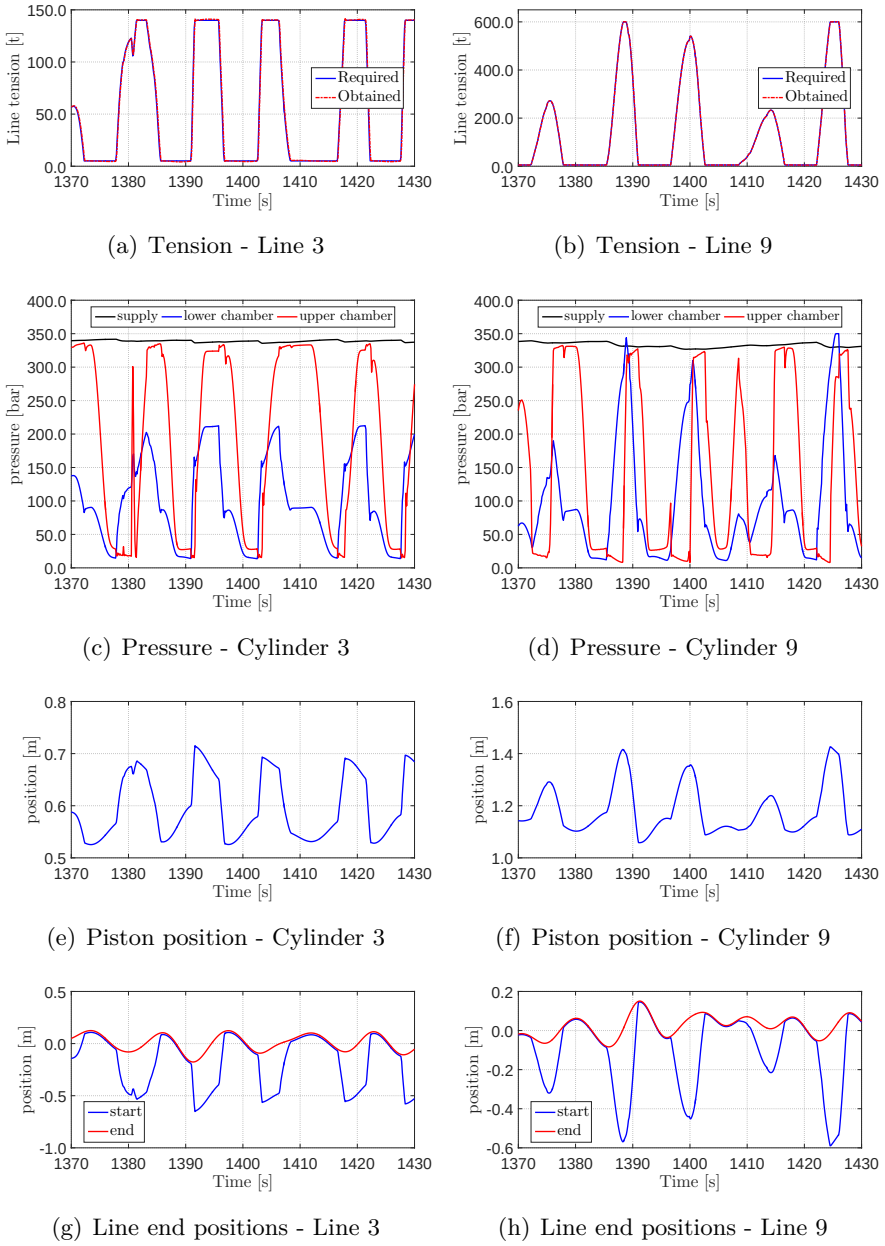

(a) Tension - Line 3

(b) Tension - Line 9

(c) Pressure - Cylinder 3

(d) Pressure - Cylinder 9

(e) Piston position - Cylinder 3

(f) Piston position - Cylinder 9

(g) Line end positions - Line 3

(h) Line end positions - Line 9

Figure 7.14: LTAS performance

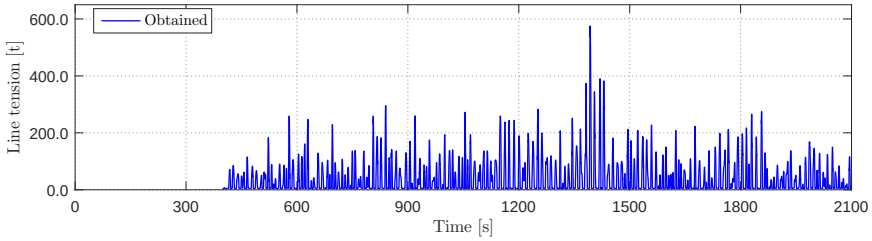

(a) Tension - Line 14

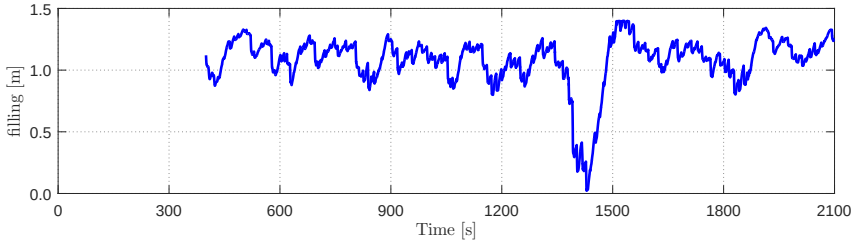

(b) Accumulator filling - Line 14

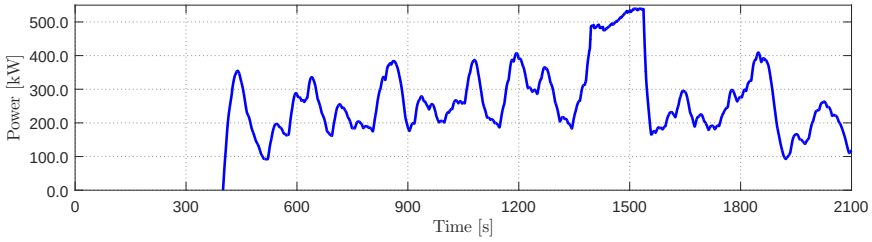

(c) Pump Power - Line 14

Figure 7.15: Accumulator and hydraulic pump power for line 14

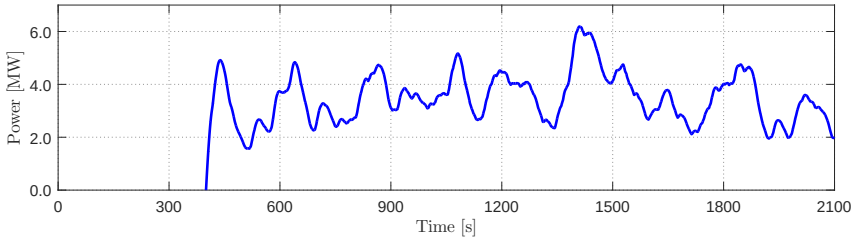

Figure 7.16: Total hydraulic pump power

Design and Engineering

CHAPTER 8

Design Aspects for Offshore Loading and Discharge

With the solutions outlined in previous sections, it is possible to accurately predict the relative motions. To establish whether or not an offshore loading or discharge operation is technically feasible, the design of equipment and required limiting environmental conditions need to be matched. Of course, the technical solution will depend on limitations of physical parameters, like cargo strength or size of equipment, or operational limits, for example if mooring lines can be handled by crew.

Also, economical aspects will determine if an offshore loading or discharge operation is feasible; here equipment costs, weather downtime, operation time and many other cost drivers are important. The economical feasibility will depend on profitability for the operator and cost saving for the client. The operation will be profitable when workability is high enough to ensure timely execution, thus aim is to design a system and operation to improve the workability, while it optimizes the development cost for the client. The economical feasibility diminishes when the risk of failure due to waiting on weather becomes to large, such that the offshore loading or discharge cannot be executed and the client needs to revert to standard approach of installation works.

Below, technical design aspect are discussed, which are important to establish project feasibility. First, a short description of the operational phases for an offshore loading operation is given. General considerations and design aspects are mentioned. Second, the minimum required analysis scope for Tender and Execution Phase (see Table 2.1) are addressed. Next, some specific design aspects are discussed related to respectively

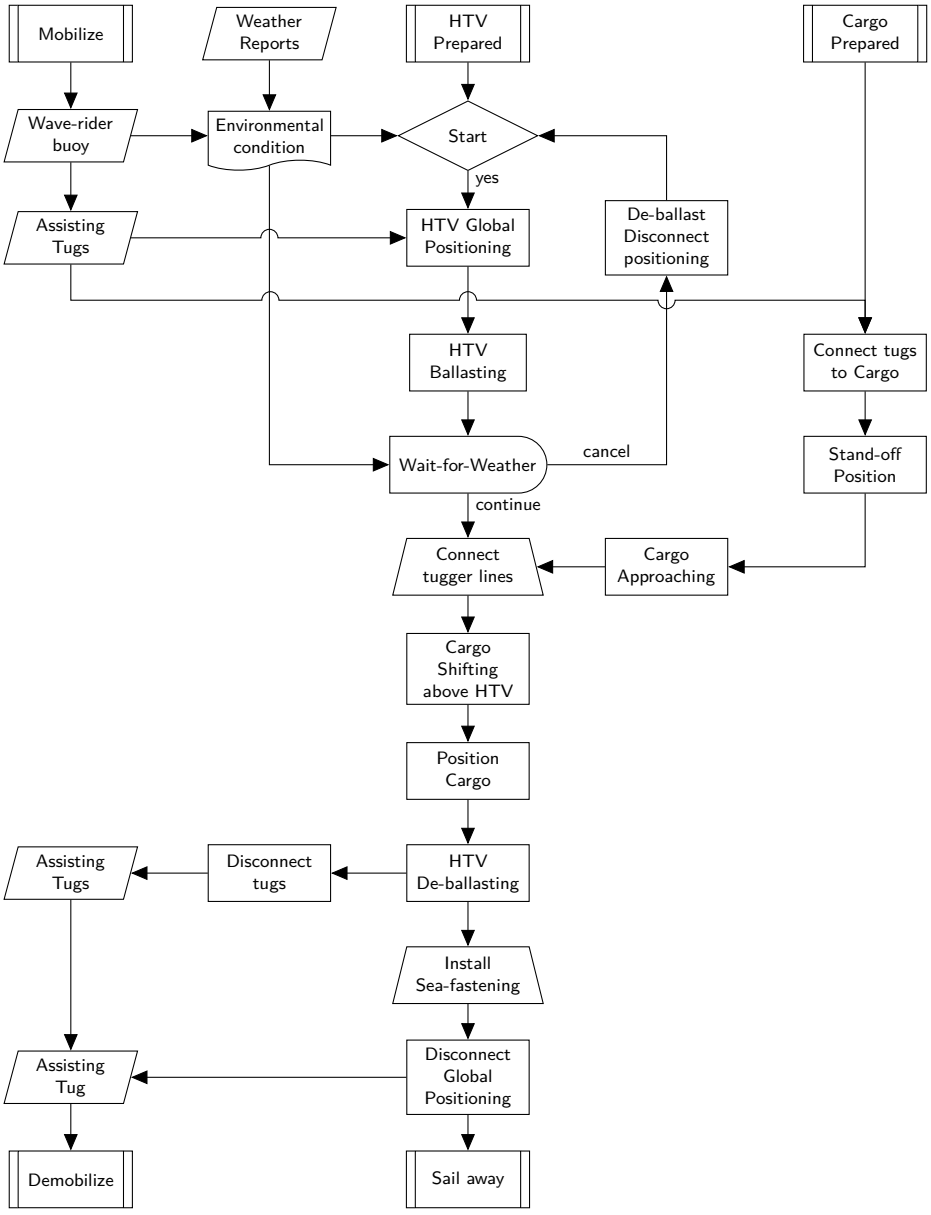

Figure 8.1: Loading Operational Flow Diagram

the vertical and horizontal relative motions. The economical feasibility is not further investigated as this depends too much on project specific parameters.

8.1 Operational Phases

In Section 1.2 a short description of a typical loading operation is given and is illustrated in Figure 1.3. An examples of the operational flow diagrams is shown in Figure 8.1. A short description of the most important phases of an offshore loading operation is given:

1. **Start** — When all required assets are mobilized and both HTV and Cargo are prepared, a decision to start the operation can be made based on available weather forecast, possible supported by motion monitoring and motion forecast information. The weather forecast is verified against a wave rider buoy present as near as possible to the execution zone.

2. **HTV Global Positioning** — Depending on water depth, a way to globally position the HTV at the operational area needs to be established. When operating in limited water depth own anchors or pre-installed anchors may be used, optionally assisted by tugs and/or own propulsion system. For large water depth use of anchors may not be possible. It may also be possible to consider slowly drifting; still tug assistance or own propulsion may be needed to control heading of the HTV. Heading control may depend on the operational phase; for example during HTV submerging a specific heading to the environment is not required. Aspect for heading control requirements are minimize (relative) motions and operational safety. The latter may be clear by looking at Figure 1.3; when wind and waves are coming from port side of the HTV the cargo will drift away to starboard side without risk of hitting the obstructions like the casings and guideposts.

3. **HTV Ballasting** — The HTV will be submerged to a draft such that enough clearance between HTV deck and cargo bottom is ensured. Meanwhile, the cargo is moved to the stand-off position. After ballasting, the weather forecast is again evaluated. It is possible

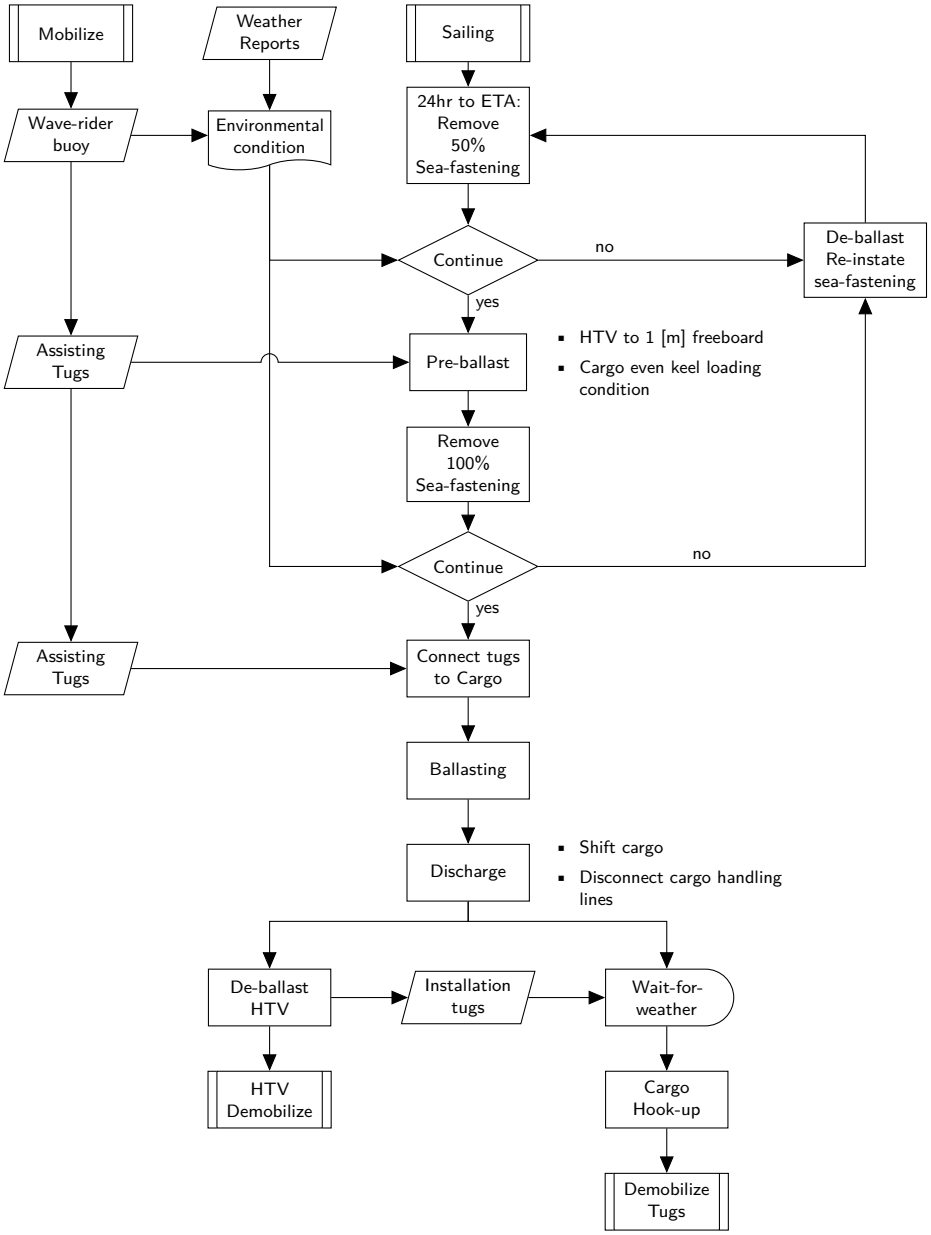

Figure 8.2: Discharge Operational Flow Diagram

to wait for the weather to reduce to the float-on criteria. At this stage, it is also easy to abandon the operation.

4. **Cargo Approaching and Shifting** — When the operation is continued, the cargo is moved alongside/aft of the HTV, such that the tugger lines can be connected. Then, the cargo is shifted above the HTV deck. This may be a continuous process of shifting and connecting lines.

5. **Positioning Cargo** — At this stage, the cargo handling equipment is connected and/or engaged to accurately position the cargo within the required tolerance.

6. **HTV De-ballasting** — While monitoring the cargo position, the HTV starts de-ballasting. During the de-ballasting phase the assisting tugs may be or have to be disconnected from the cargo.

7. **Install Sea-fastening and Sail away** — When enough free-board is established the sea-fastening can be installed. The decision to sail away may depend on the amount of sea-fastening installed and the weather forecast.

For each phase, minimum and maximum duration has to be estimated. Together with the environmental limits for each phase a detailed workability and persistency analysis can be performed. Also, time required to abandon the operation and a point-of-no-return need to be established; for example when de-ballasting is started during loading, it is desirable to finish the operation.

A discharge operation is in general terms executed in reverse order of the loading operation. An example operational flow diagram for an offshore discharge operation is shown in Figure 8.2, where the cargo needs to be hooked up in the field directly after the discharge. A short description of the most important phases of an offshore discharge operation is given:

1. **Remove Sea-fastening and Pre-ballast** — Normally, the sea-fastening is designed for the worst condition encountered during the transit voyage. It can generally be expected that during the last few days of the transit these condition will not be encountered, such that part of the sea-fastening may be removed before arrival. After arrival

and the the decision to start the discharge operation, pre-ballasting will start and further removal of sea-fastening will commence.

2. **Ballasting** — When weather permitted, the operation continues by further ballasting the HTV. The critical phase will be when the cribbing load will be less than the dynamic wave loads. At this stage, impact loads may start to occur. Therefore, it is important that the horizontal relative position of the cargo is controlled. At this stage, it is generally faster to finish the discharge operation than to reverse the operation, so the point-of-no-return is reached.

3. **Discharge** — The weather is not allowed to deteriorate to allow for the cargo to be shifted away from the HTV.

8.2 Analysis Scope

8.2.1 Tender phase

During tender phase, limited time is available to assess the offshore loading and discharge operation. During this phase, indicative analysis is sufficient, meaning that a linear frequency-domain assessment of the vertical relative motion would be appropriate. As such the squeeze flow effect cannot be accounted for in detail. An estimate in frequency-domain could be done by adding linearised frequency independent damping, however as shown in Section 5.2 some simulations in regular waves may need to be done to establish how much linearised damping should be applied.

Also the assessment of horizontal relative motions can be carried out only to a limited extent. By assessing the wave loads, as shown in Section 7.1, an indication of expected loads to control the motions can be made. Most important part of the scope for tender phase is to layout a concept of the required systems and assume design criteria like for example the positioning tolerance, which influences the cribbing layout and thus the project costs. Also, the prevailing site-specific weather conditions need to be investigated, with a first indication of workability, possibly for a number of weather criteria. The workability study will give an indication of the required operational days. With the conceptual results, the contract value can be estimated.

8.2.2 Execution phase

During execution phase, a more detailed time-domain analysis study should be performed to verify the initial tender phase assessment and to further detail and specify operational limits, required equipment and marine spread. Where during tender phase a limited amount of diffraction calculations can be done, more diffraction calculations with enough variations in relative heave, roll and pitch positions need to be carried out to be able to fully account for the non-linear squeeze flow effects in the time-domain simulations. For the different operational phases, time-domain simulation are performed to tune the systems and limiting weather conditions must be established. Where possible, the frequency-domain approach may be used to predict the behaviour, when non-linear effects are negligible or can be linearised to satisfactory accuracy; for example the sea-state limit during shifting may be determined with the assumption that minimum clearance, the net difference between static clearance and dynamic motion, is large enough.

8.3 Design Aspects

8.3.1 Vertical relative motion and deck impact

In Section 4, it is shown how to accurately predict the relative vertical motions. This means that, at a given sea-state, it will be possible to determine at which initial gap height deck impact will start to occur during a loading operation or stop to exist during a discharge operation. This determines the minimum required clearance during the steps of shifting of the cargo; note that the final position of the cargo above deck may not be leading.

During loading operation there is a transition time from the first impact to full contact between cargo and HTV deck or in case of a discharge operation from full contact the last impact when enough clearance is achieved. During this transition time several impacts will occur. The impact load will dependent on the maximum impact velocity and the stiffness of the support point and local structural stiffness of HTV deck and cargo bottom.

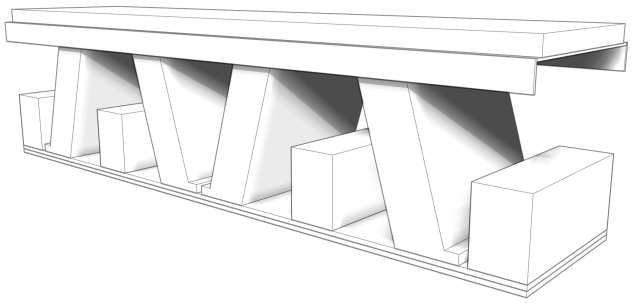

(a) Before impact

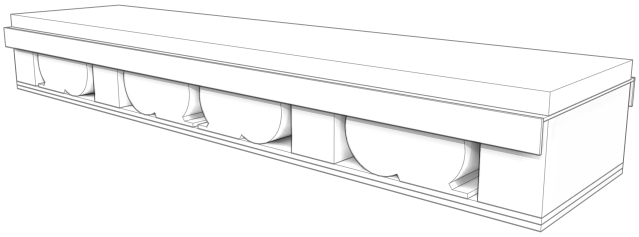

(b) Fully compressed

Figure 8.3: Shock absorber - concept 1

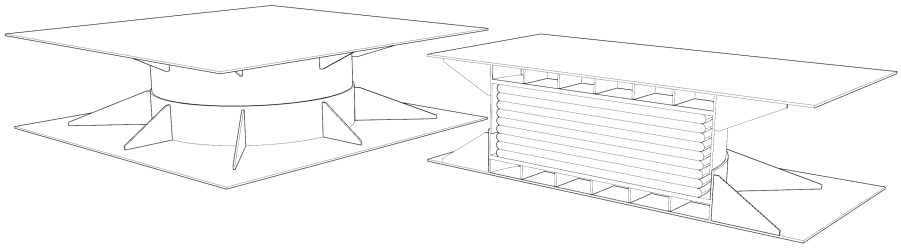

Figure 8.4: Shock absorber - concept 2

The structural stiffness of HTV and cargo is generally a given fact, however the stiffness of the support points may be influenced. As mentioned in Section 1.1 and 6.1, wood is typically used as standard support, but also plastic type cribbing has been developed. In transport condition, these type of solid cribbing beams are only compressed by a few millimetres. The difference between soft wood, hard wood and plastic beams is limited. For impact loads the lowest stiffness is preferred. Whether or not such supports have low enough stiffness to absorb the impact load depends on the HTV and cargo structure and the design environmental limit, also in relation to the horizontal relative motion reduction.

To increase the shock absorbing capacity, and thus the operational limit, special designed supports as illustrated in Figure 8.3 may be of use. The concept idea is to place shock absorbers at the locations where first impact will occur, which is likely to be at the outer corners of the cargo bottom. This system consist of a shock-board with Teflon or rubber layer, arch or leg type fender and wood or plastic blocks. The shock absorbers may be 1.5 to 2.0 times the height of the cribbing, and will be the same height at full compression. At full compression the chock board will rest on the wood or plastic blocks. The combination of the blocks and the Teflon or rubber layer should give an equivalent stiffness compared to the standard cribbing. The stiffness of the arch or leg fenders should be chosen such to maximize the allowable impact load and compression at first impact, such that the limiting operational sea-state is maximized. Another concept is shown in Figure 8.4, which shows similarities to so-called Leg Mating Units (LMU) as used during topside float-over operations. Part of the functionality of a LMU is shock absorption.

8.3.2 Cargo handling

As clearly shown in Section 6, both cargo handling equipment concepts can be very effective in reducing the relative horizontal motions. With the analysis tools available, project specific designs can be made. As mentioned in Section 6.3.3, the design will depend on operational aspects, structural design and dimensions and type of cargo. Also aspects within the systems will influence the design.

Clamping System

The design of the damped fenders will mainly depend on the structural capacity of the cargo side-shell, which should be expressed in terms of load per square meter. The guide structure shown in Figure 6.3 have a load capacity of about 300 [t]. The area of the fender-boards is about 10 [m^2], which results in a load bearing capacity of about 3 [kg/cm^2]. However, allowable load on the cargo depends on the side-shell structure. The area of the fender-board must be chosen such that enough plate stiffeners with enough length are supported. Therefore, available location where the Clamping Systems will touch the cargo need to be selected. Together with the HTV and cargo draft the desired height of the Clamping Systems is determined.

When the fender board area is known, a decision can be made about the type and size of fender, which depends on the desired stiffness and deflection. This depends on the cargo shifting phase and initial pre-load phase. During cargo shifting generally some clearance between the cargo and Clamping System is required to easily manoeuvre the cargo using the standard handling equipment, where the Clamping System may serve as guiding system. Then, during this phase the cargo may impact the Clamping System, so low stiffness and large deflection may be desirable. Whether or not it is possible to use the Clamping System as guiding system depends on how flush the cargo side is. Possibly, spacer barges and/or structures may be used to make the sides of the cargo completely flush, such that the cargo can slide along the Clamping System.

During pre-load phase before de-ballasting starts, the Clamping System is adjusted to reduce the clearance and initiate a pre-compression in the fenders. The pre-compression and expected horizontal motion may determine the desired fender size. Therefore, the Clamping System needs an adjusting mechanism to initially allow for enough clearance during cargo shifting and to pre-load the system. Two basic solution are possible, first solution is shifting the complete Clamping System over the HTV deck, second solution is an internal adjusting system, where part of the Clamping structure is pivoting, extending or sliding. The adjusting system may involve hydraulic systems, rack-and-pinion systems or rope-and-pulley systems. The size of Clamping System may be constrained by available HTV deck space around the cargo.

Other design items to consider are related to operational and contingency aspects. When crew needs to be able to manually control the systems, access ladders and walkways are required. Since the damped fenders need to work together, strategies in case of a failure in the systems need to be designed. These strategies must lead to a safe condition such that no excessive loads will occur. During transition from soft to stiff connection, the fail-safe strategy would be to return to non-damped fenders (i.e. start of transition). At the end of the transition, the fail-safe strategy would be to keep the hydraulic cylinders locked. This means that software and hardware must be designed to match these strategies.

Line Tension Actuator System

One important driver for the design of the Line Tension Actuator System is the space requirement. For the layout, enough locations around the cargo are required allowing for a variety of azimuths such that longitudinal, transverse and yawing loads can be controlled. Also, enough strong points on the cargo are required.

The design load of the tensioning system is not only a trade-off between limiting sea-state and allowable positioning offset, but is also determined by required cylinder stroke. When the connected handling line is long — thus relatively soft — a large stroke may be required. This may require a large hydraulic fluid flow, which may need to be limited to avoid hydraulic shock. As a result the cylinder diameter may be limited depending on the maximum hydraulic pressure. The stroke and cylinder load is influenced by the number of falls as shown in Figure 6.9.

Summarizing, the following main parameters determine the design of the LTAS:

- number of handling lines, depending on space requirement
- line azimuths, variety required for controllability
- line type and length, i.e. strength and stiffness
- design load, weakly dependent on positioning accuracy
- cylinder stroke, mainly depends on line stiffness
- cylinder diameter, which may be limited due to hydraulic fluid consumption

- hydraulic pressure (high duty pump with rated pressure of 350 [bar] are available); the minimum pressure should be between 80-90% of the maximum pressure, the minimum pressure determines the required cylinder diameter when the maximum required cylinder force is known.
- number of sheave falls; the cylinder load and stroke are inversely proportional.

Concluding Remarks

CHAPTER 9

Conclusions and Discussions

First, conclusions are made related to the objectives given in Section 2.3. Second, discussions and recommendations on the applicability of the research described in this thesis are made.

9.1 Conclusions

The main goal of this research was:

> *Making Offshore Loading and Discharge operation possible by finding a suitable engineering approach.*

This gave the following sub-goals:

1. Develop cargo handling equipment, which maximizes the operational conditions, while keeping a high level of safety for crew, HTV and cargo.
2. Develop an analysis method suitable for different stages of an offshore loading and discharge project, each with an appropriate level of accuracy.

The first sub-goal has been achieved. Two systems were developed to be able to control the wave frequent relative motion. The so-called Clamping System is based on the principle of adjusting the connection between HTV and Cargo from soft to stiff. This is possible by using damped fenders. The fender includes a hydraulic cylinder with a adjustable control valve. By gradually closing the valve initially damping is created, once fully closed a

stiff connection is established. The Clamping System can only be applied in one motion direction. The Line Tension Actuating System can control the 3 degrees of freedom relative motions.

The second sub-goal is partially achieved. To predict the relative vertical motions an accurate method to account for the highly non-linear effects of squeeze flow was developed. Due to the non-linearity, only time-domain analysis is suitable. This means that during Tender phase still time-consuming calculation may be required. For the horizontal relative motions estimating the wave load using standard frequency-domain calculations provides a first indication for the design of the motion control systems. Due to the complexity of the 2-body system and the application of PID control in the LTAS, time-domain analysis will be required.

9.2 Discussions and Remarks

The findings and results are discussed in this section. Advice and remarks are given on how the methods and systems should be used and applicability in other areas and possible future developments are indicated.

Application of Molin's method of changing added mass appears to be a significant improvement in the calculation accuracy. Though, as this method only covers the potential part of the non-linear squeeze flow forces, there is still some uncertainty due to the viscous contribution. In this thesis, it is shown that the viscous part may be estimated using CFD. A fairly simple set of calculations for a single body forced oscillation case can be used.

Estimation of added mass at high wave frequency has been thoroughly investigated to overcome the numerical issues involved in the narrow gap between two objects. Although an improved method is described in this thesis, industry standard diffraction programs can still be considered to give a good estimate. Also, because the improved method is not (yet) able to cover relative roll and pitch, the standard diffraction method is still in favour. Since standard method are based on discretization of the body surfaces and thus are not body exact, use of such programs still requires mesh-refinement convergence tests. Recent developments in so-called isogeometric analysis (IGA) (Meijer [21]) are promising for improvements in predicting hydrodynamic characteristics.

This thesis gives proof of concept for the control of horizontal relative motions. Whether or not the chosen examples will be physically and economically feasible may be disputable. The required line tension found for the 100,000 [t] cargo example may be too high for current design of the stability casings of the HTV *Boka Vanguard*. So strengthening or additional structures may be required, when operating with an extremely heavy cargo.

With use of either or both the Clamping System and/or the Line Tension Actuating System, reduction of the relative horizontal motion with respect to a standard passive handling system is established. As such an increase of workability is achieved. To which extend the workability can be increased is a trade-off between investment cost, physical and operational limits and the cargo and HTV characteristics.

From investment perspective, it is desired to design the systems suitable for a range of cargo types and characteristics. As the Clamping system is deck-mounted, placement is flexible, thus making it independent of cargo type. However, in the design of the Clamping System, flexibility in the operational height must be accounted for to be able to cover different types of cargo. For the LTAS, the operational height is less restrictive, but placement with respect to the cargo is less flexible as the line length to the cargo should be limited. This means that for the design of both systems, a marketing research should be done to establish for which types of cargo these systems should be suitable.

The methods and solutions presented in this thesis focussed on application to Offshore Loading & Discharge. Application to other areas is possible, for example:

- The method to account for non-linear squeeze flow effect is also applicable to shallow water vessel behaviour. The method may also be applicable to side-by-side problems, however the free surface between the bodies need to be carefully considered. The latter requires more research.
- The Line Tension Actuating System may be used on standard handling equipment in sheltered location and benign environmental conditions to ease control of the cargo position and may avoid slack in or overloading of handling lines. Also, automation contributes to the safety of the operation and crew. Crew can stay further away from

winches and handling ropes and miscommunication between winch operators and superintendents is avoided. Also, position monitoring may be easier and more reliable.

- The damped fender as presented in Figure 6.5 can be used at quay-sides. Such system could avoid that the vessel is bouncing off the quay.
- The LTAS may reduce motions of LNG carriers or very large container ships moored along berths, thus possibly increasing the operability. This system could be an extension on the passive ShoreTension® system.

List of Figures

List of Tables

Bibliography

[1] *ANSYS-AQWA™ User Manual*.

[2] D. Bass, D. Molyneux, and K. McTaggart. ''Simulating wave action inside the well deck of landing platform dock ships using computational fluid dynamics''. In *Proceedings RINA Conference Warship*, London, UK, June 2004. Royal Institute of Naval Archtects.

[3] A. Basset. *A Treatise on Hydrodynamics: With Numerous Examples*. Deighton, Bell and Company, 1888. URL `https://en.wikipedia.org/wiki/Basset_force`.

[4] J. v. Beelen. ''development of relative horizontal motion reduction systems''. MSc Thesis, `http://repository.tudelft.nl`, Delft University of Technology, Delft, The Netherlands, September 2016.

[5] C. E. Brennen. ''A review of added mass and fluid inertial forces''. Technical report, Naval Civil Engineering Laboratory, January 1985.

[6] C. Brun, D. Coache, and F. Rezende. ''Advanced computations of mooring systems''. In *8th International Confenerence on Hydrodynamics*, Nantes, France, 2008.

[7] W. E. Cummins. ''The impulse response function and ship motions''. Technical report, Department of the Navy, David Taylor Model Basin, 1962.

[8] Y. Drobyshevski. ''Hydrodynamic coefficients of a floating, truncated vertical cylinder in shallow water''. *Ocean Engineering*, (31):269—304, 2004.

[9] Y. Drobyshevski. ''An efficient method for hydrodynamic analysis of a floating vertical sided structure in shallow water''. *International Conference on Offshore Mechanics and Arctic Engineering*, (OMAE2006-92118), 2006.

[10] Z. Fang. ‘‘A Comparison of integral equation methods for calculation of hydrodynamic forces on large offshore structures’’. In *Proceedings of MARINTEC*, Shanghai, China, 1985.

[11] P. Guérin. ‘‘TPG500 Analyse de essais sur un pied en oscillations forcées’’. Technical Report RET 75.206.01, Principia, Nantes, France, 1997.

[12] S. Y. Hong, J. H. Kim, S. K. Cho, Y. R. Choi, and Y. S. Kim. ‘‘Numerical and experimental study on hydrodynamic interaction of side-by-side moored multiple vessels’’. In *Deepwater Mooring Systems; Design, Analysis and Materials — Deepwater Mooring Systems*, volume 32, issue 7, page 783 — 801. Ocean Engineering, May 2005.

[13] L. B. E. Hoogenhuyze and H. Vandersmissen. *‘‘The Dutch and the Sea’’.* De Boer Maritiem / Unieboek, 1984. ISBN 9022818985.

[14] F. van Hoorn. ‘‘Heavy-lift transport ships — Overview of existing fleet and future developments’’. *Proceedings of the Marine Operations Specialty Symposium*, (MOSS-32), 2008.

[15] R. H. M. Huijsmans, J. A. Pinkster, and J. J. de Wilde. ‘‘Diffraction and radiation of waves around side-by-side moored vessels’’. In *Proceedings of Eleventh International Offshore and Polar Engineering Conference*, volume I, pages 406--412. ISOPE, June 2001.

[16] R. Johnson. *The Handbook of Fluid Dynamics.* Mechanical engineering. Springer Berlin Heidelberg, 1998. ISBN 9783540646129.

[17] J. B. de Jonge. ‘‘An accurate and efficient hydrodynamic analysis method for offshore discharge operations’’. Msc thesis, Delft University of Technology, Delft, The Netherlands, 2008.

[18] L. Kerner. ‘‘CFD calculations of non-linear loads using FINE™/Marine’’. Technical Report RF-Dockwise-210814-v2, NUMFLO s.a., Ocktober 2014.

[19] R. Krabbendam and M. Beerendonk. ‘‘Exceeding the limits, from 60 to 60,000 tons in 50 years’’. In *Marine Heave Transport & Lift.* Royal Institute of Naval Archtects, 2005.

[20] P. S. C. Lee. ‘‘Investigation of a method for controlling the relative horizontal motions between an htv and its cargo’’. Msc thesis, Delft University of Technology, Delft, The Netherlands, August 2012.

[21] J. H. A. Meijer. ‘‘Isogeometric potential flow analysis of linear surface waves’’. MSc Thesis, `http://repository.tudelft.nl`, Delft University of Technology, Delft, The Netherlands, 2018.

[22] A. J. Metrikine. ‘‘Slender structures and an introduction to continuum mechanics’’. Lecture Notes CT4145, Delft University of Technology, The Netherlands, 2006.

[23] B. Molin, P. Guérin, D. Martigny, and P. Weber. ‘‘Étude théorique et expérimentale des efforts hydrodynamiques sur une embase plane a l’approche du fond marin’’. In *7e Journées de l’Hydrodynamique*, Marseille, France, 8-10 March 1999.

[24] M. Naciri, O. Waals, and J. J. de Wilde. ‘‘Time domain simulations of side-by-side moored vessels lessons learnt from a benchmark test’’. *International Conference on Offshore Mechanics and Arctic Engineering*, (OMAE2007-29756), 2007.

[25] J. N. Newman. ‘‘Algorithms for the free-surface green function’’. *Journal of Engineering Mathematics*, 19:57--67, 1985.

[26] F. G. Nielsen. ‘‘How to estimate hydrodynamic coefficients applicable for lifting from the sea bed’’. Lecture Notes, 2007.

[27] F. T. Ogilvie. ‘‘Recent progress toward the understanding and prediction of ship motions’’. In *5th Symposium on Naval Hydrodynamics*, page 3 — 128, Bergen, Norway, 1964.

[28] J. A. Pinkster. ‘‘Hydrodynamic interaction effects in waves’’. In *Proceedings of Fifth International Offshore and Polar Engineering Conference*, volume III, pages 414--419, The Hague, The Netherlands, June 1995. ISOPE.

[29] J. A. Pinkster. ‘‘Suction, seiche and wash effects of passing ships in ports’’. In *SNAME Annual meeting conference*, number 024.R3, Providence, Rhode Island, 2009.

[30] J. A. Pinkster. ‘‘A multi-domain approach in 3-D diffraction calculations’’. *International Conference on Offshore Mechanics and Arctic Engineering*, (OMAE2011-49414), 2011.

[31] M. St.Denis and W. J. Pierson. ‘‘On the motion of ships in confused seas’’. In *SNAME*, pages 61:1--53, 1953.

[32] M. D. Symans, M. C. Constantinou, D. P. Taylor, , and K. D. Garjost. ‘‘Semi-active fluid viscous dampers for seismic response control’’. In *Proc. 1st World Conf. on Struct. Control*, pages FA4--3--FA4--l2. University of Southern California, 1994.

[33] T. Terpstra and E. A. Hellinga. ‘‘Offshore dry-docking of FPSOs: a response to industry needs’’. In *OTC Brasil*, number OTC-24330. Offshore Technology Conference, 2013.

[34] F. Ursell. ‘‘On the heaving motion of a circular cylinder in the surface of a fluid’’. In *Quarterly Journal of Mechanics & Applied Mathematics*, volume II, pages 218--231, 1949.

[35] T. Vinje. ‘‘Fluid flow through perforated structures’’. Technical report, MarinConsult Report, 2001.

[36] A. C. M. Vreeburg. ‘‘ShoreTension as cargo handling system: Controlling the relative horizontal motions between the HTV and the cargo during offshore loading and discharge’’. Msc thesis, `http://repository.tudelft.nl`, Delft University of Technology, Delft, The Netherlands, March 2015.

[37] J. E. W. Wichers and M. F. van Sluijs. ‘‘The influence of waves on the low-frequency hydrodynamic coefficients of moored vessels’’. In *OTC Houston*, number OTC-24330. Offshore Technology Conference, 1979.

[38] R. W. Yeung. ‘‘Added mass and damping of a vertical cylinder in finite-depth waters’’. *Applied Ocean Research*, (3 (3)):119--133, 1981.

[39] R. Zhu and K. Saito. ‘‘Fluid motion in a tank with internal structure’’. In *Proceedings of 16th Workshop on Water Waves and Floating Bodies*, pages 185--188, April 2001.

Appendices

APPENDIX A

Ship Hydrodynamics

A.1 History

As early as the late 18th century, naval architects have explored methods of model testing. In 1758, the Society of Arts offered prizes for what were known as "ship blocks" (i.e. scale models of ships) in order to "ascertain by experiments the principles on which a good ship is founded". Water resistance and resistance to rolling were two of the main qualities it was desired to test. It was not until 1761 that sufficient models had been submitted for the prizes, but that year six entries — four 32-gun frigates and two 74-gun ships — were tried out at Peerless Pool, near Old Street, in the City of London, as shown in the scene reproduced here, which was especially painted for the Society by Miss Anna Zinkeisen (Figure A.1).

Figure A.1: Model tests at Peerless Pool, 1761

Figure A.2: The world's first towing tanks

Mark Beaufoy performed the first systematic series of tests between 1793 and 1798. Clearly shown is that these tests were mainly qualitative comparison of resistance of different shapes. It took about another century before the well known scientist William Froude developed scaling laws to be able to relate model test measurements to full scale physics. He built the first indoor towing tank in 1872 for the British Admiralty, see Figure A.2. In 1883, the first commercial towing tank was built. Many other towing tanks followed, which were often equipped with a waver maker, making it possible to investigate the sea-keeping characteristics of ships. At first, only tests with regular waves were done, because of the long narrow shape of the basins and simple wave makers and controls. Also, results from sea-keeping test could not yet be used to relate the behaviour of a model in a regular wave to the behaviour of ship in confused ocean seas. The techniques for this were developed and described by St.Denis and Pierson [31] in the 1950's, being the principle of super positioning regular waves to get an irregular wave.

A.2 Theory and mathematical formulations

At about the same time as developments by St.Denis and Pierson [31], theoretical methods to predict the behaviour of ships in a regular wave were developed. With the work of Ursell [34] published in 1949, formulating the analytical solution of the potential theory for a circular cross section, a major step forward was made towards the development of a theoretical

method for the prediction of the behaviour of ships in a seaway.

In principle, developments based on two approaches — both using the potential or radiation-diffraction theory — have been followed. First the two-dimensional strip theory and second the more general three-dimensional diffraction theory. These theories are all based on the assumption that the fluid is incompressible, inviscid and irrotational, without any effects of surface tension. Further it is assumed that the motion amplitudes and velocities are small enough, so that all but the linear terms of the free surface condition, the kinematic boundary condition on the body and the Bernoulli equation may be neglected.

For many years the main difference between the two approaches — next to the principle difference in 2D and 3D potential solution — was that the 2D-strip theory method included the forward speed problem. Only during recent years, some advances have been made to account for forward speed in the 3D-diffraction solution.

Another important difference is that the 3D-diffraction is suitable for arbitrary shapes, like semi-submersible structures, whereas the 2D-strip theory has more difficulty in predicting the behaviour of these shapes. In fact the 2D method is most suitable for slender ship shape bodies. Further, 3D methods provide wave drift characteristics needed for mooring analysis. And finally, the 3D method is used to investigate the behaviour of floating structures close to each other, i.e. the hydrodynamic interaction problem.

Other important methods are also developing rapidly, as there are Computational Fluid Dynamics (CFD) and Volume of Fluid (VoF) method. Also developments are taking place to couple the different methods mentioned, like shown by Bass et al. [2] and the EXPRO-CFD project where coupling between CFD and 3D-diffraction was investigated.

A.3 Computer power and numerical methods

Since the 1970's the computer power has been growing first gradually and than rapidly in the last decade. This made it possible to perform calculations using dedicated software and large and complex models. Also in the area of hydrodynamics, developments made it possible to perform complex calculation with many variations in a time-effective way.

Where in the 1980's single bodies with a small amount of panels were used, still with long computing time, nowadays complex multi-body systems with a large amount of panels are used with reasonable processing time, where in principle solution time of numeric diffraction problems are quadratic dependent on the number of panels.

A.4 Basic Linear Potential Theory

Linear potential theory — also called diffraction theory — is widely used to predict motion behaviour of floating bodies. The diffraction theory is based on using the gradient of a scalar potential Φ to describe the velocity of the fluid around a number of bodies within a control volume. When this scalar at any location is known, the pressure at that location is known; subsequently, with pressure known on each body, forces are known and finally motions can be determined.

For completeness, the well-known basic assumptions and principles , as applied in linear potential theory, are given here:

- The fluid is assumed to be inviscid, homogeneous, incompressible and irrotational
- There is a gravity force field g
- The method is restricted to bodies with zero mean forward speed
- The amplitudes of waves and motions are assumed to be small compared to the wave length
- The surface of a body is defined by its mean wetted surface
- A wave is long-crested, regular of shape and are defined by a wave frequency ω and a wave amplitude ζ_a.
- In regular waves a linear potential, which is a function of the field-point position vector $\vec{x} = (x, y, z)$ in the earth fixed co-ordinate system and of time t, can be written as a product of a co-ordinate dependent part and a harmonic time dependent part as follows:

$$\Phi(\vec{x}, t) = \phi(\vec{x})\ e^{-i\omega t} \tag{A.1}$$

Within the diffraction theory the potential in an arbitrary point is the sum of the undisturbed incident wave potential Φ_w, potential due to diffraction

of the undisturbed wave on all bodies Φ_d and potential due to radiated waves by the moving bodies Φ_R:

$$\Phi = \Phi_w + \Phi_d + \Phi_R \tag{A.2}$$

with:

$$\Phi_R = \sum_{j=1}^{6} \Phi_j \tag{A.3}$$

As such, the total spatial velocity potential can be writen as:

$$\phi = -i\omega \left\{ (\phi_w + \phi_d)\zeta_a + \sum_{j=1}^{6} \phi_j x_j \right\} \tag{A.4}$$

The potential Φ_w is an input parameter of the calculation, and is defined by the wave frequency, wave height and earth fixed co-ordinate. The potentials Φ_d and Φ_R are dependent of the undisturbed wave and the body shapes; as these potentials are unknown, these will have to be solved to get the forces and motions of the bodies. In following equations Φ_w is represented by Φ_0 and Φ_d is represented by Φ_7. The control volume is described by the bodies, the free-water surface, the sea-bottom and a cylindrical surface at great distance of the bodies. In the fluid domain of the control volume the potentials have to satisfy the equation of continuity or Laplace equations:

$$\frac{\partial^2 \Phi}{\partial x^2} + \frac{\partial^2 \Phi}{\partial y^2} + \frac{\partial^2 \Phi}{\partial z^2} = 0 \tag{A.5}$$

At the boundary of the control volume, the boundary conditions have to be satisfied, which are:

- pressure is constant at and fluid particles cannot pass the free-water surface

$$g \frac{\partial \Phi}{\partial z} + \frac{\partial^2 \Phi}{\partial t^2} = 0 \tag{A.6}$$

- fluid cannot pass the sea-bottom

$$\frac{\partial \Phi}{\partial z} = 0 \; \forall \; z = -h \tag{A.7}$$

  where h is the global water depth.

- fluid cannot pass the bodies

$$\frac{\partial \Phi}{\partial n} = \vec{v}\,\vec{n} \tag{A.8}$$

- at the cylindrical surface at great distance r of the bodies, the body motions and diffraction potentials need to satisfy the radiation condition, i.e. at great distance Φ_d and Φ_j go to zero

$$\lim_{r\to\infty} \sqrt{r}\left(\frac{\partial \Phi_j}{\partial r} - i\nu\Phi_j\right) = 0 \;\forall\; j = 1..7 \tag{A.9}$$

  where ν is the dispersion relation to describe the relation between wave length λ (or wave number being $\kappa = 2\pi/\lambda$), wave frequency ω and water depth h:

$$\nu = \frac{\omega^2}{g} = \kappa \tanh \kappa h \tag{A.10}$$

The velocity potential associated with undisturbed long-crested regular wave in water of finite depth h with direction α is defined by:

$$\phi_0 = \frac{g}{\omega^2}\frac{\cosh \kappa(z+h)}{\cosh \kappa h} e^{i\kappa(x\cos\alpha + y\sin\alpha)} \tag{A.11}$$

The velocity potentials of the undisturbed wave, diffracted wave and the six modes of motion can be represented by a continuous distribution of sources on the surface of the body S:

$$\phi_j(\vec{x}) = \frac{1}{4\pi}\iint_S \sigma_j(\vec{\xi}) G(\vec{x},\vec{\xi}) dS \;\forall\; j = 0..7 \tag{A.12}$$

The parameter σ_j is the source strength at a point with earth fixed coordinates $\vec{\xi}$ on the mean wetted surface of a body, due to the motion of that body in the j-mode; $G(..)$ is the Green's function (Newman [25]) or ''influence function'' of a pulsating source located in $\vec{\xi}$ on the potential in a point located at $\vec{x}$ on body surface. This function, also referred to as the wave source potential, is the velocity potential at point $\vec{x}$ due to a point source of strength -4π located at point $\vec{\xi}$; and satisfies the equation of continuity, the linearised boundary condition on the free surface and on

the sea floor and the radiation condition at infinity. For finite water depth h, the general formulation of the Green's function is given by:

$$G(\vec{x},\vec{\xi}) = \frac{1}{r} + \frac{1}{r_1} + \ldots \int_1^\infty \frac{2(\kappa+\nu)e^{-\kappa h}\cosh\kappa(\zeta+h)\cosh\kappa(z+h)}{\kappa\sinh\kappa h - \nu\cosh\kappa h} J_0(\kappa R)d\kappa + \ldots \quad i\frac{2\pi(\mu_0^2-\nu^2)\cosh\mu_0(\zeta+h)\cosh(\mu_0(z+h)}{(\mu_0^2-\nu^2)h+\nu} J_0(\nu R) \quad \text{(A.13)}$$

With:

$$r = \sqrt{(\xi-x)^2+(\eta-y)^2+(\zeta-z)^2}$$

$$r_1 = \sqrt{(\xi-x)^2+(\eta-y)^2+(2h+\zeta+z)^2}$$

$$R = \sqrt{(\xi-x)^2+(\eta-y)^2}$$

J_0 is the Bessel function of the first kind of zero order, and μ_0 is the positive real root of the dispersion relation $\nu = \mu\tanh\mu h$.

The unknown source strength $\sigma_j(\vec{x})$ are found by solving normal velocity boundary conditions:

$$N_j = -\frac{1}{2}\sigma_j(\vec{x}) + \frac{1}{4\pi}\iint_S \sigma_j(\vec{\xi})\frac{\partial}{\partial n}G(\vec{x},\vec{\xi})dS \;\forall\; j = 0..7 \quad \text{(A.14)}$$

Equation (A.14) can be written as:

$$\mathcal{G}\,\sigma_j = N_j \;\forall\; j = 0..7 \quad \text{(A.15)}$$

In (A.14), the operator $\partial/\partial n$ signifies the gradient in the direction normal to the body surface. For the solution of the motion potentials, the right hand side of (A.15) is given by the direction cosines (A.16). For the solution of the wave potential the right hand side is given by (A.18) and of the diffraction potential it is given by (A.17).

$$\begin{aligned} N_1 &= \cos(n,x)\\ N_2 &= \cos(n,y)\\ N_3 &= \cos(n,z)\\ N_4 &= yn_3 - zn_2\\ N_5 &= zn_1 - xn_3\\ N_6 &= xn_2 - yn_1 \end{aligned} \quad \text{(A.16)}$$

$$N_0 = \frac{\partial \phi_w}{\partial n} \tag{A.17}$$

$$N_7 = \frac{\partial \phi_d}{\partial n} = -\frac{\partial \phi_w}{\partial n} \tag{A.18}$$

Equation (A.15) is solved numerically by subdividing the surface S in a discrete number of panels. The Green's function is computed in each panel with acceptable accuracy with the assumption that the source strength is concentrated in the center of the panel. This assumption is however not valid when the control point and the center of the panel are in too close proximity of each other. This is the case for the influence of a panel on its own, and in case the panel is too close to another boundary (such as the another surface panel, the sea-bottom or the free-water surface). Techniques are available to improve the Green's function computation (Fang [10]).

The fluid pressure follows from Bernoulli's Law:

$$\mathbf{p}(\vec{x}, t) = -\rho \frac{\partial \Phi}{\partial t} = p(\vec{x}) e^{-i\omega t} \tag{A.19}$$

With use of (A.1) and (A.4), the spacial fluid pressure is written as:

$$p(\vec{x}) = -\rho \omega^2 \left\{ (\phi_w + \phi_d)\zeta_a + \sum_{j=1}^{6} \phi_j x_j \right\} \tag{A.20}$$

With the hydrodynamic pressure known, the wave force on surface S is found from:

$$\tilde{\mathbf{F}}_{\mathbf{w}} = -\rho \omega^2 \iint_S (\phi_w + \phi_d)\zeta_a \vec{N} dS \tag{A.21}$$

Furthermore, the added mass and radiation damping are found from the real and imaginary part of the radiation component of the velocity potential, as follows:

$$\mathbf{A}_{n,m} = -\Re \left[\rho \iint_S \phi_m N_n dS \right] \quad \forall\, n = 1..6 \wedge m = 1..6 \tag{A.22}$$

$$\mathbf{B}_{n,m} = -\Im\left[\rho\omega \iint\limits_{S} \phi_m N_n dS\right] \;\forall\; n = 1..6 \wedge m = 1..6 \tag{A.23}$$

A.5 Multi Body Problems

The above theory can easily be extended to multi-body problems, where two or more free-floating and/or fixed bodies interact with each other (Pinkster [28]). Basically, for a system with n_b bodies, (A.3), (A.12) and (A.14) are respectively changed to:

$$\Phi_R = \sum_{ib=1}^{n_b} \sum_{j=1}^{6} \Phi_{ib,j} \tag{A.24}$$

$$\phi_{ib,j}(\vec{x}) = \sum_{jb=1}^{n_b} \frac{1}{4\pi} \iint\limits_{S_{jb}} \sigma_{jb,j}(\vec{\xi_{jb}}) G(\vec{x}, \vec{\xi_{jb}}) dS_{jb}$$
$$\forall\; j = 0..7 \wedge \vec{x} \in S_{ib} \tag{A.25}$$

$$N_{ib,j} = -\frac{1}{2}\sigma_{ib,j}(\vec{x}) + \sum_{jb=1}^{n_b} \frac{1}{4\pi} \iint\limits_{S_{jb}} \sigma_{jb,j}(\vec{\xi_{jb}}) \frac{\partial}{\partial n} G(\vec{x}, \vec{\xi_{jb}}) dS_{jb}$$
$$\forall\; j = 0..7 \wedge \vec{x} \in S_{ib} \tag{A.26}$$

As a result, (A.15) is now expressed as follows:

$$\begin{bmatrix} \mathcal{G}_{1,1} & \mathcal{G}_{1,2} & \cdots & \mathcal{G}_{1,n_b} \\ \mathcal{G}_{2,1} & \mathcal{G}_{2,2} & \cdots & \mathcal{G}_{2,n_b} \\ \vdots & \vdots & \ddots & \vdots \\ \mathcal{G}_{n_b,1} & \mathcal{G}_{n_b,2} & \cdots & \mathcal{G}_{n_b,n_b} \end{bmatrix} \begin{bmatrix} \sigma_{1,j} \\ \sigma_{2,j} \\ \vdots \\ \sigma_{n_b,j} \end{bmatrix} = \begin{bmatrix} N_{1,j} \\ N_{2,j} \\ \vdots \\ N_{n_b,j} \end{bmatrix} \tag{A.27}$$

The wave force on each body is found by applying equation (A.21). The added mass and radiation damping are found by extending (A.22) and (A.23) to also find the interaction terms, as follows:

$$\mathbf{A}_{ib,jb,n,m} = -\Re\left[\rho \iint\limits_{S_{ib}} \phi_{jb,m} N_{ib,n} dS_{ib}\right] \tag{A.28}$$

$$\mathbf{B}_{ib,jb,n,m} = -\Im\left[\rho\omega \iint\limits_{S_{ib}} \phi_{jb,m} N_{ib,n} dS_{ib}\right] \tag{A.29}$$

A.6 Multi Domain Diffraction Method

In the following sections, the principle of multi-domain diffraction method is further illustrated by giving two examples. First, a single body with two domains, resembling a shallow water problem, is investigated. Second, the example is extended to a two body system with three domains, representing a HTV with a cargo floating just above the deck.

A.6.1 Case: One-body-two-domains

Let's first examine a single body problem with two domains as shown in Figure A.3. This is basically a standard diffraction problem of one body in the global domain $\mathbb{A}$ with an additional domain $\mathbb{B}$ underneath the body. The boundaries of each domain are as follows:

- Domain $\mathbb{A}$ is bound by the body surface $S_{1,\mathbb{A}}$, boundary domain D, the free surface (at $z = 0$), the sea floor (at $z = -h$) and a cylindrical surface at great distance r of the body.
- Domain $\mathbb{B}$ is bound by surface $S_{1,\mathbb{B}}$, boundary surface D and the sea floor.

Standard boundary conditions as given in Section A.4 are applied to domain $\mathbb{A}$. In domain $\mathbb{B}$ another solution than the 3-dimensional linear potential theory may be applied, which is discussed in Section 4.1.2.

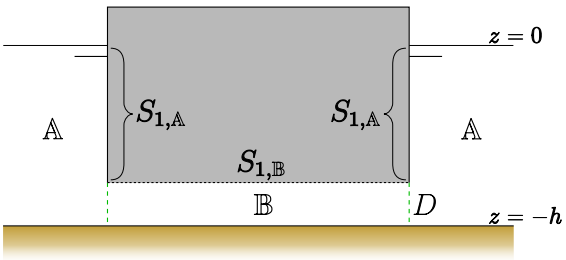

Figure A.3: Domain boundary definition - single body with two domains

For domain $\mathbb{A}$, the spacial part of Φ^a in (4.1) can be written as:

$$\phi^a = \frac{1}{4\pi} \iint\limits_{S_{1,\mathbb{A}}+D_{a\leftarrow b}} \sigma_j^a G^{\mathbb{A}} dS \tag{A.30}$$

Similar, for domain $\mathbb{B}$, the spacial part of Φ^b in equation (4.2) can be written as:

$$\phi^b = \frac{1}{4\pi} \iint\limits_{S_{1,\mathbb{B}}+D_{b\leftarrow a}} \sigma_j^b G^{\mathbb{B}} dS \tag{A.31}$$

Similar to (A.14), the unknown source strength are found by solving normal velocity boundary conditions:

$$\begin{aligned} N_j = &-\frac{1}{2}\sigma_j^a(\vec{x}) + \frac{1}{4\pi} \iint\limits_{S_{1,\mathbb{A}}} \sigma_j^a(\vec{\xi}) \frac{\partial}{\partial n} G^{\mathbb{A}}(\vec{x},\vec{\xi}) dS + \dots \\ &\dots \frac{1}{4\pi} \iint\limits_{D_{a\leftarrow b}} \sigma_j^a(\vec{\xi}) \frac{\partial}{\partial n} G^{\mathbb{A}}(\vec{x},\vec{\xi}) dS \;\forall\; j = 0..7 \wedge \vec{x} \in S_{1,\mathbb{A}} \end{aligned} \tag{A.32}$$

And:

$$\begin{aligned} N_j = &-\frac{1}{2}\sigma_j^b(\vec{x}) + \frac{1}{4\pi} \iint\limits_{S_{1,\mathbb{B}}} \sigma_j^b(\vec{\xi}) \frac{\partial}{\partial n} G^{\mathbb{B}}(\vec{x},\vec{\xi}) dS + \dots \\ &\dots \frac{1}{4\pi} \iint\limits_{D_{b\leftarrow a}} \sigma_j^b(\vec{\xi}) \frac{\partial}{\partial n} G^{\mathbb{B}}(\vec{x},\vec{\xi}) dS \;\forall\; j = 0..7 \wedge \vec{x} \in S_{1,\mathbb{B}} \end{aligned} \tag{A.33}$$

On all body surfaces $S_{ib,id}$ the no-leak boundary condition applies. On surface $S_{1,\mathbb{A}}$ the boundary conditions are known; as the wave potential is applied in domain $\mathbb{A}$, the standard conditions given in (A.16), (A.17) and (A.18) need to be applied. On surface $S_{1,\mathbb{B}}$ the boundary conditions can also be defined; to find the added mass and damping contribution the boundary condition as given in (A.16), since the wave potential is not directly applied in domain $\mathbb{B}$ the boundary conditions for $j = 0$ and $j = 7$ need to be zero.

As mentioned in Section A.6, additional boundary conditions need to be defined to be able to solve also the unknown sources on surface D, i.e. for $\vec{x} \in D$. The normal velocity condition at boundary surface D is defined as follows:

$$\left\{ -\frac{1}{2}\sigma_j^a + \frac{1}{4\pi} \iint\limits_{S_{1,\mathbb{A}}} \sigma_j^a \frac{\partial}{\partial n} G^{\mathbb{A}} dS + \frac{1}{4\pi} \iint\limits_{D_{a\leftarrow b}} \sigma_j^a \frac{\partial}{\partial n} G^{\mathbb{A}} dS \right\}_a + \ldots$$
$$\ldots \left\{ -\frac{1}{2}\sigma_j^b + \frac{1}{4\pi} \iint\limits_{S_{1,\mathbb{B}}} \sigma_j^b \frac{\partial}{\partial n} G^{\mathbb{B}} dS + \frac{1}{4\pi} \iint\limits_{D_{b\leftarrow a}} \sigma_j^b \frac{\partial}{\partial n} G^{\mathbb{B}} dS \right\}_b = v_j^D \tag{A.34}$$

The pressure condition at boundary surface D is defined as follows:

$$\left\{ \frac{1}{4\pi} \iint\limits_{S_{1,\mathbb{A}}} \sigma_j^a G^{\mathbb{A}} dS + \frac{1}{4\pi} \iint\limits_{D_{a\leftarrow b}} \sigma_j^a G^{\mathbb{A}} dS \right\}_a - \ldots$$
$$\ldots \left\{ \frac{1}{4\pi} \iint\limits_{S_{1,\mathbb{B}}} \sigma_j^b G^{\mathbb{B}} dS + \frac{1}{4\pi} \iint\limits_{D_{b\leftarrow a}} \sigma_j^b G^{\mathbb{B}} dS \right\}_b = \phi_j^D \tag{A.35}$$

In the above equations $D_{a\leftarrow b}$ denotes the boundary surface D between domain $\mathbb{A}$ and domain $\mathbb{B}$ with the normal direction towards domain $\mathbb{A}$; vice versa $D_{b\leftarrow a}$ denotes the boundary surface D between domain $\mathbb{B}$ and domain $\mathbb{A}$ with the normal direction towards domain $\mathbb{B}$. The expression within brackets denoted with index a or b refers to the influence of all sources on the body of domain $\mathbb{A}$ or $\mathbb{B}$ respectively to the normal velocity on the

boundary panels on respectively each side of the boundary. The influence functions $G^{\mathbb{A}}$ and $G^{\mathbb{B}}$ depend on the chosen solution in the domains.

The right-hand side value of (A.34) (i.e. v_j^D) depends on the potential component j and the kind of domains $\mathbb{A}$ and $\mathbb{B}$. For $j = 1..6$, the value of v_j^D is zero. In this case — as we are looking at a boundary between the standard outer domain and an inner domain — the value of v_j^D equals the normal velocity potentials of the undisturbed and diffracted wave:

$$v_0^D = \frac{\partial \phi_w}{\partial n} \qquad v_7^D = -\frac{\partial \phi_d}{\partial n} \tag{A.36}$$

Similar, the value of the right-hand side of (A.35) (i.e. ϕ_j^D) depends on the potential component j and the kind of domains $\mathbb{A}$ and $\mathbb{B}$. Again, for $j = 1..6$, the value of ϕ_j^D is zero. And for $j = 0$ and $j = 7$, the value of ϕ_j^D equals the pressure due to the undisturbed incoming wave and the diffracted wave, respectively:

$$\phi_0^D = \phi_w \qquad \phi_7^D = -\phi_d \tag{A.37}$$

With all boundary conditions defined, the basic linear system of equations, like (A.15), is now defined by:

$$\begin{array}{l} \\ \text{domain } \mathbb{A} \\ \text{domain } \mathbb{B} \\ \text{vel. at } D \\ \text{pres. at } D \end{array} \begin{array}{c} \overbrace{}^{S_{1,\mathbb{A}}} \overbrace{}^{S_{1,\mathbb{B}}} \overbrace{}^{D_{a\leftarrow b}} \overbrace{}^{D_{b\leftarrow a}} \\ \begin{bmatrix} \mathcal{G}_{1,1}^{\mathbb{A}} & 0 & \mathcal{G}_{1,ab}^{\mathbb{A}} & 0 \\ 0 & \mathcal{G}_{1,1}^{\mathbb{B}} & 0 & \mathcal{G}_{1,ba}^{\mathbb{B}} \\ \mathcal{G}_{ab,1}^{\mathbb{A}} & \mathcal{G}_{ba,1}^{\mathbb{B}} & \mathcal{G}_{ab,ab}^{\mathbb{A}} & \mathcal{G}_{ba,ba}^{\mathbb{B}} \\ \mathbf{G}_{ab,1}^{\mathbb{A}} & -\mathbf{G}_{ba,1}^{\mathbb{B}} & \mathbf{G}_{ab,ab}^{\mathbb{A}} & -\mathbf{G}_{ba,ba}^{\mathbb{B}} \end{bmatrix} \end{array} \begin{bmatrix} \{\sigma_j^a\}_{S_{1,\mathbb{A}}} \\ \{\sigma_j^b\}_{S_{1,\mathbb{B}}} \\ \{\sigma_j^a\}_{D_{a\leftarrow b}} \\ \{\sigma_j^b\}_{D_{b\leftarrow a}} \end{bmatrix} = \vec{N}_j \tag{A.38}$$

With:

$$\vec{N}_0 = \begin{bmatrix} \left\{\frac{\partial \phi_w}{\partial n}\right\}_{S_{1,\mathbb{A}}} \\ 0 \\ \left\{\frac{\partial \phi_w}{\partial n}\right\}_{D_{a\leftarrow b}} \\ \{\phi_w\}_{D_{a\leftarrow b}} \end{bmatrix} \quad \vec{N}_7 = \begin{bmatrix} \left\{-\frac{\partial \phi_d}{\partial n}\right\}_{S_{1,\mathbb{A}}} \\ 0 \\ \left\{-\frac{\partial \phi_d}{\partial n}\right\}_{D_{a\leftarrow b}} \\ \{-\phi_d\}_{D_{a\leftarrow b}} \end{bmatrix} \tag{A.39}$$

And:

$$\vec{N}_j = \begin{bmatrix} \{N_j\}_{S_{1,\mathbb{A}}} \\ \{N_j\}_{S_{1,\mathbb{B}}} \\ 0 \\ 0 \end{bmatrix} \quad \forall\ j = 1..6 \tag{A.40}$$

A.6.2 Case: Two-body-three-domains

Now, let's examine the multi body problem with three domains as shown in Figure A.4. This two body system represents a cargo floating above the deck of a HTV, naturally both being present in domain $\mathbb{A}$ (with the sea floor at $z = -h_{\mathbb{A}}$). The fluid between cargo and HTV deck is domain $\mathbb{B}$ similar to the domain described in Section A.6.1. In addition, there is a fluid domain $\mathbb{C}$ above the HTV deck, which can be considered as a local shallow water region (at $z = -h_{\mathbb{C}}$). Now, the domain boundaries can be described as follows:

- Domain $\mathbb{A}$ is bound by the body surfaces $S_{1,\mathbb{A}}$ and $S_{2,\mathbb{A}}$, boundary domain $D_{a\leftarrow b}$ and $D_{a\leftarrow c}$, the free surface (at $z = 0$), the sea floor and a cylindrical surface at great distance r of the body.
- Domain $\mathbb{B}$ is bound by surface $S_{1,\mathbb{B}}$ and $S_{2,\mathbb{B}}$ and boundary surface $D_{b\leftarrow a}$ and $D_{b\leftarrow c}$.
- Domain $\mathbb{C}$ is bound by surface $S_{1,\mathbb{C}}$ and $S_{2,\mathbb{C}}$ and boundary surface $D_{c\leftarrow a}$ and $D_{c\leftarrow b}$.

Again, standard boundary conditions as given in Section A.4 are applied to domain $\mathbb{A}$. In principle also in domain $\mathbb{C}$ the standard boundary condition should be applied, accept for the different local water depth; this is further discussed in paragraph A.6.4. Similar to Section A.6.1, another solution applies in domain $\mathbb{B}$.

Similar to (A.32) and (A.33), the unknown source strength are found by

solving normal velocity boundary conditions, for domain $\mathbb{A}$:

$$N_j = -\frac{1}{2}\sigma_j^a(\vec{x}) + \frac{1}{4\pi}\sum_{ib=1}^{n_b}\iint_{S_{ib,\mathbb{A}}}\sigma_j^a(\vec{\xi})\frac{\partial}{\partial n}G^{\mathbb{A}}(\vec{x},\vec{\xi})dS + \ldots$$

$$\ldots\frac{1}{4\pi}\sum_{id}^{\{b,c\}}\iint_{D_{a\leftarrow id}}\sigma_j^a(\vec{\xi})\frac{\partial}{\partial n}G^{\mathbb{A}}(\vec{x},\vec{\xi})dS\ \forall\ j = 0..7 \wedge \vec{x} \in \{S_{1,\mathbb{A}}, S_{2,\mathbb{A}}\} \tag{A.41}$$

For domain $\mathbb{B}$:

$$N_j = -\frac{1}{2}\sigma_j^b(\vec{x}) + \frac{1}{4\pi}\sum_{ib=1}^{n_b}\iint_{S_{ib,\mathbb{B}}}\sigma_j^b(\vec{\xi})\frac{\partial}{\partial n}G^{\mathbb{B}}(\vec{x},\vec{\xi})dS + \ldots$$

$$\ldots\frac{1}{4\pi}\sum_{id}^{\{a,c\}}\iint_{D_{b\leftarrow id}}\sigma_j^b(\vec{\xi})\frac{\partial}{\partial n}G^{\mathbb{B}}(\vec{x},\vec{\xi})dS\ \forall\ j = 0..7 \wedge \vec{x} \in \{S_{1,\mathbb{B}}, S_{2,\mathbb{B}}\} \tag{A.42}$$

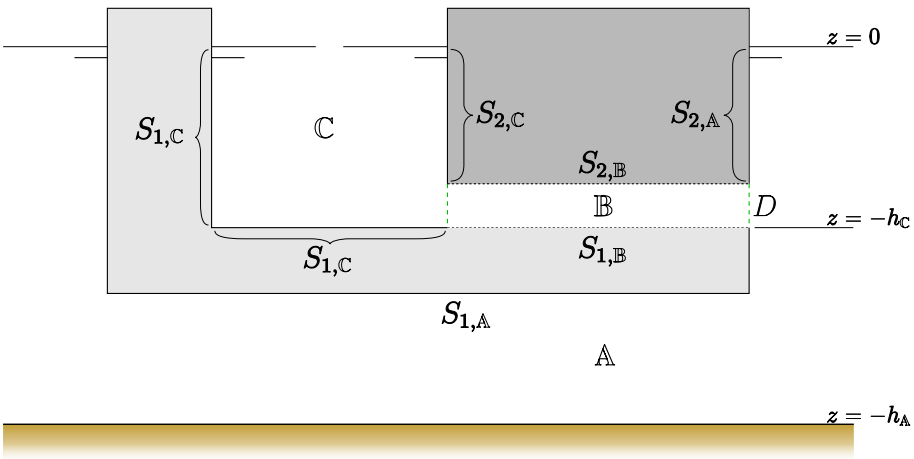

Figure A.4: Domain boundary definition - two bodies with three domains

And, for domain $\mathbb{C}$:

$$N_j = -\frac{1}{2}\sigma_j^c(\vec{x}) + \frac{1}{4\pi}\sum_{ib=1}^{n_b}\iint_{S_{ib,\mathbb{C}}}\sigma_j^c(\vec{\xi})\frac{\partial}{\partial n}G^{\mathbb{C}}(\vec{x},\vec{\xi})dS + \ldots$$
$$\frac{1}{4\pi}\sum_{id}^{\{a,b\}}\iint_{D_{c\leftarrow id}}\sigma_j^c(\vec{\xi})\frac{\partial}{\partial n}G^{\mathbb{C}}(\vec{x},\vec{\xi})dS$$
$$\forall\ j = 0..7 \wedge \vec{x} \in \{S_{1,\mathbb{C}}, S_{2,\mathbb{C}}\} \quad \text{(A.43)}$$

As before, additional boundary conditions for the domain interface surfaces need to be defined. Rewriting (A.34)) and (A.35) in a more general form, the following equations apply for the three combinations $\{id, jd, kd\} = \{a, b, c\}, \{a, c, b\}, \{b, c, a\}$:

$$\left\{-\frac{1}{2}\sigma_j^{id} + \frac{1}{4\pi}\sum_{ib=1}^{n_b}\iint_{S_{ib,id}}\sigma_j^{id}\frac{\partial}{\partial n}G^{id}dS + \frac{1}{4\pi}\sum_{ld}^{\{jd,kd\}}\iint_{D_{id\leftarrow ld}}\sigma_j^{id}\frac{\partial}{\partial n}G^{id}dS\right\}_{id} + \ldots$$
$$\left\{-\frac{1}{2}\sigma_j^{jd} + \frac{1}{4\pi}\sum_{ib=1}^{n_b}\iint_{S_{ib,jd}}\sigma_j^{jd}\frac{\partial}{\partial n}G^{jd}dS + \frac{1}{4\pi}\sum_{ld}^{\{id,kd\}}\iint_{D_{jd\leftarrow ld}}\sigma_j^{jd}\frac{\partial}{\partial n}G^{jd}dS\right\}_{jd} = v_j^D \quad \text{(A.44)}$$

$$\left\{\frac{1}{4\pi}\sum_{ib=1}^{n_b}\iint_{S_{ib,id}}\sigma_j^{id}G^{id}dS + \frac{1}{4\pi}\sum_{ld}^{\{jd,kd\}}\iint_{D_{id\leftarrow ld}}\sigma_j^{id}G^{id}dS\right\}_{id} - \ldots$$
$$\left\{\frac{1}{4\pi}\sum_{ib=1}^{n_b}\iint_{S_{ib,jd}}\sigma_j^{jd}G^{jd}dS + \frac{1}{4\pi}\sum_{ld}^{\{id,kd\}}\iint_{D_{jd\leftarrow ld}}\sigma_j^{jd}G^{jd}dS\right\}_{jd} = \phi_j^D \quad \text{(A.45)}$$

For v_j^D and ϕ_j^D the same applies as described in Section A.6.1; the value depends on the potential mode j and the kind of neighbouring domains. Again the values are zero for all domain boundary surfaces, except for those intersecting with domain $\mathbb{A}$, for which (A.36) and (A.37) apply. The linear system of equations for this case is defined by (A.46), (A.47) and (A.48).

$$\mathbf{G} = \left[\begin{array}{r|cccccc|cccccc}
 & S_{1,\mathbb{A}} & S_{1,\mathbb{B}} & S_{1,\mathbb{C}} & S_{2,\mathbb{A}} & S_{2,\mathbb{B}} & S_{2,\mathbb{C}} & D_{a\leftarrow b} & D_{a\leftarrow c} & D_{b\leftarrow c} & D_{b\leftarrow a} & D_{c\leftarrow a} & D_{c\leftarrow b} \\
\hline
\mathbb{A} & \mathcal{G}^{\mathbb{A}}_{1,1} & & 0 & \mathcal{G}^{\mathbb{A}}_{1,2} & & 0 & \mathcal{G}^{\mathbb{A}}_{1,ab} & \mathcal{G}^{\mathbb{A}}_{1,ac} & & & 0 & \\
\text{body 1:}\quad \mathbb{B} & & \mathcal{G}^{\mathbb{B}}_{1,1} & & & \mathcal{G}^{\mathbb{B}}_{1,2} & & & & \mathcal{G}^{\mathbb{B}}_{1,bc} & \mathcal{G}^{\mathbb{B}}_{1,ba} & & \\
\mathbb{C} & 0 & & \mathcal{G}^{\mathbb{C}}_{1,1} & 0 & & \mathcal{G}^{\mathbb{C}}_{1,2} & 0 & & & & \mathcal{G}^{\mathbb{C}}_{1,ca} & \mathcal{G}^{\mathbb{C}}_{1,cb} \\
\hdashline
\mathbb{A} & \mathcal{G}^{\mathbb{A}}_{2,1} & & 0 & \mathcal{G}^{\mathbb{A}}_{2,2} & & 0 & \mathcal{G}^{\mathbb{A}}_{2,ab} & \mathcal{G}^{\mathbb{A}}_{2,ac} & & & 0 & \\
\text{body 2:}\quad \mathbb{B} & & \mathcal{G}^{\mathbb{B}}_{2,1} & & & \mathcal{G}^{\mathbb{B}}_{2,2} & & & & \mathcal{G}^{\mathbb{B}}_{2,bc} & \mathcal{G}^{\mathbb{B}}_{2,ba} & & \\
\mathbb{C} & 0 & & \mathcal{G}^{\mathbb{C}}_{2,1} & 0 & & \mathcal{G}^{\mathbb{C}}_{2,2} & 0 & & & & \mathcal{G}^{\mathbb{C}}_{2,ca} & \mathcal{G}^{\mathbb{C}}_{2,cb} \\
\hline
D_{a-b} & \mathcal{G}^{\mathbb{A}}_{ab,1} & \mathcal{G}^{\mathbb{B}}_{ba,1} & 0 & \mathcal{G}^{\mathbb{A}}_{ab,2} & \mathcal{G}^{\mathbb{B}}_{ba,2} & 0 & \mathcal{G}^{\mathbb{A}}_{ab,ab} & \mathcal{G}^{\mathbb{A}}_{ab,ac} & \mathcal{G}^{\mathbb{B}}_{ba,bc} & \mathcal{G}^{\mathbb{B}}_{ba,ba} & 0 & \\
\text{vel. at } D_{b-c} & 0 & \mathcal{G}^{\mathbb{B}}_{bc,1} & \mathcal{G}^{\mathbb{C}}_{cb,1} & 0 & \mathcal{G}^{\mathbb{B}}_{bc,2} & \mathcal{G}^{\mathbb{C}}_{cb,2} & 0 & & \mathcal{G}^{\mathbb{B}}_{bc,bc} & \mathcal{G}^{\mathbb{B}}_{bc,ba} & \mathcal{G}^{\mathbb{C}}_{cb,ca} & \mathcal{G}^{\mathbb{C}}_{cb,cb} \\
D_{a-c} & \mathcal{G}^{\mathbb{A}}_{ac,1} & 0 & \mathcal{G}^{\mathbb{C}}_{ca,1} & \mathcal{G}^{\mathbb{A}}_{ac,2} & 0 & \mathcal{G}^{\mathbb{C}}_{ca,2} & \mathcal{G}^{\mathbb{A}}_{ac,ab} & \mathcal{G}^{\mathbb{A}}_{ac,ac} & 0 & & \mathcal{G}^{\mathbb{C}}_{ca,ca} & \mathcal{G}^{\mathbb{C}}_{ca,cb} \\
\hline
D_{a-b} & \mathbf{G}^{\mathbb{A}}_{ab,1} & -\mathbf{G}^{\mathbb{B}}_{ba,1} & 0 & \mathbf{G}^{\mathbb{A}}_{ab,2} & -\mathbf{G}^{\mathbb{B}}_{ba,2} & 0 & \mathbf{G}^{\mathbb{A}}_{ab,ab} & \mathbf{G}^{\mathbb{A}}_{ab,ac} & -\mathbf{G}^{\mathbb{B}}_{ba,bc} & -\mathbf{G}^{\mathbb{B}}_{ba,ba} & 0 & \\
\text{pres. at} D_{b-c} & 0 & \mathbf{G}^{\mathbb{B}}_{bc,1} & -\mathbf{G}^{\mathbb{C}}_{cb,1} & 0 & \mathbf{G}^{\mathbb{B}}_{bc,2} & -\mathbf{G}^{\mathbb{C}}_{cb,2} & 0 & & \mathbf{G}^{\mathbb{B}}_{bc,bc} & \mathbf{G}^{\mathbb{B}}_{bc,ba} & -\mathbf{G}^{\mathbb{C}}_{cb,ca} & -\mathcal{G}^{\mathbb{C}}_{cb,cb} \\
D_{a-c} & \mathbf{G}^{\mathbb{A}}_{ac,1} & 0 & -\mathbf{G}^{\mathbb{C}}_{ca,1} & \mathbf{G}^{\mathbb{A}}_{ac,2} & 0 & -\mathbf{G}^{\mathbb{C}}_{ca,2} & \mathbf{G}^{\mathbb{A}}_{ac,ab} & \mathbf{G}^{\mathbb{A}}_{ac,ac} & 0 & & -\mathbf{G}^{\mathbb{C}}_{ca,ca} & -\mathbf{G}^{\mathbb{C}}_{ca,cb}
\end{array}\right] \tag{A.46}$$

$$\boldsymbol{\sigma}_j = \begin{bmatrix} \{\sigma_j^a\}_{S_{1,\mathbb{A}}} \\ \{\sigma_j^a\}_{S_{1,\mathbb{B}}} \\ \{\sigma_j^b\}_{S_{1,\mathbb{C}}} \\ \{\sigma_j^b\}_{S_{2,\mathbb{A}}} \\ \{\sigma_j^c\}_{S_{2,\mathbb{B}}} \\ \{\sigma_j^c\}_{S_{2,\mathbb{C}}} \\ \{\sigma_j^a\}_{D_{a\leftarrow b}} \\ \{\sigma_j^a\}_{D_{a\leftarrow c}} \\ \{\sigma_j^b\}_{D_{b\leftarrow c}} \\ \{\sigma_j^b\}_{D_{b\leftarrow a}} \\ \{\sigma_j^c\}_{D_{c\leftarrow a}} \\ \{\sigma_j^c\}_{D_{c\leftarrow b}} \end{bmatrix} \tag{A.47}$$

$$\vec{N}_0 = \begin{bmatrix} \left\{\frac{\partial \phi_w}{\partial n}\right\}_{S_{1,\mathbb{A}}} \\ 0 \\ 0 \\ \left\{\frac{\partial \phi_w}{\partial n}\right\}_{S_{2,\mathbb{A}}} \\ 0 \\ 0 \\ \left\{\frac{\partial \phi_w}{\partial n}\right\}_{D_{a,b}} \\ \left\{\frac{\partial \phi_w}{\partial n}\right\}_{D_{a,c}} \\ 0 \\ \{\phi_w\}_{D_{a,b}} \\ \{\phi_w\}_{D_{a,c}} \\ 0 \end{bmatrix} \quad \vec{N}_7 = \begin{bmatrix} \left\{-\frac{\partial \phi_d}{\partial n}\right\}_{S_{1,\mathbb{A}}} \\ 0 \\ 0 \\ \left\{-\frac{\partial \phi_d}{\partial n}\right\}_{S_{2,\mathbb{A}}} \\ 0 \\ 0 \\ \left\{-\frac{\partial \phi_d}{\partial n}\right\}_{D_{a,b}} \\ \left\{-\frac{\partial \phi_d}{\partial n}\right\}_{D_{a,c}} \\ 0 \\ \{-\phi_d\}_{D_{a,b}} \\ \{-\phi_d\}_{D_{a,c}} \\ 0 \end{bmatrix} \quad \vec{N}_j = \begin{bmatrix} \{N_j\}_{S_{1,\mathbb{A}}} \\ \{N_j\}_{S_{1,\mathbb{B}}} \\ \{N_j\}_{S_{1,\mathbb{C}}} \\ \{N_j\}_{S_{2,\mathbb{A}}} \\ \{N_j\}_{S_{2,\mathbb{B}}} \\ \{N_j\}_{S_{2,\mathbb{C}}} \\ 0 \\ 0 \\ 0 \\ 0 \\ 0 \\ 0 \end{bmatrix} \quad \forall\, j = 1..6 \tag{A.48}$$

A.6.3 General Equations

As shown by the examples, in MDDM domains are defined by a number of surface parts. Therefore, (A.30) to (A.35) and (A.41) to (A.45) can be generalized. For domain id, the spacial part of Φ^{id} can be written as:

$$\phi^{id} = \frac{1}{4\pi} \sum_{k=1}^{n_b} \sum_{id}^{\{n_{k,id}\}} \iint_{S_{k,id}} \sigma_j^{id} G^{id} dS \tag{A.49}$$

And, the unknown source strength are found by solving normal velocity boundary conditions:

$$N_j = -\frac{1}{2}\sigma_j^{id}(\vec{x}) + \frac{1}{4\pi} \sum_{k=1}^{n_b} \sum_{id}^{\{n_{k,id}\}} \iint_{S_{k,id}} \sigma_j^{id}(\vec{\xi}) \frac{\partial}{\partial n} G^{id}(\vec{x}, \vec{\xi}) dS \ldots$$
$$\ldots \; \forall \; j = 0..7 \wedge \vec{x} \in \{S_{k,id} \; \forall \; k = 1, n_b \wedge id = 1, n_d\} \tag{A.50}$$

The additional boundary conditions for interface surfaces between domain id and jd become:

$$\left\{ -\frac{1}{2}\sigma_j^{id} + \frac{1}{4\pi} \sum_{k=1}^{n_b} \sum_{id}^{\{n_{k,id}\}} \iint_{S_{k,id}} \sigma_j^{id} \frac{\partial}{\partial n} G^{id} dS \right\}_{id} + \ldots$$
$$\ldots \left\{ -\frac{1}{2}\sigma_j^{jd} + \frac{1}{4\pi} \sum_{k=1}^{n_b} \sum_{id}^{\{n_{k,id}\}} \iint_{S_{k,jd}} \sigma_j^{jd} \frac{\partial}{\partial n} G^{jd} dS \right\}_{jd} = v_j^D \tag{A.51}$$

$$\left\{ \frac{1}{4\pi} \sum_{k=1}^{n_b} \sum_{id}^{\{n_{k,id}\}} \iint_{S_{k,id}} \sigma_j^{id} G^{id} dS \right\}_{id} - \left\{ \frac{1}{4\pi} \sum_{k=1}^{n_b} \sum_{id}^{\{n_{k,id}\}} \iint_{S_{k,jd}} \sigma_j^{jd} G^{jd} dS \right\}_{jd} = \phi_j^D \tag{A.52}$$

A.6.4 Local Shallow Water Domain

As mentioned in Section A.6.2, the same solution as in the standard domain $\mathbb{A}$ should be applied to the local shallow water domain, with water depth h being the local water depth. However, the submerged deck surface would coincide with the virtual local ‘‘sea bottom’’ and is free to move in space, whereas the standard solution method assumes that the sea bottom is a non-moving horizontal flat surface. Therefore, one can not simply apply the local water depth to the standard solution, as numerically this results in a singular solution of the potential problem. To overcome this issue, a simple solution is to increase the local water depth; increasing the depth with the average equivalent element radius should suffice.

Further, one needs to consider cases, where an extremely small water level is present, as seen in Figure 2.2(b). One can imagine the similarity with the gap flow, such that also for this domain a 2D-flow solution may be applicable. On the other hand some phenomenon will be difficult to assess, like deck getting 'dry' locally, water running from the deck edge, breaking waves. These kind of phenomena are observed during tests with a submerged deck carried out in 2013 and during test carried out by MARIN in 2017.

A.6.5 Verification

To verify the source code of the multi-domain diffraction method, a set of calculations has been carried out; the set contains a standard diffraction calculation and a multi-domain calculation. The calculation shows that waves are transmitted through a boundary surface; the same type of comparison is shown by Pinkster [30].

The hydrodynamic properties are determined for a rectangular barge, with a length of 150 m, a width of 25 m and a draft of 4 m, without and with a surrounding domain boundary (Figure A.5); the number of elements at the boundary domain are varied. For this case the linear system of equations

becomes:

$$\begin{array}{l} \\ \text{domain } \mathbb{B} \\ \text{vel. at } D \\ \text{pres. at } D \end{array} \begin{array}{c} \overbrace{}^{S_{1,\mathbb{B}}} \quad \overbrace{}^{D_{a\leftarrow b}} \quad \overbrace{}^{D_{b\leftarrow a}} \\ \left[\begin{array}{ccc} \mathcal{G}^{\mathbb{B}}_{1,1} & 0 & \mathcal{G}^{\mathbb{B}}_{1,ba} \\ \mathcal{G}^{\mathbb{B}}_{ba,1} & \mathcal{G}^{\mathbb{A}}_{ab,ab} & \mathcal{G}^{\mathbb{B}}_{ba,ba} \\ -\mathbf{G}^{\mathbb{B}}_{ba,1} & \mathbf{G}^{\mathbb{A}}_{ab,ab} & -\mathbf{G}^{\mathbb{B}}_{ba,ba} \end{array}\right] \end{array} \left[\begin{array}{c} \{\sigma^b_j\}_{S_{1,\mathbb{B}}} \\ \{\sigma^a_j\}_{D_{a\leftarrow b}} \\ \{\sigma^b_j\}_{D_{b\leftarrow a}} \end{array}\right] = \vec{N}_j \tag{A.53}$$

With:

$$\vec{N}_0 = \left[\begin{array}{c} 0 \\ \left\{\frac{\partial \phi_w}{\partial n}\right\}_{D_{a\leftarrow b}} \\ \{\phi_w\}_{D_{a\leftarrow b}} \end{array}\right] \quad \vec{N}_7 = \left[\begin{array}{c} 0 \\ \left\{-\frac{\partial \phi_d}{\partial n}\right\}_{D_{a\leftarrow b}} \\ \{-\phi_d\}_{D_{a\leftarrow b}} \end{array}\right] \tag{A.54}$$

And:

$$\vec{N}_j = \left[\begin{array}{c} \{N_j\}_{S_{1,\mathbb{B}}} \\ 0 \\ 0 \end{array}\right] \forall\, j = 1..6 \tag{A.55}$$

In Figure A.6 a comparison of added mass and radiation damping based on the standard diffraction and the multi-domain method is given. Clearly, at high frequencies small difference between both methods are observed. The results are converging with increasing number of domain boundary elements.

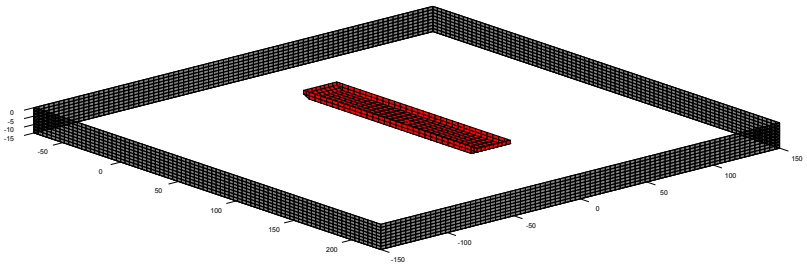

Figure A.5: Rectangular barge inside a domain

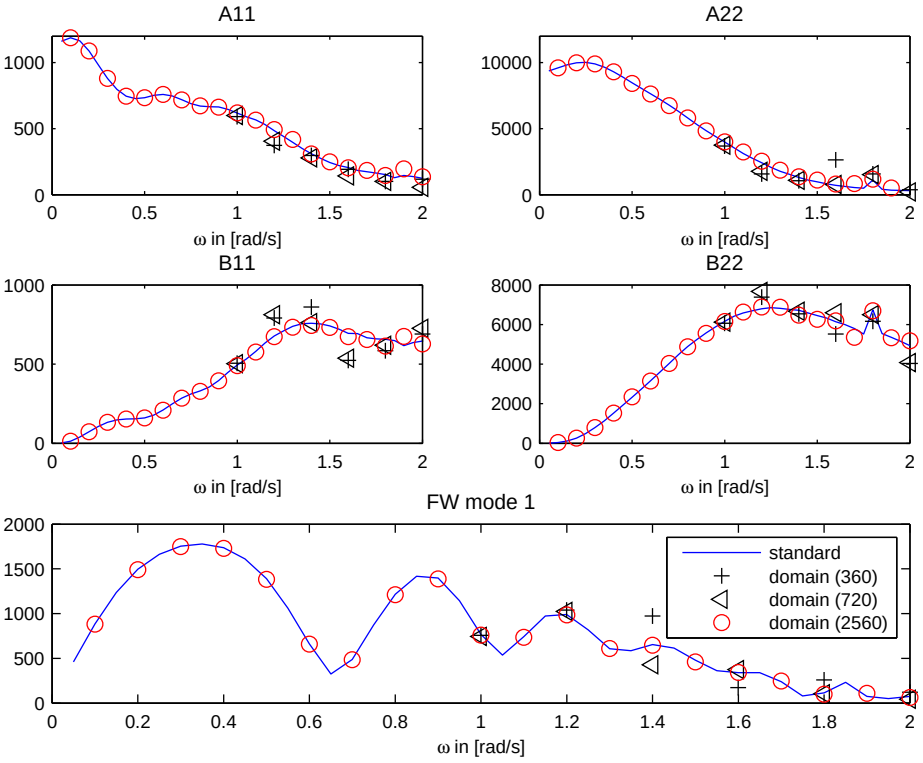

Figure A.6: Verification results barge inside a domain

APPENDIX B

Design Analysis Methods

B.1 Rigid Body Dynamics

B.1.1 Equation of Motions

In physics, rigid body dynamics is the study of the motion of rigid bodies. Unlike particles, which move only in three degrees of freedom (translation in three directions), rigid bodies occupy space and have geometrical properties, such as a center of mass, moments of inertia, etc., that characterize motion in six degrees of freedom (translation in three directions plus rotation in three directions). Rigid bodies are also characterized as being non-deformable, as opposed to deformable bodies. As such, rigid body dynamics is used heavily in analyses and computer simulations of physical systems and machinery where rotational motion is important, but material deformation does not have a significant effect on the motion of the system. Newton's Second Law states that the rate of change of the linear momentum of a particle with constant mass is equal to the sum of all external forces acting on the particle. When realizing that a floating body can be treated as a damped mass-spring system, the external force in Newton's Second Law is defined by the wave excitation force, radiation force and restoring force. Next, the radiation force is split in to a force proportional to acceleration and a force proportional to velocity. As such, the most basic form of equation of motions as used in marine hydrodynamics is found:

$$(\mathbf{M} + \mathbf{A}(\omega))\ddot{\tilde{x}} + \mathbf{B}(\omega)\dot{\tilde{x}} + \mathbf{C}\tilde{x} = \tilde{\mathbf{F}}_{\mathbf{w}}(\omega) \tag{B.1}$$

The radiation term proportional to the acceleration is called added mass. In fluid mechanics, added mass or virtual mass is the inertia added to

a system because an accelerating or decelerating body must move some volume of surrounding fluid as it moves through it, since the object and fluid cannot occupy the same physical space simultaneously. For simplicity this can be modelled as some volume of fluid moving with the object, though in reality "all" the fluid will be accelerated, to various degrees. The radiation term proportional to the velocity is the radiation or potential damping; it represents the dissipated energy due to the surface wave generated by the body motions. The derivation of the added mass $\mathbf{A}$, radiation damping $\mathbf{B}$ and wave force $\tilde{\mathbf{F}}_{\mathbf{w}}$ is given in Section A.4.

B.1.2 Multi body dynamics

The offshore loading or discharge operation is a multi body dynamics problem, which can be schematically presented in the free body diagram in Figure B.1. The two bodies S_1 and S_2 — respectively the HTV and the cargo — are floating in the fluid domain $\mathbb{A}$. The two bodies are separated by a small gap, we call this fluid domain $\mathbb{B}$. Reason for mentioning this domain becomes clear from the outline of the multi domain diffraction method as given in Section A.6. An important influence parameter in this domain is the damping effect between the two bodies ($\mathbf{B_{1,2}} = \mathbf{B_{2,1}}$). Each body is loaded by waves ($\tilde{\mathbf{F}}_{\mathbf{w,1}}$ and $\tilde{\mathbf{F}}_{\mathbf{w,2}}$), has it's damping term ($\mathbf{B_{1,1}}$ and $\mathbf{B_{2,2}}$) and restoring term ($\mathbf{C_{1,1}}$ and $\mathbf{C_{2,2}}$). Furthermore, the HTV positioning — possibly be an anchor mooring system — is giving the term $\mathbf{C_{moor}}$; this represents global positioning of the complete system. And finally the cargo is controlled by the cargo handling system — working between the two bodies — giving term $\mathbf{C_{cargo}}$.

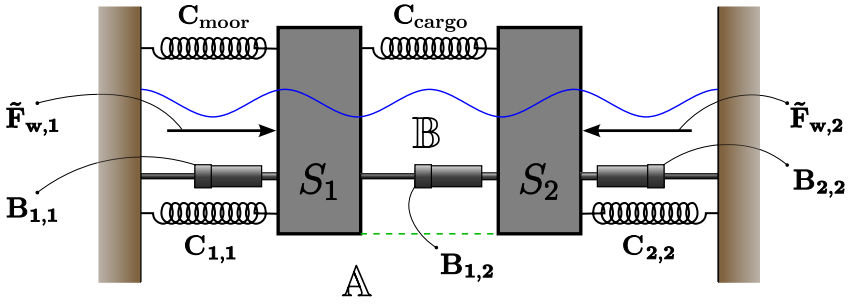

Figure B.1: Free body diagram

By extending (B.1), the above described multi body dynamics system is formulated in the following equation:

$$\begin{bmatrix} \mathbf{M_1} + \mathbf{A_{1,1}} & \mathbf{A_{1,2}} \\ \mathbf{A_{2,1}} & \mathbf{M_2} + \mathbf{A_{2,2}} \end{bmatrix} \begin{bmatrix} \ddot{\tilde{x}}_1 \\ \ddot{\tilde{x}}_2 \end{bmatrix} + \begin{bmatrix} \mathbf{B_{1,1}} & \mathbf{B_{1,2}} \\ \mathbf{B_{2,1}} & \mathbf{B_{2,2}} \end{bmatrix} \begin{bmatrix} \dot{\tilde{x}}_1 \\ \dot{\tilde{x}}_2 \end{bmatrix} + \cdots$$
$$\begin{bmatrix} \mathbf{C_{moor}} + \mathbf{C_{cargo}} + \mathbf{C_{1,1}} & -\mathbf{C_{cargo}} \\ -\mathbf{C_{cargo}} & \mathbf{C_{cargo}} + \mathbf{C_{2,2}} \end{bmatrix} \begin{bmatrix} \tilde{x}_1 \\ \tilde{x}_2 \end{bmatrix} = \begin{bmatrix} \tilde{\mathbf{F}}_{\mathbf{w,1}} \\ \tilde{\mathbf{F}}_{\mathbf{w,2}} \end{bmatrix} \tag{B.2}$$

B.1.3 Cargo Mooring Stiffness Matrix

The cargo mooring (or handling) system can be considered as a set of lines. The mooring lines may be composed of a number of sections, where line sections can be constructed of plastic fiber rope (like polyester or dyneema®) or steel wire rope; often different sections are combined. Normally, chains are not used for cargo handling. In general, the mooring line mass is relative small, such that mooring lines can be considered as weightless springs. As such, catenary equations are not required when determining the stiffness characteristics of a cargo mooring line.

The tension in a mooring line which mass is considered negligible, and thus has no deflection, may be expressed in terms of a series of coefficients and its extension (e) from an unstretched length. The reaction force, which direction is given by the vector joining the two attachment points of the mooring line, exerted on a structure by the mooring line (R) may therefore be written as:

$$R(e) = a_1 e + a_2 e^2 + a_3 e^3 + ... \tag{B.3}$$

The elastic stiffness in the direction of the force follows from the derivative of (B.3), being:

$$S(e) = a_1 + 2a_2 e + 3a_3 e^2 + ... \tag{B.4}$$

If this elastic stiffness for a given extension is S, and the tension is R, then the 3x3 stiffness matrix ($\mathbf{K}$), relating the force to the translational

displacements at the attachment point of the structure, may be expressed as (ref. [1]):

$$\mathbf{K} = S\mathbf{N} + (\mathbf{I} - \mathbf{N})\frac{R}{L} \tag{B.5}$$

where

$$\begin{aligned} \mathbf{N} &= \begin{pmatrix} l_1 & l_2 & l_3 \end{pmatrix} \begin{pmatrix} l_1 \\ l_2 \\ l_3 \end{pmatrix} \\ \begin{pmatrix} l_1 & l_2 & l_3 \end{pmatrix} &= \text{unit vector joining the attachment points of the cable} \\ \mathbf{I} &= \text{3x3 unit matrix} \\ \mathbf{L} &= \text{stretched length of the mooring line} \end{aligned}$$

The first term, $S\mathbf{N}$, represents the "mechanical" stiffness, which depends only on the material properties of the mooring lines. The second term, $(\mathbf{I} - \mathbf{N})\frac{R}{L}$, represents the "geometric" stiffness, which depends only on the length and tension of the line.

The stiffness matrix $\mathbf{K}$, for each mooring line is defined at the attachment point on the structure and must be translated to a common reference point. This, formulated as the transformation procedure, is applied to any local stiffness matrix. The formulation of a vector translation may be applied directly to a force and displacement in order to translate the stiffness matrix $\mathbf{K}$, from the point of definition to the reference point. The full 6x6 stiffness matrix $\mathbf{C}_{line}$ for each mooring line, which relates the displacement of the reference point of structure m to the change in forces and moments applied to that reference point a, is given by:

$$\mathbf{C}_{line} = \begin{bmatrix} \mathbf{I} \\ \mathbf{T}_a^\top \end{bmatrix} [\mathbf{K}] \begin{bmatrix} \mathbf{I} & \mathbf{T}_a \end{bmatrix} + \begin{bmatrix} 0 & \cdots & 0 \\ \vdots & \ddots & \vdots \\ 0 & \cdots & \mathbf{R}_m \mathbf{T}_a^\top \end{bmatrix} \tag{B.6}$$

where

$$\mathbf{T}_a = \begin{bmatrix} 0 & z & -y \\ -z & 0 & x \\ y & -x & 0 \end{bmatrix}, \; \mathbf{R}_m = \begin{bmatrix} 0 & R_z & -R_y \\ -R_z & 0 & R_x \\ R_y & -R_x & 0 \end{bmatrix} \tag{B.7}$$

$\mathbf{T}_a$ = the transformation matrix for attachment point a

x, y, z = coordinates of the attachment point with respect to the reference point

R_x, R_y, R_z = the x, y and z components of the tension in the mooring line at the attachment point

The last term in (B.6) calculates the change in moment generated by a constant force which is applied at the reference point where the structure is rotated.

When two structures are attached by a mooring line, this results in a fully-coupled stiffness matrix, where the displacement of structure m results in a force on the other structure n. This stiffness matrix may be obtained simply by considering that the displacement of the attachment point a on one structure is equivalent to a negative displacement of the attachment point b on the other structure. Similar to (B.6), the 12x12 stiffness matrix $\mathbf{C}_{line}$ becomes:

$$\mathbf{C}_{line} = \begin{bmatrix} \mathbf{I} \\ \mathbf{T}_a^\top \\ -\mathbf{I} \\ -\mathbf{T}_b^\top \end{bmatrix} [\mathbf{K}] \begin{bmatrix} \mathbf{I} & \mathbf{T}_a & -\mathbf{I} & -\mathbf{T}_b \end{bmatrix} + \cdots \begin{bmatrix} 0 & \cdots & 0 & 0 & \cdots & 0 \\ \vdots & \ddots & \vdots & \vdots & \ddots & \vdots \\ 0 & \cdots & \mathbf{R}_m\mathbf{T}_a^\top & 0 & \cdots & 0 \\ 0 & \cdots & 0 & 0 & \cdots & 0 \\ \vdots & \ddots & \vdots & \vdots & \ddots & \vdots \\ 0 & \cdots & 0 & 0 & \cdots & \mathbf{R}_m\mathbf{T}_a^\top \end{bmatrix} \tag{B.8}$$

With n_l cargo mooring lines attached between HTV and cargo the stiffness matrix in (B.2) becomes:

$$\begin{bmatrix} \mathbf{C_{moor}} + \mathbf{C_{1,1}} & 0 \\ 0 & \mathbf{C_{2,2}} \end{bmatrix} + \sum_{i=1}^{n_l} \mathbf{C}_{line,i} \tag{B.9}$$

B.2 Frequency Domain

The frequency-domain method is an efficient and fast approach for systematic parametric studies, where a large number of possible combinations of environmental conditions have to be investigated, different operational steps need to be analysed, or where optimization of the solution is desired. Only linear systems can be solved in frequency domain, which means that linearisation may be required. Linearisation should be done around the mean equilibrium position of the system, and may need to be applied to both the damping and stiffness matrices.

The general equation of motions for a linear dynamic system with n_b bodies in the frequency domain is solved by rewriting (B.1) to:

$$[-\omega^2(\mathbf{M}+\mathbf{A}) - i\omega\mathbf{B} + \mathbf{C}]\mathbf{X} = \tilde{\mathbf{F}}_\mathbf{w} \tag{B.10}$$

Where $\mathbf{M}$, $\mathbf{A}$, $\mathbf{B}$ and $\mathbf{C}$ being $6n_b \times 6n_b$ matrices for mass, added mass, damping and stiffness respectively, and $\tilde{\mathbf{F}}_\mathbf{w}$ being a $6n_b \times 1$ vector for external force are know entities, generally at the centres of gravity of the bodies.

Then, the response $\mathbf{X}$ being a $6n_b \times 1$ vector, referred to as the fully-coupled response amplitude operators (RAOs) at the centre of gravity of the bodies, is found by:

$$\mathbf{X} = \mathbf{H}\tilde{\mathbf{F}}_\mathbf{w} \tag{B.11}$$

with:

$$\mathbf{H} = [-\omega^2(\mathbf{M}+\mathbf{A}) - i\omega\mathbf{B} + \mathbf{C}]^{-1} \tag{B.12}$$

The external force $\tilde{\mathbf{F}}_\mathbf{w}$ consists only of the first order wave excitation force induced by a regular wave with unit amplitude, and the stiffness matrix includes both the hydrostatic and mechanical stiffness components like the stiffness due to mooring lines (see Appendix B.1.3) and articulations.

Sometimes quadratic damping is included in dynamic systems. Equation (B.1) may then be extended to:

$$(\mathbf{M}+\mathbf{A})\ddot{\tilde{x}} + \mathbf{B}\dot{\tilde{x}} + \mathbf{B}^*|\dot{\tilde{x}}|\dot{\tilde{x}} + \mathbf{C}\tilde{x} = \tilde{\mathbf{F}}_\mathbf{w} \tag{B.13}$$

To solve this system in frequency-domain, linearisation of the quadratic term is required. This is done through replacing the absolute velocity term by an estimated value. Iteratively, determining the response for a specific sea-state is then matched to this value by changing it after each iteration. This approach is often used to predict roll motion governed by non-linear roll damping.

The stiffness matrix for a system with bodies connected by mooring is presented by (B.8) and the right term of (B.9). Linearisation is done by using the tension and line-stiffness values from (B.3) and (B.4) at mean extension e.

Similarly, the PID controller of the LTAS presented in Figure 6.8 can partly be included in the frequency-domain equations. The proportional term P is included in the stiffness matrix. The derivative term D is included in the damping matrix. Although the integral term contributes to stiffness in the system, it is assumed that the contribution to the stiffness is low compared to the proportional term. Therefore, the integrator term is ignored in the frequency-domain equation. As the PID control force is based on relative motions between the reference locations at a distance from the body centres of gravity, transformation of the unknown response $\mathbf{X}$ is needed. And, as the required force is allocated to line tension at the connections of the LTAS, a transformation the the centre of effort is required. The latter is problematic as the allocation does not account for the vertical force, the roll moment and the pitch moment. Due to relative vertical motions, a vertical force will exist as the actuator connections will be out of plane. The roll and pitch moments will be non-zero as the centre of effort is not at the reference locations. Furthermore, the vertical centre of effort is not exactly known due to the complexity of the actuator configuration and allocation. Therefore, the centre of effort is assumed at an average height above the reference locations.

The stiffness matrix for PID control becomes:

$$\mathbf{C}_{\text{PID}} = \begin{bmatrix} \mathbf{I} & 0 & 0 & 0 \\ \mathbf{T}_{m,1}^{\top} & \mathbf{I} & 0 & 0 \\ 0 & 0 & \mathbf{I} & 0 \\ 0 & 0 & \mathbf{T}_{m,2}^{\top} & \mathbf{I} \end{bmatrix} \begin{bmatrix} \mathbf{P} & -\mathbf{P} \\ -\mathbf{P} & \mathbf{P} \end{bmatrix} \begin{bmatrix} \mathbf{I} & \mathbf{T}_{r,1} & 0 & 0 \\ 0 & \mathbf{I} & 0 & 0 \\ 0 & 0 & \mathbf{I} & \mathbf{T}_{r,2} \\ 0 & 0 & 0 & \mathbf{I} \end{bmatrix} \tag{B.14}$$

where:

$$\begin{aligned}
\mathbf{P} &= \text{diag}(P_x, P_y, 0, 0, 0, P_\psi) \\
\mathbf{T}_{r,ib} &= \text{the transformation matrix for reference point of body } ib \\
\mathbf{T}_{m,ib} &= \text{the transformation matrix for centre of effort on body } ib \\
P_x, P_y, P_\psi &= \text{the proportional terms for surge, sway and yaw}
\end{aligned}$$

Similarly, the damping matrix $\mathbf{B}_{\text{PID}}$ is found by replacing $\mathbf{P}$ by $\mathbf{D} = \text{diag}(D_x, D_y, 0, 0, 0, D_\psi)$.

B.3 Time Domain

If the external force $\mathbf{F}(t)$ in a time domain analysis is not periodic with constant amplitude, the equation of motion in the frequency domain (B.10) cannot be directly converted into the following form in the time domain:

$$(\mathbf{M} + \mathbf{A})\ddot{\mathbf{X}}(t) + \mathbf{B}\dot{\mathbf{X}}(t) + \mathbf{C}\mathbf{X}(t) = \mathbf{F}(t) \tag{B.15}$$

This is caused by the added mass in the mass matrix $\mathbf{A}$ and the hydrodynamic damping in the damping matrix $\mathbf{B}$ being frequency dependent.

The external force $\mathbf{F}(t)$ may consist of constant and time-varying excitation and reaction forces, like:

- the time-varying first order wave load $\tilde{\mathbf{F}}_{\mathbf{w}}(t)$,
- the mean and time-varying second order wave drift load $\tilde{\mathbf{F}}_{\mathbf{d}}(t)$,
- the current and wind drag force, where current and wind velocity may be time-varying and relative with respect to the body motions,
- mooring and articulation reaction forces.
- any other (user-defined) external force.

The time-domain approach using the convolution theorem is the most appropriate method (Cummins [7] and Ogilvie [27]) when the non-linear loads have a significant influence. With the convolution theorem, the frequency dependent hydrodynamic characteristics are accounted for appropriately. The well-known general motion equation in time domain with convolution

has the following expression:

$$\{\mathbf{M}+\mathbf{A}_{\infty}\}\ddot{\mathbf{X}}(t)+\mathbf{b}\dot{\mathbf{X}}(t)+\mathbf{C}\mathbf{X}(t)+\int_0^t \mathbf{H}(t-\tau)\dot{\mathbf{X}}(\tau)d\tau=\mathbf{F}(t) \quad \text{(B.16)}$$

The radiation force is expressed as the convolution form, in which $\mathbf{H}(t-\tau)$ is the Convolution Integral Function (CIF):

$$\mathbf{H}(t)=\frac{2}{\pi}\int_0^{\infty}\mathbf{B}(\omega)\cos(\omega t)d\omega=\frac{2}{\pi}\int_0^{\infty}\{\mathbf{A}(\omega)-\mathbf{A}_{\infty}\}\frac{\sin(\omega t)}{\omega}d\omega \quad \text{(B.17)}$$

Generally, the values of the added damping coefficients at zero frequency and infinite frequency are null. It is therefore more practical to use the added damping coefficient matrix in (B.17) to obtain the required impulse response function matrix.

Wave-drift damping, resulting from low-frequency oscillatory motions of a floating body in the presence of an incident wave field, can be included in the sampling matrix **b**. The relevance of wave-drift damping was suggested in an experimental study by Wichers and van Sluijs [37].

APPENDIX C

Investigating the Gap Flow Phenomenon

C.1 Squeeze Flow Tests

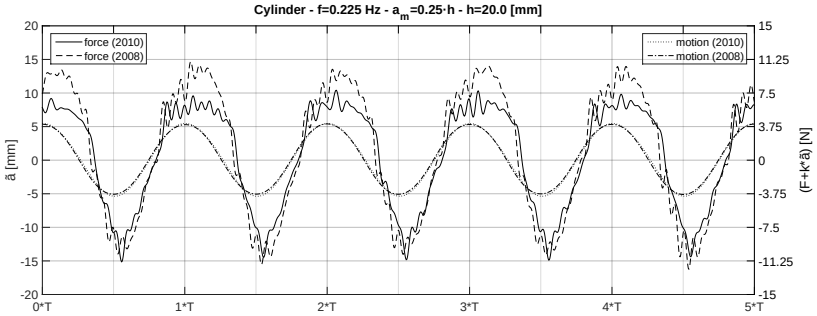

(a)

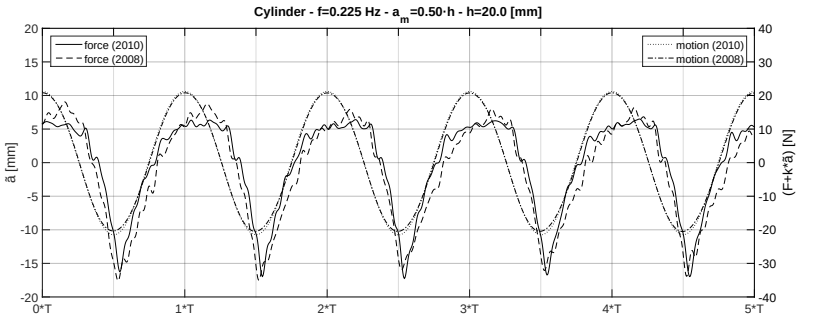

(b)

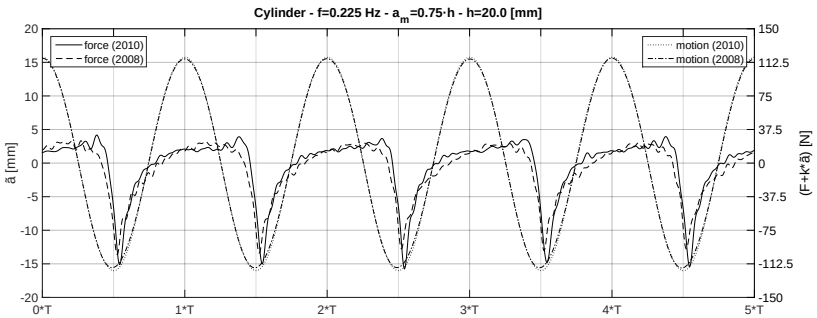

(c)

Figure C.1: Comparison 2008 and 2010, f=0.225 Hz

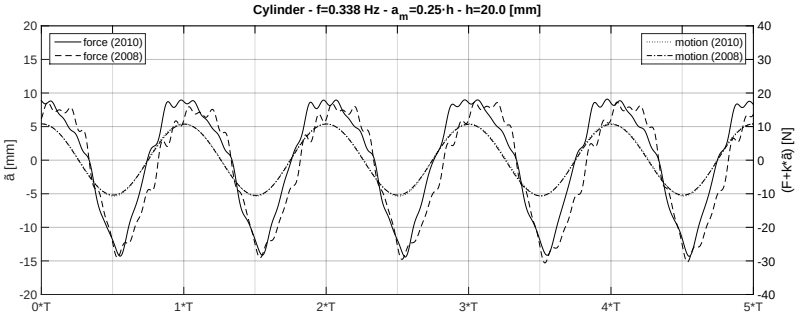

(a)

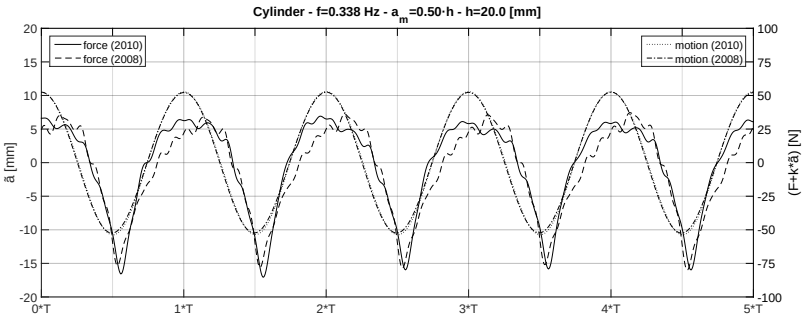

(b)

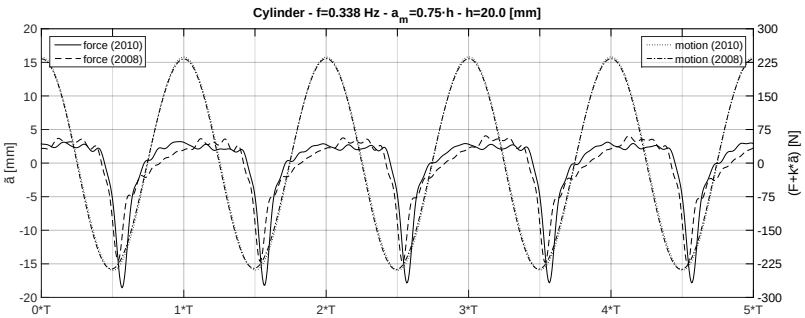

(c)

Figure C.2: Comparison 2008 and 2010, f=0.338 Hz

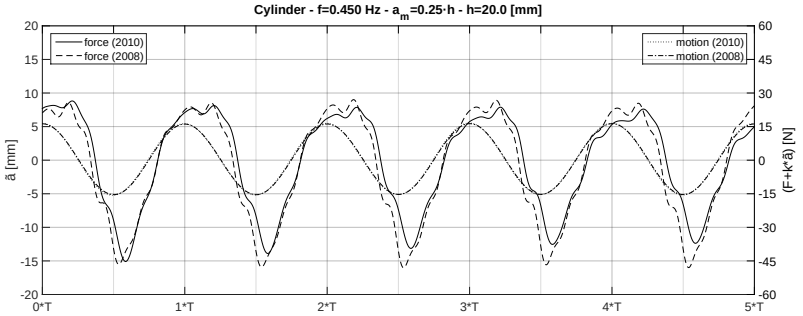

(a)

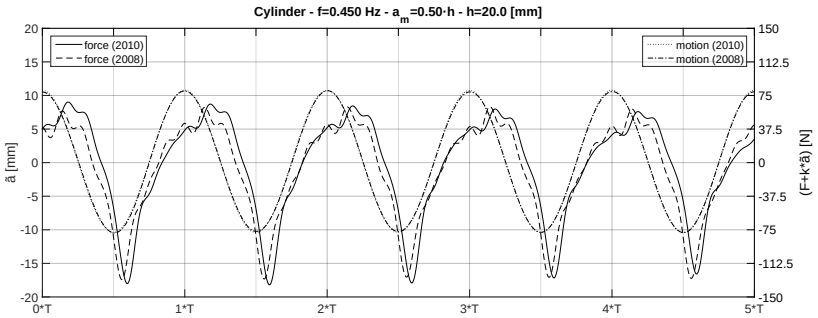

(b)

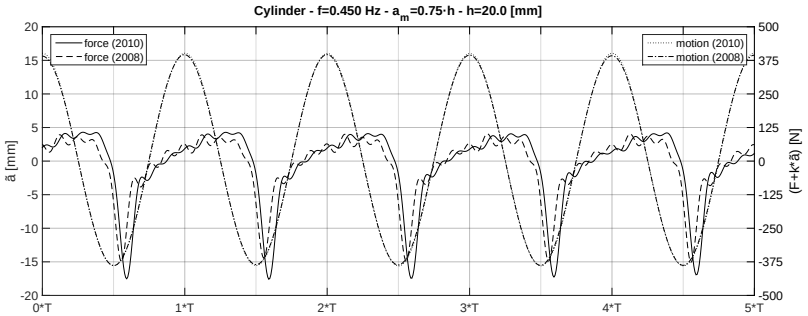

(c)

Figure C.3: Comparison 2008 and 2010, f=0.445 Hz

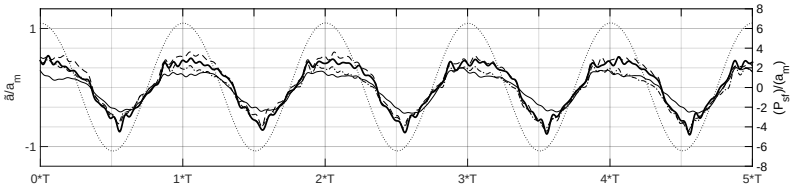

(a) f=0.225 [Hz]

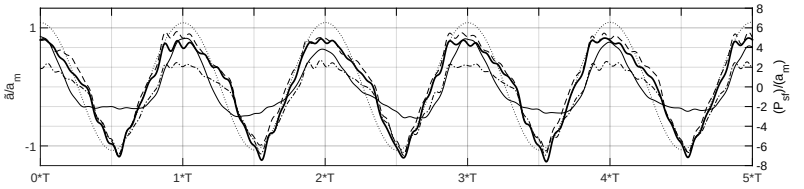

(b) f=0.281 [Hz]

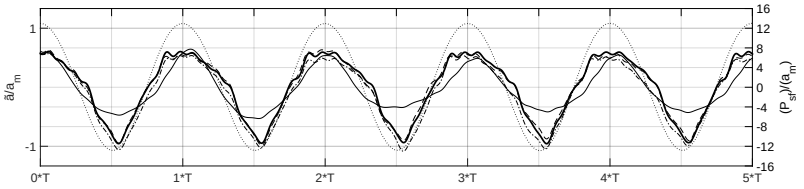

(c) f=0.338 [Hz]

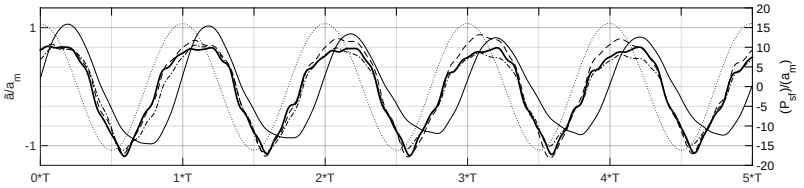

(d) f=0.394 [Hz]

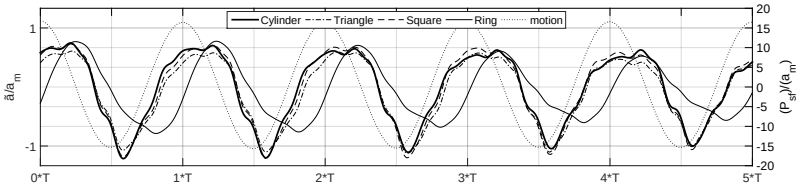

(e) f=0.450 [Hz]

Figure C.4: Shape comparison, $a_m = 5$ [mm], $h = 20$ [mm] (2010)

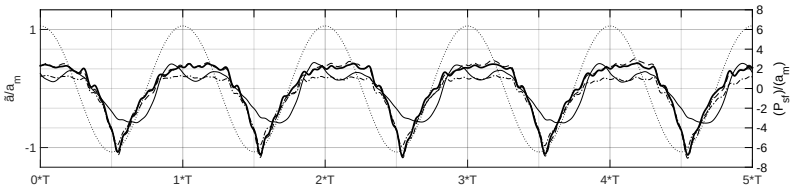

(a) f=0.225 [Hz]

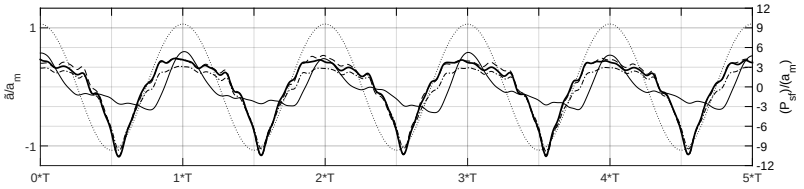

(b) f=0.281 [Hz]

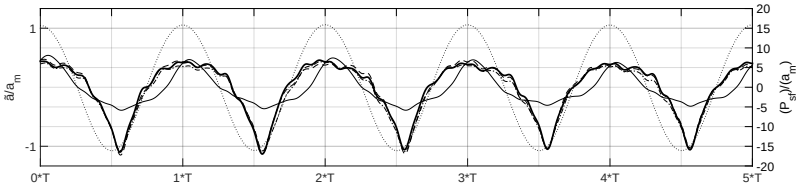

(c) f=0.338 [Hz]

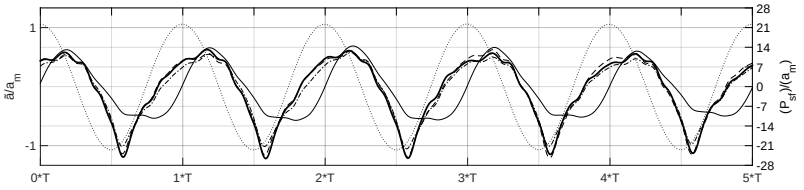

(d) f=0.394 [Hz]

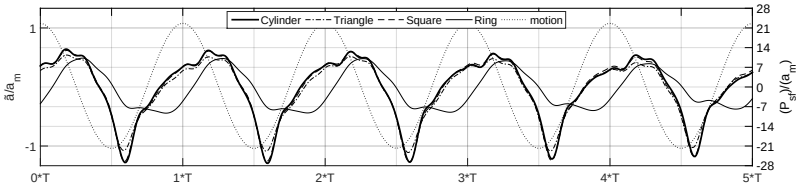

(e) f=0.450 [Hz]

Figure C.5: Shape comparison, $a_m = 10$ [mm], $h = 20$ [mm] (2010)

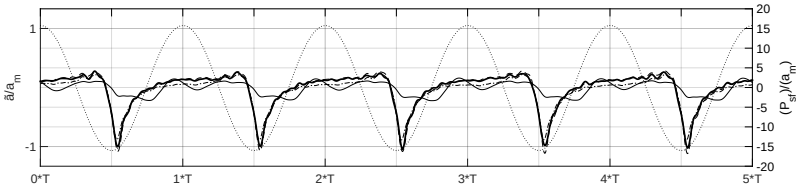

(a) f=0.225 [Hz]

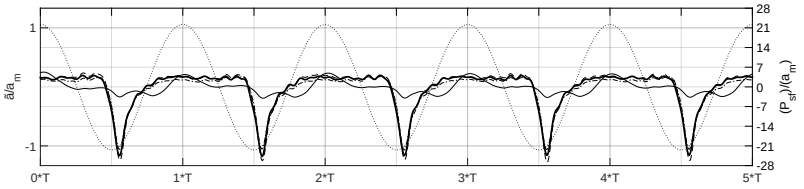

(b) f=0.281 [Hz]

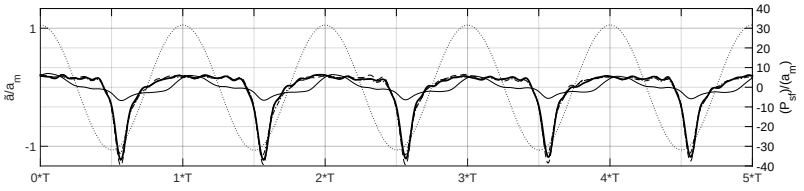

(c) f=0.338 [Hz]

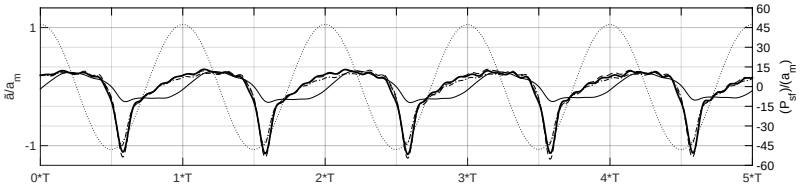

(d) f=0.394 [Hz]

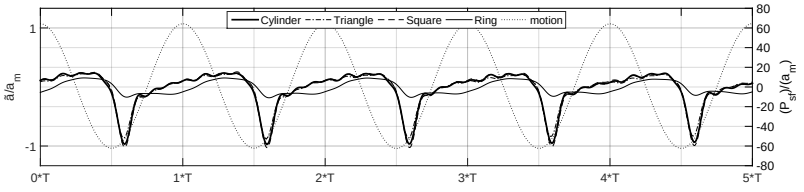

(e) f=0.450 [Hz]

Figure C.6: Shape comparison, $a_m = 15$ [mm], $h = 20$ [mm] (2010)

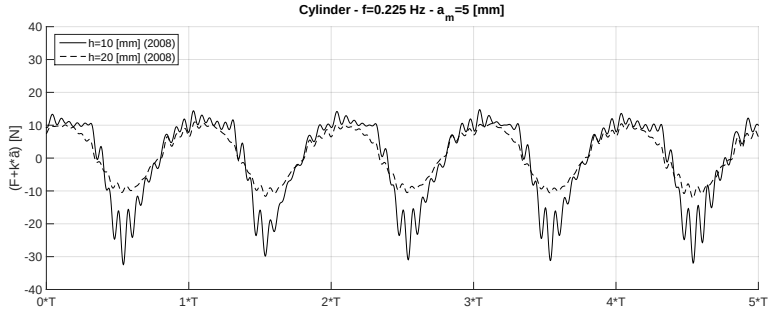

(a)

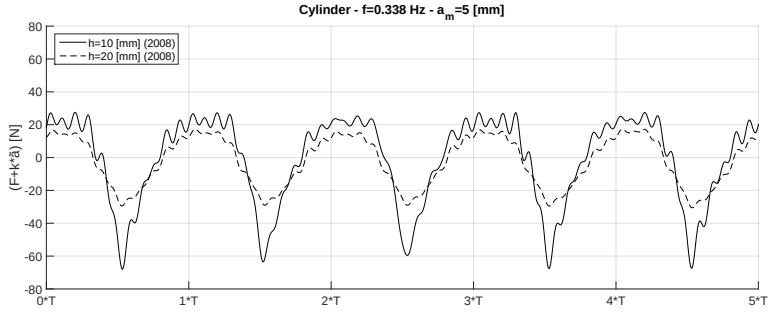

(b)

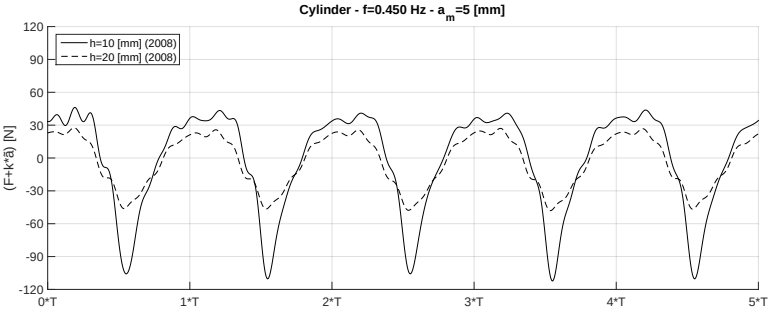

(c)

Figure C.7: Influence gap height h (2008)

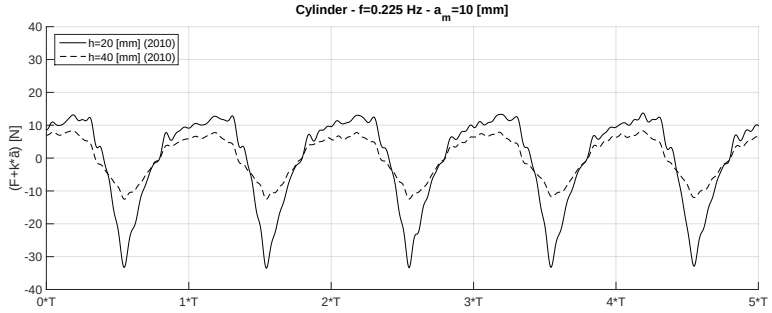

(a)

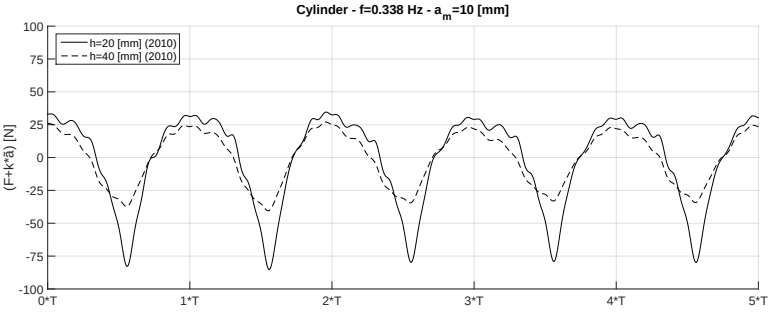

(b)

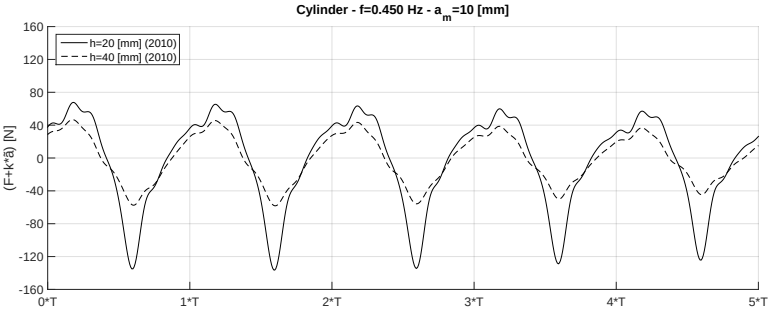

(c)

Figure C.8: Influence gap height h (2010)

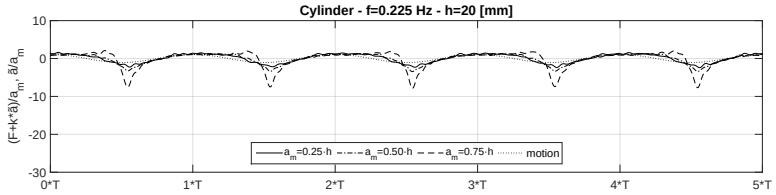

(a)

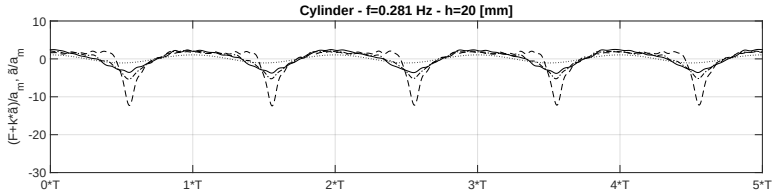

(b)

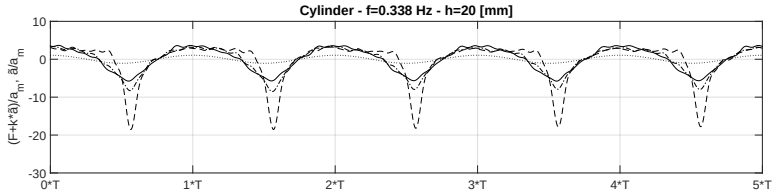

(c)

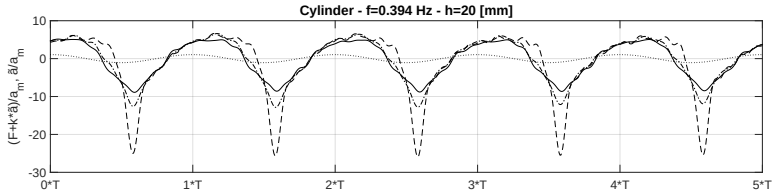

(d)

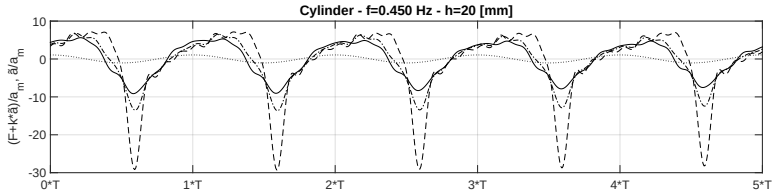

(e)

Figure C.9: Influence amplitude a_m at gap height $h = 20$ [mm](2010)

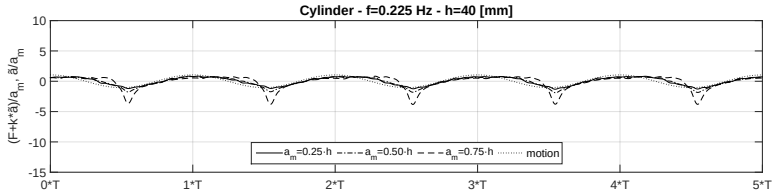

(a)

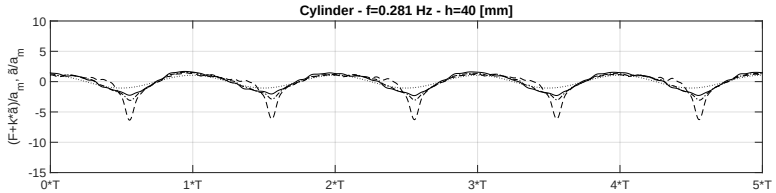

(b)

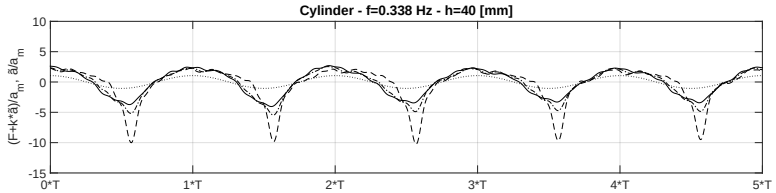

(c)

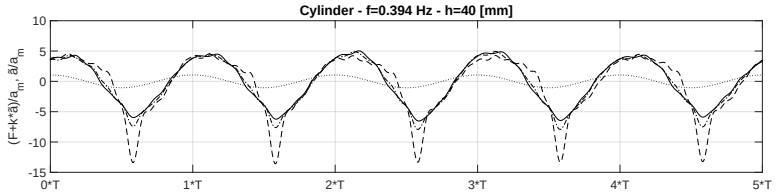

(d)

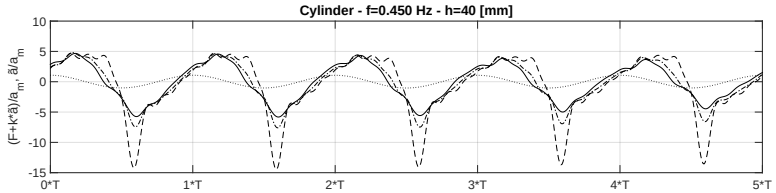

(e)

Figure C.10: Influence amplitude a_m at gap height $h = 40$ [mm](2010)

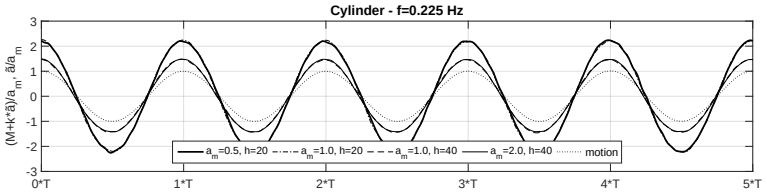

(a)

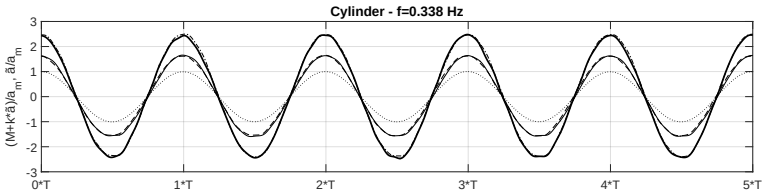

(b)

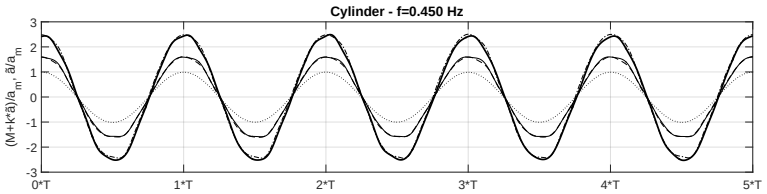

(c)

Figure C.11: Pitch oscillation results - Cylinder

C.2 Squeeze Flow CFD Analysis

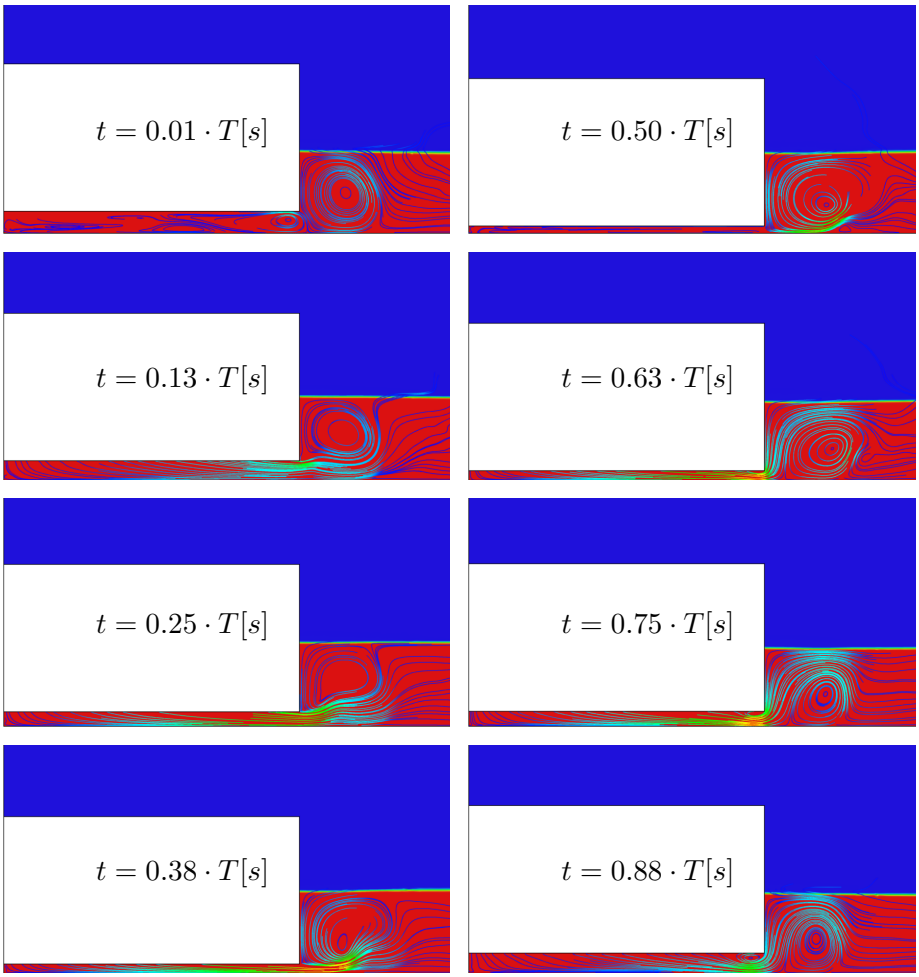

Figure C.12: CFD streamlines - reference simulation

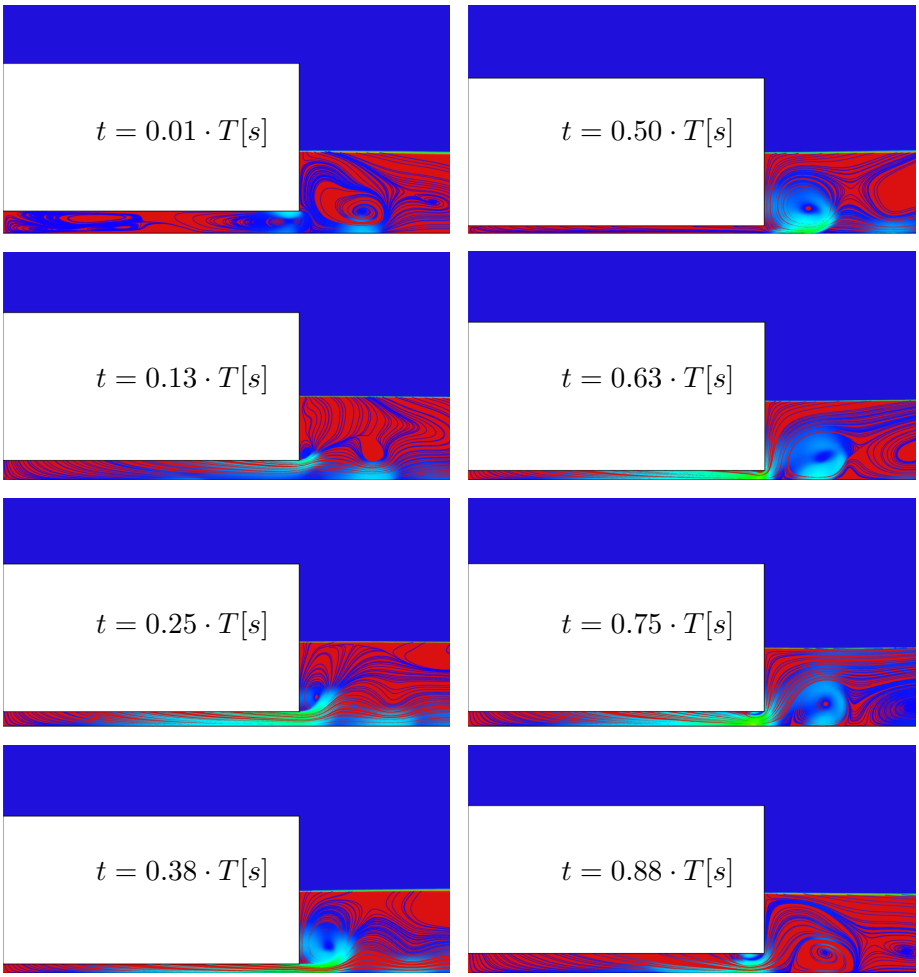

Figure C.13: CFD streamlines - full scale simulation

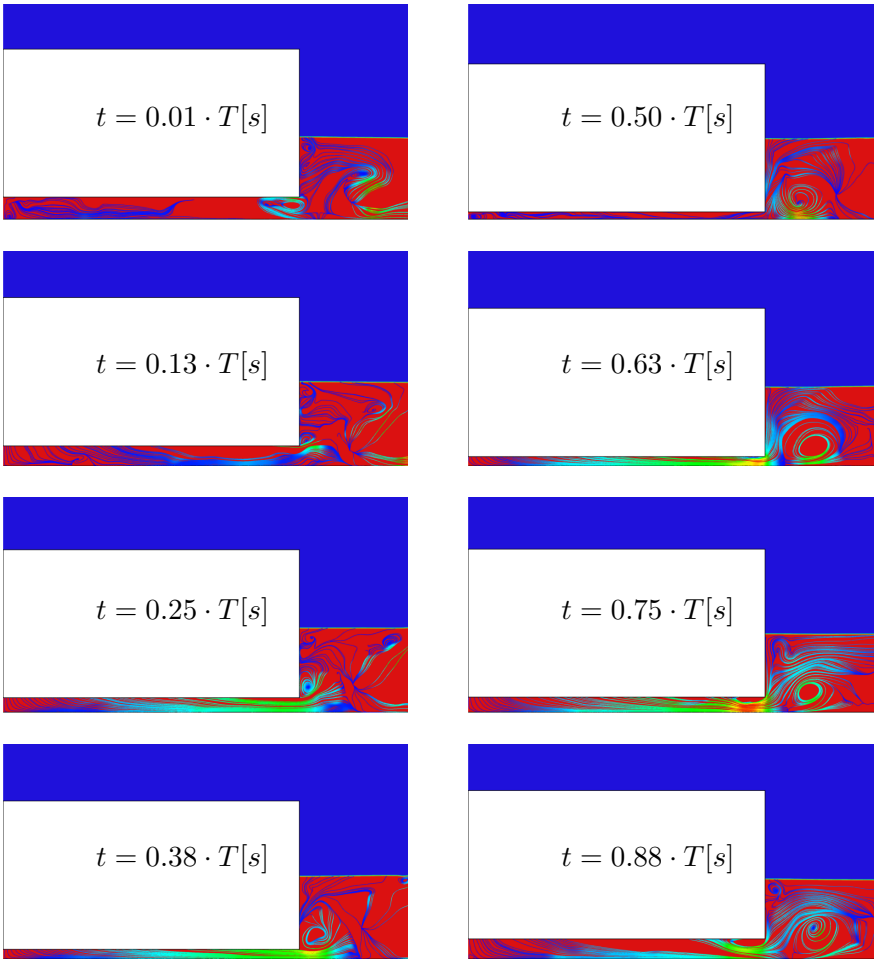

Figure C.14: CFD streamlines - Euler simulation

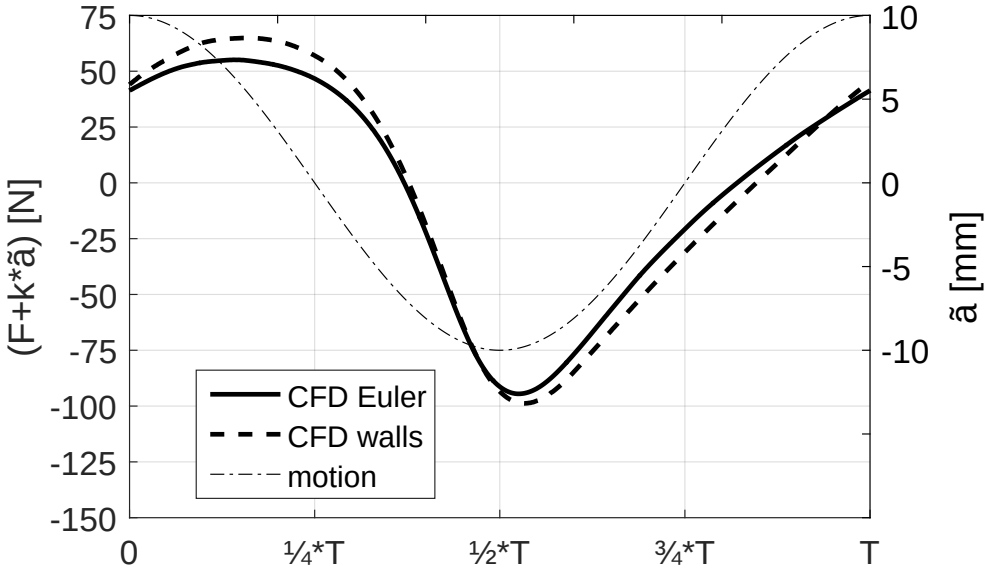

Figure C.15: Comparison effort Euler case vs. wall effect case

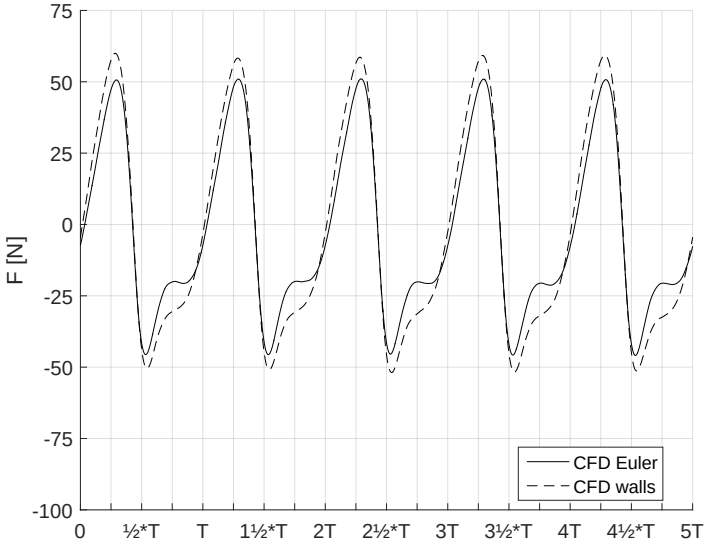

(a) CFD

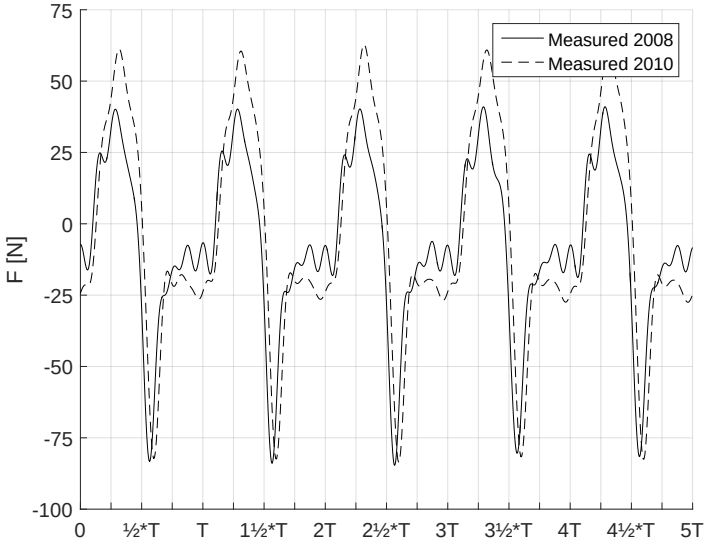

(b) Measured

Figure C.16: Wall effect

C.3 Measurement versus Analytical

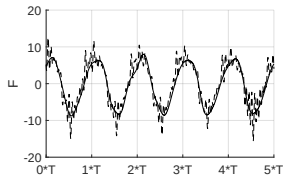

(a) $f = 0.225\text{Hz} a_m = 0.25h$

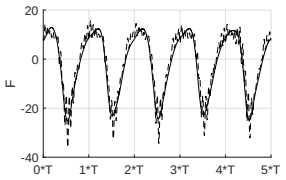

(b) $f = 0.225\text{Hz} a_m = 0.50h$

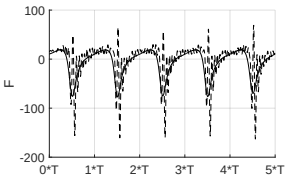

(c) $f = 0.225\text{Hz} a_m = 0.75h$

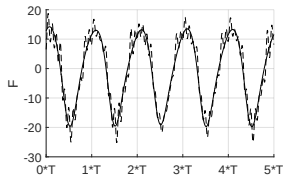

(d) $f = 0.338\text{Hz} a_m = 0.25h$

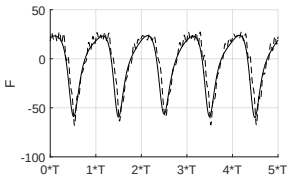

(e) $f = 0.338\text{Hz} a_m = 0.50h$

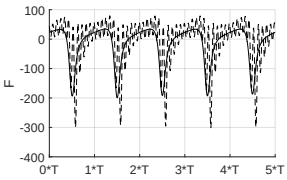

(f) $f = 0.338\text{Hz} a_m = 0.75h$

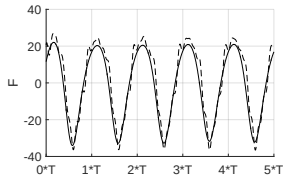

(g) $f = 0.450\text{Hz} a_m = 0.25h$

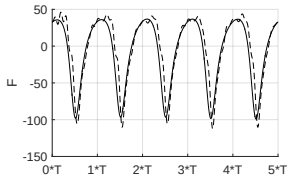

(h) $f = 0.450\text{Hz} a_m = 0.50h$

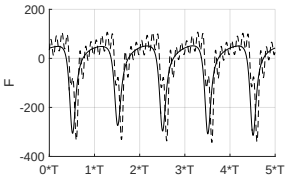

(i) $f = 0.450\text{Hz} a_m = 0.75h$

Figure C.17: Comparison Molin(—) vs. measured(2008)(- -), $h = 10[mm]$

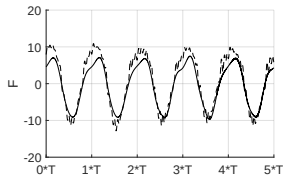

(a) $f = 0.225\text{Hz} a_m = 0.50h$

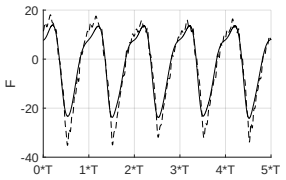

(b) $f = 0.225\text{Hz} a_m = 0.50h$

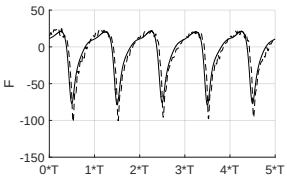

(c) $f = 0.225\text{Hz} a_m = 0.75h$

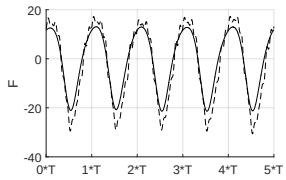

(d) $f = 0.338\text{Hz} a_m = 0.25h$

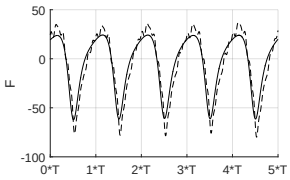

(e) $f = 0.338\text{Hz} a_m = 0.50h$

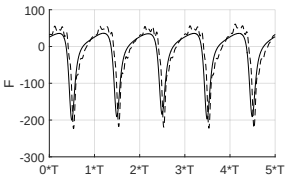

(f) $f = 0.338\text{Hz} a_m = 0.75h$

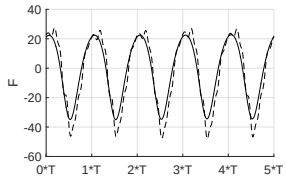

(g) $f = 0.450\text{Hz} a_m = 0.25h$

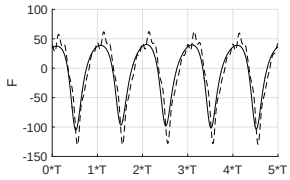

(h) $f = 0.450\text{Hz} a_m = 0.50h$

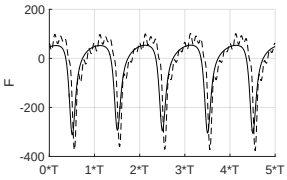

(i) $f = 0.450\text{Hz} a_m = 0.75h$

Figure C.18: Comparison Molin(—) vs. measured(2008)(- -), $h = 20[mm]$

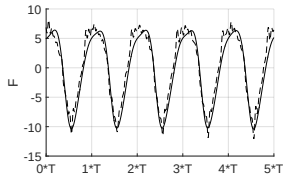

(a) $f = 0.225\text{Hz} a_m = 0.25h$

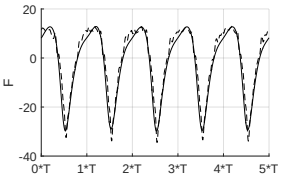

(b) $f = 0.225\text{Hz} a_m = 0.50h$

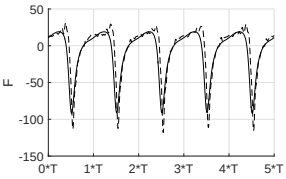

(c) $f = 0.225\text{Hz} a_m = 0.75h$

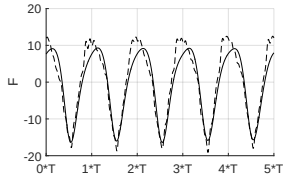

(d) $f = 0.281\text{Hz} a_m = 0.25h$

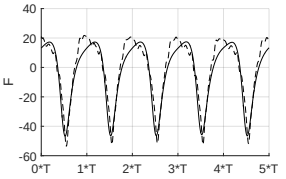

(e) $f = 0.281\text{Hz} a_m = 0.50h$

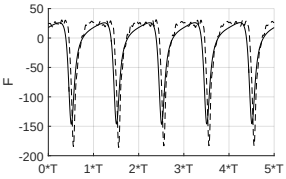

(f) $f = 0.281\text{Hz} a_m = 0.75h$

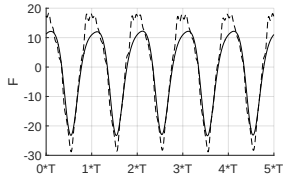

(g) $f = 0.338\text{Hz} a_m = 0.25h$

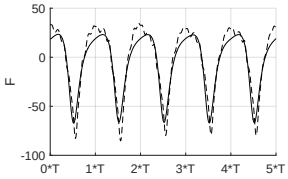

(h) $f = 0.338\text{Hz} a_m = 0.50h$

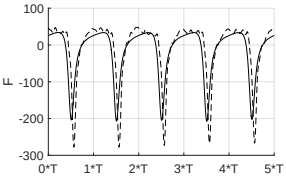

(i) $f = 0.338\text{Hz} a_m = 0.75h$

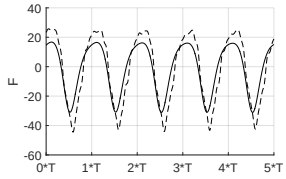

(j) $f = 0.394\text{Hz} a_m = 0.25h$

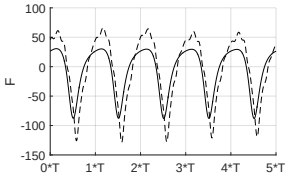

(k) $f = 0.394\text{Hz} a_m = 0.50h$

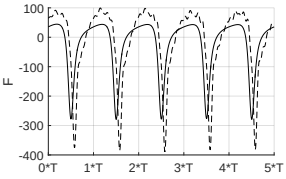

(l) $f = 0.394\text{Hz} a_m = 0.75h$

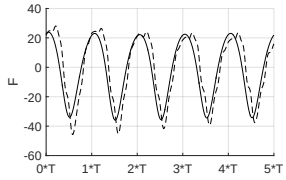

(m) $f = 0.450\text{Hz} a_m = 0.25h$

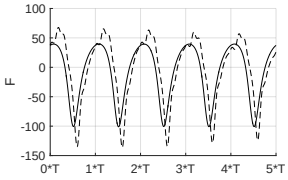

(n) $f = 0.450\text{Hz} a_m = 0.50h$

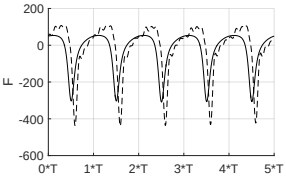

(o) $f = 0.450\text{Hz} a_m = 0.75h$

Figure C.19: Comparison Molin(—) vs. measured(2010)(- -), $h = 20[mm]$

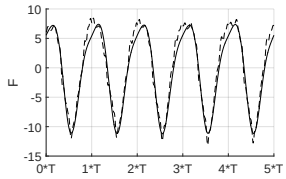

(a) $f = 0.225\text{Hz} a_m = 0.25h$

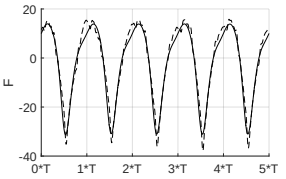

(b) $f = 0.225\text{Hz} a_m = 0.50h$

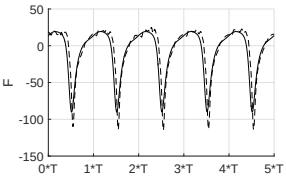

(c) $f = 0.225\text{Hz} a_m = 0.75h$

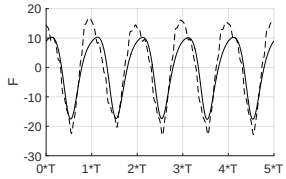

(d) $f = 0.281\text{Hz} a_m = 0.25h$

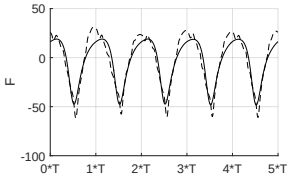

(e) $f = 0.281\text{Hz} a_m = 0.50h$

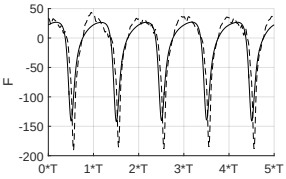

(f) $f = 0.281\text{Hz} a_m = 0.75h$

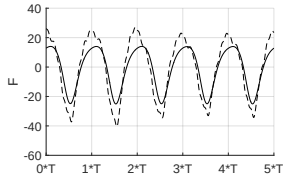

(g) $f = 0.338\text{Hz} a_m = 0.25h$

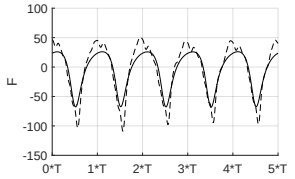

(h) $f = 0.338\text{Hz} a_m = 0.50h$

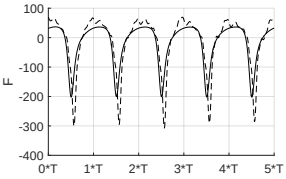

(i) $f = 0.338\text{Hz} a_m = 0.75h$

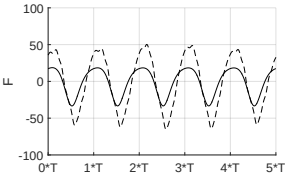

(j) $f = 0.394\text{Hz} a_m = 0.25h$

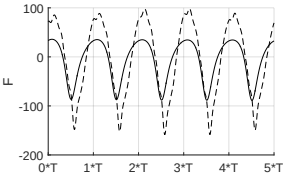

(k) $f = 0.394\text{Hz} a_m = 0.50h$

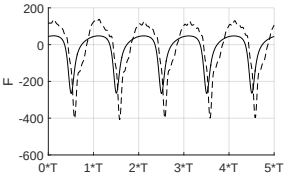

(l) $f = 0.394\text{Hz} a_m = 0.75h$

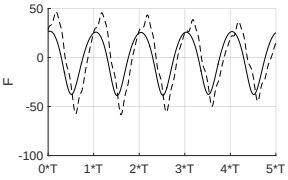

(m) $f = 0.450\text{Hz} a_m = 0.25h$

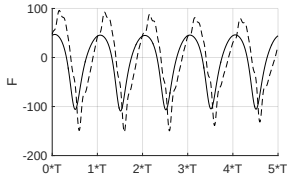

(n) $f = 0.450\text{Hz} a_m = 0.50h$

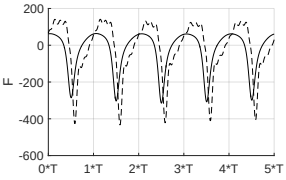

(o) $f = 0.450\text{Hz} a_m = 0.75h$

Figure C.20: Comparison Molin(—) vs. measured(2010)(- -), $h = 40[mm]$

APPENDIX D

Model Test

Submerged HTV with Cargo and Passive Cargo Handling System

In 2011, a model test campaign with the Type-0 HTV and a 110,000-t ring-shape semi-submersible were executed. The model set-up is shown in Figure D.1. The model tests consisted of:

A. submerged HTV without cargo

B. submerged HTV with centred cargo at 1 [m] deck clearance

C. submerged HTV with centred cargo at 2 [m] deck clearance

D. submerged HTV with shifted cargo at 2 [m] deck clearance

Configurations B and C represented the ballasting stage (two gap heights were used, 1 [m] and 2 [m] respectively), configuration D represented shifting the cargo sideways. Test in head, quartering and beam seas were carried out. The target operational limit were wind seas up to $H_s = 2.0$ [m] or swell condition up to $H_s = 1.0$ [m]. Figure D.2 shows the sea-states used during the model tests; data is provided in Table D.1.

The following observations were made:

1. The relative motions are calculated based on post-processing the measured motions of the separate bodies. The processed relative vertical motions proofed to be much larger than visually observed and physically possible. An attempt was made to register impacts through voltage-contact. However, assessment of impact was most clear by investigating the cargo vertical acceleration measurement

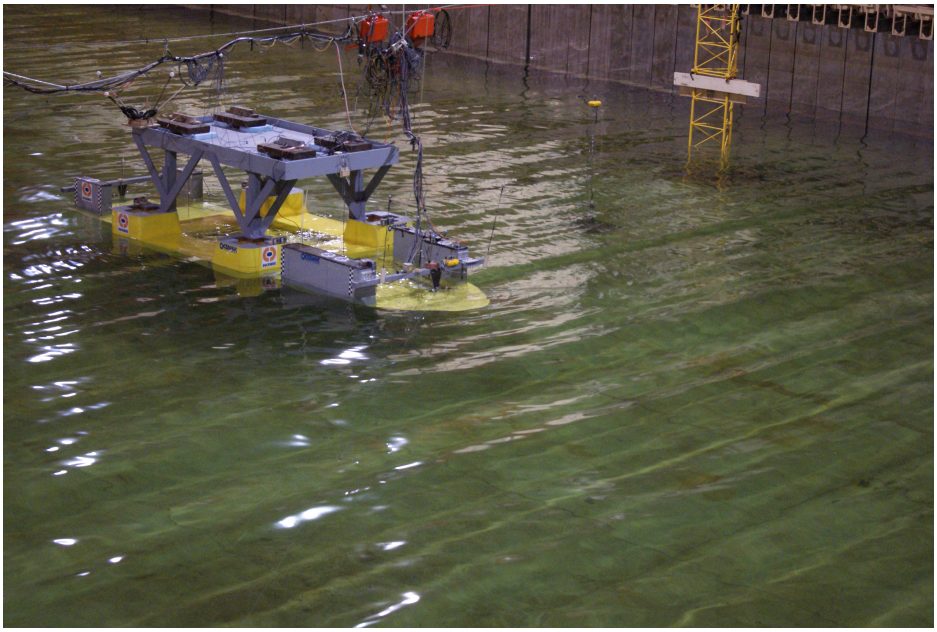

Figure D.1: Model test set-up

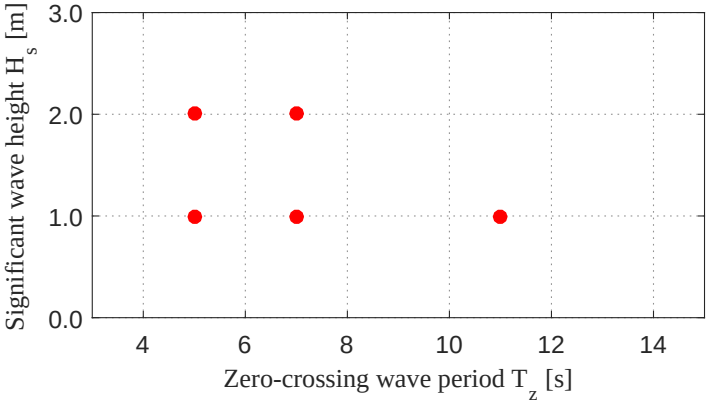

Figure D.2: Target operational limit

(see Figure D.3); these signals clearly showed impact events. The vertical motion signals were difficult to correlate with the assessment of impacts. Explanation could be:

- poor accuracy of the measurement, especially for roll and pitch motion; as the reference locations are at large distance from the measurement location, the error may become large.
- uncertainty in the actual initial draft and trim of both bodies, throughout the test the draft seemed to have changed, however trim and heel were reset to zero at start of each test.

Examples of the signal of the cargo accelerometer and the relative motions are shown in Figure D.4. The accelerometer signal clearly indicate the impact events. The figures clearly show large zero overshoots. Still, some events may not have been registered when impact velocity was low.

2. The ring-semi showed an increase in draft (i.e. set-down) due to waves flowing over the pontoon deck. Maximum set-down was as much as 0.5 [m] in $H_s = 2.0$ [m]. Even with such level of set-down, a 2.0 [m] clearance (as per configuration C and D) was enough to avoid impacts for the target operational limit.

3. The tests show that — although mooring loads were in a realistic range — optimization of the cargo handling system is needed. Main issue is that, with the standard equipment on board of the HTV, the possible pretension in the cargo handling lines is low relative to the maximum line loads. As a result, slack in the lines existed and as a reaction large peak loading and large motions occurred. In reality part of the slack may be reduced by winching in the lines, however timely holding on static brake is needed, which is risky during manual handling of the winches.

The relative horizontal motion at reference locations MP1 to MP4 (at the four corners of the HTV deck and Cargo bottom intersection) are shown in Figure D.5 to D.19. The ellipses are based on 1.7 times the significant relative surge and sway motion, which approximately represents the expected 1-hour extreme footprint. The plots for the wave condition Z show that larger horizontal oscillation occur than may be expected from comparison with condition W, where based on the assumption of linear

Table D.1: Model test sea-states

	Hs	Tp	Tz	type
V	1.0	7.0	5.4	Pierson Moskowitz
W	1.0	9.9	7.7	Pierson Moskowitz
X	1.0	14.1	11.0	JONSWAP
Y	2.0	7.0	5.4	Pierson Moskowitz
Z	2.0	9.9	7.7	Pierson Moskowitz

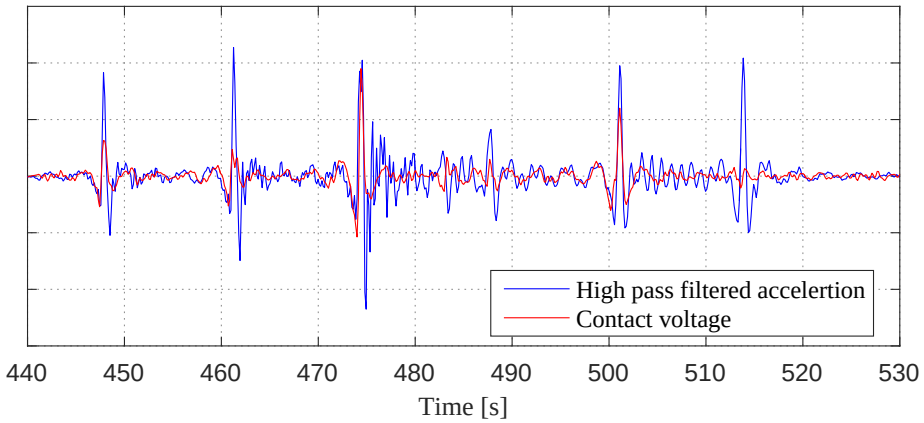

Figure D.3: Contact registration

relation with wave height only a factor 2 is expected. This is explained by the non-linear effect of the continues slacking of the cargo handling lines. Furthermore, tests BBS-Z, BQS-Z and BHS-X show large overshoot of the footprint. Partly, this is explained by the slacking of the cargo handling lines, however it is also caused by impact events prior to the overshoot events.

An attempt was made to reproduce the model test using the time-domain software ANSYS-AQWA. Reproduction is done by using the measured wave registration of the model tests. Furthermore, mass properties and mooring properties from the model tests were used. Initial calculations showed numerical instability, which seemed related to the complex hydrodynamic interaction and the difficulty to establish an accurate convolution integral function for all (i.e. 2 times 6 by 6) added mass or radiation damping terms. Furthermore, it is important to realize that hull and viscous drag effects were ignored in the simulations. To account for these effects, to overcome numeric instability and to tune the results, frequency independent damping — only for the (2 times 6) main diagonal terms — have been added. It must be noted that the main focus of the reproduction is on the horizontal relative motions, and that vertical relative motions may be larger than the clearance. So, physical impact was not modelled, and thus it's possible effect on the horizontal motions is not included in the simulations. The tuning is done by comparing significant amplitude motions of relevant signals, see Figure D.20 to D.25.

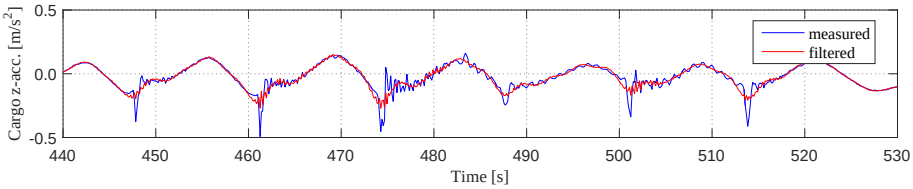

(a) Heave acceleration

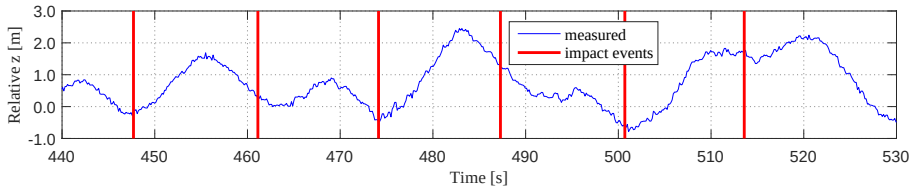

(b) Heave motion MP1

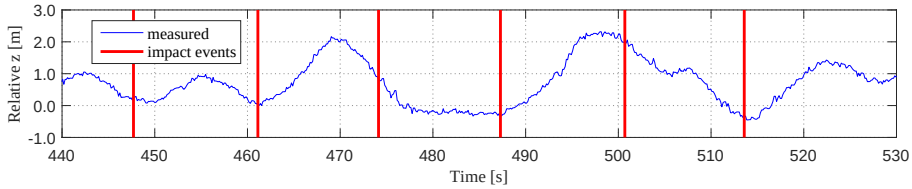

(c) Heave motion MP2

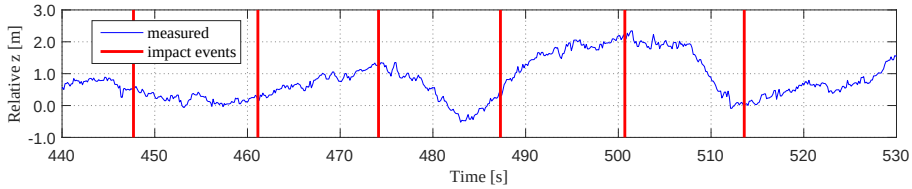

(d) Heave motion MP3

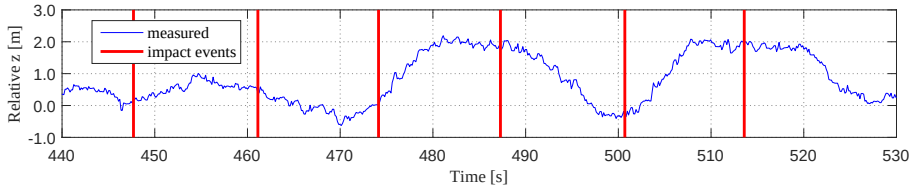

(e) Heave motion MP4

Figure D.4: Impact registration

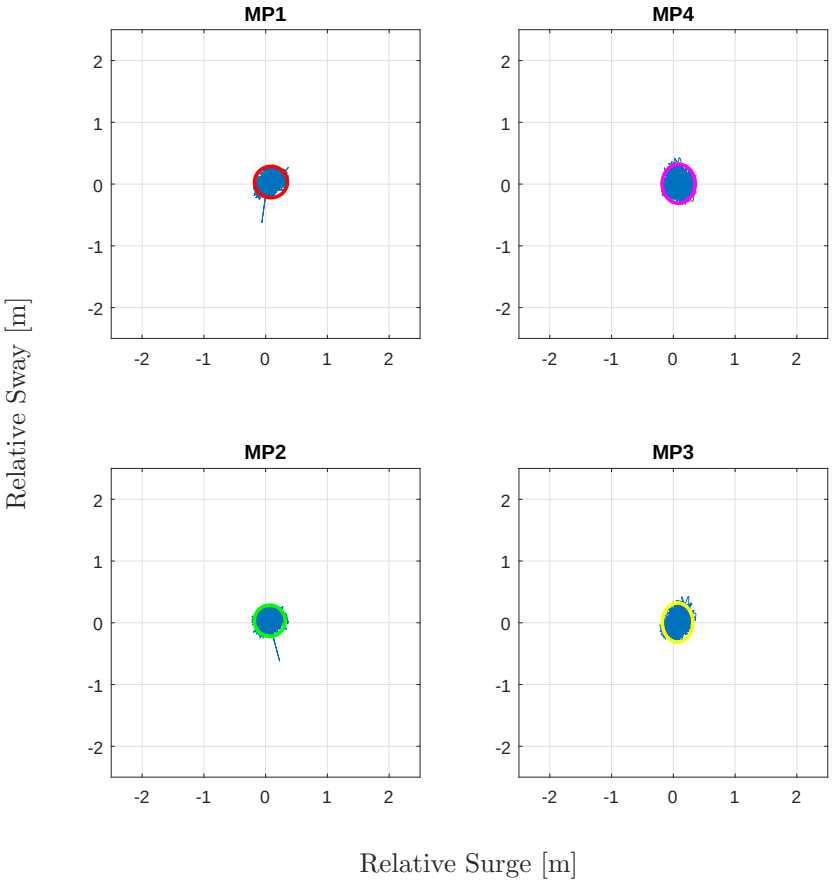

Figure D.5: Motion at reference points - beam sea - BBS-V-001

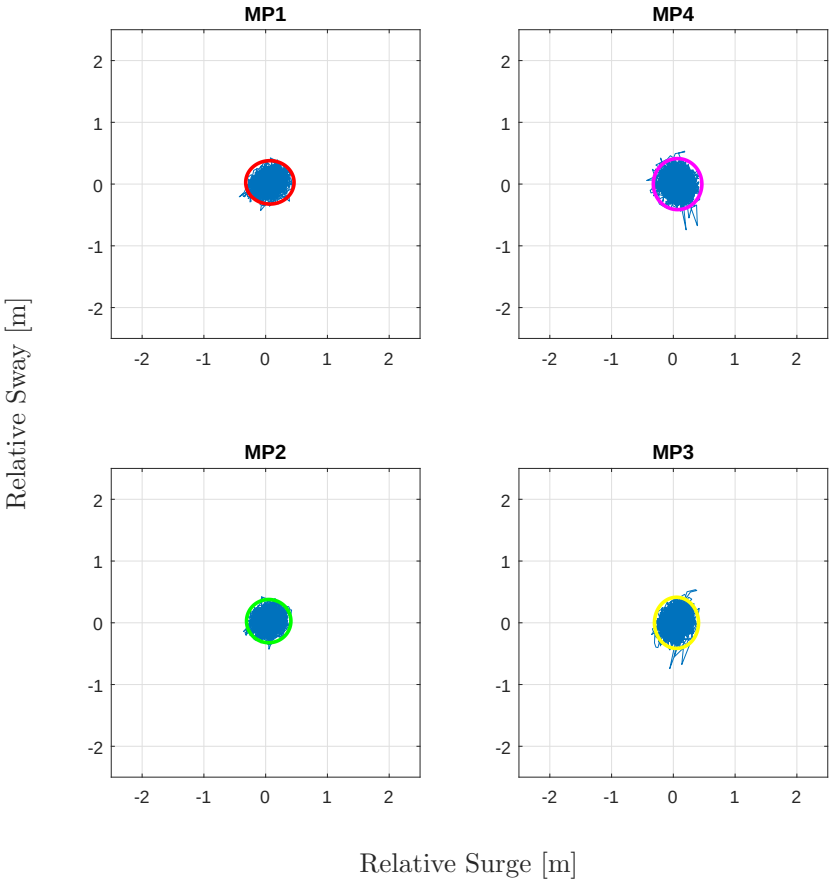

Figure D.6: Motion at reference points - beam sea - BBS-W-001

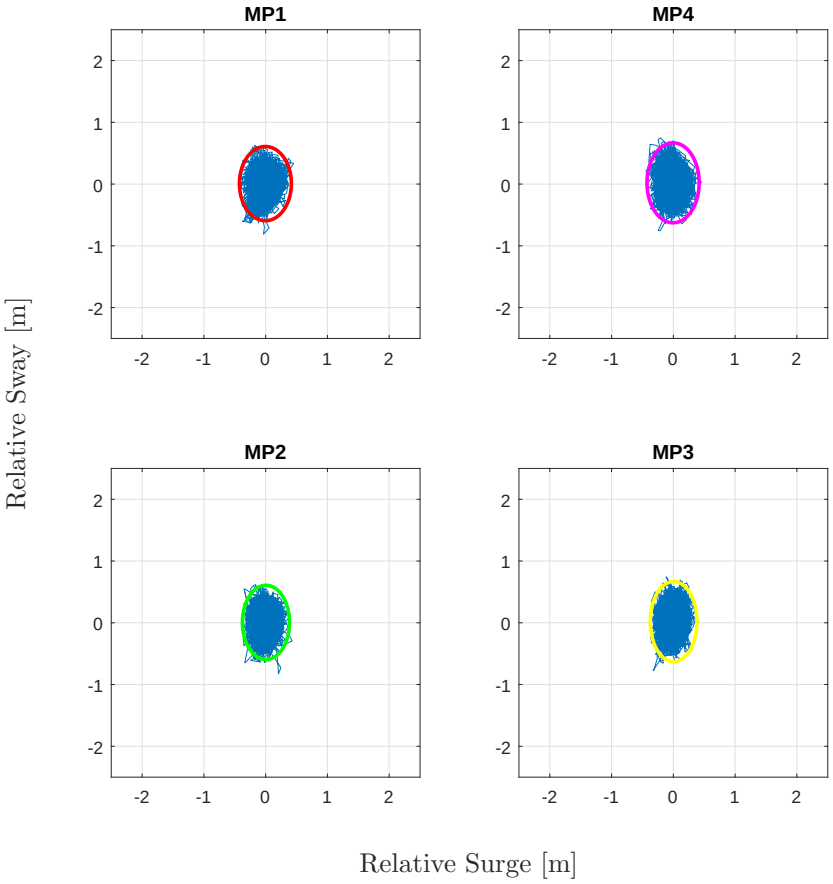

Figure D.7: Motion at reference points - beam sea - BBS-X-001

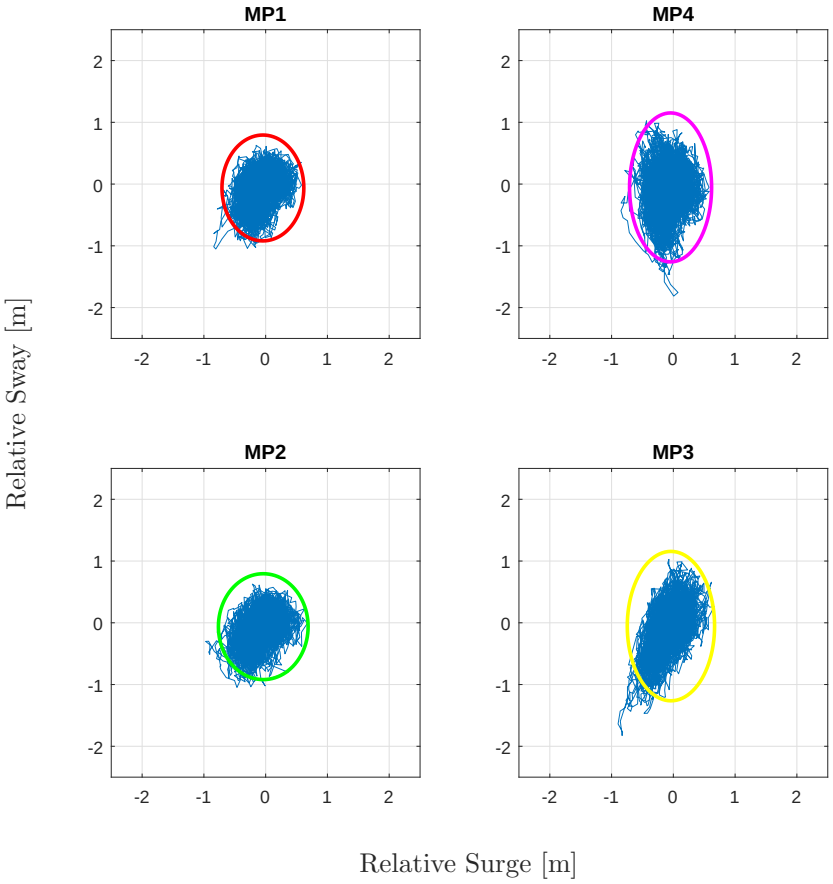

Figure D.8: Motion at reference points - beam sea - BBS-Y-001

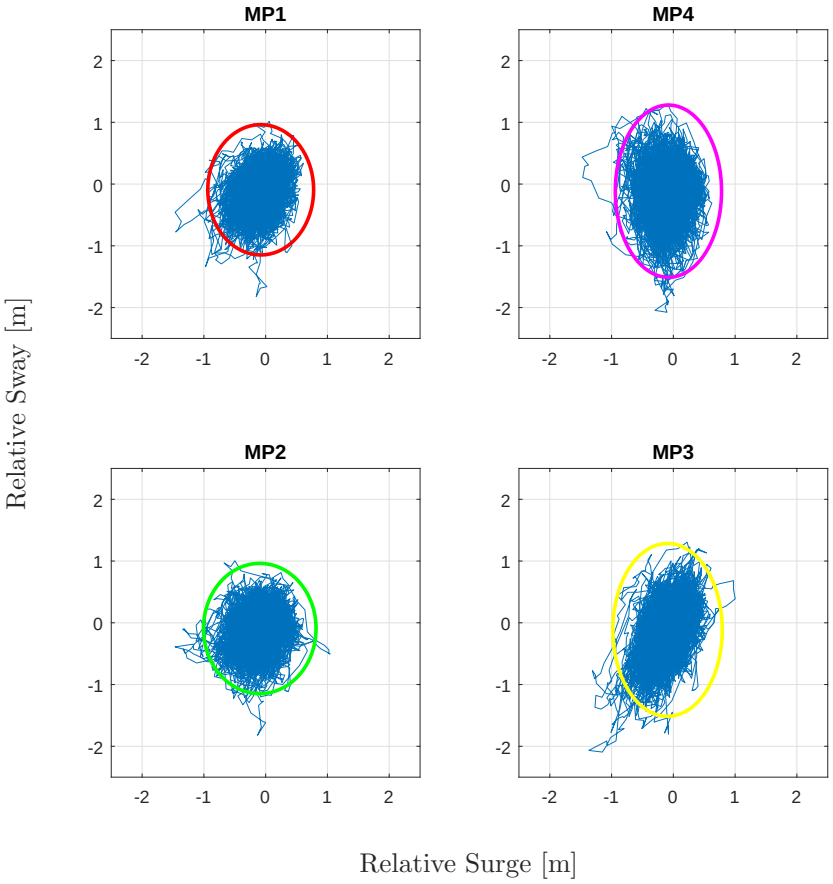

Figure D.9: Motion at reference points - beam sea - BBS-Z-001

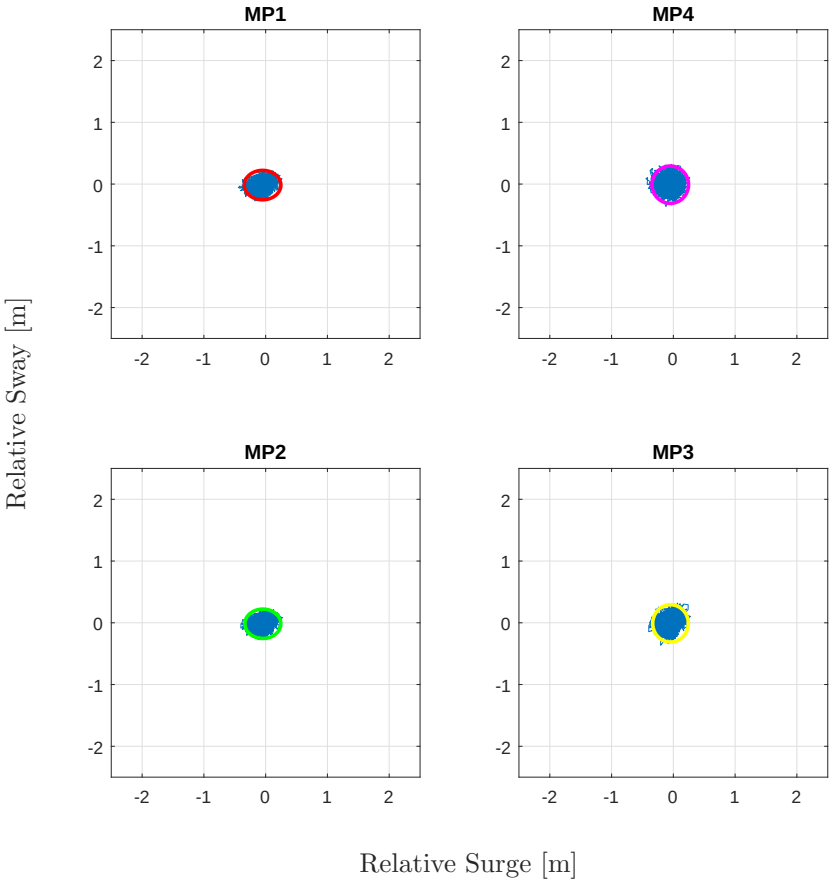

Figure D.10: Motion at reference points - quartering sea - BQS-V-003

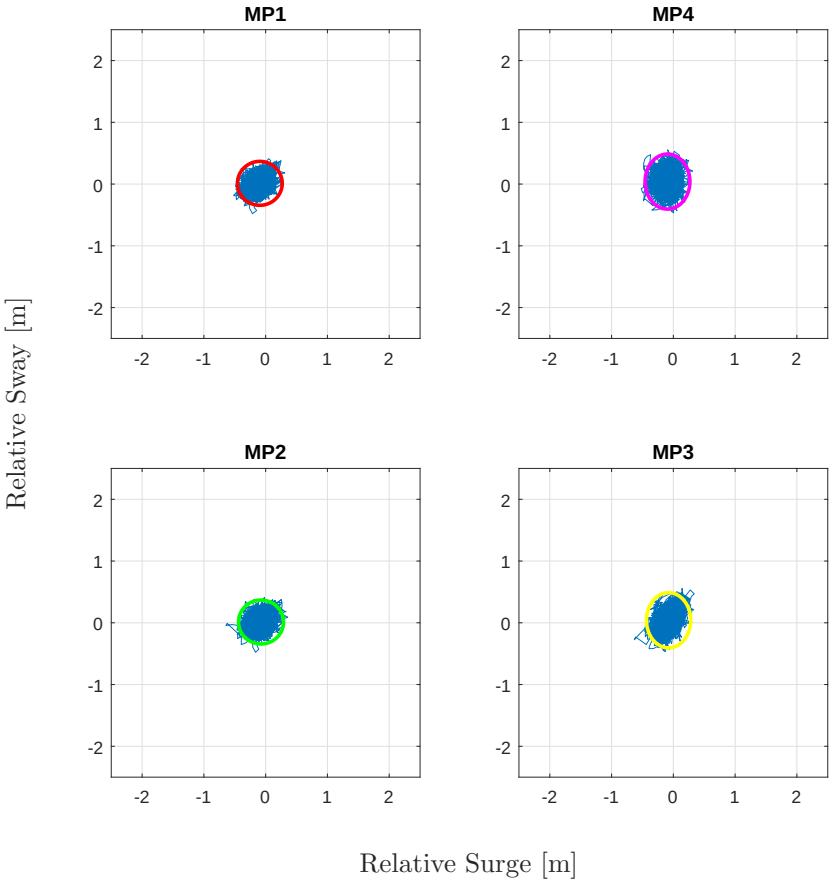

Figure D.11: Motion at reference points - quartering sea - BQS-W-001

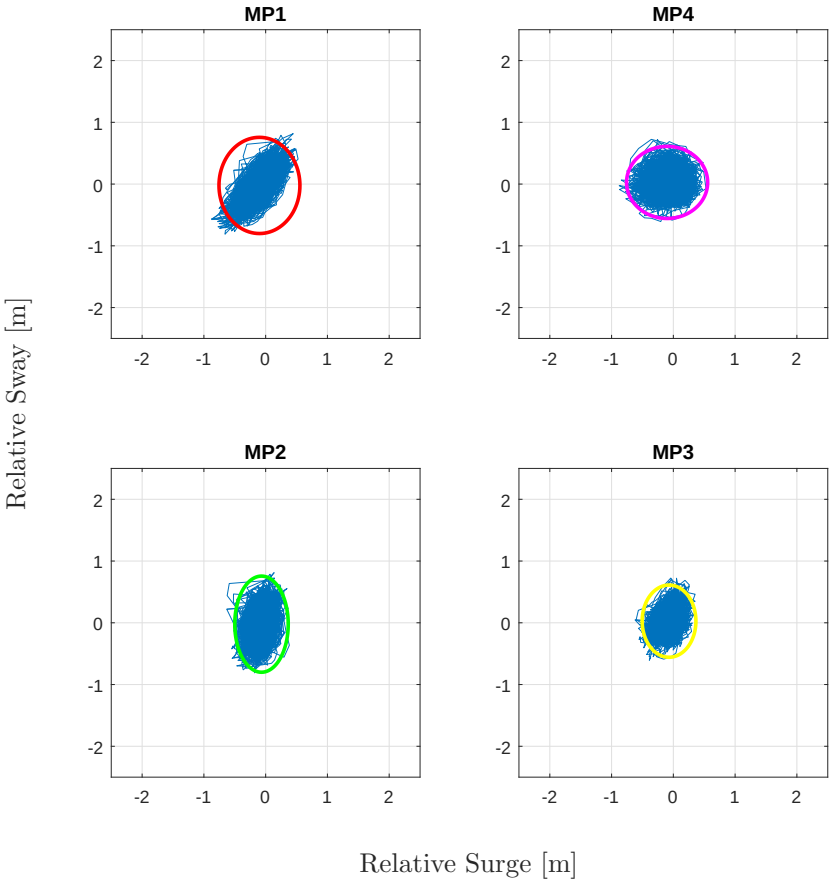

Figure D.12: Motion at reference points - quartering sea - BQS-X-001

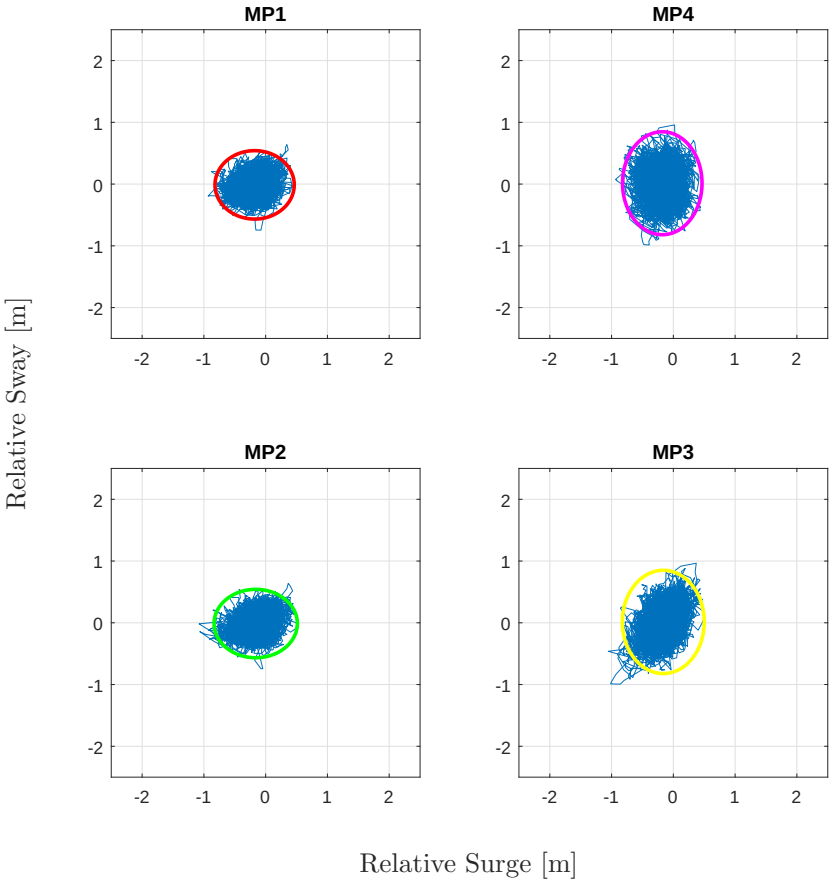

Figure D.13: Motion at reference points - quartering sea - BQS-Y-001

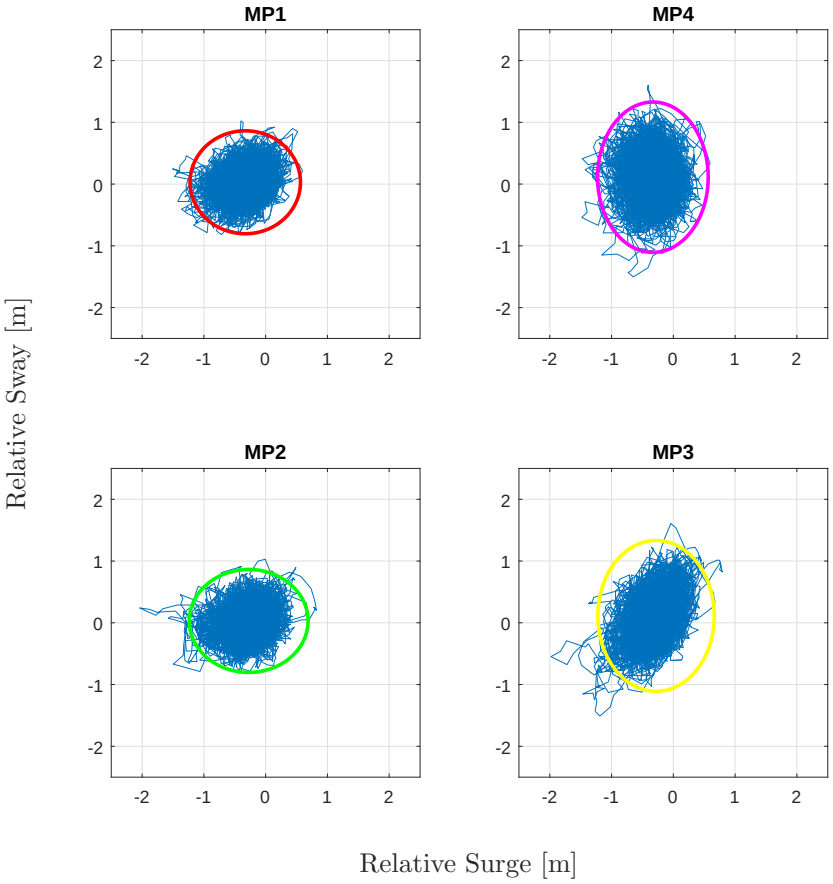

Figure D.14: Motion at reference points - quartering sea - BQS-Z-001

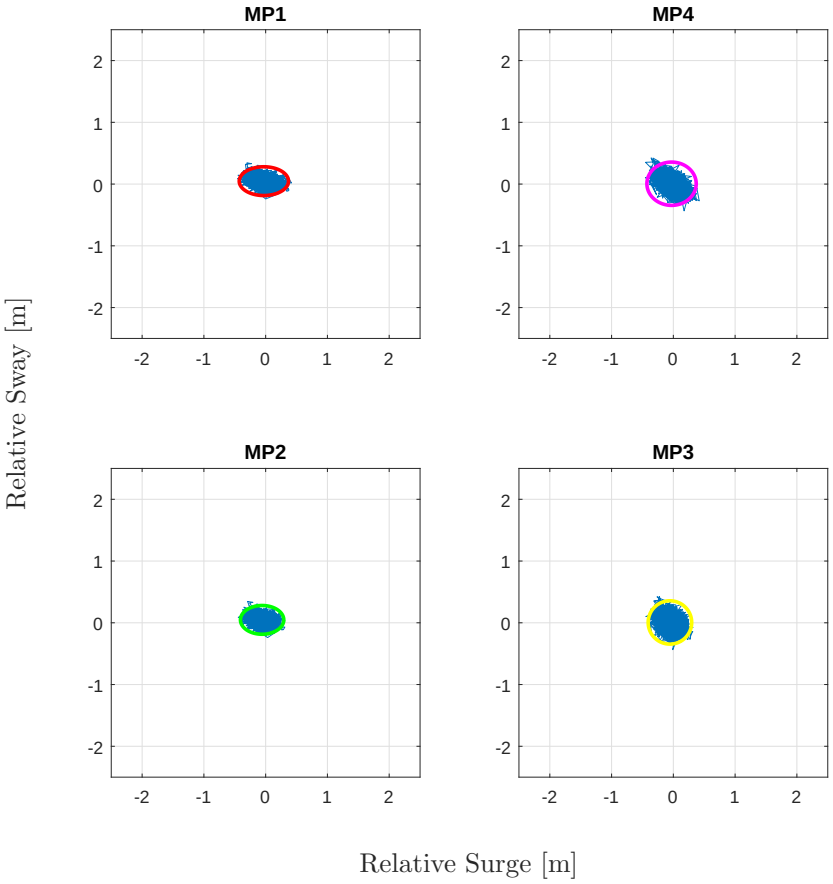

Figure D.15: Motion at reference points - head sea - BHS-V-001

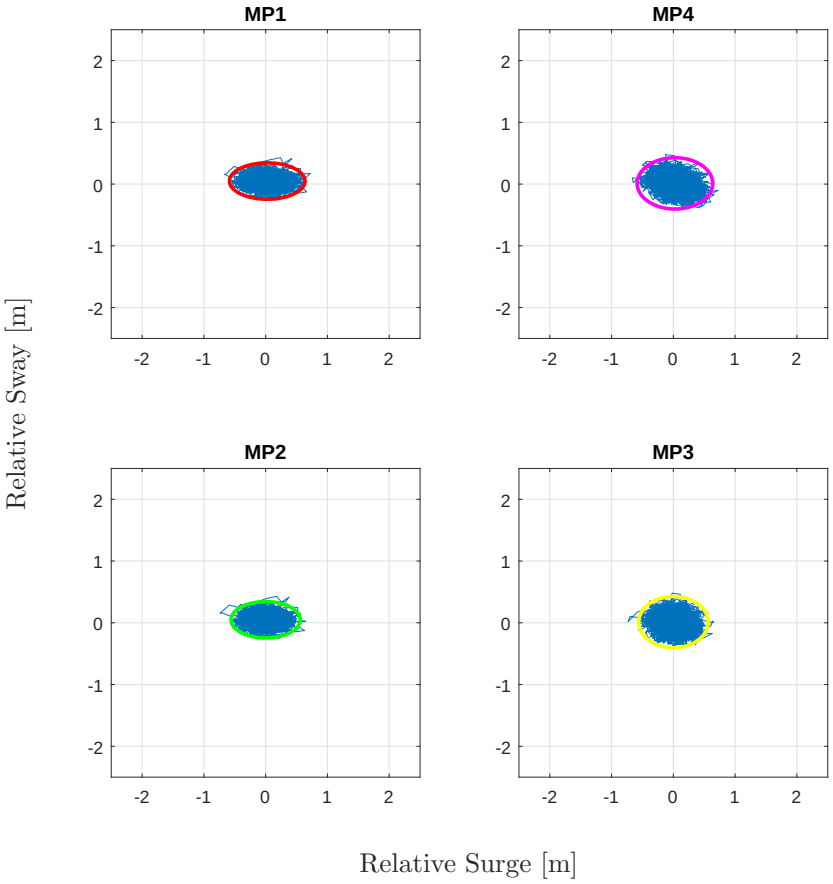

Figure D.16: Motion at reference points - head sea - BHS-W-001

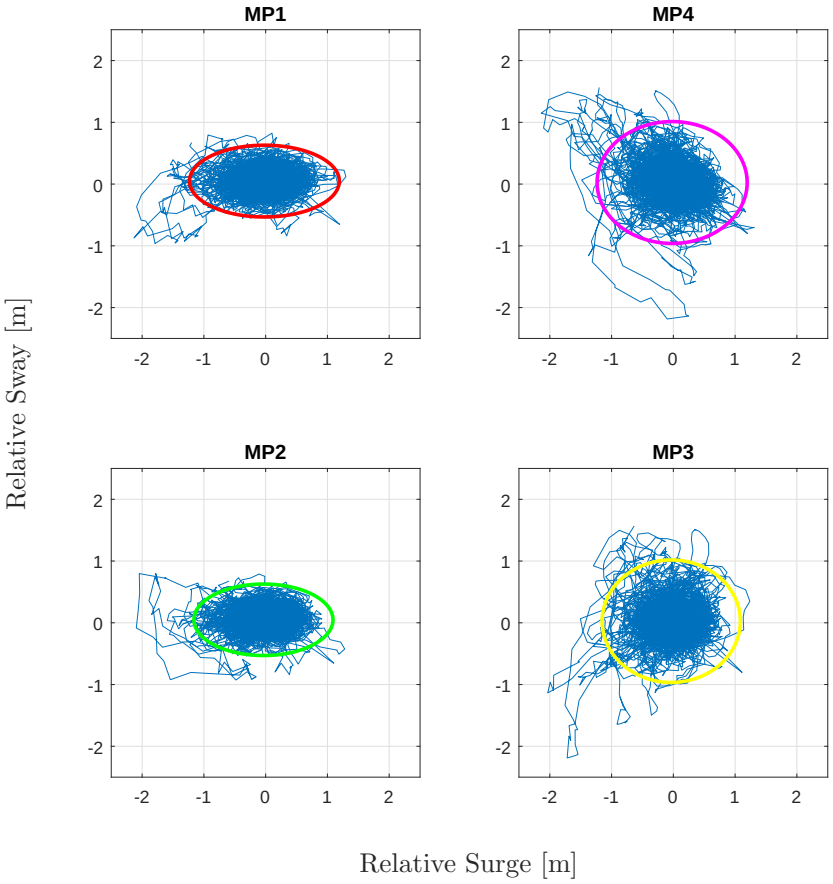

Figure D.17: Motion at reference points - head sea - BHS-X-001

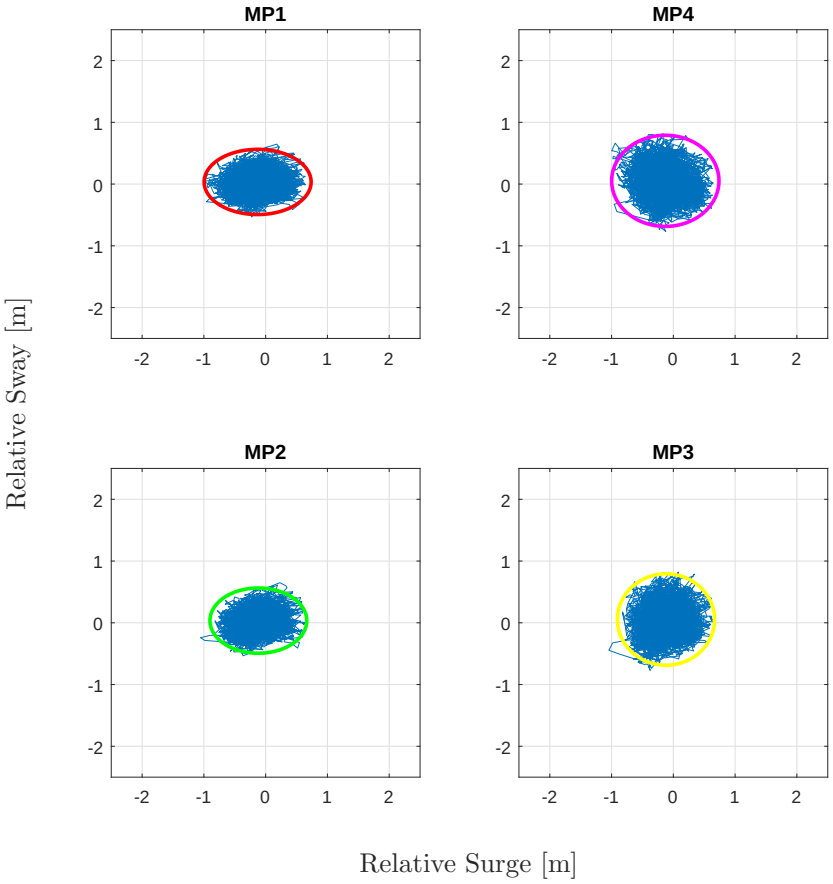

Figure D.18: Motion at reference points - BHS-Y-001

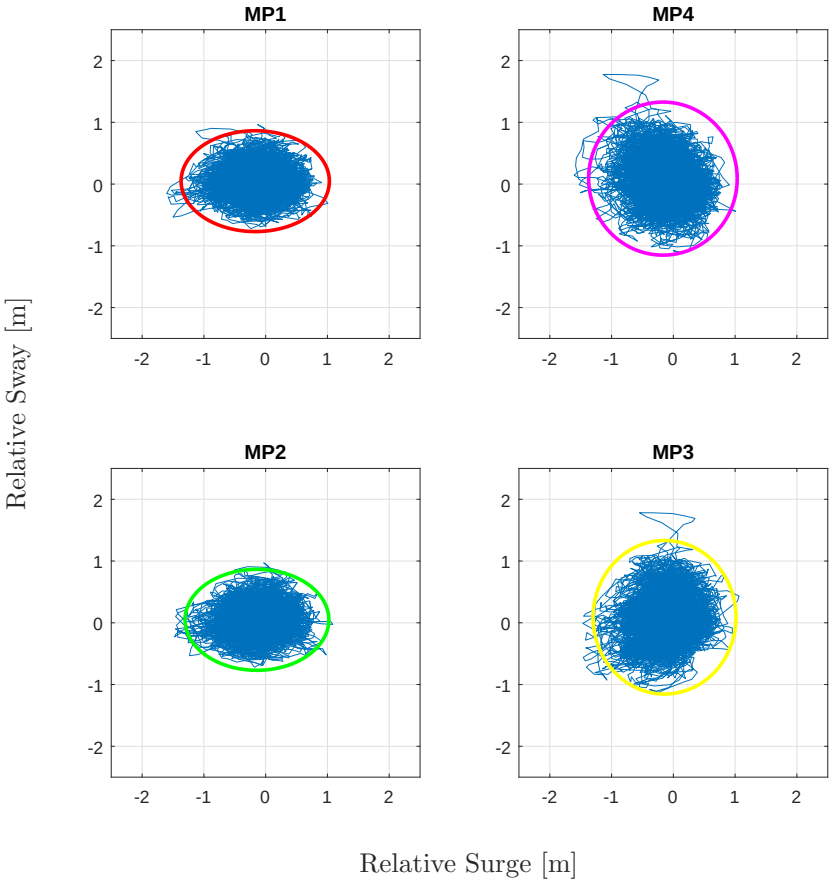

Figure D.19: Motion at reference points - head sea - BHS-Z-001

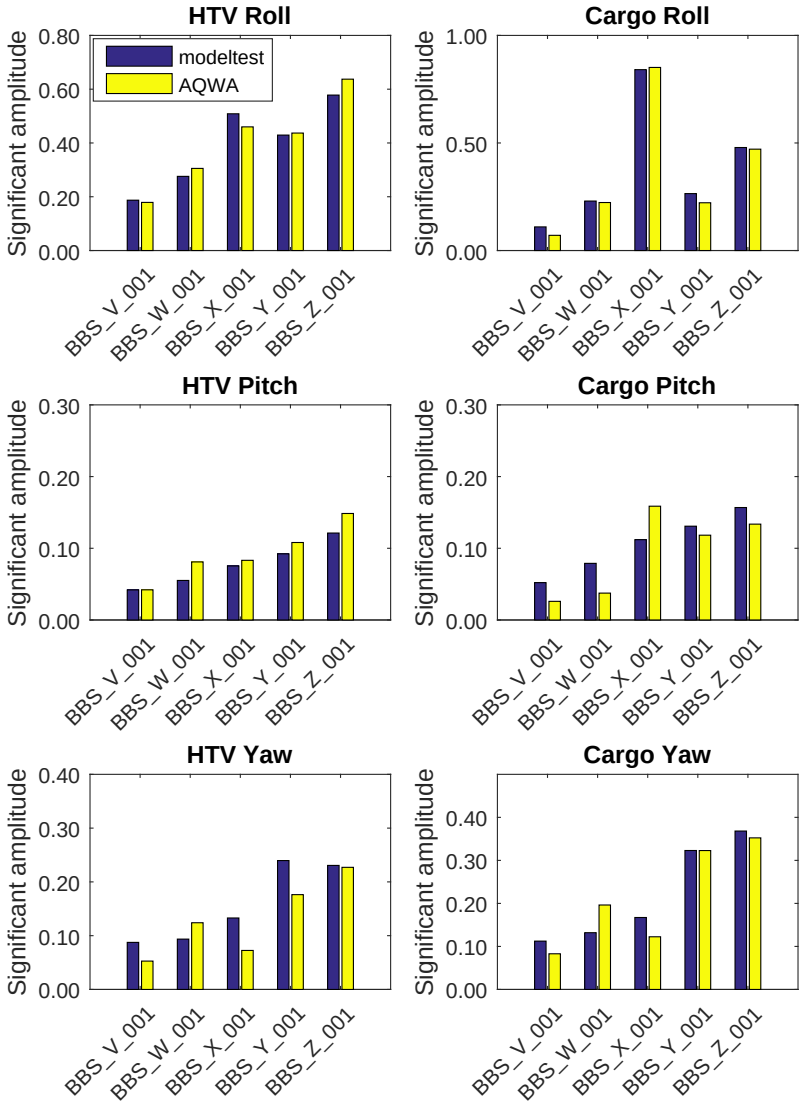

Figure D.20: Comparison model test and simulation - beam sea

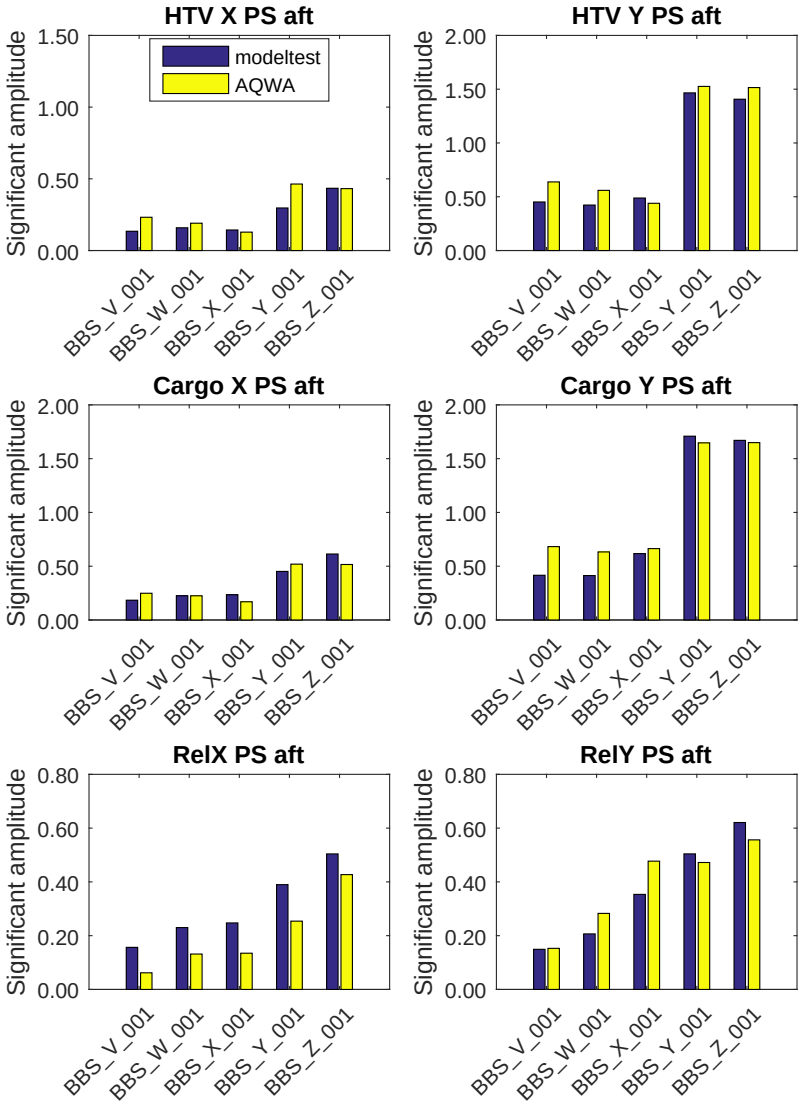

Figure D.21: Comparison model test and simulation - beam sea

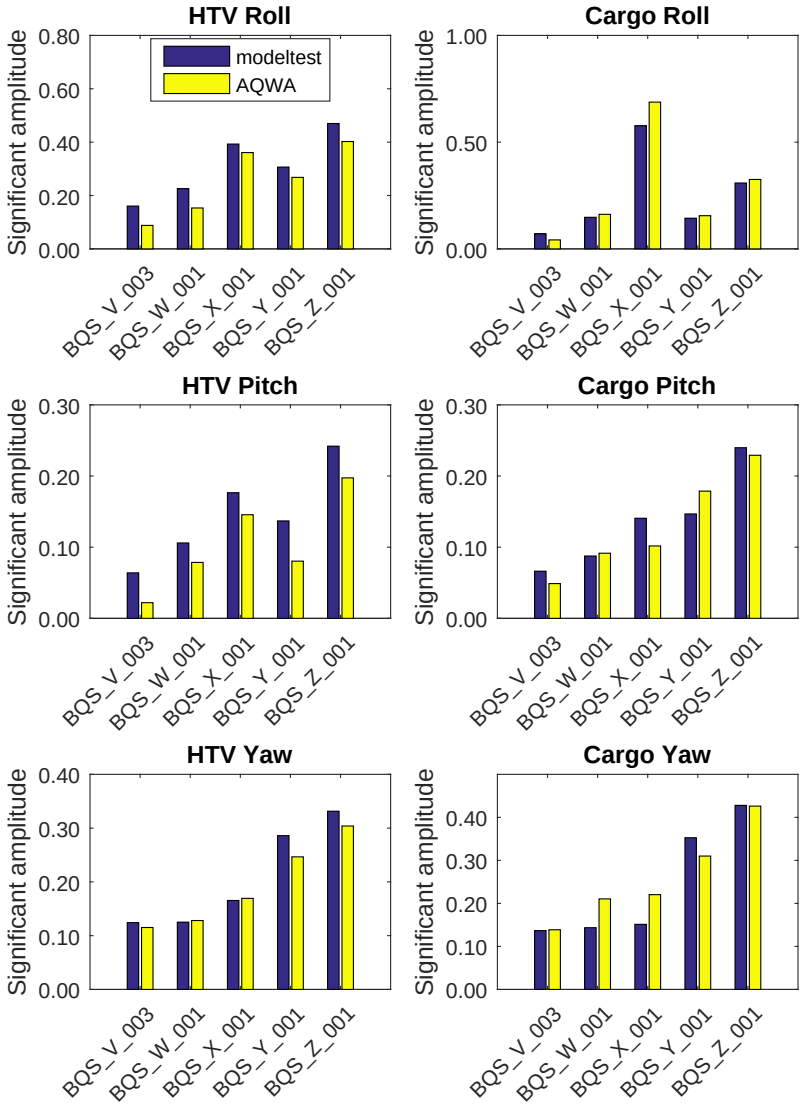

Figure D.22: Comparison model test and simulation - quartering sea

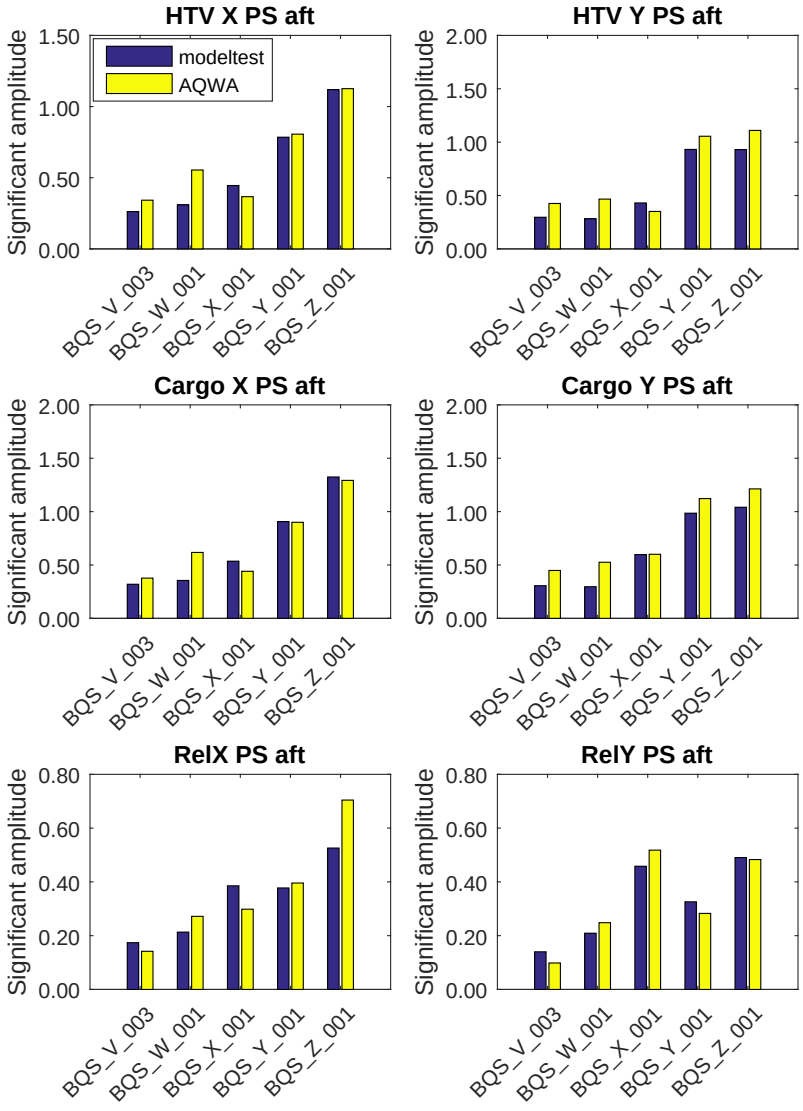

Figure D.23: Comparison model test and simulation - quartering sea

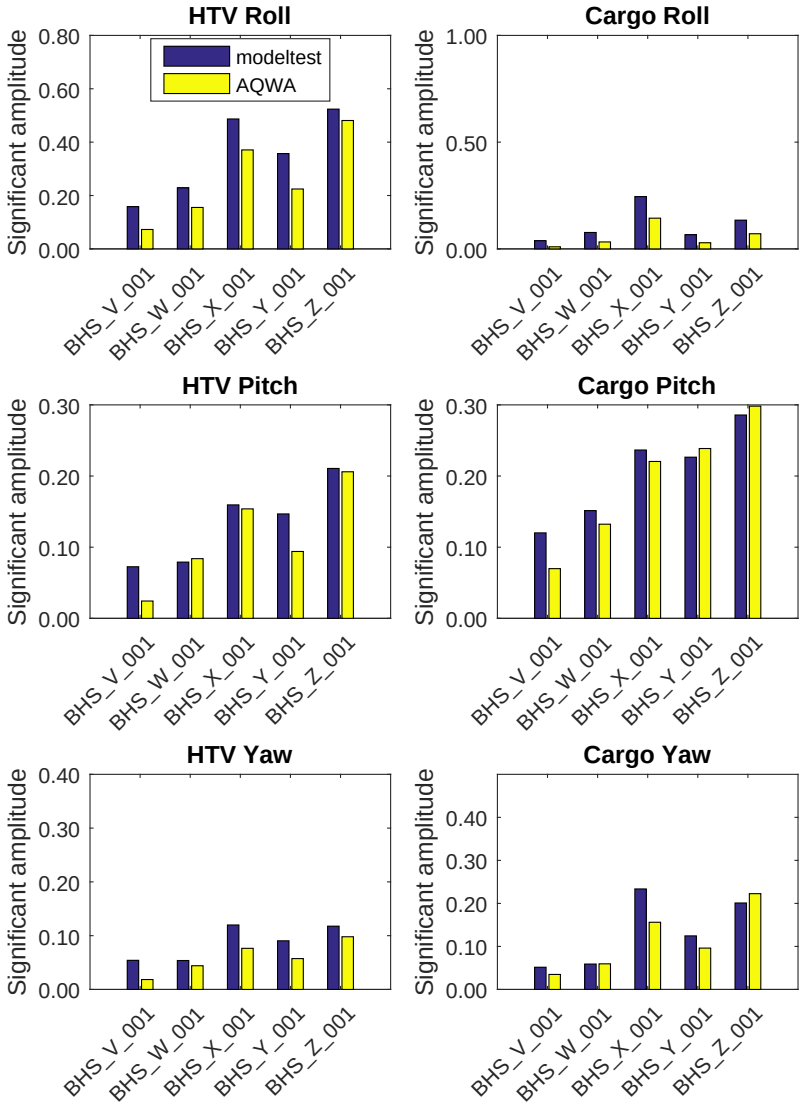

Figure D.24: Comparison model test and simulation - head sea

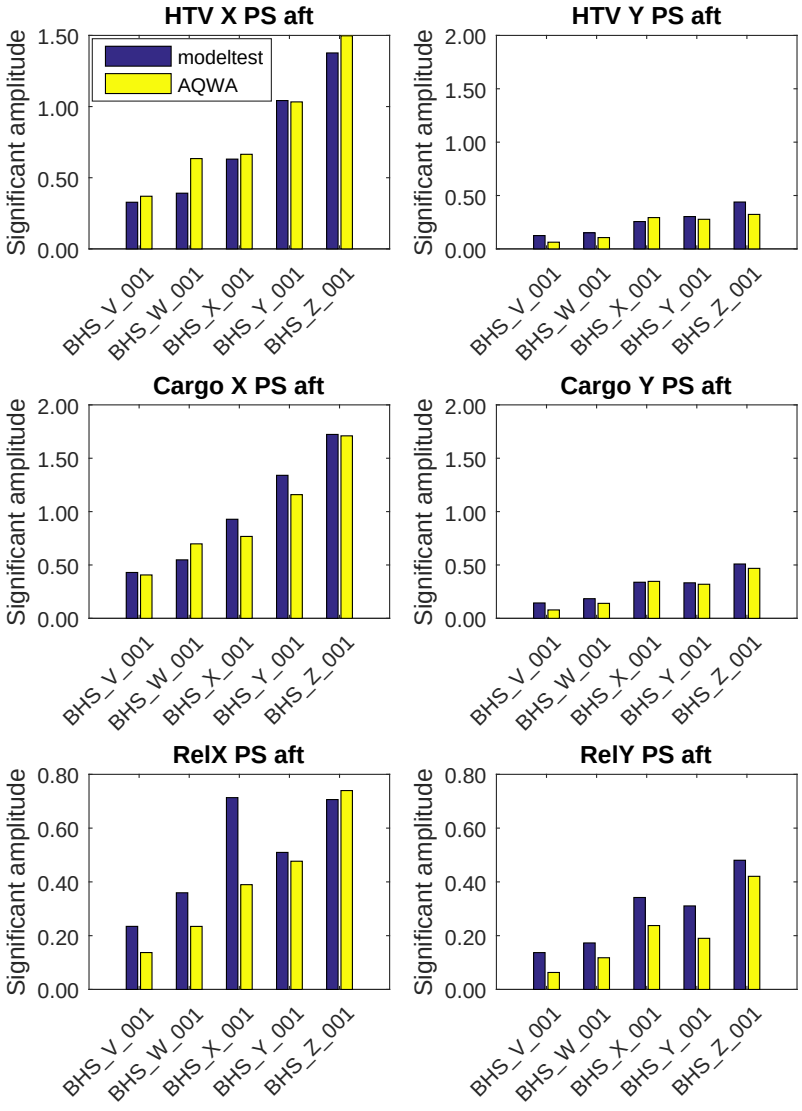

Figure D.25: Comparison model test and simulation - head sea

APPENDIX E

Line Tension Actuator System

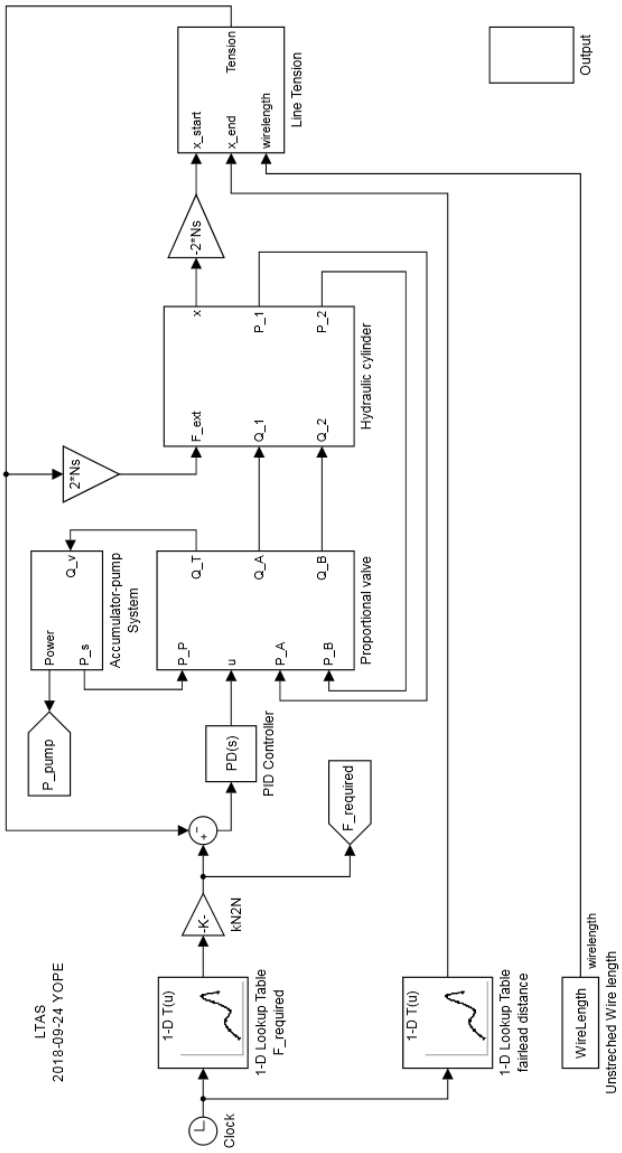

Figure E.1: Simulink model - LTAS

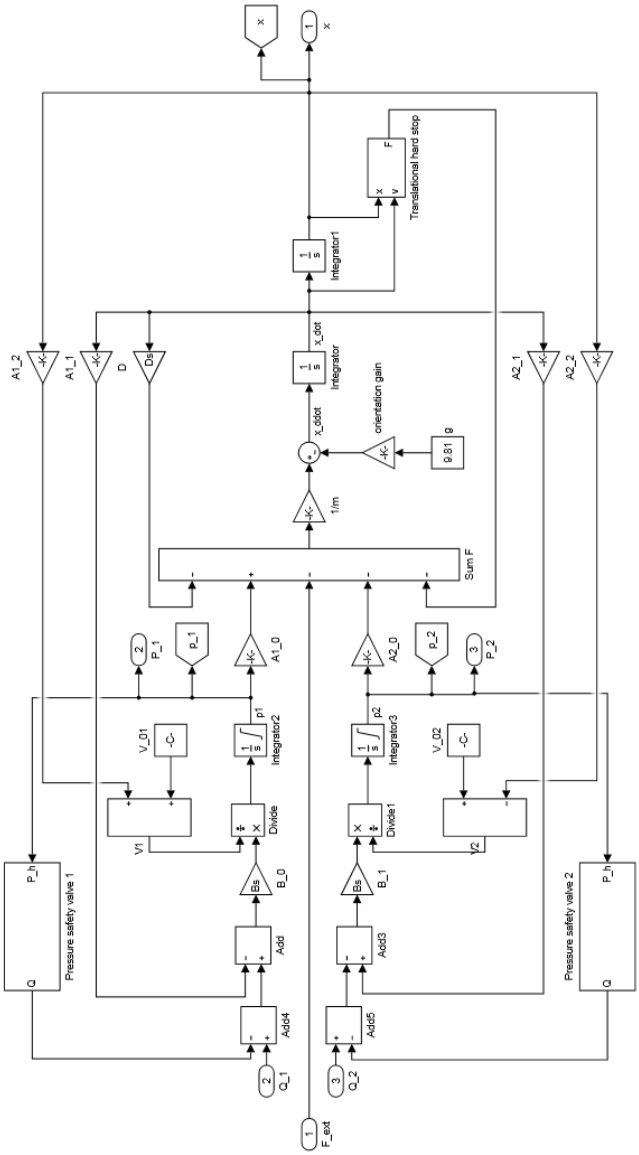

Figure E.2: Simulink model - Cylinder

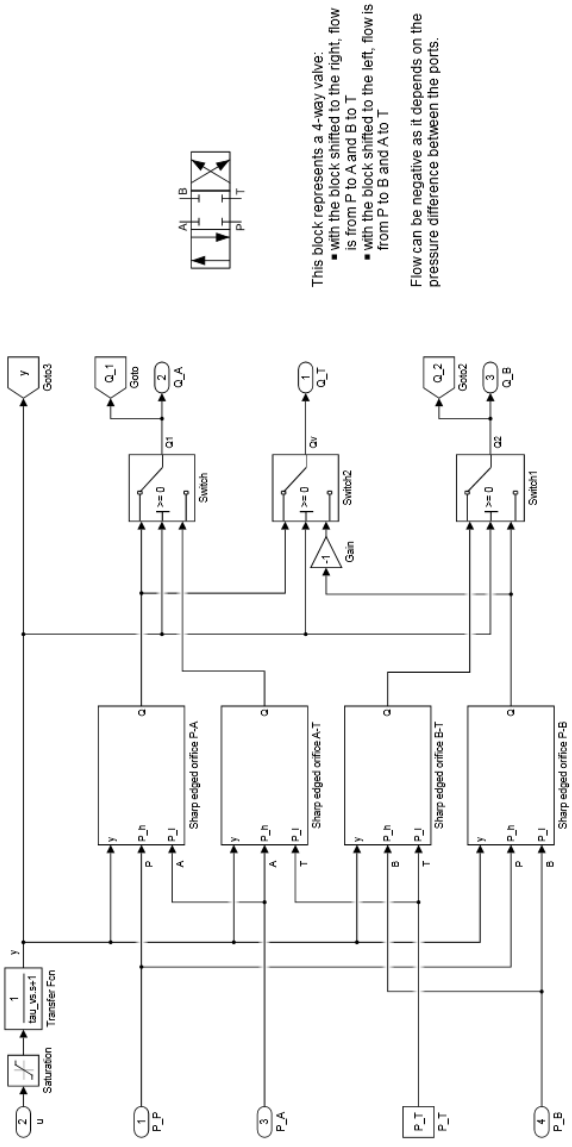

Figure E.3: Simulink model - 4-way valve

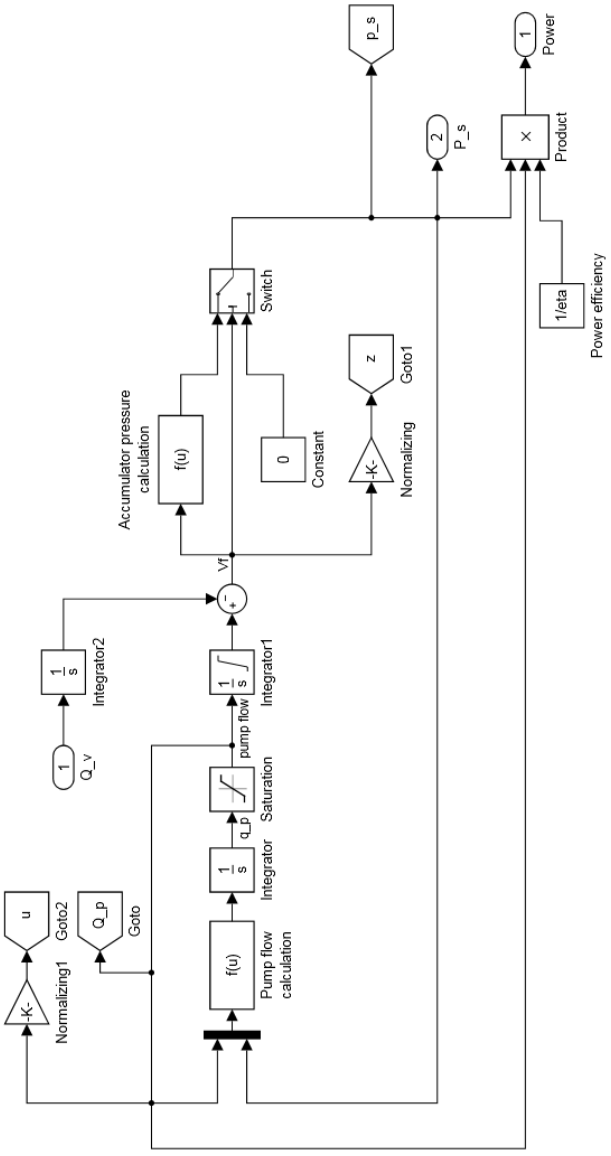

Figure E.4: Simulink model - accumulator pump system

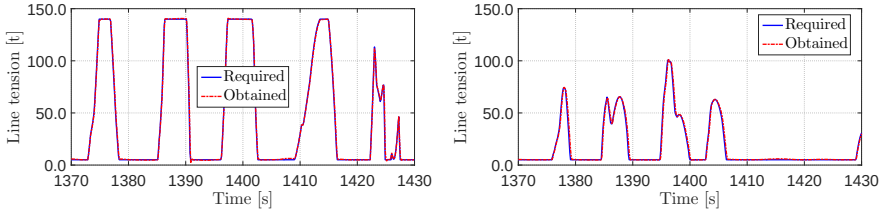

(a) Tension - Line 1

(b) Tension - Line 2

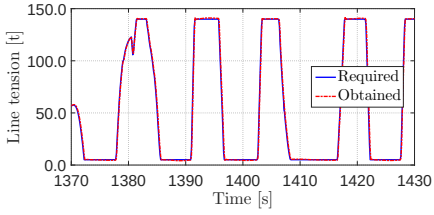

(c) Tension - Line 3

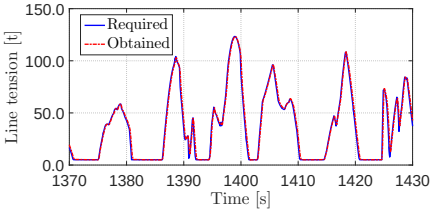

(d) Tension - Line 4

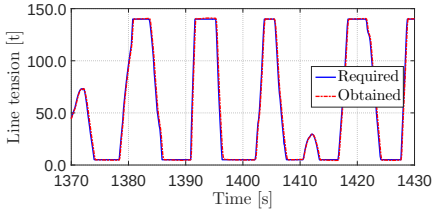

(e) Tension - Line 5

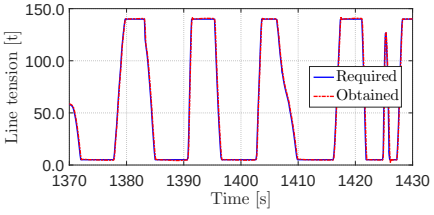

(f) Tension - Line 6

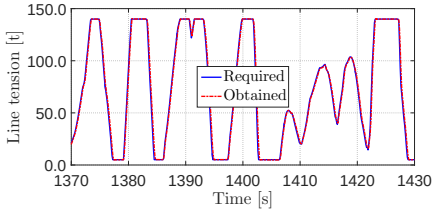

(g) Tension - Line 7

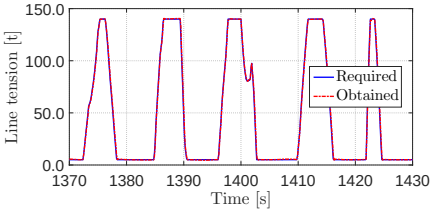

(h) Tension - Line 8

Figure E.5: LTAS performance - tension 1 to 8

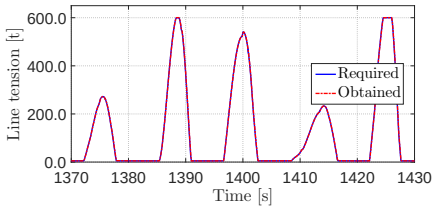

(a) Tension - Line 9

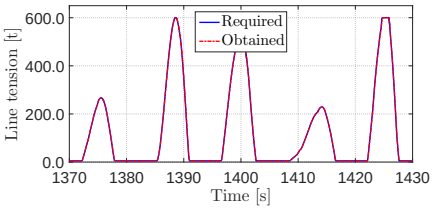

(b) Tension - Line 10

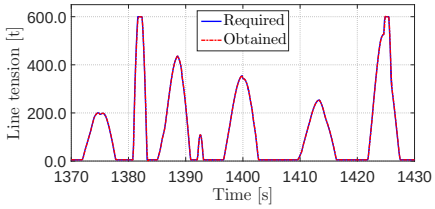

(c) Tension - Line 11

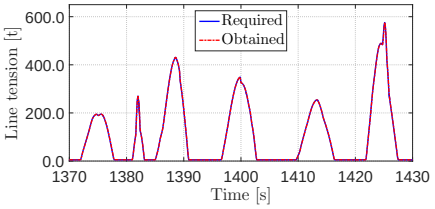

(d) Tension - Line 12

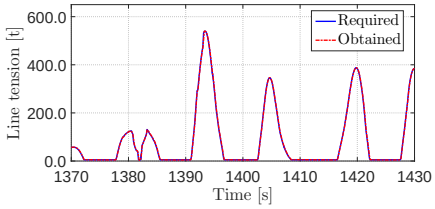

(e) Tension - Line 13

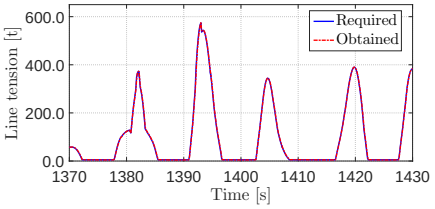

(f) Tension - Line 14

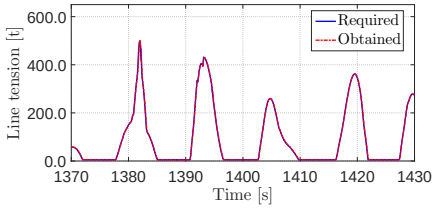

(g) Tension - Line 15

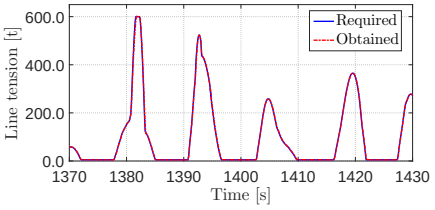

(h) Tension - Line 16

Figure E.6: LTAS performance - tension 9 to 16

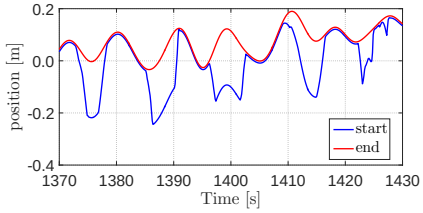

(a) Line end positions - Line 1

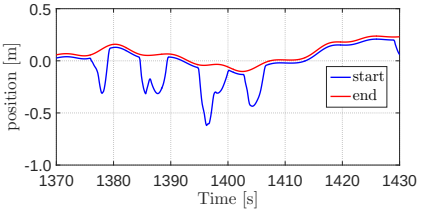

(b) Line end positions - Line 2

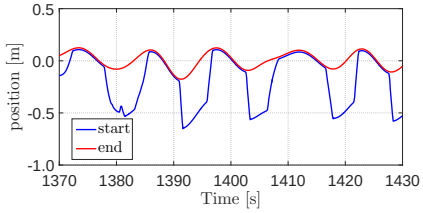

(c) Line end positions - Line 3

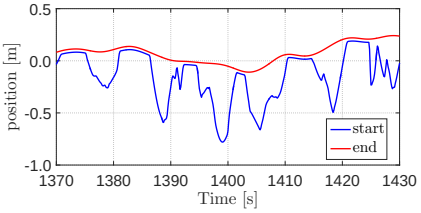

(d) Line end positions - Line 4

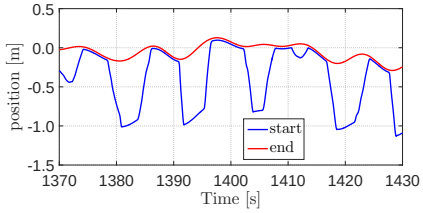

(e) Line end positions - Line 5

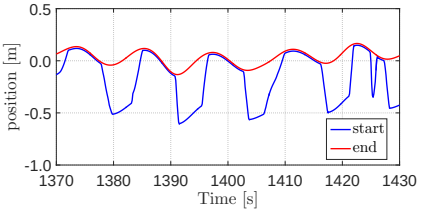

(f) Line end positions - Line 6

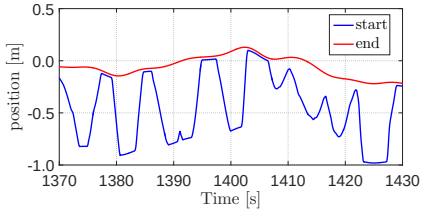

(g) Line end positions - Line 7

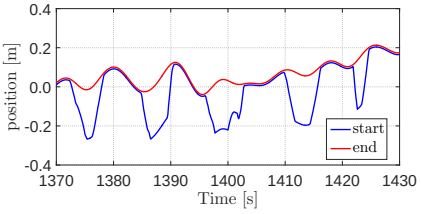

(h) Line end positions - Line 8

Figure E.7: LTAS performance - line end positions 1 to 8

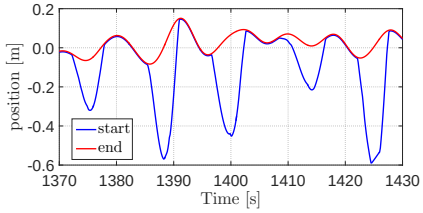

(a) Line end positions - Line 9

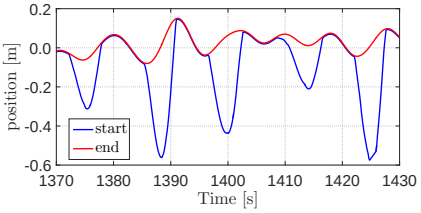

(b) Line end positions - Line 10

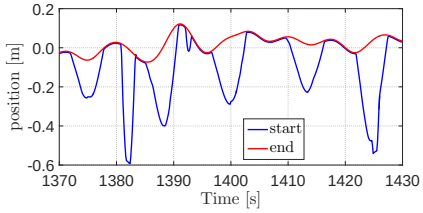

(c) Line end positions - Line 11

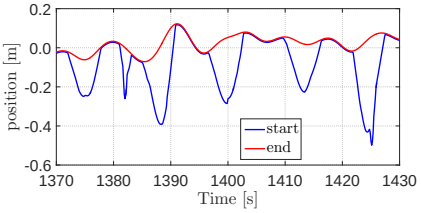

(d) Line end positions - Line 12

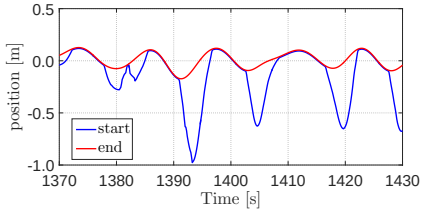

(e) Line end positions - Line 13

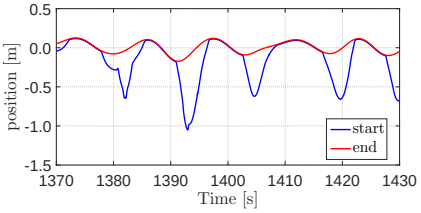

(f) Line end positions - Line 14

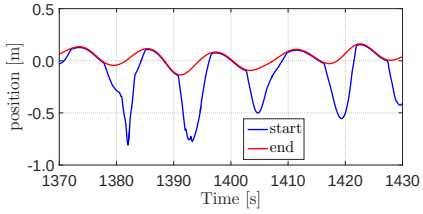

(g) Line end positions - Line 15

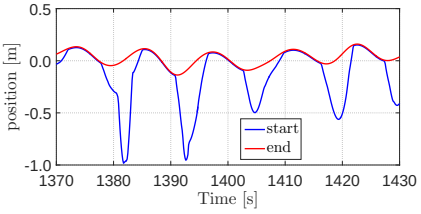

(h) Line end positions - Line 16

Figure E.8: LTAS performance - line end positions 9 to 16

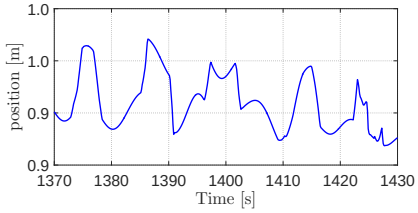

(a) Cylinder position - Line 1

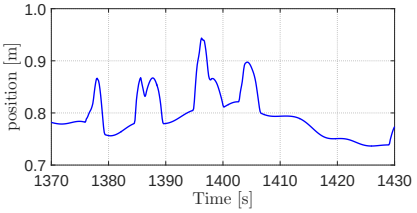

(b) Cylinder position - Line 2

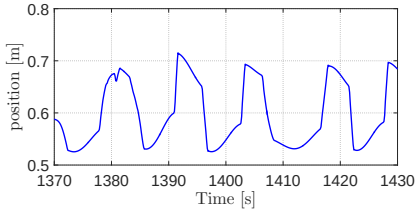

(c) Cylinder position - Line 3

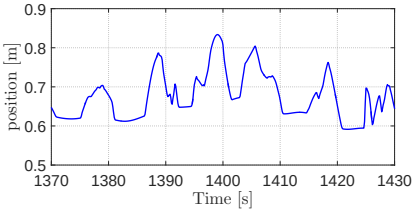

(d) Cylinder position - Line 4

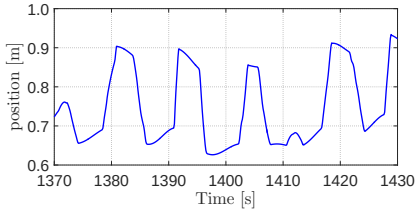

(e) Cylinder position - Line 5

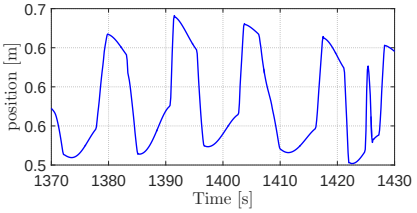

(f) Cylinder position - Line 6

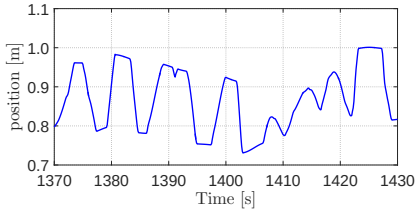

(g) Cylinder position - Line 7

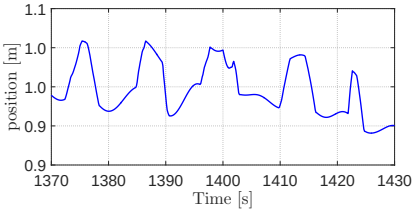

(h) Cylinder position - Line 8

Figure E.9: LTAS performance - cylinder positions 1 to 8

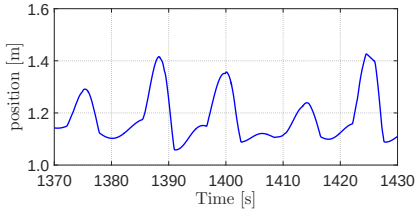

(a) Cylinder position - Line 9

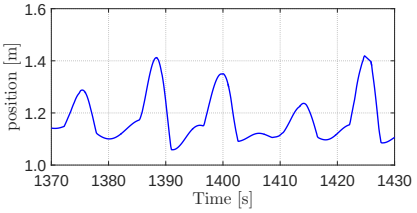

(b) Cylinder position - Line 10

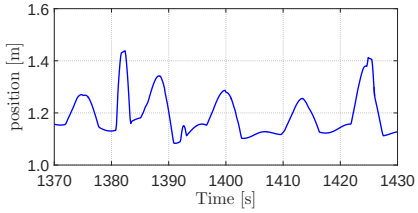

(c) Cylinder position - Line 11

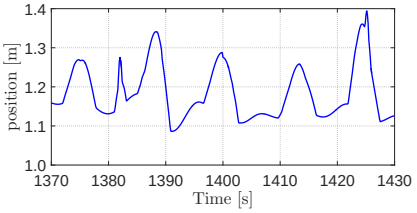

(d) Cylinder position - Line 12

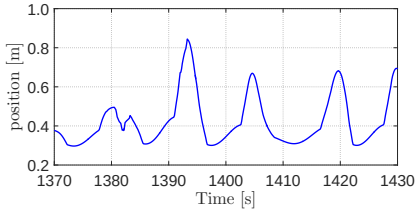

(e) Cylinder position - Line 13

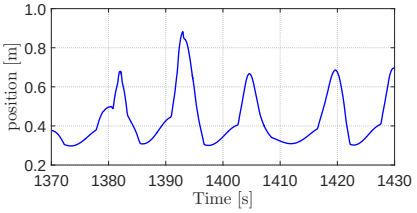

(f) Cylinder position - Line 14

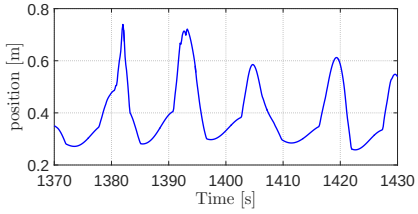

(g) Cylinder position - Line 15

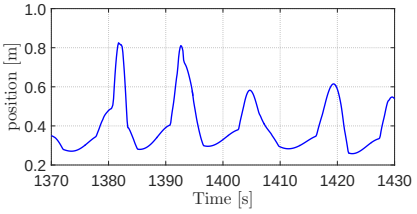

(h) Cylinder position - Line 16

Figure E.10: LTAS performance - cylinder positions 9 to 16

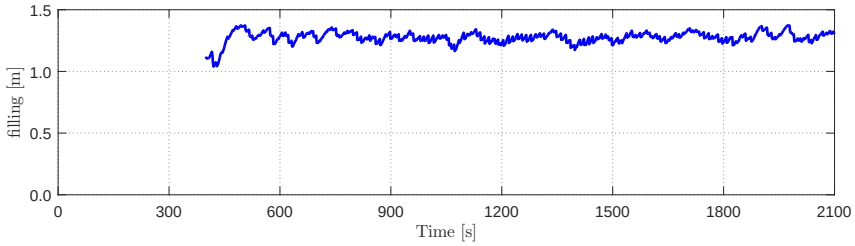

(a) Accumulator filling - Line 1

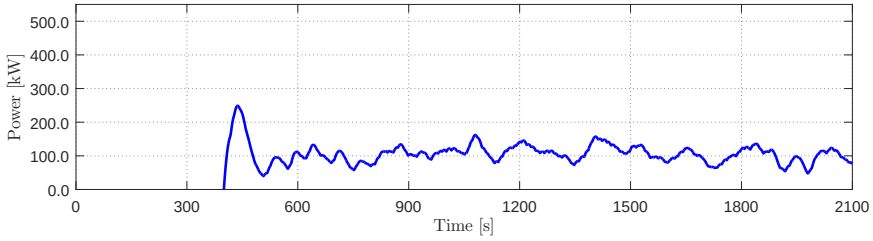

(b) Pump Power - Line 1

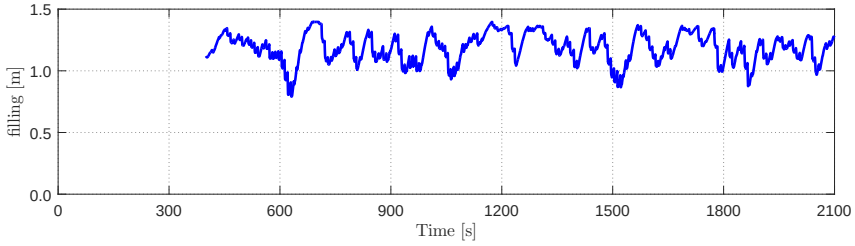

(c) Accumulator filling - Line 2

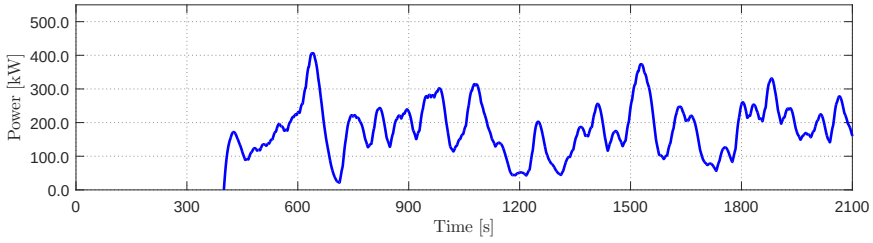

(d) Pump Power - Line 2

Figure E.11: LTAS performance - filling and power 1 and 2

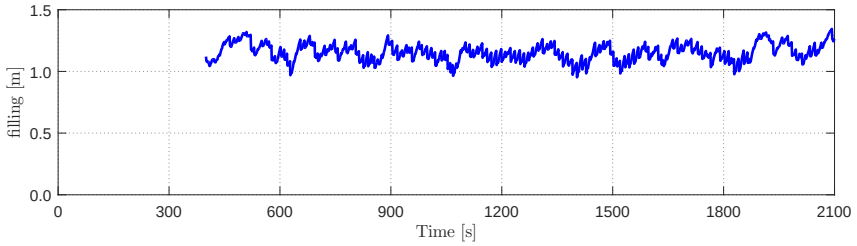

(a) Accumulator filling - Line 3

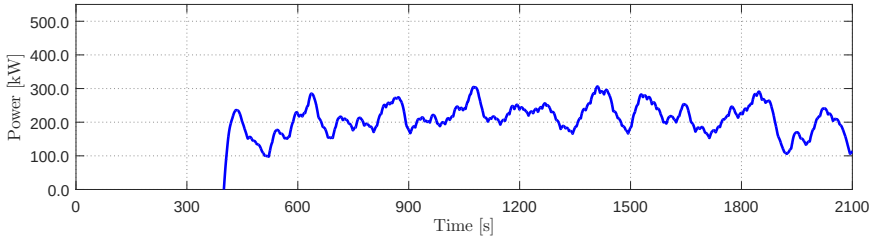

(b) Pump Power - Line 3

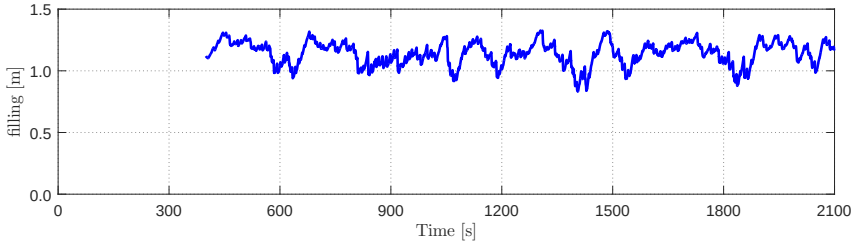

(c) Accumulator filling - Line 4

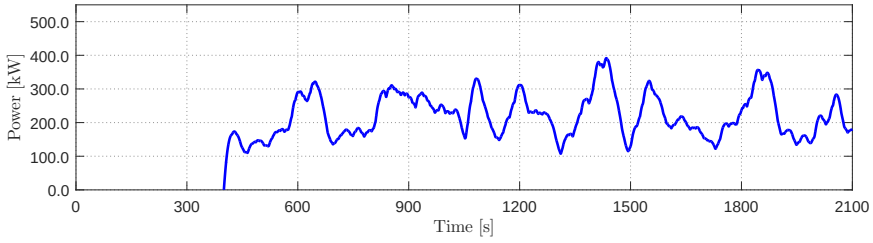

(d) Pump Power - Line 4

Figure E.12: LTAS performance - filling and power 3 and 4

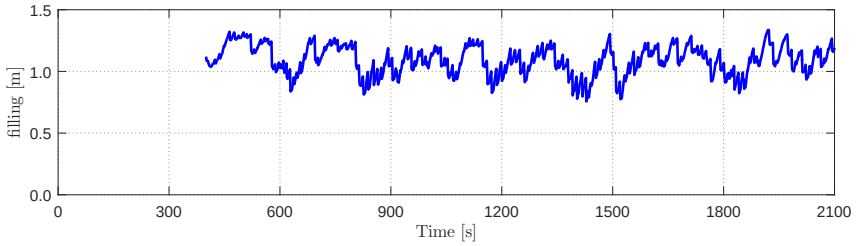

(a) Accumulator filling - Line 5

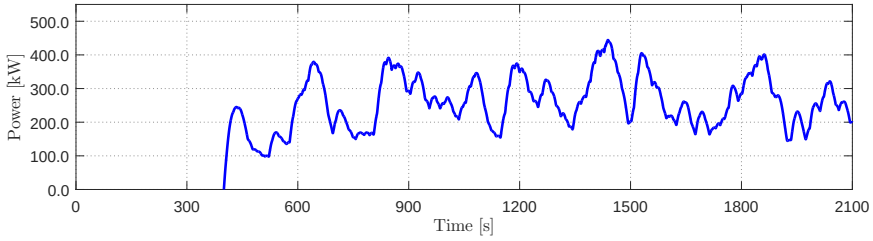

(b) Pump Power - Line 5

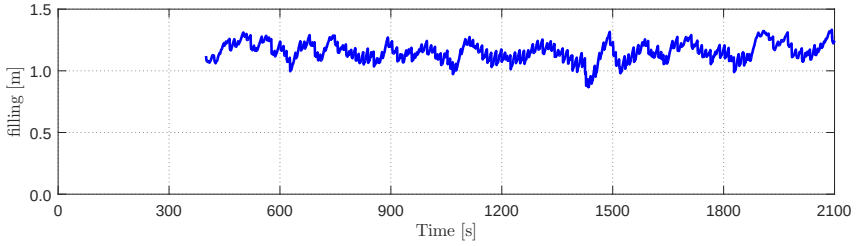

(c) Accumulator filling - Line 6

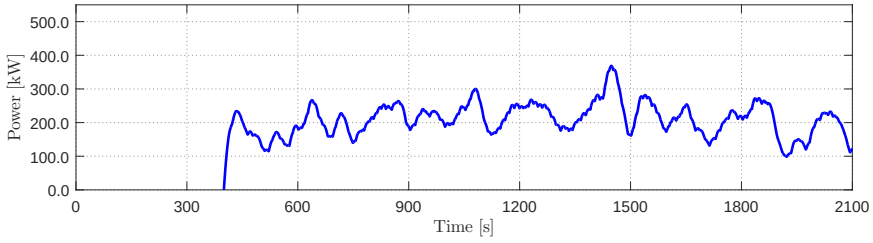

(d) Pump Power - Line 6

Figure E.13: LTAS performance - filling and power 5 and 6

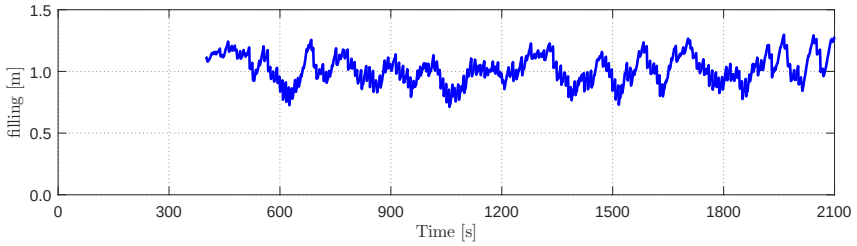

(a) Accumulator filling - Line 7

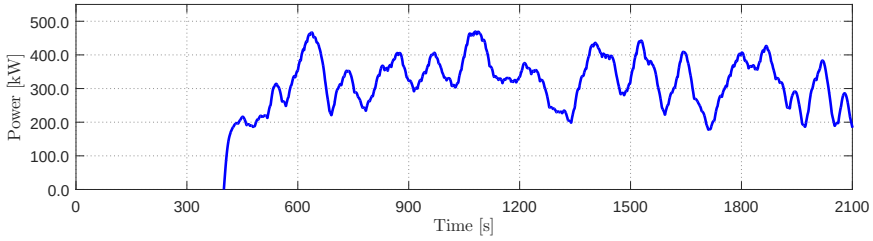

(b) Pump Power - Line 7

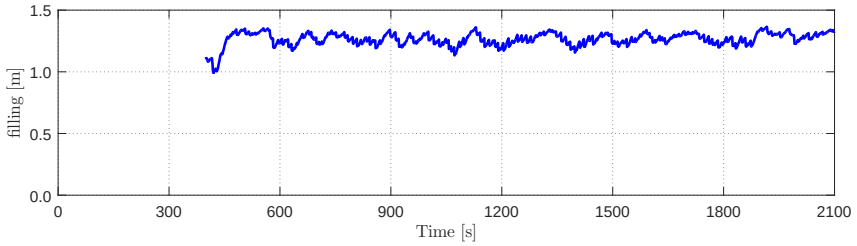

(c) Accumulator filling - Line 8

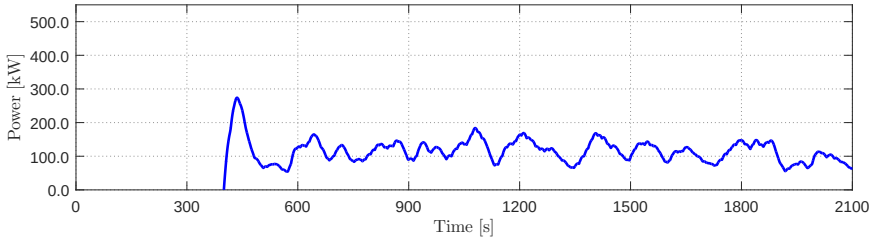

(d) Pump Power - Line 8

Figure E.14: LTAS performance - filling and power 7 and 8

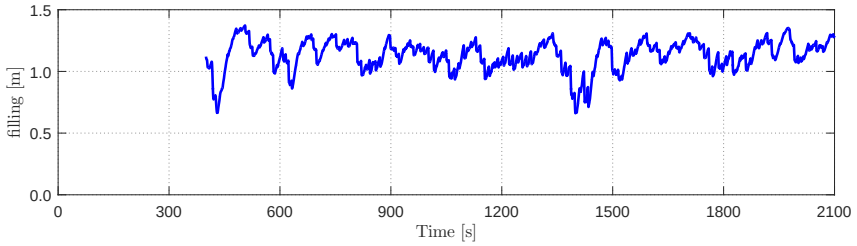

(a) Accumulator filling - Line 9

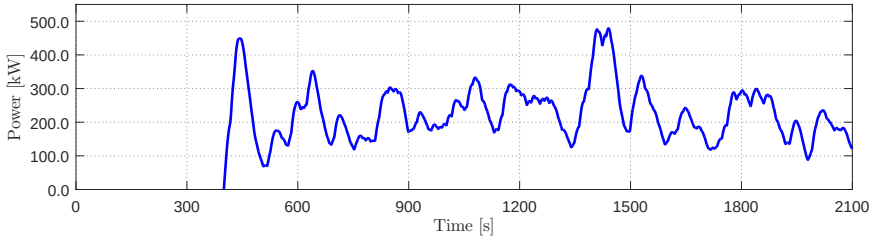

(b) Pump Power - Line 9

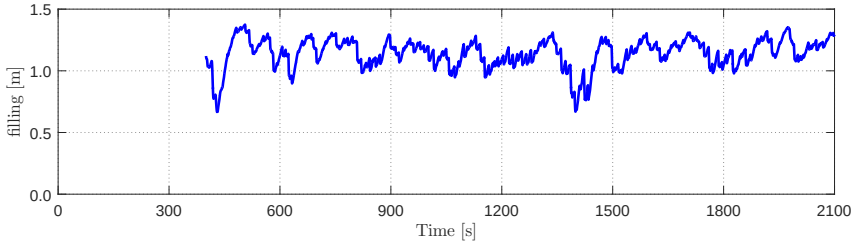

(c) Accumulator filling - Line 10

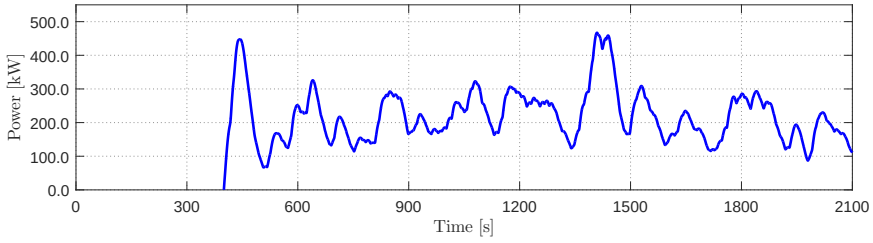

(d) Pump Power - Line 10

Figure E.15: LTAS performance - filling and power 9 and 10

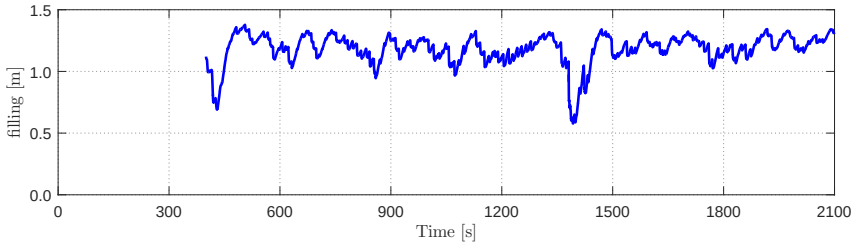

(a) Accumulator filling - Line 11

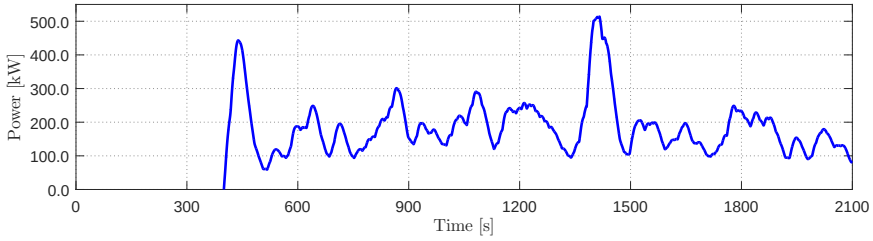

(b) Pump Power - Line 11

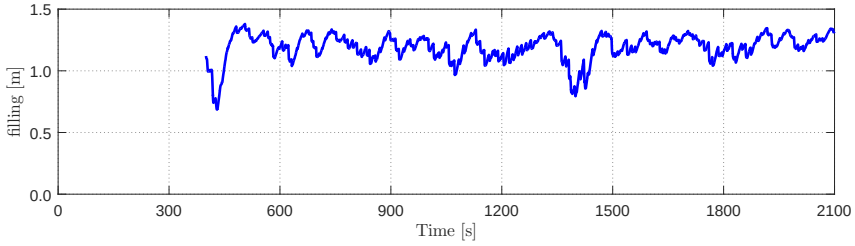

(c) Accumulator filling - Line 12

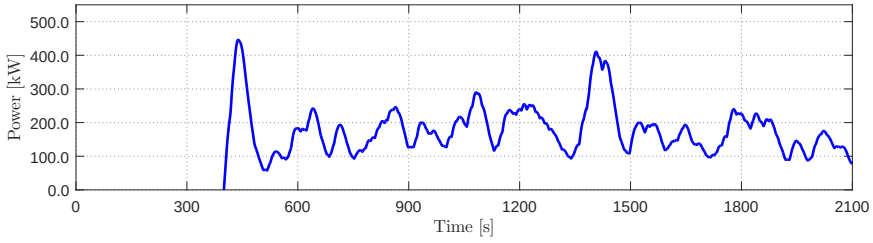

(d) Pump Power - Line 12

Figure E.16: LTAS performance - filling and power 11 and 12

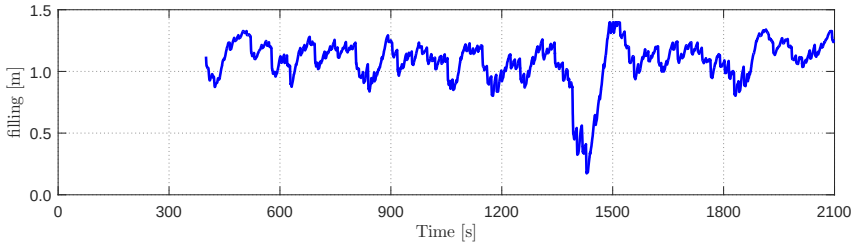

(a) Accumulator filling - Line 13

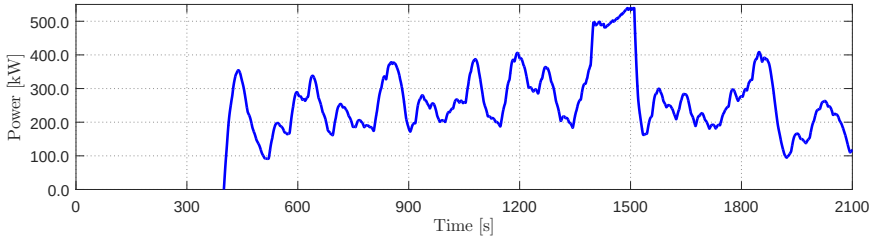

(b) Pump Power - Line 13

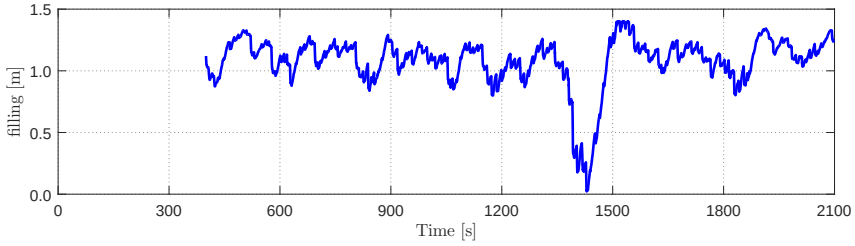

(c) Accumulator filling - Line 14

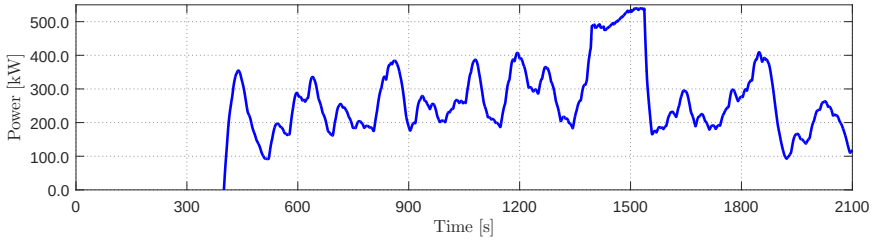

(d) Pump Power - Line 14

Figure E.17: LTAS performance - filling and power 13 and 14

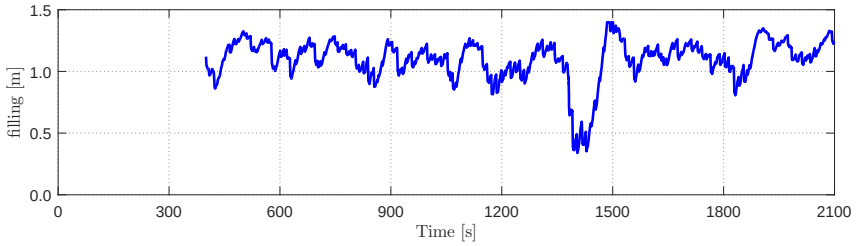

(a) Accumulator filling - Line 15

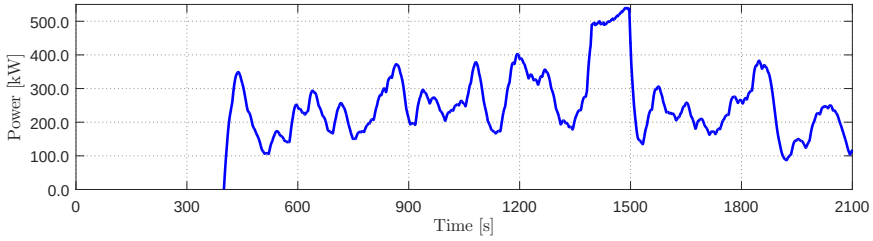

(b) Pump Power - Line 15

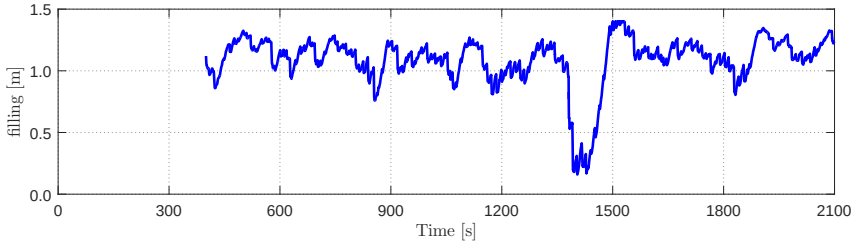

(c) Accumulator filling - Line 16

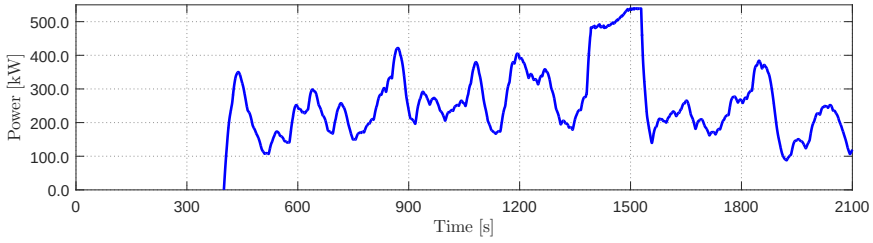

(d) Pump Power - Line 16

Figure E.18: LTAS performance - filling and power 15 and 16

Samenvatting

Het droog transporteren van grote zware drijvende constructies is een belangrijke ontwikkeling in de innovatieve geschiedenis van Heavy Marine Transport. Dit wordt gedaan door dit type lading op het dek van zwareladingschepen te vervoeren. Laden en lossen wordt uitgevoerd door het zwareladingschip af te zinken en de lading boven het dek te positioneren met behulp van lieren. Traditioneel vinden deze operaties plaats op beschutte locaties, zoals havens, waar vrijwel geen golven voorkomen.

Vanaf het begin heeft Heavy Marine Transport de olie- en gasindustrie bediend in de exploratie, ontwikkeling en productiefase van offshore olie- en gasvelden. Zoekend naar het verbeteren van de winstgevendheid van de afgelegen offshore-velden, is het optimaliseren van de fabricage en installatie van faciliteiten essentieel. Het rechtstreeks leveren van de faciliteiten op de afgelegen velden wordt herkend als een potentiële kostenbesparing. Inspectie, onderhoud en reparatie door offshore droogdokken is ook een potentiële kostenoptimalisatie. Beide impliceren dat laad- en losoperaties moeten worden uitgevoerd in niet beschutte gebieden, waar golfcondities wel voorkomen. Het is duidelijk dat het voor een aanvaardbare werkbaarheid van belang is om de dynamische bewegingen nauwkeurig te voorspellen en de afmeer- en handlingequipment te beoordelen en te ontwerpen.

Ervaring en modeltesten hebben aangetoond dat voorspelling van verticale relatieve bewegingen met behulp van industriestandaard software onnauwkeurig was; over het algemeen werden de relatieve verticale bewegingen significant over-voorspeld. Ook heeft het aangetoond dat horizontale relatieve bewegingen te groot zijn om de lading veilig op de ondersteuning te plaatsen, terwijl de standaard handlingequipment wordt gebruikt. Deze problemen hebben geresulteerd in de ontwikkeling van een nauwkeurige methode om relatieve verticale bewegingen te voorspellen en in de ontwikkeling van handling-equipment voor het nauwkeurig positioneren van de lading.

Het eerste deel van het onderzoek richtte zich op de relatieve verticale bewegingen. Op basis van de fundamentele modeltest, CFD-berekeningen en literatuur zijn de sterk niet-lineaire effecten van de squeeze-flow tussen de bodem van de lading en het dek van het transportschip bewezen. De grootste bijdrage aan dit niet-lineaire effect is het veranderen van de toegevoegde massa, afhankelijk van de afstand tussen de bodem van de lading en het scheepsdek. In mindere mate zijn ook viskeuze effecten in termen van wervelvorming aanwezig. Om de toegevoegde massa te bepalen, afhankelijk van de opening, worden lineaire potentiaal stroming programma's gebruikt. Er bestaan echter numerieke problemen voor industrie standaard software, wanneer zeer kleine openingen worden geanalyseerd. Verschillende methoden zijn onderzocht om de nauwkeurigheid van het voorspellen van de toegevoegde massa te verbeteren.

Validatie met geforceerde oscillatietesten toonde een goede overeenkomst tussen meting en simulatie. Ook wordt een grote reductie van de verticale beweging voor een vrij drijvende object getoond wanneer de niet-lineaire effecten worden meegenomen.

Het tweede deel van het onderzoek omvat de ontwikkeling van systemen om de horizontale relatieve bewegingen ten opzichte van de bewegingen als gevolg van het gebruik van standaardapparatuur aanzienlijk te verminderen. Bij het ontwerpen van de systemen, zijn de drie belangrijkste overwegingen, namelijk het creëren van een stijve verbinding en / of demping van de bewegingen en / of het toepassen van actieve besturing. Dit heeft geleid tot twee concepten.

Het eerste concept is het Clamping System, dat is gebaseerd op het creëren van een stijve verbinding waarbij de stijfheid overeenkomt met een structurele ondersteuning. Om dit veilig te realiseren zonder de lading te beschadigen, moet het systeem overstappen van een slappe naar een stijve verbinding. Dit wordt bereikt door een hydraulische cilinder in een fender aan te brengen. De cilinder bevat een regelklep waardoorheen de hydraulische vloeistof stroomt wanneer de fender wordt ingedrukt, en het bevat een terugslagklep waardoorheen de hydraulische vloeistof stroomt wanneer fender zich uitdrukt. Door het regelventiel van de cilinder geleidelijk te sluiten, zal de reactiebelasting hoger zijn dan de compressiebelasting van de fender bij compressieslag, terwijl de terugslagklep ervoor zorgt dat de reactiebelasting lager is

dan de compressiebelasting van de fender bij teruggaande slag. Als zodanig wordt voldoende demping gecreëerd om resonerend gedrag te vermijden wanneer de natuurlijke periode van het veranderende systeem de golfexcitatieperioden passeert. Uiteindelijk, wanneer de regelklep volledig gesloten is, wordt een stijve verbinding bereikt.

Het tweede concept is het Line Tension Actuating System (LTAS). Dit systeem komt voort uit het idee om de uitrekking in de afmeerlijnen te compenseren. Een systeem dat zou reageren op lijnspanning zou onstabiel zijn, daarom is een actief systeem met closed-loop-regeling ontwikkeld. Een dergelijk systeem is vergelijkbaar met Dynamic Positioning Systems, maar de LTAS compenseert ook de golffrequente bewegingen. Op basis van gemeten relatieve beweging wordt de vereiste compensatiebelasting bepaald, die wordt toegewezen aan een reeks lijnspanningsactuators. De actuator is gebaseerd op een hydraulische cilinder, waarvan de belasting wordt geregeld met behulp van opgeslagen pneumatische energie. Opgeslagen energie is nodig om hoge belastingen te kunnen uitoefenen, mogelijk tot 600 [t], binnen 2 tot 3 seconden.

Analyses hebben aangetoond dat beide concepten de relatieve horizontale bewegingen op een gecontroleerde en veilige manier kunnen verminderen. Of beide systemen of alleen de LTAS voor een specifieke operatie worden gebruikt, hangt voornamelijk af van het type en / of de omvang van de vracht. De grootte en sterkte van de systemen zal afhangen van toegestane positioneringsoffset, operationele limiet voor zeegaand en structurele sterkte van zowel HTV als lading. Ook moeten operationele aspecten zoals het hanteren van afmeerlijnen door bemanning in overweging worden genomen tijdens het ontwerp van de systemen.

Concluderend, met dit onderzoek is het mogelijk om de relatieve bewegingen tussen HTV en lading tijdens Offshore Loading or Discharge Operations nauwkeurig te voorspellen en om operationele limieten te definiëren en zo de verwerkbaarheid te bepalen.

Acknowledgement

It's been a long road with the familiar ups and downs, but finally I am done with satisfaction and gratitude. First of all I want to thank all the former managers of Dockwise, back in 2008, who gave me the opportunity to start this research. That year the question was raised whether this research could be done as external PhD candidate at the Delft University of Technology. It took a while, but finally in 2010, I could really start.

A special thanks goes to Michel Seij, who is the constant factor through the years in a continuously changing company. Michel, together with Bart Horsten and Ralph Postma, thank you for keeping faith in me and for encouraging me to continue.

Next, I would like to thank all the master students who helped me with this research. I enjoyed giving guidance to you all. Together we have come to the right solution. Thank you Peter Lee, Paul Kieft, Anne Vreeburg, Xuelei Feng and Jelle van Beelen.

Further, my appreciation goes to my promotor Professor René Huijsmans for his guidance and review, to my promotor Sape Miedema for his review and pleasant discussion about topics outside this research and to Professor Riaan van 't Veer for convincing me that I am delivering scientific work. Also, my appreciation goes to Professor Jo Pinkster for his interest, help and discussions. I would also like to thank all the other committee members for spending their valuable time on reviewing my work and for attending my doctoral defence.

Finally, my thanks to my whole family. My father and Lia, whom we dearly miss. My mother, I hope I make you proud. Eric, thanks for your support and interest. But most of all, thanks Manon, my wife, and my kids Puck, Kick and Luiz, for whom I do everything and who are the most important persons in my life.

CurriculumVitea

The author was born in 1971. He grew up in the village of Empel, part of the municipality of 's-Hertogenbosch. In 1990 he passed the VWO exam at the Jeroen Bosch College. In that year the author Maritime Technology went to study at Delft University of Technology, and graduated as a Maritime Engineer in 1997. The graduation work, under the supervision of Prof. dr. ir. J.A. Pinkster was performed for the company, then IHC Gusto Engineering BV. After about 9 years as a Naval Architect specialized in hydrodynamics, he left the company Gusto (then part of SBM Offshore). In 2006, he started as a Senior Marine Engineer at the Dockwise company, where he was offered in 2008 to continue the research on Offshore Loading and Discharge in Heavy Marine Transport. In the meantime, after Boskalis took over Dockwise, the author now works as Specialist Marine Engineer.